Journal of
Mechanics of
Materials and Structures

JOURNAL OF MECHANICS OF MATERIALS AND STRUCTURES

msp.org/jomms

Founded by Charles R. Steele and Marie-Louise Steele

See msp.org/jomms for submission guidelines.

∎msp

FORMULAS FOR THE H/V RATIO OF RAYLEIGH WAVES IN COMPRESSIBLE PRESTRESSED HYPERELASTIC HALF-SPACES

PHAM CHI VINH, THANH TUAN TRAN, VU THI NGOC ANH AND LE THI HUE

This paper concerns the propagation of Rayleigh waves in compressible prestressed elastic half-spaces. The main aim is to derive formulas for the H/V ratio (ellipticity), which is the ratio of the amplitude of the horizontal displacement to the amplitude of the vertical displacement of Rayleigh waves. First, the equation for the H/V ratio is obtained using the secular equation and the relation between the H/V ratio and the Rayleigh wave velocity. Then, formulas for the H/V ratio are derived for a general strain-energy function. They are then specified for some strain-energy functions. Since the H/V ratio is a good tool for nondestructively evaluating the prestresses of structures before and during loading, the obtained formulas will be very useful in practical applications.

1. Introduction

Nowadays, prestressed materials are widely used in many technical applications. Evaluating nondestructively prestresses of structures before and during loading is necessary and important, and the Rayleigh wave is a convenient tool for this task; see, for example, [Hirao et al. 1981; Delsanto and Clark 1987; Makhort et al. 1990; Duquennoy et al. 1999; 2006] (noting that an error in the second paper was corrected by Song and Fu [2007]). First, a Rayleigh wave is generated (excited) and it propagates in the structure of which the prestresses are needed to evaluate. Then its velocity is measured. Based on the explicit secular equations of the Rayleigh wave and the measured values of the Rayleigh wave velocity, an inverse problem is solved to determine the prestresses. Suppose we have in hand the explicit formulas for the Rayleigh wave velocity, then the inverse problem will be much simpler if it is solved by using them, instead of using the secular equations.

As shown recently by M. Junge and Jacobs [Junge et al. 2006], the H/V ratio is more sensitive to the state of stress than the Rayleigh velocity, and, further, in contrast to the Rayleigh velocity, it is reference-free, so the H/V ratio of Rayleigh waves is a more convenient tool than the Rayleigh wave velocity for characterizing the state of stress. When using the H/V ratio, the explicit H/V ratio equations are employed as a mathematical base for extracting the prestresses from measured values of the H/V ratio. The inverse problem will become much simpler if its formulation is based on the explicit H/V ratio formulas. While the explicit secular equation [Dowaikh and Ogden 1991] and the explicit exact formulas for the velocity [Vinh 2011] of Rayleigh waves propagating in compressible prestressed elastic half-spaces have been found, no explicit equations and explicit exact formulas for the H/V ratio have appeared in the literature so far.

The main aim of this paper is to derive the explicit exact H/V ratio formulas for compressible prestressed elastic half-spaces. First, the H/V ratio equation is established by using the secular equation and

Keywords: Rayleigh waves, prestressed half-spaces, H/V ratio, H/V ratio formulas.

the relation between the H/V ratio and the Rayleigh wave velocity. This relation is obtained by using the surface impedance matrix of Rayleigh waves propagating in compressible prestressed half-spaces. Solving analytically the H/V ratio equation, we arrive at the explicit exact H/V ratio formulas which are valid for a general strain-energy function. They are then written down for some specific strain-energy functions. These obtained formulas express directly the H/V ratio in terms of material parameters and prestresses. Since the obtained H/V ratio formulas are totally explicit, they will be a powerful tool for evaluating the prestresses appearing in structures before and during loading.

It is worth noting that the H/V ratio is an important quantity which reflects fundamental properties of the elastic material [Malischewsky and Scherbaum 2004]. Therefore, it can be used for the nondestructive evaluation of the elastic constants of the material as well.

2. Equations for the H/V ratio

Relation between the H/V ratio and the Rayleigh wave velocity. Consider a Rayleigh wave propagating in an elastic half-space $x_2 \geq 0$ with velocity $c > 0$, wave number $k > 0$ in the x_1-direction, and decaying in the x_2-direction. Then, the displacement vector $\boldsymbol{u}$ and the traction vector $\boldsymbol{t}$ at the planes $x_2 =$ constant of the Rayleigh wave are of the form

$$\boldsymbol{u} = \boldsymbol{U}(y)e^{ik(x_1 - ct)}, \quad \boldsymbol{t} = ik\boldsymbol{\Sigma}(y)e^{ik(x_1 - ct)}, \quad y = kx_2. \tag{1}$$

Matrix $\boldsymbol{M}$ is called the surface impedance matrix of the Rayleigh wave if it relates the vectors $\boldsymbol{U}(0)$ and $\boldsymbol{\Sigma}(0)$ by the equality [Ingebrigtsen and Tonning 1969; Chadwick and Smith 1977; Barnett and Lothe 1985; Fu and Mielke 2002; Destrade and Fu 2006]

$$\boldsymbol{\Sigma}(0) = i\boldsymbol{M}\boldsymbol{U}(0). \tag{2}$$

It is well-known that matrix $\boldsymbol{M}$ is Hermitian and it is an important tool for studying the existence and uniqueness of Rayleigh waves in generally anisotropic solids [Barnett and Lothe 1985].

Let the half-space $x_2 \geq 0$ be a compressible prestressed isotropic elastic half-space that is assumed to be deformed from the unstressed half-space $X_2 \geq 0$ by application of a pure homogeneous strain of the form

$$x_1 = \lambda_1 X_1, \quad x_2 = \lambda_2 X_2, \quad x_3 = \lambda_3 X_3, \quad \lambda_i = \text{constant}, \quad i = 1, 2, 3, \tag{3}$$

where $\lambda_i > 0$ are the principal stretches of the deformation. In the deformed configuration, the elastic half-space is characterized by the fourth-order elasticity tensor A_{ijkl} defined as [Dowaikh and Ogden 1991; Vinh 2011; Ogden 1984; Fu and Ogden 2001]

$$
\begin{aligned}
J A_{iijj} &= \lambda_i \lambda_j \frac{\partial^2 W}{\partial \lambda_i \partial \lambda_j}, \\
J A_{ijij} &= \begin{cases} (\lambda_i\, \partial W/\partial \lambda_i - \lambda_j\, \partial W/\partial \lambda_j)\, \lambda_i^2/(\lambda_i^2 - \lambda_j^2) & (i \neq j, \lambda_i \neq \lambda_j), \\ \frac{1}{2}(A_{iiii} - A_{iijj} + \lambda_i\, \partial W/\partial \lambda_i) & (i \neq j, \lambda_i = \lambda_j), \end{cases} \\
J A_{ijji} &= J A_{jiij} = J A_{ijij} - \lambda_i \frac{\partial W}{\partial \lambda_i} \ (i \neq j),
\end{aligned}
\tag{4}
$$

for $i, j \in \{1, 2, 3\}$, $J = \lambda_1 \lambda_2 \lambda_3$, and where $W = W(\lambda_1, \lambda_2, \lambda_3)$ is the strain-energy function per unit volume in the unstressed state, all other components being zero. For simplicity we introduce the following

notations:

$$\alpha_{11} = JA_{1111}, \quad \alpha_{22} = JA_{2222}, \quad \alpha_{12} = JA_{1122},$$
$$\gamma_1 = JA_{1212}, \quad \gamma_2 = JA_{2121}, \quad \gamma_* = JA_{2112}. \tag{5}$$

From the strong-ellipticity condition, α_{ij}, γ_i are required to satisfy the inequalities [Dowaikh and Ogden 1991; Ogden 1984]

$$\alpha_{11} > 0, \quad \alpha_{22} > 0, \quad \gamma_1 > 0, \quad \gamma_2 > 0. \tag{6}$$

According to Dowaikh and Ogden [1991] and Vinh [2011], the Rayleigh wave is a two-component surface wave: $U = [U_1 \, U_2]^T$, $\Sigma = [\Sigma_1 \, \Sigma_2]^T$. The surface impedance matrix M is therefore a 2×2 matrix

$$M = \begin{bmatrix} M_{11} & \hat{M}_{12} + i M_{12} \\ \hat{M}_{12} - i M_{12} & M_{22} \end{bmatrix}, \tag{7}$$

where M_{11}, M_{22}, M_{12}, $\hat{M}_{12} \in \mathbb{R}$. According to Fu and Mielke [2002, (4.2)–(4.4) and (5.4)],

$$M_{22} = M_{11} \sqrt{\frac{\alpha_{22}}{\gamma_2}} \sqrt{\frac{\gamma_1 - X}{\alpha_{11} - X}}, \quad \hat{M}_{12} = 0, \tag{8}$$

where $X = \rho c^2$ and ρ is the mass density at the unstrained state. It has been shown that [Vinh and Seriani 2009; Vinh 2011], if a Rayleigh wave exists, then

$$0 < X < \min\{\alpha_{11}, \gamma_1\}. \tag{9}$$

Suppose that the half-space is free of traction, i.e., $\Sigma(0) = 0$. Then, from (2), (7), and the second part of (8) we have

$$M_{11} \frac{U_1(0)}{U_2(0)} + i M_{12} = 0, \quad -i M_{12} \frac{U_1(0)}{U_2(0)} + M_{22} = 0. \tag{10}$$

These two equations give immediately

$$\left[\frac{U_1(0)}{U_2(0)} \right]^2 = -\frac{M_{22}}{M_{11}}. \tag{11}$$

By κ we denote the H/V ratio: $\kappa = |U_1(0)/U_2(0)|$. From (6), the first part of (8), (9), and (11) it follows that

$$\kappa^2 = \sqrt{\frac{\alpha_{22}}{\gamma_2}} \sqrt{\frac{\gamma_1 - X}{\alpha_{11} - X}}. \tag{12}$$

This is the relation between the H/V ratio and the Rayleigh wave velocity.

Secular equation. According to Dowaikh and Ogden [1991], Fu and Mielke [2002], and Vinh [2011], the secular equation of Rayleigh waves propagating in the x_1-direction and decaying in the x_2-direction is given by

$$\sqrt{\gamma_2} \, [\alpha_{22}(\alpha_{11} - X) - \alpha_{12}^2] \sqrt{\frac{\gamma_1 - X}{\alpha_{11} - X}} + \sqrt{\alpha_{22}} \, [\gamma_2(\gamma_1 - X) - \gamma_*^2] = 0. \tag{13}$$

Equation for the H/V ratio. From (12) it follows that

$$X = \frac{\alpha_{22}\gamma_1 - \alpha_{11}\gamma_2 \kappa^4}{\alpha_{22} - \gamma_2\kappa^4}. \tag{14}$$

Introducing (12) and (14) into (13) yields the H/V ratio equation, namely,

$$(1-d)w^3 + (1-a\theta)w^2 + b\theta(d-\theta)w + b\theta^2(a-1) = 0, \quad w = \kappa^2 \in (0, +\infty), \tag{15}$$

where the dimensionless parameters a, b, d, and θ are defined as

$$a = 1 - \frac{\gamma_*^2}{\gamma_1\gamma_2}, \quad b = \frac{\alpha_{11}\alpha_{22}}{\gamma_1\gamma_2}, \quad d = 1 - \frac{\alpha_{12}^2}{\alpha_{11}\alpha_{22}}, \quad \theta = \frac{\gamma_1}{\alpha_{11}}. \tag{16}$$

It is clear from (16) and (6) that

$$a \le 1 \ (a = 1 \text{ when } \gamma_* = 0), \quad d \le 1 \ (d = 1 \text{ when } \alpha_{12} = 0), \quad b > 0, \quad \theta > 0. \tag{17}$$

As (15) has no positive roots for the case $d = a = 1$ ($\Leftrightarrow \alpha_{12} = \gamma_* = 0$), we consider three remaining possibilities: $d < 1, a < 1$; $d = 1, a < 1$; $d < 1, a = 1$.

When $d < 1, a < 1$ ($\Leftrightarrow \alpha_{12} \ne 0, \gamma_* \ne 0$), (15) can be rewritten as

$$f(w) := w^3 + a_2 w^2 + a_1 w + a_0 = 0, \tag{18}$$

where the coefficients a_k of (18) are given by

$$a_0 = \frac{b\theta^2(1-a)}{d-1}, \quad a_1 = \frac{b\theta(\theta-d)}{d-1}, \quad a_2 = \frac{1-a\theta}{1-d}. \tag{19}$$

For the cases $d < 1, a = 1$ ($\Leftrightarrow \alpha_{12} \ne 0, \gamma_* = 0$) and $d = 1, a < 1$ ($\Leftrightarrow \alpha_{12} = 0, \gamma_* \ne 0$), (15) is respectively equivalent to

$$(1-d)w^2 + (1-\theta)w + b\theta(d-\theta) = 0, \tag{20}$$

and

$$(1-a\theta)w^2 + b\theta(1-\theta)w + b\theta^2(a-1) = 0. \tag{21}$$

The existence of solution of the H/V ratio equations. Because $w = \sqrt{\alpha_{22}/\gamma_2}$ when $\gamma_1 = \alpha_{11}$ ($\theta = 1$), according to (12), in the rest of the paper we assume that $\gamma_1 \ne \alpha_{11}$ ($\theta \ne 1$). Now we introduce the squared dimensionless Rayleigh wave velocity defined as $x = X/\gamma_1$. From (9) it follows that

$$0 < x < 1 \text{ if } 0 < \theta < 1, \quad 0 < x < 1/\theta \text{ if } \theta > 1. \tag{22}$$

In terms of x, the relation (12) is of the form

$$w = \sqrt{b}\,\theta\sqrt{\frac{1-x}{1-\theta x}}. \tag{23}$$

It is not difficult to verify that:

 (i) The mapping defined by (23) is 1-1.
 (ii) If $0 < \theta < 1$, (23) maps $x \in (0, 1)$ to $w \in (0, \sqrt{b}\,\theta)$.
 (iii) If $\theta > 1$, (23) maps $x \in (0, 1/\theta)$ to $w \in (\sqrt{b}\,\theta, +\infty)$.

By w_r we denote a solution of H/V equations which belongs to interval $(0, \sqrt{b}\theta)$ if $0 < \theta < 1$ and belongs to interval $(\sqrt{b}\theta, +\infty)$ if $\theta > 1$. It also called a solution corresponding to a Rayleigh wave.

Since the mapping (23) is 1-1 as mentioned above, it follows that (15) has a solution if and only if (13) does as well. From this fact and [Vinh 2011, Propositions 3 and 6] (see also [Dowaikh and Ogden 1991, Equations (5.19), (5.33), and (5.34)]) we have immediately the following results:

Proposition 1. *Suppose that $d < 1$, $a < 1$ and $\theta > 0$, $\theta \neq 1$, $b > 0$. Then, (18) has a unique root w_r if*

$$a + \sqrt{b}d > 0, \tag{24}$$

otherwise, it has no solution corresponding to a Rayleigh wave.

Proposition 2. *Let $d < 1$ and $\theta > 0$, $\theta \neq 1$, $b > 0$:*

(i) *If*

$$\theta - d > 0, \quad 1 + \sqrt{b}d > 0, \tag{25}$$

   then (20) has a unique root w_r.

(ii) *If (25) is not valid, then (20) has no root corresponding to a Rayleigh wave.*

Applying Proposition 2 for $d := a$, $\theta := 1/\theta$, $b := 1/b$, and $w := 1/w$ we have:

Proposition 3. *Let $a < 1$ and $\theta > 0$, $\theta \neq 1$, $b > 0$:*

(1) *If*

$$1 - a\theta > 0, \quad a + \sqrt{b} > 0, \tag{26}$$

   then (21) has a unique root w_r.

(2) *If (26) is not valid, then (21) has no root corresponding to a Rayleigh wave.*

Proposition 4. *Suppose $d < 1$, $a < 1$, $\theta > 0$, $\theta \neq 1$, $b > 0$, and (24) holds. If (18) has two or three distinct real roots, then its w_r is the largest root.*

Proof. Let $d < 1$, $a < 1$, $\theta > 0$, $\theta \neq 1$, $b > 0$, and (24) holds. If (18) has two or three distinct real roots, then the equation $f'(w) = 0$ has two distinct roots, denoted by $w_{\max}$ and $w_{\min}$, so that either:

(a) $w_{\max} < w_{\min} \leq 0$, or

(b) $w_{\max} < 0 < w_{\min}$ due to $w_{\max} + w_{\min} = -\frac{2}{3}a_2 < 0$ for $0 < \theta < 1$ and $w_{\max}w_{\min} = \frac{1}{3}a_1 < 0$ for $\theta > 1$.

If (a) holds, since $f(w)$ is strictly monotonically increasing in $(0, +\infty)$, $f(0) < 0$ and $f(+\infty) = +\infty$, the equation $f(w) = 0$ has a unique root in $(0, +\infty)$ and it is w_r. If (b) is valid, then $f(w_{\min}) < 0$ because $f(w)$ is strictly monotonically decreasing in $(w_{\max}, w_{\min})$ and $f(0) < 0$. As $f(w)$ is strictly monotonically increasing in $(w_{\min}, +\infty)$, $f(w_{\min}) < 0$, and $f(+\infty) = +\infty$, therefore equation $f(w) = 0$ has a unique root in $(w_{\min}, +\infty)$, so it is a unique root in $(0, +\infty)$ and it is w_r. That means w_r is the largest root. $\qquad\square$

3. Formulas for the H/V ratio for a general strain-energy function

Theorem 5. *If there exists a (unique) Rayleigh wave propagating along the x_1-direction, and attenuating in the x_2-direction in a compressible isotropic elastic half-space subject to a homogeneous initial deformation (Equation (3)), then its squared H/V ratio κ^2 is determined as follows*:

(i) *If $d < 1$, $a < 1$ (i.e., $\alpha_{12} \neq 0$, $\gamma_* \neq 0$), then*

$$\kappa^2 = -\tfrac{1}{3}a_2 + \sqrt[3]{R + \sqrt{D}} + \frac{(a_2^2 - 3a_1)}{9\sqrt[3]{R + \sqrt{D}}}, \tag{27}$$

where each radical is understood as the complex root taking its principal value; R and D are given by

$$R = \tfrac{1}{54}(9a_1a_2 - 27a_0 - 2a_2^3), \quad D = \tfrac{1}{108}(4a_0a_2^3 - a_1^2a_2^2 - 18a_0a_1a_2 + 27a_0^2 + 4a_1^3), \tag{28}$$

where a_0, a_1, and a_2 are determined by (19).

(ii) *If $d < 1$, $a = 1$ (i.e., $\alpha_{12} \neq 0$, $\gamma_* = 0$), then*

$$\kappa^2 = \frac{\theta - 1 + \sqrt{(1 - \theta)^2 + 4b\theta(\theta - d)(1 - d)}}{2(1 - d)}. \tag{29}$$

(iii) *If $d = 1$, $a < 1$ (i.e., $\alpha_{12} = 0$, $\gamma_* \neq 0$), then*

$$\kappa^2 = \frac{b\theta(\theta - 1) + \sqrt{b\theta}\sqrt{b(1 - \theta)^2 + 4(1 - a)(1 - a\theta)}}{2(1 - a\theta)}. \tag{30}$$

Proof.

(i): Suppose $d < 1$, $a < 1$, ($\theta > 0$, $\theta \neq 1$, $b > 0$) and (24) holds. According to Proposition 1, a unique Rayleigh wave can propagate in the half-space, and its H/V ratio is a root of (18). Let $z = w + \tfrac{1}{3}a_2$, then in terms of z (18) takes the form

$$z^3 - 3q^2z + r = 0, \tag{31}$$

where

$$r = -2R, \quad q^2 = \tfrac{1}{9}(a_2^2 - 3a_1). \tag{32}$$

According to the theory of cubic equations, three roots z_k ($k = 1, 2, 3$) of (31) are calculated by [Cowles and Thompson 1947]

$$z_1 = S + T, \quad z_2 = -\tfrac{1}{2}(S + T) + \tfrac{1}{2}i\sqrt{3}(S - T), \quad z_3 = -\tfrac{1}{2}(S + T) - \tfrac{1}{2}i\sqrt{3}(S - T), \tag{33}$$

where

$$S = \sqrt[3]{R + \sqrt{D}}, \quad T = \sqrt[3]{R - \sqrt{D}}, \quad D = R^2 + Q^3, \quad Q = -q^2. \tag{34}$$

In relation to (34), we emphasize two points:

- The cube root of a negative real number is taken as the real negative root.
- If, in the expression S, $R + \sqrt{D}$ is complex, the phase angle in T is taken as the negative of the phase angle in S so that $T = S^*$, where S^* is the complex conjugate of S.

Remark 6. • If $D > 0$, then (31) has one real root and two complex conjugate roots.

- If $D = 0$, this equation has three real roots, at least two of which are equal.

- If $D < 0$, it has three real distinct roots.

Let $z_r = \frac{1}{3}a_2 + w_r$, then z_r is a real root of (31) and if (31) has two or three real roots, z_r is the largest real root, according to Proposition 4. We will show that z_r is given by

$$z_r = \sqrt[3]{R + \sqrt{D}} + \frac{q^2}{\sqrt[3]{R + \sqrt{D}}}, \tag{35}$$

where each radical is understood as a complex root taking its principal value, R and D are calculated by (28), and q^2 is given by (32)$_2$. Then (27) is derived directly from (35) taking into account $w_r = -\frac{1}{3}a_2 + z_r$. In order to prove (35) we consider the distinct cases dependent on the values of D:

- If $D > 0$, according to Remark 6, (31) has a unique real root, which is z_r, calculated by (33)$_1$; in particular,

  $$z_r = \sqrt[3]{R + \sqrt{D}} + \sqrt[3]{R - \sqrt{D}}, \tag{36}$$

  in which the radicals are understood as real. To prove (35) we have to show that the right-hand side of (36), in which the radicals are understood as real, coincides with the right-hand side of (35), where each radical is understood as complex taking its principal value. Since

  $$\sqrt[3]{R - \sqrt{D}} = \frac{q^2}{\sqrt[3]{R + \sqrt{D}}}, \tag{37}$$

  this will be proved if we show that $R + \sqrt{D} > 0$. Note that, because (31) has a unique real root, (18) must have a unique real root. To prove $R + \sqrt{D} > 0$, we examine the distinct cases dependent on the values of $\Delta' = a_2^2 - 3a_1$, the discriminant of $f'(w) = 0$:

  - If $\Delta' \leq 0$, then $f(w)$ is strictly monotonically increasing in $(-\infty, +\infty)$ and $0 < \theta < 1$ because if $\theta > 1 \ (> d) \Longrightarrow a_1 < 0 \Longrightarrow \Delta' > 0$. By w_N we denote the abscissa of the point of inflexion N of the cubic curve $y = f(w)$, then $w_N = -\frac{2}{3}a_2 < 0$ because $a_2 > 0$ (noting that $0 < \theta < 1$). This fact along with $f(0) = a_0 < 0$ and the strictly increasing monotonousness of $f(w)$ lead to $f(w_N) < 0$. Since $r = f(w_N)$ it follows $r < 0$, or equivalently $R > 0$. This gives $R + \sqrt{D} > 0$.
  - If $\Delta' > 0$, $f'(w) = 0$ has two distinct roots, $w_{\max}$ and $w_{\min}$, and either $w_{\max} < w_{\min} \leq 0$ or $w_{\max} < 0 < w_{\min}$ (see the proof of Proposition 4). In both cases we always have that $f(w_{\min}) < 0$, as shown in the proof of Proposition 4. As (18) has a unique real root as addressed above, $f(w_{\max})f(w_{\min}) > 0$, otherwise it has two or three real roots; consequently, $f(w_{\max}) < 0$. This and $f(w_{\min}) < 0$ provides $r = f(w_N) < 0 \Longrightarrow R = -r/2 > 0$; therefore we have $R + \sqrt{D} > 0$.

- If $D = 0$, analogously as above, one can see that $r < 0$, and consequently $R > 0$. When $D = 0$ we have $R^2 = -Q^3 = q^6 \ (q > 0) \Longrightarrow R = q^3 \Longrightarrow r = -2R = -2q^3$, so (31) becomes $z^3 - 3q^2 z - 2q^3 = 0$ whose roots are $z_1 = 2q$, $z_2 = -q$ (double root). This says $z_r = 2q$, since it is the largest root. With the help of $q > 0$ and $D = 0$ it is easy to see that z_r calculated by (35) is $2q$.

- If $D < 0$, according to Remark 6, (31) has three distinct real roots, and z_r is the largest one according to Proposition 4. Using the arguments presented in [Vinh and Ogden 2004, p. 255], one can verify

that in this case the largest real root of (31) is

$$z_r = \sqrt[3]{R + \sqrt{D}} + \sqrt[3]{R - \sqrt{D}}, \tag{38}$$

in which each radical is understood as a complex root taking its principal value. By 3θ we denote the phase angle of $R + i\sqrt{-D}$. Then, it is not difficult to prove that

$$\sqrt[3]{R + \sqrt{D}} = qe^{i\theta}, \quad \sqrt[3]{R - \sqrt{D}} = qe^{-i\theta}, \tag{39}$$

where radicals are understood as complex roots taking their principal value. From (39) we have immediately (37) and then (35) by taking into account (38).

(ii), (iii): Let $d < 1$, $a = 1$ (and $\theta > 0$, $\theta \neq 1$). According to Proposition 2, a Rayleigh wave can propagate in the half-space if and only if (25) holds, and the H/V ratio is computed by (20). It is easy to see that with (25), Equation (20) has two distinct real roots w_1 and w_2 so that $w_1 < 0 < w_2$, $w_2 = w_r$, and w_r is calculated by (29). Equation (30) is proved analogously. $\qquad\square$

4. Formulas for the H/V ratio for specific strain-energy functions

4.1. *Neo-Hookean material.* For the neo-Hookean material, the strain-energy function is of the form [Roxburgh and Ogden 1994]

$$W = \tfrac{1}{2}\mu(\lambda_1^2 + \lambda_2^2 + \lambda_3^2 - 3 - 2\ln(\lambda_1\lambda_2\lambda_3)), \tag{40}$$

where μ is a Lame coefficient and λ_i $(i = \overline{1,3})$ are the principal stretches of the deformation. From (5), (4), and (40) we have

$$\alpha_{11} = \mu(\lambda_1^2 + 1), \quad \alpha_{22} = \mu(\lambda_2^2 + 1), \quad \gamma_1 = \mu\lambda_1^2, \quad \gamma_2 = \mu\lambda_2^2, \quad \gamma_* = \mu, \quad \alpha_{12} = 0. \tag{41}$$

In this case, $\alpha_{12} = 0$, $\gamma_* = \mu \neq 0$; therefore, the H/V ratio equation is of the form (21) with

$$a = 1 - \frac{1}{\lambda_1^2\lambda_2^2}, \quad b = \frac{(1 + \lambda_1^2)(1 + \lambda_2^2)}{\lambda_1^2\lambda_2^2}, \quad \theta = \frac{\lambda_1^2}{1 + \lambda_1^2}, \tag{42}$$

and according to Theorem 5 (iii), the squared H/V ratio is calculated by (30). Introducing (42) into (30) yields

$$\kappa^2 = \tfrac{1}{2}(\sqrt{1 + 4/\lambda_2^2} - 1). \tag{43}$$

The necessary and sufficient condition for a (unique) Rayleigh wave to exist in this case, according to Proposition 3, (26), is

$$1 - \frac{1}{\lambda_1^2\lambda_2^2} + \frac{\sqrt{(1 + \lambda_1^2)(1 + \lambda_2^2)}}{\lambda_1\lambda_2} > 0. \tag{44}$$

Figure 1, left, shows the existence domain of Rayleigh waves (shaded) in the space of λ_1 and λ_2 and some contour lines of the squared H/V ratio in this domain. They are horizontal lines parallel to λ_1 axis since the H/V ratio depends only on λ_2 in this case. The right figure shows the graph of the squared H/V ratio as a function of λ_2. The graph is decreasing and asymptotes to both axes. That means there is no horizontal vibration on the surface, when the material is stretched remarkably along the x_2-direction. And there is no vertical vibration when the material is significantly squeezed along the x_2-direction.

compressible neo-Hookean material

compressible neo-Hookean material
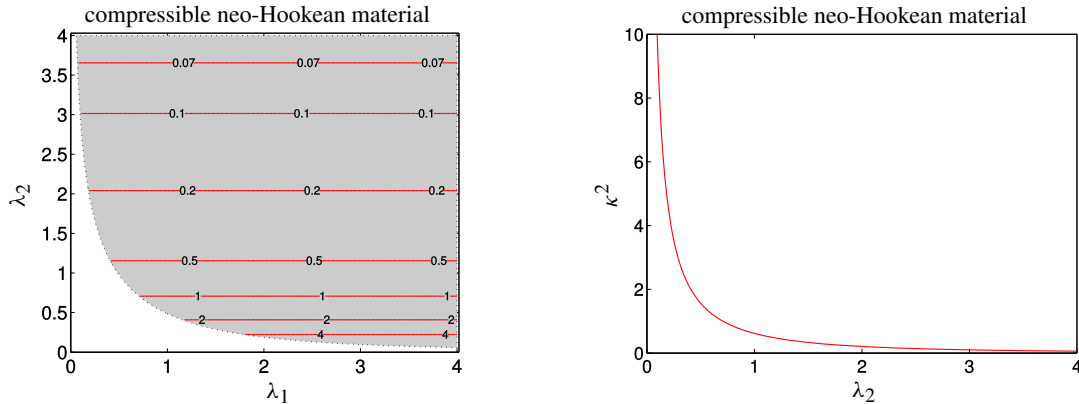
Figure 1. Left: some contours of the squared H/V ratio in the space of λ_1 and λ_2 for the neo-Hookean material. The shaded area is the domain where a Rayleigh wave is possible. Right: the dependence of the squared H/V ratio on λ_2.

4.2. *Varga material.* The strain-energy function for this material is [Roxburgh and Ogden 1994]

$$W = \mu(\lambda_1 + \lambda_2 + \lambda_3 - 3 - \ln(\lambda_1\lambda_2\lambda_3)). \tag{45}$$

From (5), (4), and (45) we have

$$\alpha_{11} = \mu, \quad \alpha_{22} = \mu, \quad \gamma_1 = \frac{\mu\lambda_1^2}{\lambda_1 + \lambda_2}, \quad \gamma_2 = \frac{\mu\lambda_2^2}{\lambda_1 + \lambda_2}, \quad \gamma_* = \mu\left(1 - \frac{\lambda_1\lambda_2}{\lambda_1 + \lambda_2}\right), \quad \alpha_{12} = 0. \tag{46}$$

Substituting (46) into (16) gives

$$a = 1 - \frac{(\lambda_1 + \lambda_2 - \lambda_1\lambda_2)^2}{\lambda_1^2\lambda_2^2}, \quad b = \frac{(\lambda_1 + \lambda_2)^2}{\lambda_1^2\lambda_2^2}, \quad \theta = \frac{\lambda_1^2}{\lambda_1 + \lambda_2}. \tag{47}$$

Similar to the neo-Hookean material, $\alpha_{12} = 0$ and $\gamma_* \neq 0$ except at points where $1 - \lambda_1\lambda_2/(\lambda_1 + \lambda_2) = 0$. As noted in Section 2, at these points a Rayleigh wave is impossible due to $\alpha_{12} = \gamma_* = 0$. According to Theorem 5 (iii), the squared H/V ratio is determined by (30). Introducing (47) into (30) yields

$$\kappa^2 = \frac{1}{2}\frac{\lambda_1 + \lambda_2 - \lambda_1^2}{\lambda_1 + \lambda_2 + \lambda_2^2 - 2\lambda_1\lambda_2} \times \left(\sqrt{1 + \frac{4(\lambda_1 + \lambda_2 - \lambda_1\lambda_2)^2(\lambda_1 - \lambda_2)^2}{\lambda_2^2(\lambda_1 + \lambda_2 - \lambda_1^2)^2} + \frac{4(\lambda_1 + \lambda_2 - \lambda_1\lambda_2)^2}{\lambda_2^2(\lambda_1 + \lambda_2 - \lambda_1^2)}} - 1\right). \tag{48}$$

The existence condition of Rayleigh waves for this material, according to (26), is

$$3\lambda_1\lambda_2 - (\lambda_1 + \lambda_2) > 0, \quad 2\lambda_1\lambda_2 - (\lambda_1 + \lambda_2 + \lambda_2^2) < 0. \tag{49}$$

The H/V ratio for this case is a function of two variables: λ_1 and λ_2. Figure 2 shows some contour lines with different values of the squared H/V ratio computed by (48) in the (shaded) domain of variables λ_1 and λ_2, where a Rayleigh wave is possible. The left-lower dotted line represents the condition $(49)_1$, and the right-upper one shows the condition $(49)_2$. The H/V ratio increases and approaches infinity at the upper boundary line since the denominator of (48) goes to zero. The thick curve is the collection of points $1 - \lambda_1\lambda_2/(\lambda_1 + \lambda_2) = 0$, where a Rayleigh wave is impossible, as mentioned above. The H/V ratio reduces to zero at points approaching to this curve. This could be seen from (48) by letting $\lambda_1 + \lambda_2$

compressible Varga material
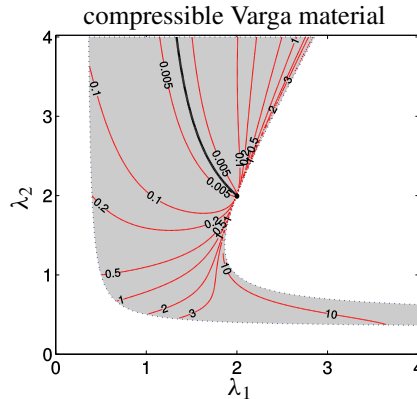
Figure 2. Some contour lines with different values of the squared H/V ratio in the space of λ_1 and λ_2 for the Varga material.
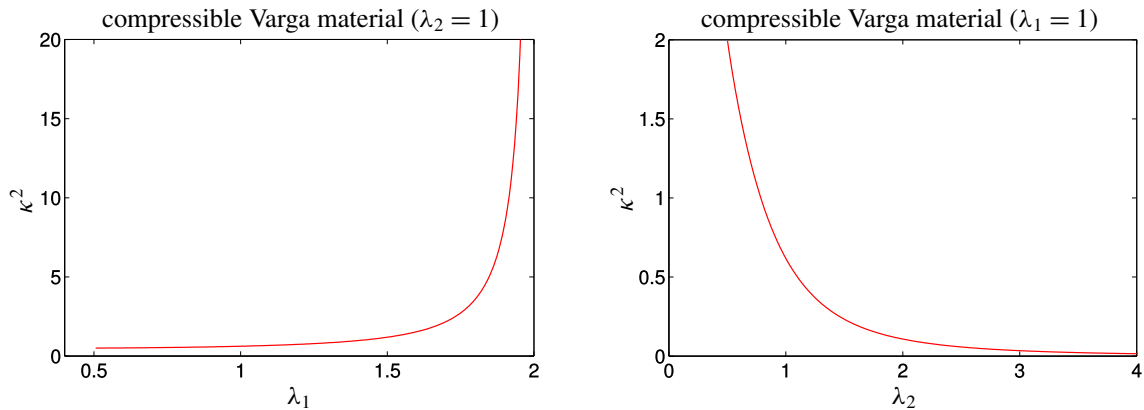
Figure 3. The squared H/V ratio as a function of λ_1 with $\lambda_2 = 1$ (left) and of λ_2 with $\lambda_1 = 1$ (right) for the Varga material.

go to $\lambda_1\lambda_2$. Therefore, the H/V ratio could vary from 0^+ to infinity for λ_1 and λ_2, varying between the thick curve and the right-upper boundary curve.

Figure 3 shows the dependence of the squared H/V ratio on λ_1 (left) and λ_2 (right) when the other λ is fixed and equals 1, i.e., there is no stretch in the other direction. When $\lambda_2 = 1$, λ_1 varies from 0.5 to 2, and the squared H/V ratio increases from 0.5 to infinity. This means there are no vertical vibrations of particles on the surface when the material is stretched along the x_1-direction by a factor of nearly 2. When $\lambda_1 = 1$, λ_2 varies from 0.5 to infinity, and the squared H/V ratio decreases from 2 to 0.

4.3. *Blatz–Ko material.* The strain-energy function of this material is [Roxburgh and Ogden 1994]

$$W = \tfrac{1}{2}\mu(\lambda_1^{-2} + \lambda_2^{-2} + \lambda_3^{-2} + 2\lambda_1\lambda_2\lambda_3 - 5). \tag{50}$$

From (5), (4), and (50) we have

$$\alpha_{11} = \frac{3\mu}{\lambda_1^2}, \quad \alpha_{22} = \frac{3\mu}{\lambda_2^2}, \quad \gamma_1 = \frac{\mu}{\lambda_2^2}, \quad \gamma_2 = \frac{\mu}{\lambda_1^2},$$
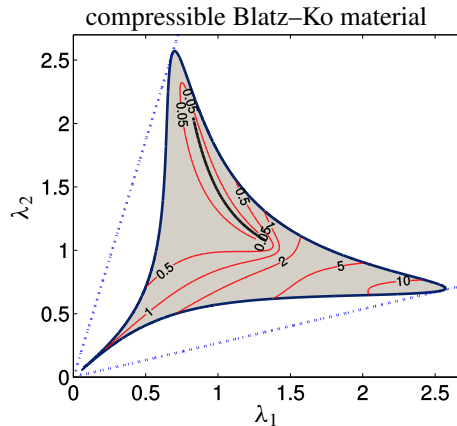
Figure 4. Several contour lines of the squared H/V ratio in the space of λ_1 and λ_2 with $\lambda_3 = 1$ for the Blatz–Ko material.

$$\gamma_* = \mu\left(\frac{1}{\lambda_1^2} + \frac{1}{\lambda_2^2} - \lambda_1\lambda_2\lambda_3\right), \quad \alpha_{12} = \mu\lambda_1\lambda_2\lambda_3. \tag{51}$$

Consider $\lambda_3 = 1$. It is clear from (51) that $\alpha_{12} \neq 0$ ($\Leftrightarrow d < 1$) for this case. Hence, the H/V ratio equation is the cubic equation (15) with

$$a = 1 - \left(\frac{\lambda_1}{\lambda_2} + \frac{\lambda_2}{\lambda_1} - \lambda_1^2\lambda_2^2\right)^2, \quad b = 9, \quad d = 1 - \tfrac{1}{9}\lambda_1^4\lambda_2^4, \quad \theta = \frac{\lambda_1^2}{3\lambda_2^2}. \tag{52}$$

If $\gamma_* \neq 0$ ($\Leftrightarrow a < 1$), i.e.,

$$\frac{1}{\lambda_1^2} + \frac{1}{\lambda_2^2} - \lambda_1\lambda_2 \neq 0, \tag{53}$$

then by Theorem 5 (i), the squared H/V ratio κ^2 is given by (27) and (28) with

$$a_2 = 9\left\{\frac{1}{\lambda_1^4\lambda_2^4} - \frac{1}{3\lambda_1^2\lambda_2^6}\left[1 - \lambda_1^2\lambda_2^2\left(\frac{1}{\lambda_1^2} + \frac{1}{\lambda_2^2} - \lambda_1\lambda_2\right)^2\right]\right\},$$

$$a_1 = \frac{3}{\lambda_2^8}\left(-3 + \frac{9\lambda_2^2}{\lambda_1^2} - \lambda_1^2\lambda_2^6\right), \quad a_0 = -\frac{9\lambda_1^2}{\lambda_2^6}\left(\frac{1}{\lambda_1^2} + \frac{1}{\lambda_2^2} - \lambda_1\lambda_2\right)^2, \tag{54}$$

and the existence condition of Rayleigh waves, according to Proposition 1, (24), is

$$4 - \tfrac{1}{3}\lambda_1^4\lambda_2^4 - \lambda_1^2\lambda_2^2\left(\frac{1}{\lambda_1^2} + \frac{1}{\lambda_2^2} - \lambda_1\lambda_2\right)^2 > 0. \tag{55}$$

It could be easily checked from the equation of the H/V ratio (18) that the squared H/V ratio takes value $\sqrt{b}\theta$ when either $\theta = 1$ or $a + \sqrt{b}d = 0$. Therefore, the squared H/V ratio goes to $\sqrt{b}\theta$ at the boundary of the existence domain of Rayleigh waves given in (55).

Figure 4 shows some contour lines of the squared H/V ratio on the (shaded) domain of λ_1 and λ_2, defined by the condition (55), where a Rayleigh wave can exist. The two dotted lines are expressed by the equations $\lambda_1/\lambda_2 = 2 + \sqrt{3}$ and $\lambda_1/\lambda_2 = 2 - \sqrt{3}$, and in the domain located between them the strong
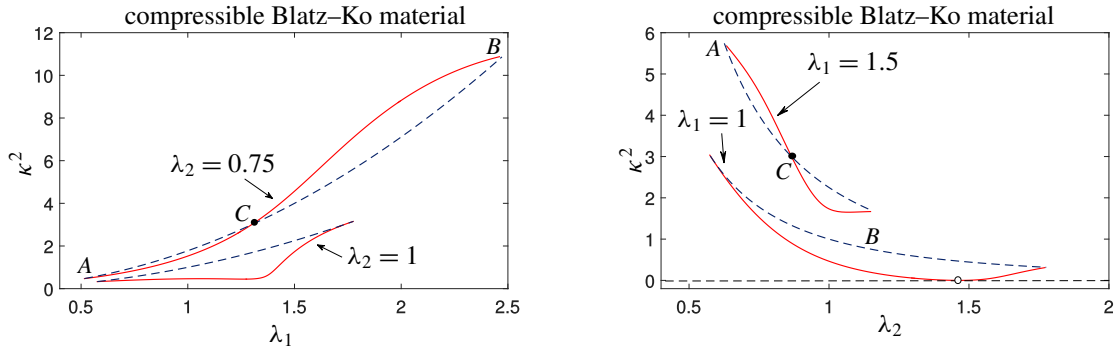
Figure 5. The squared H/V ratio (continuous line) and the quantity $\sqrt{b}\theta$ (dotted line) as a function of λ_1 (left) and λ_2 (right) with $\lambda_3 = 1$ for the Blatz–Ko material.

ellipticity condition stated by Roxburgh and Ogden [1994] is satisfied. The existence domain of Rayleigh waves is a subset of this domain.

When $\gamma_* = 0$, i.e., the left-hand side of (53) equals zero, for a Rayleigh wave to exist, λ_1 and λ_2 must satisfy the two conditions (25) given in Proposition 2. The thick continuous curve in the shaded area in Figure 4 shows the set of points which do not satisfy the first condition. The two end-points of this thick curve are $(\lambda_1, \lambda_2) = (0.8223, 2.0770)$ and $(1.3450, 1.0657)$. A Rayleigh wave is impossible on this curve.

The left figure in Figure 5 shows the dependence of κ^2 on λ_1 for two fixed values of $\lambda_2 = 0.75$ and $\lambda_2 = 1$ plotted by continuous curves. The dotted curves show the value of $\sqrt{b}\theta$, which is λ_1^2/λ_2^2 in this case. This value is mentioned in Section 2 as the separation of two ranges of κ^2 depending on if θ is less than or greater than one. When $\lambda_2 = 0.75$, for a Rayleigh wave to exist, it is deduced from (55) that $0.51 < \lambda_1 < 2.48$. The two end-points are denoted by A and B. The continuous curve and the dotted curve meet each other at these end-points because the squared H/V ratio goes to $\sqrt{b}\theta$ at the boundary of the existence domain of Rayleigh waves, as mentioned above. These two curves cross at point C at which $\theta = 1$. One can see that the phase velocity $x < 1$ and the squared H/V ratio $\kappa^2 < \sqrt{b}\theta$ in the segment AC, and $x < 1/\theta$, $\kappa^2 > \sqrt{b}\theta$ in the segment CB. When $\lambda_2 = 1$, the possible range of λ_1 is $(0.57, 1.78)$ and $\theta < 1$ in this range, therefore $\kappa^2 < \sqrt{b}\theta$. The right figure in Figure 5 shows the dependence of κ^2 on λ_2 for two fixed values of $\lambda_1 = 1$ and $\lambda_1 = 1.5$ with the same description as the left figure. When $\lambda_1 = 1$, there is an undefined point of the H/V ratio at $\lambda_2 = 1.465$. This is a point of the thick curve shown in Figure 4 where the H/V ratio does not exist.

4.4. *Foam rubber strain-energy function.* According to Murphy and Destrade [2009], in the plane-strain $\lambda_3 = 1$, the foam rubbers are well-characterized by the strain-energy function

$$W = \tfrac{1}{2}\mu\left(I - 2 + \frac{\epsilon}{1-\epsilon}(J^{2(\epsilon-1)/\epsilon} - 1)\right), \tag{56}$$

where

$$I = \lambda_1^2 + \lambda_2^2, \quad J = \lambda_1\lambda_2, \quad \lambda_2 = \lambda_1^{\epsilon-1}, \quad 0 < \epsilon < 1. \tag{57}$$

From (5), (4) and (56), (57) it is not difficult to verify that

$$\alpha_{11} = \mu\lambda_1^2[1 + (2/\epsilon - 1)\lambda_1^{2(\epsilon-2)}], \quad \alpha_{22} = (2\mu/\epsilon)\lambda_1^{2(\epsilon-1)},$$

$$\alpha_{12} = (1 - \epsilon)\alpha_{22}, \quad \gamma_1 = \mu\lambda_1^2, \quad \gamma_2 = \mu\lambda_1^{2(\epsilon-1)}, \quad \gamma_* = \gamma_2. \tag{58}$$
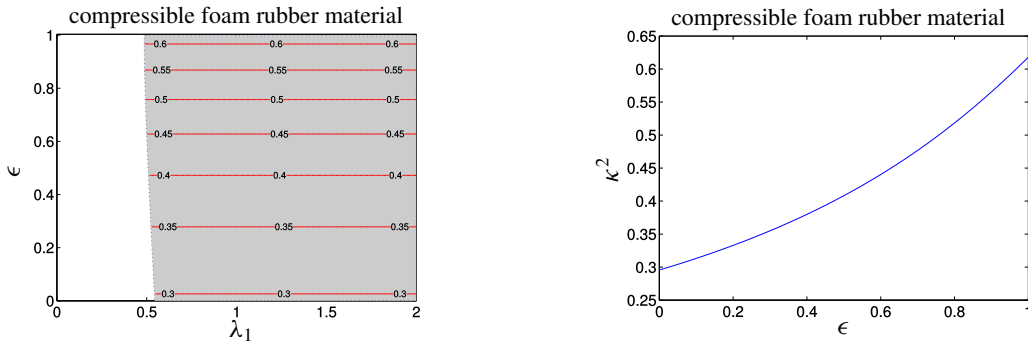
Figure 6. Some contour lines of κ^2 in the possible domain of λ_1 and ϵ (left). The dependence of the squared H/V ratio κ^2 on $\epsilon \in (0, 1)$ for the foam rubber material (right).

By using (16), (19) along with (58), the H/V ratio equation for this material is (18) with

$$a_0 = -\frac{1}{(1-\epsilon)^2}, \quad a_1 = \frac{3 - 2\epsilon}{(1-\epsilon)^2}, \quad a_2 = \frac{1}{(1-\epsilon)^2}. \tag{59}$$

As $0 < \epsilon < 1$ and $\lambda_1 > 0$ it is clear from (58) that $\alpha_{12} > 0 \ (\Rightarrow d < 1)$ and $\gamma_* > 0 \ (\Rightarrow a < 1)$. According to Theorem 5 (i), κ^2 is calculated by (27) in which a_k is given by (59), and R, D are given by (28); in particular,

$$
\begin{aligned}
R &= \frac{(3\epsilon - 2)(9\epsilon^3 - 36\epsilon^2 + 51\epsilon - 26)}{54(1-\epsilon)^6}, \\
D &= -\frac{(2-\epsilon)^2(32\epsilon^3 - 107\epsilon^2 + 124\epsilon - 44)}{108(1-\epsilon)^8}.
\end{aligned}
\tag{60}
$$

It is interesting that H/V ratio depends only on ϵ, it does not depend on λ_1. The condition for a Rayleigh wave to exist according to Proposition 1 is

$$1 - \lambda_1^{2(\epsilon-2)} + \sqrt{2}\frac{1 + \lambda_1^{2(\epsilon-2)}(3 - 2\epsilon)}{\sqrt{\epsilon + \lambda_1^{2(\epsilon-2)}(2 - \epsilon)}} > 0. \tag{61}$$

The left figure in Figure 6 shows the existence domain of Rayleigh waves in the space of ϵ and λ_1 (shaded) and some contour lines of κ^2 in this domain. Since κ^2 is a function of ϵ only, these contour lines are horizontal. The right figure in Figure 6 shows the value of κ^2 depending on the whole range of ϵ from 0 to 1.

5. Conclusions

In this paper, the relation between the H/V ratio and the velocity of Rayleigh waves propagating in a compressible prestressed elastic half-space is established. Based on it and the secular equation, the equation determining the H/V ratio is obtained. Then, the exact H/V ratio formulas have been derived by solving analytically the H/V ratio equation. These formulas are valid for a general strain-energy function. Some particular strain-energy functions are employed to specify these formulas. Since the

H/V ratio is a convenient tool for nondestructively evaluating the prestresses of structures before and during loading, the obtained formulas will be very useful in practical applications.

Acknowledgments

References

[Barnett and Lothe 1985] D. M. Barnett and J. Lothe, "Free surface (Rayleigh) waves in anisotropic elastic half-spaces: the surface impedance method", *Proc. R. Soc. Lond. A* **402**:1822 (1985), 135–152.

[Chadwick and Smith 1977] P. Chadwick and G. D. Smith, "Foundations of the theory of surface waves in anisotropic elastic materials", pp. 303–376 Advances in Applied Mechanics **17**, Elsevier, 1977.

[Cowles and Thompson 1947] W. H. Cowles and J. E. Thompson, *Algebra for Colleges and Engineering Schools*, 2nd ed., Van Nostrand, New York, 1947.

[Delsanto and Clark 1987] P. P. Delsanto and A. V. Clark, "Rayleigh wave propagation in deformed orthotropic materials", *J. Acoust. Soc. Am.* **81**:4 (1987), 952–960.

[Destrade and Fu 2006] M. Destrade and Y. B. Fu, "The speed of interfacial waves polarized in a symmetry plane", *Int. J. Eng. Sci.* **44**:1-2 (2006), 26–36.

[Dowaikh and Ogden 1991] M. A. Dowaikh and R. W. Ogden, "On surface waves and deformations in a compressible elastic half-space", *Stability Appl. Anal. Contin. Media* **1**:1 (1991), 27–45.

[Duquennoy et al. 1999] M. Duquennoy, M. Ouaftouh, and M. Ourak, "Ultrasonic evaluation of stresses in orthotropic materials using Rayleigh waves", *NDT & E Int.* **32**:4 (1999), 189–199.

[Duquennoy et al. 2006] M. Duquennoy, D. Devos, M. Ouaftouh, D. Lochegnies, and E. Roméro, "Ultrasonic evaluation of residual stresses in flat glass tempering: comparing experimental investigation and numerical modeling", *J. Acoust. Soc. Am.* **119**:6 (2006), 3773–3781.

[Fu and Mielke 2002] Y. B. Fu and A. Mielke, "A new identity for the surface-impedance matrix and its application to the determination of surface-wave speeds", *Proc. R. Soc. Lond. A* **458**:2026 (2002), 2523–2543.

[Fu and Ogden 2001] Y. B. Fu and R. W. Ogden (editors), *Nonlinear elasticity: theory and applications*, London Mathematical Society Lecture Note Series **283**, Cambridge University Press, 2001.

[Hirao et al. 1981] M. Hirao, H. Fukuoka, and K. Hori, "Acoustoelastic effect of Rayleigh surface wave in isotropic material", *J. Appl. Mech.* (*ASME*) **48** (1981), 119–124.

[Ingebrigtsen and Tonning 1969] K. A. Ingebrigtsen and A. Tonning, "Elastic surface waves in crystals", *Phys. Rev.* **184** (1969), 942–951.

[Junge et al. 2006] M. Junge, J. Qu, and L. J. Jacobs, "Relationship between Rayleigh wave polarization and state of stress", *Ultrasonics* **44**:3 (2006), 233–237.

[Makhort et al. 1990] F. G. Makhort, O. I. Gushcha, and A. A. Chernoochenko, "Theory of acoustoelasticity of Rayleigh surface waves", *Sov. Appl. Mech.* **26**:4 (1990), 346–350.

[Malischewsky and Scherbaum 2004] P. G. Malischewsky and F. Scherbaum, "Love's formula and H/V-ratio (ellipticity) of Rayleigh waves", *Wave Motion* **40**:1 (2004), 57–67.

[Murphy and Destrade 2009] J. Murphy and M. Destrade, "Surface waves and surface stability for a pre-stretched, unconstrained, non-linearly elastic half-space", *Int. J. Non-Linear Mech.* **44**:5 (2009), 545–551.

[Ogden 1984] R. W. Ogden, *Nonlinear elastic deformations*, Ellis Horwood Ltd., Chichester, England, 1984.

[Roxburgh and Ogden 1994] D. G. Roxburgh and R. W. Ogden, "Stability and vibration of pre-stressed compressible elastic plates", *Int. J. Eng. Sci.* **32**:3 (1994), 427–454.

[Song and Fu 2007] Y. Q. Song and Y. B. Fu, "A note on perturbation formulae for the surface-wave speed due to perturbations in material properties", *J. Elasticity* **88**:3 (2007), 187–192.

[Vinh 2011] P. C. Vinh, "On formulas for the Rayleigh wave velocity in pre-stressed compressible solids", *Wave Motion* **48**:7 (2011), 614–625.

[Vinh and Ogden 2004] P. C. Vinh and R. W. Ogden, "Formulas for the Rayleigh wave speed in orthotropic elastic solids", *Arch. Mech. Stos.* **56**:3 (2004), 247–265.

[Vinh and Seriani 2009] P. C. Vinh and G. Seriani, "Explicit secular equations of Rayleigh waves in a non-homogeneous orthotropic elastic medium under the influence of gravity", *Wave Motion* **46**:7 (2009), 427–434.

PHAM CHI VINH: pcvinh@gmail.com
Faculty of Mathematics, Mechanics and Informatics, Hanoi University of Science, Hanoi, Vietnam

THANH TUAN TRAN: tranthanhtuan@hus.edu.vn
Faculty of Mathematics, Mechanics and Informatics Hanoi University of Science, Hanoi, Vietnam

VU THI NGOC ANH: anhvungoc.khtn@gmail.com
Faculty of Mathematics, Mechanics and Informatics, Hanoi University of Science, Hanoi, Vietnam

LE THI HUE: hue100988@gmail.com
Vietnam National University of Forestry, Hanoi, Vietnam

GEOMETRICAL NONLINEAR DYNAMIC ANALYSIS OF TENSEGRITY SYSTEMS VIA THE COROTATIONAL FORMULATION

XIAODONG FENG

An efficient finite element formulation is presented for geometrical nonlinear dynamic analysis of tensegrity systems based on the corotational formulation. In this method, large displacement of a space rod element is decomposed into a rigid body motion in the global coordinate system and a pure small deformation in the local coordinate system. A new form of tangent stiffness matrix, including both static and dynamic stages, is derived based on the proposed approach. The Newmark constant acceleration method in conjunction with modified Newton–Raphson method is employed to solve the nonlinear dynamic equation of motion. A five-module quadruplex tensegrity beam is given as the numerical example to illustrate the validity and efficiency of the proposed algorithm for geometrical nonlinear dynamic analysis of tensegrity structures.

1. Introduction

Research into active structures has been at the forefront of aerospace, biological, civil and mechanical engineering for recent years [Domer and Smith 2005; Ziegler 2005; Korkmaz 2011; Luo et al. 2008; Paul et al. 2006; Rovira and Tur 2009]. Advances in theory and practice of active structural control have changed the general perception of structures. Upon integration of active components, structures become dynamic objects capable of interacting with their environments. Increasingly, the ability to adapt to performance demands and environmental conditions has become key design criteria for a range of structural and mechanical systems. Among many structural topologies, the tensegrity might be the most promising actively controlled structures for its large motion amplitude and high strength-to-mass ratio [Adam and Smith 2008; Masic and Skelton 2006; Raja and Narayanan 2007; Sultan and Skelton 2003; Wroldsen et al. 2009; Skelton et al. 2014]. A fundamental aspect of tensegrities is the stress unilateral property of the compression: cables and struts must be under tension and compression, respectively. That is to say, the cables will be slacking when compressive loads are applied, which makes tensegrity systems flexible and easily controllable using small amounts of energy [Tibert and Pellegrino 2003; Juan and Tur 2008]. Another main requirement for a structure to be categorized as a tensegrity structure is that its initial pre-stressed configuration must be in stable equilibrium in absence of external forces, and which to a high degree decides the response properties, e.g. the stiffness to external loading. The design of a tensegrity structure thereby has to include these aspects in addition to the definition of a special geometry.

A complete analysis of the tensegrity structures comprises two parts. The first one is the evaluation of pre-stressed configurations, known as form-finding, which has been and is currently object of extensive research [Tibert and Pellegrino 2003]. The second part is the investigation of behavior under external

loads. In the literature, the form-finding step has been widely studied by different approaches [Barnes 1999; Xu and Luo 2010; Chen et al. 2012; Tran and Lee 2010; Koohestani and Guest 2013; Lee and Lee 2014; Feng and Guo 2015; Zhang et al. 2014]. On the other hand, however, the structure analysis step for nonlinear behavior, especially in the regime of large displacement, is still a difficult issue for structural engineers since tensegrities are in general both kinematically and statically indeterminate. Nevertheless, as is known to all, the total Lagrangian (TL) approach and update Lagrangian (UL) approach have been used widely for large-displacement analysis. Kebiche et al. [1999] performed a geometrical, nonlinear, elastic analysis for a basic quadruplex module (four-strut tensegrity prism) subjected to axial, flexural and torsional loads and a multi-cell beam under traction based on TL approach. Kebiche and Kahla [2000] developed nonlinear elasto-plastic investigations of a five quadruplex module tensegrity system based on an UL formulation. Murakami [2001] analyzed static and dynamic characteristics of tensegrity structure using both Eulerian and Lagrangian formulations of large-displacement kinematics and kinetics. The modal analysis performed by Murakmi indicated that the tensegrity had low natural frequency modes like thin members and it can be regarded as a typically flexible structure which usually has a complicated nonlinear behavior. Recently, Tran and Lee [2011] performed geometric and material analysis of tensegrity structures based on both total and updated Lagrangian formulations, and the updated Lagrangian formulation was recommended for large deflection analysis. Oliveto and Sivaselvan [2011] studied dynamic properties of tensegrity structures using a complementarity framework in the small displacement regime.

Lately, an alternative and more attractive approach, known as the corotational (CR) method, was proposed to investigate nonlinear behavior of tensegrity structures. Several researchers have proved that the CR formulation is computational more convenient and efficient for large-displacement and small-strain problems [Crisfield and Moita 1996; Felippa and Haugen 2005; Zhang et al. 2013; Zhang et al. 2015]. Relative literatures also demonstrated that the CR formulation offers exceptional benefits for an element which has more rigid body modes than deformational modes in a static analysis [Faroughi and Lee 2014; Feng and Guo 2017; Faroughi et al. 2017]. Because space rod element have five rigid body modes (three translations and two rotations) and only one deformational mode, i.e. the axial compression or extension, the CR formulation seems more attractive for the investigation of dynamic behavior of tensegrity systems. Although dynamic analysis of structural components (e.g. beam and membrane) have been performed successfully by the CR method [Le et al. 2011; Le et al. 2012; Eriksson and Faroughi 2013; Faroughi and Eriksson 2017], to our knowledge, dynamic analysis of tensegrity structures via the CR approach was rarely seen.

The main objective of this paper is to develop a 3D corotational model for geometrical nonlinear dynamic analysis of tensegrity structures. The CR formulation, which decomposes a large displacement into a rigid body motion and a pure small deformation, is adapted to achieve the internal force vector, the static tangent stiffness matrix, the inertial force vector, the mass matrix and the dynamic tangent stiffness matrix. By means of the CR approach, the space rod element is utilized to model the geometrical nonlinear dynamic behavior of tensegrity structures in local coordinates. The advantage of the proposed method is that behaviors of rod elements can be described utilizing engineering strain and stress which are calculated directly by the small-deformation elastic theory, although geometrical nonlinearity must be taken into account. The rod element has deformation only along its longitudinal direction (small strain), this makes the orientation of the 2nd and 3rd axes arbitrary and therefore torsion and bending

have been ignored in this paper. In the process of analyzing tensegrities at any equilibrium configuration with and without loads, the slackening constraints of cable elements have been taken into account. It is assumed that the form-finding procedure has been completed and the self-stress coefficients are known in advance [Feng and Guo 2015; Feng 2017].

The organization of this paper is as follows: Section 2 presents the derivations of the internal force vector, the static tangent stiffness matrix, the inertial force vector, the mass matrix and the dynamic tangent stiffness matrix. In Section 3, the Newmark constant acceleration method in conjunction with modified Newton–Raphson method are employed to solve the nonlinear dynamic equation of motion. A numerical example is performed to illustrate the validity and convergence of the proposed approach, which is presented in Section 4. Finally, some conclusions are summarized.

2. Global corotational formulation

In establishing the stress-strain relation to account for yielding behavior of an axially-loaded rod, the following assumptions are adopted for tensegrity structures:

- Members are connected by pin joints.
- Struts are elements that carry axial tensile or compressive forces.
- Cables are elements that carry only axial tensile forces.
- The materials are considered to be linear and elastic.
- The tensegrity structures are subjected to external load only at nodes.
- Both local and global buckling of strut element are not considered.
- There are no dissipative forces acting on the system.

2.1. *Derivation of the internal force vector.* Figure 1 displays a rod finite element with two end nodes (i, j). As can be seen, there are two coordinate systems. The first one is the global coordinate system XYZ and the other is the local coordinate system x_l, y_l, z_l that is fixed on and moves with the element. The initial configuration "ij" goes to the current configuration "$i''j''$", via a large-rotation and small-strain motion. The motion can thus be divided into two steps. The first step is a rigid body motion and translation from the configuration "ij" to "$i'j'$" in the global coordinate system XYZ; the second one is a small-strain deformation from the configuration "$i'j'$" to "$i''j''$" in the local coordinate system $x_l y_l z_l$. Therefore, the transformation relation between local and global coordinate systems needs to be found.

The element nodal coordinates at initial time and time t in the global coordinate system XYZ are denoted by $(^0x_i, {}^0y_i, {}^0z_i)$, $(^0x_j, {}^0y_j, {}^0z_j)$, $(^tx_i, {}^ty_i, {}^tz_i)$, $(^tx_j, {}^ty_j, {}^tz_j)$, respectively.

Thus, the global displacement vector is given by

$$
\begin{aligned}
\boldsymbol{d} &= \begin{bmatrix} u_i & v_i & w_i & u_j & v_j & w_j \end{bmatrix}^T \\
&= \begin{bmatrix} {}^tx_i - {}^0x_i & {}^ty_i - {}^0y_i & {}^tz_i - {}^0z_i & {}^tx_j - {}^0x_j & {}^ty_j - {}^0y_j & {}^tz_j - {}^0z_j \end{bmatrix}^T,
\end{aligned} \tag{1}
$$

and the local displacement along the rod element is

$$
\Delta l = {}^t l - {}^0 l, \tag{2}
$$
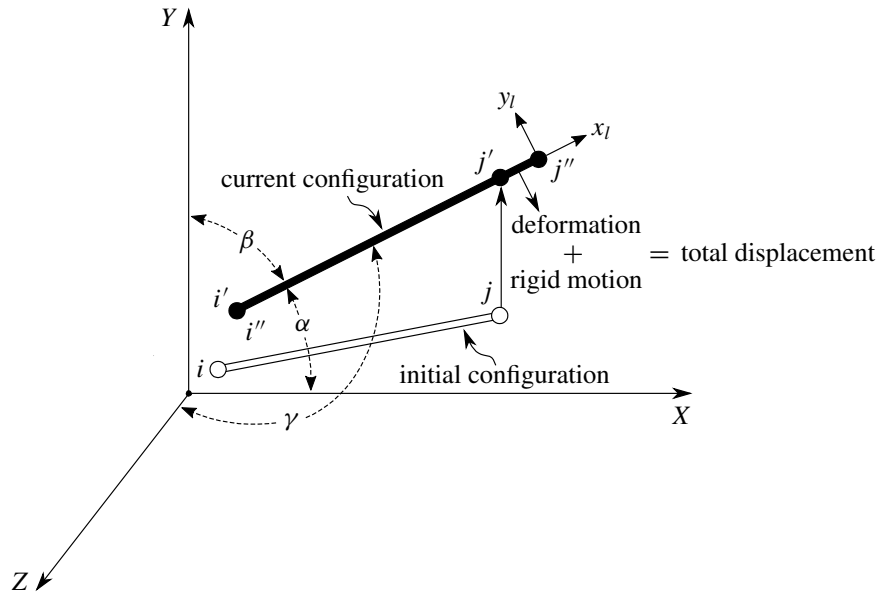
Figure 1. Illustration of the corotational method of a space rod element.

where ^0l and ^tl are the lengths of the rod element at initial time and time t, respectively, given by

$$^0l = \sqrt{(^0x_j - {}^0x_i)^2 + (^0y_j - {}^0y_i)^2 + (^0z_j - {}^0z_i)^2}, \tag{3}$$

$$^tl = \sqrt{(^0x_j - {}^0x_i + u_j - u_i)^2 + (^0y_j - {}^0y_i + v_j - v_i)^2 + (^0z_j - {}^0z_i + w_j - w_i)^2}. \tag{4}$$

Let c_1, c_2 and c_3 be the cosine angles of the x_l-axis with respect to the global coordinate system XYZ:

$$c_1 = \cos\alpha = (^0x_j - {}^0x_i + u_j - u_i)/{}^tl$$
$$c_2 = \cos\beta = (^0y_j - {}^0y_i + v_j - v_i)/{}^tl \tag{5}$$
$$c_3 = \cos\gamma = (^0z_j - {}^0z_i + w_j - w_i)/{}^tl.$$

Taking the variation of (2) gives

$$\delta\Delta l = \delta^tl = t\delta d, \tag{6}$$

where

$$t = \begin{bmatrix} -c_1 & -c_2 & -c_3 & c_1 & c_2 & c_3 \end{bmatrix}. \tag{7}$$

For cable elements, the local nodal internal force vector can be given by

$$q^l = \sigma A = E\varepsilon A, \tag{8}$$

where A is the cross-sectional area and σ is the stress of cables or struts. Engineering strain at time t can be calculated by

$$\varepsilon = \Delta l/{}^0l + \varepsilon_0, \tag{9}$$

in which ε_0 is the initial strain determined by pre-stressed or self-stress state.

Introducing (9) into (8), the local internal force vector can be rewritten as

$$q^l = \frac{EA}{^0l}\Delta l + EA\varepsilon_0. \tag{10}$$

Based on the principle of virtual work, i.e. the internal virtual work is equal in both the local and global coordinate systems, the relationship between the global nodal internal force vector $\boldsymbol{q}^g$ and local nodal internal force vector q^l is obtained from (12) as

$$\delta\boldsymbol{d}^T\boldsymbol{q}^g = (\delta\Delta l)^T q^l = (\boldsymbol{t}\delta\boldsymbol{d})^T \Rightarrow \boldsymbol{q}^g = \boldsymbol{t}^T q^l. \tag{11}$$

2.2. *Derivation of the static tangent stiffness matrix.* According to the static equilibrium relationship, the global tangent stiffness matrix $\overline{\boldsymbol{K}}_T$ is acquired from

$$\delta\boldsymbol{q}^g = \overline{\boldsymbol{K}}_T\delta\boldsymbol{d} = \overline{\boldsymbol{K}}_E\,\delta\boldsymbol{d} + \overline{\boldsymbol{K}}_G\,\delta\boldsymbol{d}, \tag{12}$$

where $\overline{\boldsymbol{K}}_E$ and $\overline{\boldsymbol{K}}_G$ denote the material and geometrical tangent stiffness matrices in the global coordinate system, respectively [Guest 2006].

Taking the variation of (11) gives

$$\delta\boldsymbol{q}^g = \boldsymbol{t}^T\delta q^l + \delta\boldsymbol{t}^T q^l. \tag{13}$$

Taking the variation of the local force vector q^l from (9), the first term in (13) can be obtained:

$$\delta q^l = \frac{EA}{^0l}\delta\Delta l = \frac{EA}{^0l}\boldsymbol{t}\delta\boldsymbol{d}. \tag{14}$$

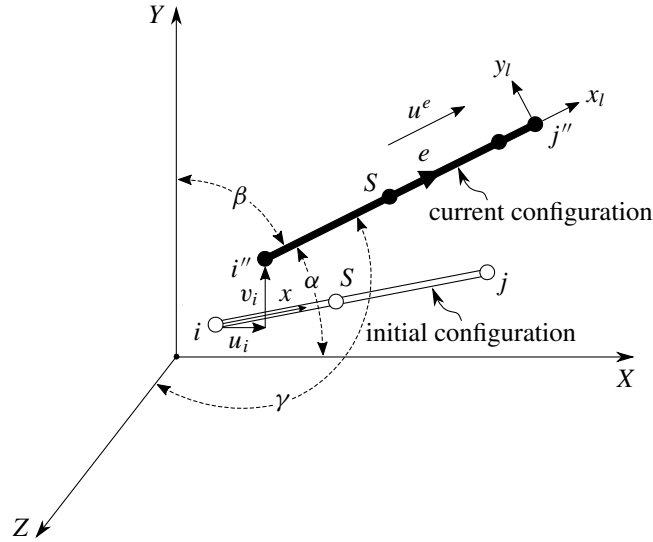In order to achieve the second term in (13), the variation of $\boldsymbol{t}$ from (7) is computed, results in

$$\delta\boldsymbol{t}^T = \frac{1}{^tl}\begin{bmatrix} 1-c_1^2 & -c_1c_2 & -c_1c_3 & c_1^2-1 & c_1c_2 & c_1c_3 \\ -c_1c_2 & 1-c_2^2 & -c_2c_3 & c_1c_2 & c_2^2-1 & c_2c_3 \\ -c_1c_3 & -c_2c_3 & 1-c_3^2 & c_1c_3 & c_2c_3 & c_3^2-1 \\ c_1^2-1 & c_1c_2 & c_1c_3 & 1-c_1^2 & -c_1c_2 & -c_1c_3 \\ c_1c_2 & c_2^2-1 & c_2c_3 & -c_1c_2 & 1-c_2^2 & -c_2c_3 \\ c_1c_3 & c_2c_3 & c_3^2-1 & -c_1c_3 & -c_2c_3 & 1-c_3^2 \end{bmatrix}\delta\boldsymbol{d} = \frac{1}{^tl}[\boldsymbol{R}\boldsymbol{R}^T - (\boldsymbol{R}r)(\boldsymbol{R}r)^T]\delta\boldsymbol{d}, \tag{15}$$

where matrix $\boldsymbol{R}$ and the vector $\boldsymbol{r}$ are as follows [Faroughi et al. 2015]:

$$\boldsymbol{R} = \begin{bmatrix} -1 & 0 & 0 & 1 & 0 & 0 \\ 0 & -1 & 0 & 0 & 1 & 0 \\ 0 & 0 & -1 & 0 & 0 & 1 \end{bmatrix}^T, \quad \boldsymbol{r} = \begin{Bmatrix} c_1 \\ c_2 \\ c_3 \end{Bmatrix}. \tag{16}$$

Introducing (10) into (13), the comparison between (14)–(15) and (12)–(13) gives the global tangent stiffness matrix as follows:

$$\overline{\boldsymbol{K}}_T = \frac{EA}{^0l}\boldsymbol{t}^T\boldsymbol{t} + \frac{\frac{EA}{^0l}\Delta l + EA\varepsilon_0}{^tl}[\boldsymbol{R}\boldsymbol{R}^T - (\boldsymbol{R}r)(\boldsymbol{R}r)^T]. \tag{17}$$

Figure 2. Illustration of the kinetic energy of a space rod element.

2.3. *Derivation of the inertial force vector and the mass matrix.* Using the notation shown in Figure 2, the global position can be written as

$$OS = (x_i + u_i)e_1 + (y_i + v_i)e_2 + (z_i + w_i)e_3 + \frac{{}^t l}{{}^0 l}(\cos\alpha \cdot e_1 + \cos\beta \cdot e_2 + \cos\gamma \cdot e_3), \qquad (18)$$

where e_1, e_2 and e_3 are the three unit coordinate vectors of the corresponding coordinate axes.

Therefore the global velocity components $\dot{u}$, $\dot{v}$ and $\dot{w}$ can be achieved from differentiating (18):

$$\dot{u} = \dot{u}_i + \frac{x}{{}^0 l}(\dot{u}_j - \dot{u}_i), \quad \dot{v} = \dot{v}_i + \frac{x}{{}^0 l}(\dot{v}_j - \dot{v}_i), \quad \dot{w} = \dot{w}_i + \frac{x}{{}^0 l}(\dot{w}_j - \dot{w}_i). \qquad (19)$$

The kinetic energy of a space rod element E (not to be confused with the same symbol used for the modulus of elasticity) can be obtained as

$$E = \frac{1}{2}\rho \int A\big((\dot{u})^2 + (\dot{v})^2 + (\dot{w})^2\big)\, dl, \qquad (20)$$

where ρ represents the density of the rod element.

Transforming (20) into the vector form, gives

$$E = \frac{1}{2}\dot{u}^T \overline{M}\dot{u}, \qquad (21)$$

where $\overline{M}$ is the global mass matrix of the rod element, which can be determined by

$$\overline{M} = T^T m^l\, T, \qquad (22)$$

where T and m^l are the rotational matrix and the local mass matrix of the rod element, given by

$$T = \begin{bmatrix} c_1 & c_2 & c_3 & 0 & 0 & 0 \\ 0 & 0 & 0 & c_1 & c_2 & c_3 \end{bmatrix}, \quad m^l = \frac{\rho A l}{6}\begin{bmatrix} 2 & 1 \\ 1 & 1 \end{bmatrix}.$$

The inertial force vector q^E can be computed from the (21) by employing the Lagrangian equation of motion, as

$$q^E = \frac{d}{dt}\left[\frac{\partial E}{\partial \dot{u}}\right] - \left[\frac{\partial E}{\partial u}\right]. \tag{23}$$

By substituting (21) into (23), the first term in (23) can be computed as

$$\frac{d}{dt}\left[\frac{\partial E}{\partial \dot{u}}\right] = \overline{M}\ddot{u} + \dot{\overline{M}}\dot{u}. \tag{24}$$

Equation (22) indicates that the mass matrix $\overline{M}$ is a function of c_1, c_2 and c_3, which are functions of time, thus

$$\dot{\overline{M}} = \frac{\partial \overline{M}}{\partial c_1}\dot{c}_1 + \frac{\partial \overline{M}}{\partial c_2}\dot{c}_2 + \frac{\partial \overline{M}}{\partial c_3}\dot{c}_3, \tag{25}$$

where c_1, c_2 and c_3 are calculated as

$$\dot{c}_1 = \frac{dc_1}{dt} = \frac{dc_1}{du}\frac{du}{dt} = \frac{t_1^T}{^tl}\dot{u}, \quad \dot{c}_2 = \frac{dc_2}{dt} = \frac{dc_2}{du}\frac{du}{dt} = \frac{t_2^T}{^tl}\dot{u}, \quad \dot{c}_3 = \frac{dc_3}{dt} = \frac{dc_3}{du}\frac{du}{dt} = \frac{t_3^T}{^tl}\dot{u}, \tag{26}$$

and

$$
\begin{aligned}
t_1 &= \begin{bmatrix} c_1^2 - 1 & c_1 c_2 & c_1 c_3 & 1 - c_1^2 & -c_1 c_2 & -c_1 c_3 \end{bmatrix}^T, \\
t_2 &= \begin{bmatrix} c_1 c_2 & c_2^1 - 1 & c_2 c_3 & -c_1 c_2 & 1 - c_2^2 & -c_2 c_3 \end{bmatrix}^T, \\
t_3 &= \begin{bmatrix} c_1 c_3 & c_2 c_3 & c_3^2 - 1 & -c_1 c_3 & -c_2 c_3 & 1 - c_3^2 \end{bmatrix}^T.
\end{aligned} \tag{27}
$$

The partial derivates in (25) are calculated as

$$
\begin{aligned}
\frac{\partial \overline{M}}{\partial c_1} &= \overline{M}_{c_1} = \frac{\partial T^T}{\partial c_1}m^l T + T^T m^l \frac{\partial T}{\partial c_1} = R_1^T m^l T + T^T m^l R_1, \\
\frac{\partial \overline{M}}{\partial c_2} &= \overline{M}_{c_2} = \frac{\partial T^T}{\partial c_2}m^l T + T^T m^l \frac{\partial T}{\partial c_2} = R_2^T m^l T + T^T m^l R_2, \\
\frac{\partial \overline{M}}{\partial c_3} &= \overline{M}_{c_3} = \frac{\partial T^T}{\partial c_3}m^l T + T^T m^l \frac{\partial T}{\partial c_3} = R_3^T m^l T + T^T m^l R_3,
\end{aligned} \tag{28}
$$

where

$$
\begin{aligned}
R_1 &= \frac{\partial T}{\partial c_1} = \begin{bmatrix} 1 & -c_1/c_2 & -c_1/c_3 & 0 & 0 & 0 \\ 0 & 0 & 0 & 1 & -c_1/c_2 & -c_1/c_3 \end{bmatrix}, \\
R_2 &= \frac{\partial T}{\partial c_2} = \begin{bmatrix} -c_2/c_1 & 1 & -c_2/c_3 & 0 & 0 & 0 \\ 0 & 0 & 0 & -c_2/c_1 & 1 & -c_2/c_3 \end{bmatrix}, \\
R_3 &= \frac{\partial T}{\partial c_3} = \begin{bmatrix} -c_3/c_1 & -c_3/c_2 & 1 & 0 & 0 & 0 \\ 0 & 0 & 0 & -c_3/c_1 & -c_3/c_2 & 1 \end{bmatrix}.
\end{aligned} \tag{29}
$$

By substituting (21) into (23), the second term in (23) can be computed as

$$
\begin{aligned}
\left[\frac{\partial E}{\partial u}\right] &= \frac{\partial E}{\partial c_1}\frac{\partial c_1}{\partial u} + \frac{\partial E}{\partial c_2}\frac{\partial c_2}{\partial u} + \frac{\partial E}{\partial c_3}\frac{\partial c_3}{\partial u} \\
&= \left(\frac{1}{2}\dot{u}^T \frac{\partial \overline{M}}{\partial c_1}\dot{u}\right)\frac{t_1}{^tl} + \left(\frac{1}{2}\dot{u}^T \frac{\partial \overline{M}}{\partial c_2}\dot{u}\right)\frac{t_2}{^tl} + \left(\frac{1}{2}\dot{u}^T \frac{\partial \overline{M}}{\partial c_3}\dot{u}\right)\frac{t_3}{^tl}.
\end{aligned} \tag{30}
$$

Hence, the expression of the inertial force vector can be obtained by substituting (24) and (30) into (23):

$$q^E = \overline{M}\ddot{u} + \dot{\overline{M}}\dot{u} - \left(\frac{1}{2}\dot{u}^T\frac{\partial\overline{M}}{\partial c_1}\dot{u}\right)\frac{t_1}{^tl} - \left(\frac{1}{2}\dot{u}^T\frac{\partial\overline{M}}{\partial c_2}\dot{u}\right)\frac{t_2}{^tl} - \left(\frac{1}{2}\dot{u}^T\frac{\partial\overline{M}}{\partial c_3}\dot{u}\right)\frac{t_3}{^tl}. \tag{31}$$

2.4. Derivation of the dynamic tangent stiffness matrix. The dynamic tangent stiffness matrix $\overline{K}_{D,t}$ can be written as

$$\overline{K}_{D,t} = \frac{\partial q^g}{\partial u}\Big|_t + \frac{\partial q^E}{\partial u}\Big|_t. \tag{32}$$

Differentiating the global nodal internal force vector q^g and the inertial force vector q^E with respect to displacement, velocity and acceleration, the static tangent stiffness matrix, mass matrix and gyroscopic matrix are given as

$$\overline{K}_T = \frac{\partial q^g}{\partial u}, \quad \overline{M} = \frac{\partial q^E}{\partial \ddot{u}}, \quad \overline{C} = \frac{\partial q^E}{\partial \dot{u}} = \dot{\overline{M}} + \overline{H} - \overline{H}^T, \tag{33}$$

where

$$\overline{H} = \frac{\partial M}{\partial c_1}\left(\dot{u}\frac{t_1^T}{^tl}\right) + \frac{\partial M}{\partial c_2}\left(\dot{u}\frac{t_2^T}{^tl}\right) + \frac{\partial M}{\partial c_3}\left(\dot{u}\frac{t_3^T}{^tl}\right). \tag{34}$$

To get $\partial q^E/\partial u$, the derivative of each term of (31) with respect to the displacement is calculated as

$$\overline{K}_{E,1} = \frac{\partial\overline{M}\ddot{u}}{\partial u} = \frac{\partial\overline{M}}{\partial c_1}\left(\ddot{u}\frac{t_1^T}{^tl}\right) + \frac{\partial\overline{M}}{\partial c_2}\left(\ddot{u}\frac{t_2^T}{^tl}\right) + \frac{\partial\overline{M}}{\partial c_3}\left(\ddot{u}\frac{t_3^T}{^tl}\right) = \overline{M}_{c_1}\ddot{u}\frac{t_1^T}{^tl} + \overline{M}_{c_2}\ddot{u}\frac{t_2^T}{^tl} + \overline{M}_{c_3}\ddot{u}\frac{t_3^T}{^tl}, \tag{35}$$

$$\begin{aligned}
\overline{K}_{E,2} = \frac{\partial\dot{\overline{M}}\dot{u}}{\partial u} &= \left(\frac{t_1^T}{^tl}\dot{u}\right)\left(\frac{\partial\overline{M}_{c_1}}{\partial c_1}\left(\dot{u}\frac{t_1^T}{^tl}\right) + \frac{\partial\overline{M}_{c_1}}{\partial c_2}\left(\dot{u}\frac{t_2^T}{^tl}\right) + \frac{\partial\overline{M}_{c_1}}{\partial c_3}\left(\dot{u}\frac{t_3^T}{^tl}\right)\right) \\
&\quad + \left(\frac{t_2^T}{^tl}\dot{u}\right)\left(\frac{\partial\overline{M}_{c_2}}{\partial c_1}\left(\dot{u}\frac{t_1^T}{^tl}\right) + \frac{\partial\overline{M}_{c_2}}{\partial c_2}\left(\dot{u}\frac{t_2^T}{^tl}\right) + \frac{\partial\overline{M}_{c_2}}{\partial c_3}\left(\dot{u}\frac{t_3^T}{^tl}\right)\right) \\
&\quad + \left(\frac{t_3^T}{^tl}\dot{u}\right)\left(\frac{\partial\overline{M}_{c_3}}{\partial c_1}\left(\dot{u}\frac{t_1^T}{^tl}\right) + \frac{\partial\overline{M}_{c_3}}{\partial c_2}\left(\dot{u}\frac{t_2^T}{^tl}\right) + \frac{\partial\overline{M}_{c_3}}{\partial c_3}\left(\dot{u}\frac{t_3^T}{^tl}\right)\right) \\
&\quad + \overline{M}_{c_1}\dot{u}\dot{u}^T\frac{\partial(t_1^T/^tl)}{\partial u} + \overline{M}_{c_2}\dot{u}\dot{u}^T\frac{\partial(t_2^T/^tl)}{\partial u} + \overline{M}_{c_3}\dot{u}\dot{u}^T\frac{\partial(t_3^T/^tl)}{\partial u},
\end{aligned} \tag{36}$$

$$\begin{aligned}
\overline{K}_{E,3} = &\left(\dot{u}^T\frac{\partial\overline{M}_{c_1}}{\partial c_1}\dot{u}\right)\frac{t_1 t_1^T}{^tl^2} + \left(\dot{u}^T\frac{\partial\overline{M}_{c_1}}{\partial c_2}\dot{u}\right)\frac{t_1 t_2^T}{^tl^2} + \left(\dot{u}^T\frac{\partial\overline{M}_{c_1}}{\partial c_3}\dot{u}\right)\frac{t_1 t_3^T}{^tl^2} \\
&+ \left(\dot{u}^T\frac{\partial\overline{M}_{c_2}}{\partial c_1}\dot{u}\right)\frac{t_2 t_1^T}{^tl^2} + \left(\dot{u}^T\frac{\partial\overline{M}_{c_2}}{\partial c_2}\dot{u}\right)\frac{t_2 t_2^T}{^tl^2} + \left(\dot{u}^T\frac{\partial\overline{M}_{c_3}}{\partial c_3}\dot{u}\right)\frac{t_2 t_3^T}{^tl^2} \\
&+ \left(\dot{u}^T\frac{\partial\overline{M}_{c_3}}{\partial c_1}\dot{u}\right)\frac{t_3 t_1^T}{^tl^2} + \left(\dot{u}^T\frac{\partial\overline{M}_{c_3}}{\partial c_2}\dot{u}\right)\frac{t_3 t_2^T}{^tl^2} + \left(\dot{u}^T\frac{\partial\overline{M}_{c_3}}{\partial c_3}\dot{u}\right)\frac{t_3 t_3^T}{^tl^2} \\
&+ \left(\dot{u}^T\frac{\partial\overline{M}_{c_1}}{\partial c_1}\dot{u}\right)\frac{\partial(t_1^T/^tl)}{\partial u} + \left(\dot{u}^T\frac{\partial\overline{M}_{c_2}}{\partial c_1}\dot{u}\right)\frac{\partial(t_2^T/^tl)}{\partial u} + \left(\dot{u}^T\frac{\partial\overline{M}_{c_3}}{\partial c_1}\dot{u}\right)\frac{\partial(t_3^T/^tl)}{\partial u}.
\end{aligned} \tag{37}$$

The second derivatives of the mass matrix with respect to c_1, c_2 and c_3 in (35)–(37) are

$$\frac{\partial \overline{M}_{c_1}}{\partial c_j} = \frac{\partial R_i^T}{\partial c_j} m^l T + R_i^T m^l \frac{\partial T}{\partial c_j} + \frac{\partial T^T}{\partial c_j} m^l R_i + T^T m^l \frac{\partial R_i}{\partial c_j} \quad \text{for} \quad i, j = 1, 2, 3 \tag{38}$$

and

$$\frac{\partial (t_1^T / {}^t l)}{\partial u} = \frac{(\partial t_i / \partial u) {}^t l - t_i (\partial {}^t l / \partial u)}{{}^t l^2} = \frac{(\partial t_i / \partial u) {}^t l - t_i t}{{}^t l^2} \quad \text{for} \quad i, j = 1, 2, 3, \tag{39}$$

where t_i and t are determined by (27) and (7). Taking into account that $c_1^2 + c_2^2 + c_3^2 = 1$ and that each $\partial t_i / \partial u$ ($i = 1, 2, 3$) is a 6×6 matrix, the partials $\partial R_i / \partial c_j$ and $\partial t_i / \partial u$ can be given as

$$\frac{\partial R_1}{\partial c_1} = \begin{bmatrix} 0 & (c_3^2-1)/c_2^3 & (c_2^2-1)/c_3^3 & 0 & 0 & 0 \\ 0 & 0 & 0 & 0 & (c_3^2-1)/c_2^3 & (c_2^2-1)/c_3^3 \end{bmatrix}, \tag{40}$$

$$\frac{\partial R_2}{\partial c_1} = \begin{bmatrix} (c_3^2-1)/c_1^3 & 0 & (c_2^2-1)/c_3^3 & 0 & 0 & 0 \\ 0 & 0 & 0 & (1-c_3^2)/c_1 c_2^2 & 0 & c_1(c_3^2-c_2^2)/c_2 c_3 \end{bmatrix}, \tag{41}$$

$$\frac{\partial R_3}{\partial c_1} = \begin{bmatrix} (1-c_2^2)/c_3 c_1^2 & c_1(c_2^2-c_3^2)/c_3 c_2^3 & 0 & 0 & 0 & 0 \\ 0 & 0 & 0 & (1-c_2^2)/c_3 c_1^2 & c_1(c_2^2-c_3^2)/c_3 c_2^3 & 0 \end{bmatrix}, \tag{42}$$

$$\frac{\partial R_2}{\partial c_2} = \begin{bmatrix} (c_3^2-1)/c_2^3 & 0 & (c_2^2-1)/c_3^3 & 0 & 0 & 0 \\ 0 & 0 & 0 & (c_3^2-1)/c_2^3 & 0 & (c_2^2-1)/c_3^3 \end{bmatrix}, \tag{43}$$

$$\frac{\partial R_1}{\partial c_2} = \begin{bmatrix} 0 & (1-c_3^2)/c_1 c_2^2 & c_2(c_3^2-c_1^2)/c_1 c_3^3 & 0 & 0 & 0 \\ 0 & 0 & 0 & 0 & (1-c_3^2)/c_1 c_2^2 & c_2(c_3^2-c_1^2)/c_1 c_3^3 \end{bmatrix}, \tag{44}$$

$$\frac{\partial R_3}{\partial c_2} = \begin{bmatrix} c_2(c_1^2-c_3^2)/c_1 c_3^3 & (1-c_1^2)/c_3 c_2^3 & 0 & 0 & 0 & 0 \\ 0 & 0 & 0 & c_2(c_1^2-c_3^2)/c_1 c_3^3 & (1-c_1^2)/c_3 c_2^3 & 0 \end{bmatrix}, \tag{45}$$

$$\frac{\partial R_3}{\partial c_3} = \begin{bmatrix} (c_2^2-1)/c_1^3 & (c_1^2-1)/c_2^3 & 0 & 0 & 0 & 0 \\ 0 & 0 & 0 & (c_2^2-1)/c_1^3 & (c_1^2-1)/c_2^3 & 0 \end{bmatrix}, \tag{46}$$

$$\frac{\partial R_1}{\partial c_3} = \begin{bmatrix} 0 & c_3(c_2^2-c_1^2)/c_1 c_2^3 & (1-c_2^2)/c_1 c_3^2 & 0 & 0 & 0 \\ 0 & 0 & 0 & 0 & c_3(c_2^2-c_1^2)/c_1 c_2^3 & (1-c_2^2)/c_1 c_3^2 \end{bmatrix}, \tag{47}$$

$$\frac{\partial R_2}{\partial c_3} = \begin{bmatrix} c_3(c_1^2-c_2^2)/c_1 c_2^3 & 0 & (1-c_1^2)/c_2 c_3^2 & 0 & 0 & 0 \\ 0 & 0 & 0 & c_3(c_1^2-c_2^2)/c_1 c_2^3 & 0 & (1-c_1^2)/c_2 c_3^2 \end{bmatrix}, \tag{48}$$

$$\frac{\partial t_1}{\partial u} = \begin{bmatrix} 2c_1 \frac{t_1^T}{{}^t l} & c_2 \frac{t_1^T}{{}^t l} + c_1 \frac{t_2^T}{{}^t l} & c_3 \frac{t_1^T}{{}^t l} + c_1 \frac{t_3^T}{{}^t l} & -2c_1 \frac{t_1^T}{{}^t l} & -\left(c_2 \frac{t_1^T}{{}^t l} + c_1 \frac{t_2^T}{{}^t l}\right) & -\left(c_3 \frac{t_1^T}{{}^t l} + c_1 \frac{t_3^T}{{}^t l}\right) \end{bmatrix}^T, \tag{49}$$

$$\frac{\partial t_2}{\partial u} = \begin{bmatrix} c_2 \frac{t_1^T}{{}^t l} + c_1 \frac{t_2^T}{{}^t l} & 2c_2 \frac{t_2^T}{{}^t l} & c_3 \frac{t_2^T}{{}^t l} + c_2 \frac{t_3^T}{{}^t l} & -\left(c_2 \frac{t_1^T}{{}^t l} + c_1 \frac{t_2^T}{{}^t l}\right) & -2c_2 \frac{t_2^T}{{}^t l} & -\left(c_3 \frac{t_2^T}{{}^t l} + c_2 \frac{t_3^T}{{}^t l}\right) \end{bmatrix}^T, \tag{50}$$

$$\frac{\partial t_3}{\partial u} = \begin{bmatrix} c_3 \frac{t_1^T}{{}^t l} + c_1 \frac{t_3^T}{{}^t l} & c_3 \frac{t_2^T}{{}^t l} + c_2 \frac{t_3^T}{{}^t l} & 2c_3 \frac{t_3^T}{{}^t l} & -\left(c_3 \frac{t_1^T}{{}^t l} + c_1 \frac{t_3^T}{{}^t l}\right) & -\left(c_3 \frac{t_2^T}{{}^t l} + c_2 \frac{t_3^T}{{}^t l}\right) & -2c_3 \frac{t_3^T}{{}^t l} \end{bmatrix}^T. \tag{51}$$

Hence, the expression of $\partial \boldsymbol{q}^E / \partial \boldsymbol{u}$ is achieved by integrating (31) and (35)–(37):

$$\frac{\partial \boldsymbol{q}^E}{\partial \boldsymbol{u}} = \overline{\boldsymbol{K}}_E = \overline{\boldsymbol{K}}_{E,1} + \overline{\boldsymbol{K}}_{E,2} + \overline{\boldsymbol{K}}_{E,3}. \tag{52}$$

Substituting (17), (33) and (35)–(37) into (32), the dynamic tangent stiffness matrix can be obtained as

$$\overline{\boldsymbol{K}}_D = \overline{\boldsymbol{K}}_T + \overline{\boldsymbol{K}}_E + \frac{4}{\Delta t^2}\overline{\boldsymbol{M}} + \frac{2}{\Delta t}\overline{\boldsymbol{C}}, \tag{53}$$

where Δt denotes the time step.

Once the aforementioned vectors and matrices are acquired, the classical finite element method is utilized to assemble the global structural dynamic tangent stiffness matrix and mass matrix as

$$\overline{\boldsymbol{K}}_D = \sum \boldsymbol{L} \overline{\boldsymbol{K}}_D \boldsymbol{L}^T, \tag{54}$$

$$\boldsymbol{M} = \sum \boldsymbol{L} \overline{\boldsymbol{M}} \boldsymbol{L}^T, \tag{55}$$

where $\boldsymbol{L}$ is the element connectivity matrix, derived from structural topology and sums extend over all elements.

3. Nonlinear analysis process

The equation of dynamic equilibrium of tensegrity structures can be written as follows:

$$\boldsymbol{q}^E(\boldsymbol{u}, \dot{\boldsymbol{u}}, \ddot{\boldsymbol{u}}) = \boldsymbol{q}^{\text{ext}} - \boldsymbol{q}^g(\boldsymbol{u}), \tag{56}$$

where $\boldsymbol{q}^E$, $\boldsymbol{q}^{\text{ext}}$ and $\boldsymbol{q}^g$ represent the inertial, external and internal force vectors respectively. Note that if the seismic case is simulated, the external force $\boldsymbol{q}^{\text{ext}}$ should be replaced by $\boldsymbol{q}^{\text{ext}} - \boldsymbol{M}\ddot{\boldsymbol{u}}_g$, where $\ddot{\boldsymbol{u}}_g$ is the accelerationc vector of ground motion.

Discretization of (56) at time t gives

$$\boldsymbol{q}_{i,t} = \boldsymbol{q}_t^E(\boldsymbol{u}, \dot{\boldsymbol{u}}, \ddot{\boldsymbol{u}}) + \boldsymbol{q}_t^g(\boldsymbol{u}). \tag{57}$$

Hence

$$\boldsymbol{h}_t = \boldsymbol{q}_{i,t} - \boldsymbol{q}_t^{\text{ext}} = \boldsymbol{0}, \tag{58}$$

where $\boldsymbol{h}_t$ is the equivalent dynamic out of balance forces.

Introducing the predictor-corrector method [Kim and Yong 2001], equation (56) can be solved by using a Taylor series; thus the term $\boldsymbol{q}_{i,t+\Delta t}$ can be written as

$$\boldsymbol{q}_{i,t+\Delta t} = \boldsymbol{q}_{i,t} \left. \frac{\partial \boldsymbol{q}_{i,t+\Delta t}}{\partial \boldsymbol{u}} \right|_t (\boldsymbol{u}_{t+\Delta t} - \boldsymbol{u}_t) = \boldsymbol{q}_{i,t} + \boldsymbol{K}_{D,t}\Delta \boldsymbol{u}. \tag{59}$$

Substituting (59) into (57), the expected incremental predictor step can be computed as

$$\Delta \boldsymbol{u} = \boldsymbol{K}_{D,t}^{-1}(\boldsymbol{q}_{t+\Delta t}^{\text{ext}} - \boldsymbol{q}_t^{\text{ext}}). \tag{60}$$

By using the Newmark-average acceleration method, the updated displacement, velocity and acceleration are calculated:

$$u_{t+\Delta t} = u_t + \Delta u, \tag{61}$$

$$\dot{u}_{t+\Delta t} = \dot{u}_t + \Delta u \left(\frac{3}{4} \ddot{u}_t + \left(\frac{1}{2\Delta t^2}(u_{t+\Delta t} - u_t) - \frac{1}{2\Delta t} \dot{u}_t \right) \right), \tag{62}$$

$$\ddot{u}_{t+\Delta t} = \frac{2}{\Delta t^2}(u_{t+\Delta t} - u_t) - \frac{2}{\Delta t} \dot{u}_t. \tag{63}$$

In order that the equivalent dynamic out of balance forces can be approached to zero at each time step, the updated Newton–Raphson method should be utilized. Therefore, the improvement terms can be calculated as

$$\delta u_{t+\Delta t} = -K_{D,t+\Delta t}^{-1} h_{t+\Delta t}, \tag{64}$$

$$\delta \dot{u}_{t+\Delta t} = \frac{1}{2\Delta t} \delta u_{t+\Delta t}, \tag{65}$$

$$\delta \ddot{u}_{t+\Delta t} = \frac{2}{\Delta t^2} \delta u_{t+\Delta t}. \tag{66}$$

This procedure is then repeated until the value of nodal displacements and the equivalent dynamic out of balance forces fall below the threshold given as

$$\kappa = \max \left(\frac{\|\Delta u\|_2}{\|u_{t+\Delta t}\|_2}, \frac{\|q^{\text{ext}} - q^g\|_2}{\|q^{\text{ext}}\|_2} \right) < \text{Tol} = 10^{-6}. \tag{67}$$

Since slackening is a natural property of cables, the slackening of cable elements is taken into account in the following manner: the actual length of each cable is calculated and compared to its rest length within each iteration. If the rest length is longer than the actual length, the cable is assumed to be slack. Accordingly, its stiffness is not considered in the global structural system, and its axial force is set to zero.

4. Illustrative example

A five-module tensegrity beam (Figure 3; modules numbered M1 to M5) analyzed in [Kahla and Kebiche 2000] and [Tran and Lee 2011] is used to illustrate the proposed method. Eight infinitesimal mechanisms and nine independent self-stress modes are determined based on the rank deficiency equilibrium matrix for the tensegrity beam. In order to eliminate all the infinitesimal mechanisms, this tensegrity beam should be in the feasible self-stress mode which is a linear combination of the above nine independent self-stress modes [Tran and Lee 2010]. The initial self-stress coefficients of the structure can be determined by the mature form-finding methods [Tibert and Pellegrino 2003; Feng and Guo 2015]. Table 1 gives the initial self-stress values and material properties of the five-module quadruplex tensegrity beam.

Before observing the dynamic properties of the tensegrity beam under different seismic excitations, the modal analysis is performed as to give an intuitionistic knowledge of the natural vibration characteristics of this structure. Table 2 gives the first eight natural frequencies of the tensegrity beam modal. It is apparent that the structural natural frequencies are gradually increasing. Isometric views of the first
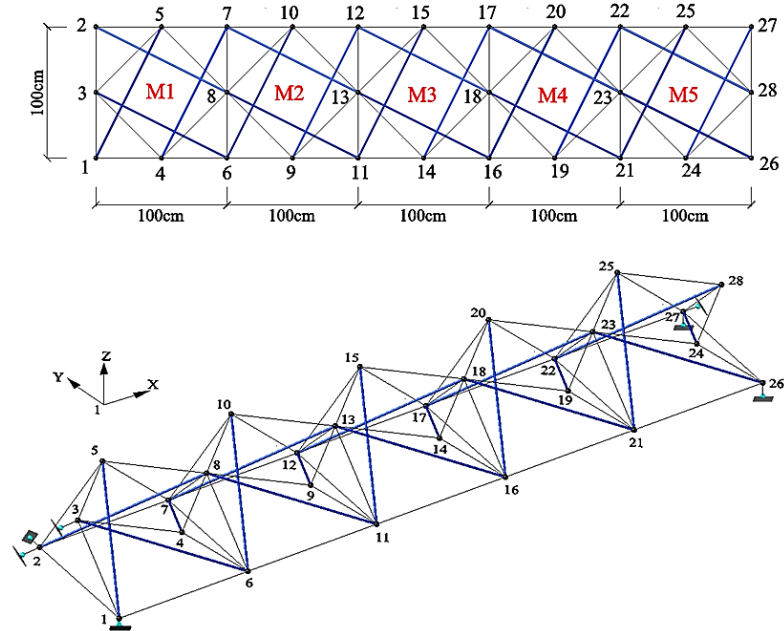
Figure 3. Geometry of a five-module quadruplex tensegrity beam: top view and perspective view.

Element	Category	Stress/KN for module #					Cross section/cm^2	Modulus /GPa
		1	2	3	4	5		
1		3.889	3.753	3.723	3.679	3.719		
2	Lower	6.870	6.517	6.552	6.559	6.963		
3	cables	3.700	7.253	6.875	6.913	6.913	0.280	40
4		7.253	6.875	6.913	6.913	3.705		
5		5.173	4.639	4.681	6.875	5.180		
6	Upper	5.158	5.040	5.053	5.040	5.180		
7	cables	5.129	4.639	4.681	4.639	5.180	0.280	40
8		5.250	5.084	5.095	5.084	5.180		
9		5.262	5.084	5.095	5.084	5.180		
10	Bracing	4.950	4.459	4.488	4.671	5.180		
11	cables	5.158	4.639	4.681	4.639	5.180	0.280	40
12		5.233	5.158	5.312	5.296	5.477		
13		−9.063	−8.472	−8.514	−8.472	−9.041		
14		−9.063	−8.472	−8.514	−8.472	−8.971		
15	Struts	−9.063	−8.780	−8.776	−8.780	−8.971	3.250	200
16		−8.934	−8.034	−8.108	−8.034	−8.971		

Table 1. Initial self-stress values and material properties of the five-module quadruplex tensegrity beam.

Mode	1	2	3	4	5	6	7	8	9	10
Frequency (Hz)	2.7	5.8	12.0	14.8	18.1	21.1	28.9	36.5	45.9	62.5

Table 2. Natural frequencies of the quadruplex unit modal (first eight modes).

four mode shapes are displayed in Figure 4, indicating that the lower order mode shapes are almost symmetrical or anti-symmetrical, while the higher order modes that involve synchronous and asynchronous deformation of adjacent modules can not be identified clearly. This might be explained by the asymmetry of the structure, i.e. the basic module and the placements of the boundary supports are not perfectly symmetrical.
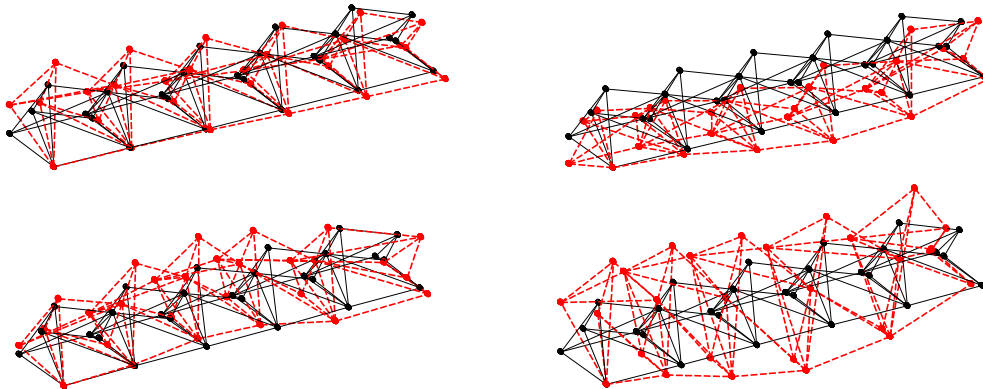

Figure 4. Mode shapes of the first four natural frequencies. Top: Mode 1 (twisting) and Mode 2 (bending). Bottom: Mode 3 (bending) and Mode 4 (higher-order).

To compare the dynamic responses of the tensegrity beam under different seismic excitations, the El Centro and the Taft earthquake data (Figure 5) is employed. The sampling time and time step size are taken as 20 s and 0.02 s, respectively. Figure 6 plots the time history response curves of typical nodal displacements of the tensegrity beam under El Centro seismic wave and Taft seismic wave. Table 3 gives the comparison of the maximum displacements of the specified nodes excited by these two different seismic waves. The numerical results from Figure 6 and Table 3 indicate that the maximum nodal displacements are less differentiating at some level considering two seismic waves, i.e. the nodal displacement distributions are approximately the same. Additionally, the possible maximum structural deflections (node 15) are 0.0209 m (El Centro) and 0.0217 m (Taft) which are less than 1/200 of the beam span. It indicates that the structure will not be damaged due to excessive deformation, and also proves that the tensegrity beam is sufficiently good for lightweight large-span structural applications.

Figure 7 plots the internal forces over time of typical cable elements excited by two different seismic waves, correspondingly, the results of the internal forces over time of typical struts elements are plotted in Figure 8. Obviously, the results from Figures 7–8 show that the changes of internal force in typical cable elements and strut elements are within 350 N and 800 N, respectively. In other words, the maximum variation amplitudes of cables and struts are with 8% and 9%, respectively. This indicates that all these typical cable elements and strut elements remain in tension and compression at all times, respectively.
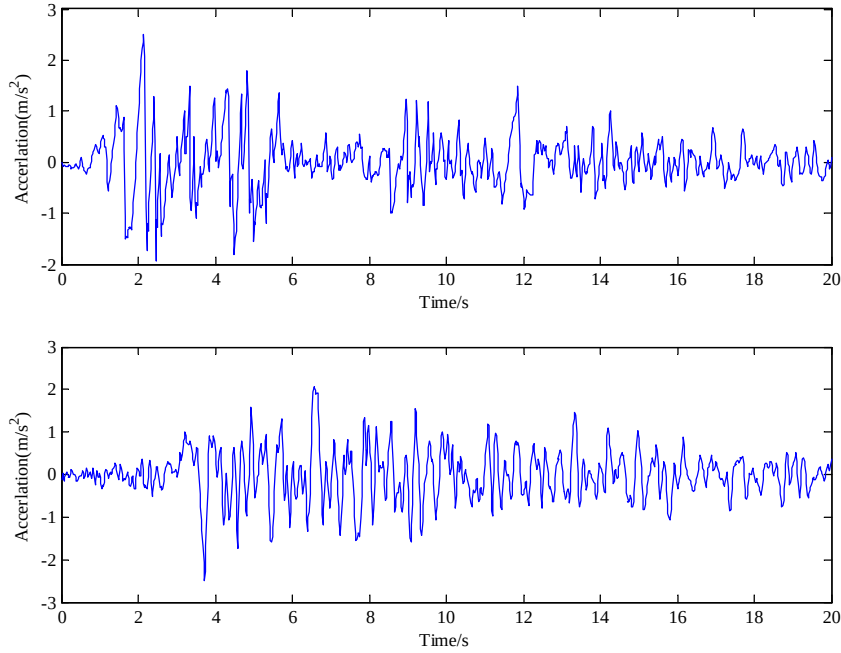
Figure 5. Seismic wave with peak value of 250 Gal. Top: El Centro; bottom: Taft.
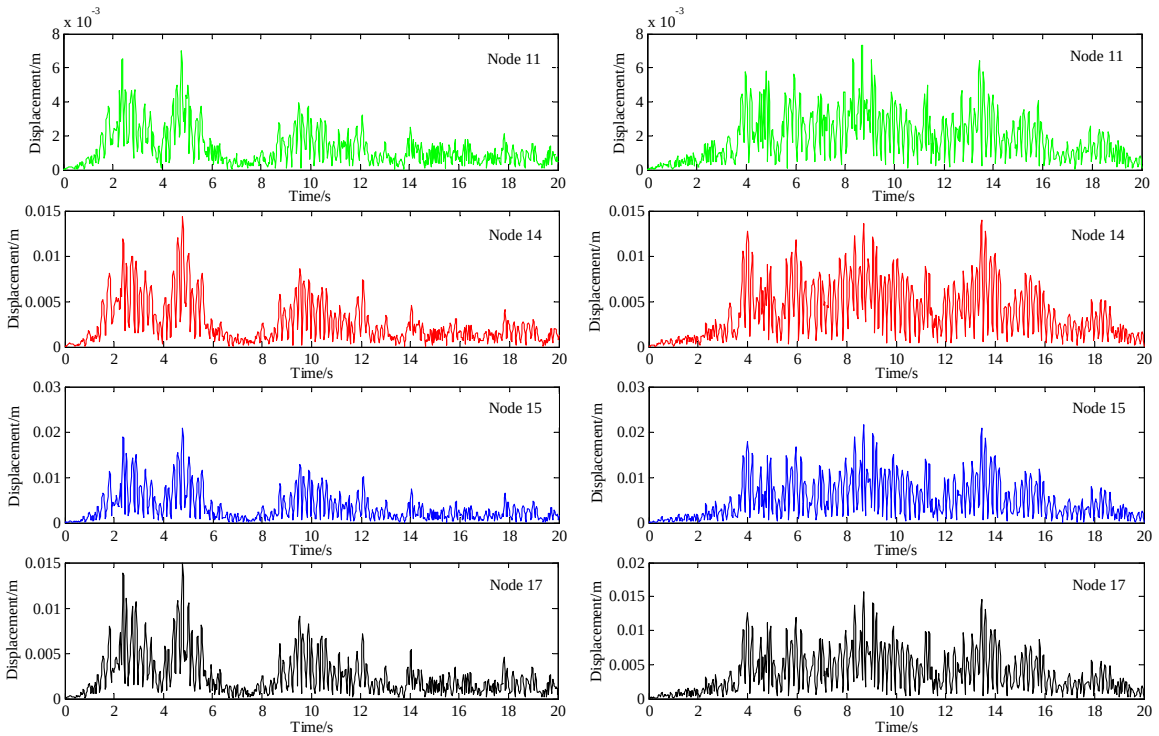
Figure 6. Displacements over time of typical nodes excited by different seismic waves.
Left column: El Centro; right column: Taft.
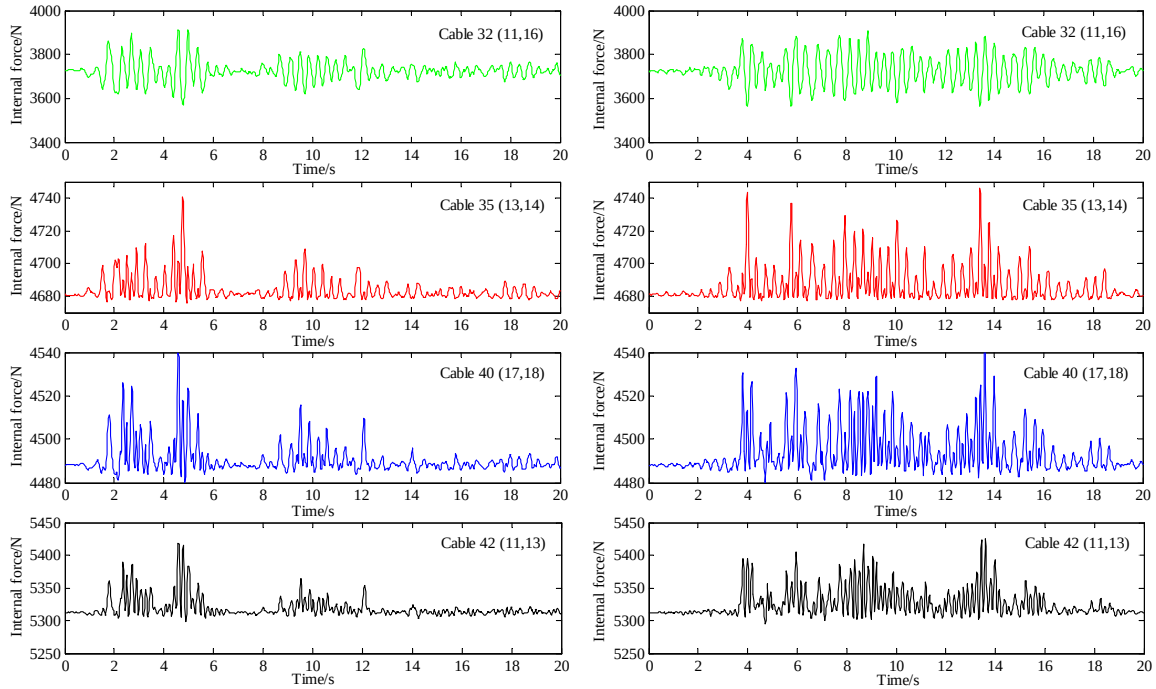
Figure 7. Internal forces over time of typical cable elements excited by different seismic waves. Left column: El Centro; right column: Taft.

That is to say, none of the components of this tensegrity beam with the properties given in Table 1 will be laid off due to the tension in struts or slackening of cables. The whole system works in the elastic range, and the structure has good seismic performance.

Table 3 gives the comparison of the maximum stresses of the specified elements excited by two seismic waves. As can be seen, the maximum elemental stresses (including cables and struts) are very close to each other for the two different seismic waves, demonstrating the phenomenon that the stress distributions of cables or struts are almost the same for the structure excited by these two seismic waves.

Finally, Table 4 gives the comparison of the convergence and efficiency of three different methods, and highlights that the CR formulation presented here is much faster than previous nonlinear formulations based on the total Lagrangian or updated Lagrangian solutions.

Node	11	14	15	17
El Centro	0.0070 m	0.0143 m	0.0209 m	0.0149 m
Taft	0.0073 m	0.0139 m	0.0217 m	0.0157 m

Table 3. Comparison of the maximum displacements of the specified nodes under two different seismic waves.

Figure 8. Internal forces over time of typical strut elements excited by different seismic waves. Left column: El Centro; right column: Taft.

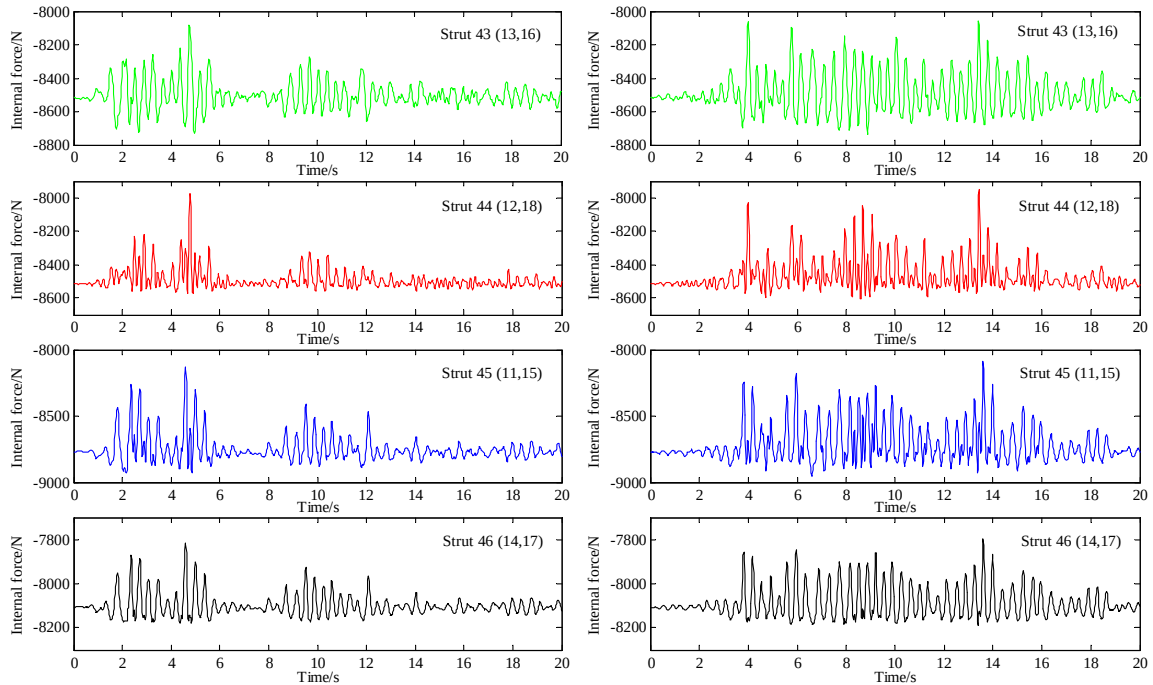|	Taft seismic wave			El Centro seismic wave		
Comparison	TL	UL	CR	TL	UL	CR
Convergence	yes	yes	yes	yes	yes	yes
Total number of iterations	2352	1986	534	2332	1896	521
CPU times	55.29	42.38	19.68	54.89	42.02	19.23

Table 4. Efficiency comparison of formulations for a five-quadruplex module tensegrity beam.

5. Conclusion

We have presented a new three-dimension corotational algorithm to investigate the nonlinear dynamic properties of tensegrity structures. A new dynamic tangent stiffness matrix of a space rod element is derived based on the corotational approach which decomposes a large displacement into a large rigid body motion and a small strain, thus the behavior of elements can be described directly in the local coordinate system utilizing an engineering strain. It is very convenient for implementation of a standard finite element procedure. The validity and efficiency of the proposed method are illustrated by numerical examples. Dynamic responses of tensegrities, including a classical tensegrity quadruplex unit and a five-module quadruplex module tensegrity beam are investigated using the proposed formulation. The outcomes of the proposed study also confirm that the CR approach is more efficient and practical than the

TL and UL formulations of the elements in the structure that have more rigid body modes of translation and rotation than they have deformation modes.

It should be noted that, however, the proposed formulation is not valid for large-strain deformation. Nevertheless, combining with other approaches or technics [Shekastehband et al. 2012; Shekastehband and Abedi 2013], the proposed method could be extended to predict collapse of a tensegrity due to fracture of cables or buckling of bars, i.e. once the axial stress-axial strain behaviors of struts and cables are evaluated by the proposed method, a nonlinear dynamic collapse analysis can then be performed to find the load-deflection responses of the tensegrity system. Additionally, dynamic elasto-plastic behavior and vibration control of tensegrity structures, especially active tensegrities, e.g., deployable tensegrities and clustered tensegrities, need to be further investigated. These are some directions for future work.

Acknowledgements

References

[Adam and Smith 2008] B. Adam and I. F. C. Smith, "Active tensegrity: a control framework for an adaptive civil-engineering structure", *Comput. Struct.* **86** (2008), 2215–2223.

[Barnes 1999] M. R. Barnes, "Form finding and analysis of tension structures by dynamic relaxation", *Int. J. Space Struct.* **14** (1999), 89–104.

[Chen et al. 2012] Y. Chen, J. Feng, and Y. Wu, "Novel form-finding of tensegrity structures using ant colony systems", *J. Mech. Robot.* **4** (2012), 031001.

[Crisfield and Moita 1996] M. A. Crisfield and G. F. Moita, "A unified co-rotational framework for solids, shells and beams", *Int. J. Solids Struct.* **33** (1996), 2969–2992.

[Domer and Smith 2005] B. Domer and I. F. C. Smith, "An active structure that learns", *J. Comput. Civil. Eng.* **19** (2005), 16–24.

[Eriksson and Faroughi 2013] A. Eriksson and S. Faroughi, "Quasi-static inflation simulations based on co-rotational triangular space membrane elements", *Int. J. Struct. Stab. Dyn.* **13** (2013), 714–733.

[Faroughi and Eriksson 2017] S. Faroughi and A. Eriksson, "Co-rotational formulation for dynamic analysis of space membranes based on triangular elements", *Int. J. Mech. Mater. Des.* **13** (2017), 229–241.

[Faroughi and Lee 2014] S. Faroughi and J. Lee, "Geometrical nonlinear analysis of tensegrity based on a co-rotational method", *Adv. Struct. Eng.* **17** (2014), 41–52.

[Faroughi et al. 2015] S. Faroughi, H. H. Khodaparast, and M. I. Friswell, "Non-linear dynamic analysis of tensegrity structures using a co-rotational method", *Int. J. Non-Linear Mech.* **69** (2015), 55–65.

[Faroughi et al. 2017] S. Faroughi, H. H. Khodaparast, M. I. Friswell, and S. H. Hosseini, "A shape memory alloy rod element based on the co-rotational formulation for nonlinear static analysis of tensegrity structures", *J. Intell. Mater. Syst. Struct.* **28** (2017), 35–46.

[Felippa and Haugen 2005] C. A. Felippa and B. Haugen, "A unified formulation of small-strain corotational finite elements: I. Theory", *Comput. Methods Appl. Mech. Eng.* **194**:21-24 (2005), 2285–2335.

[Feng 2017] X. Feng, "The optimal initial self-stress design for tensegrity grid structures", *Comput. Struct.* **193** (2017), 21–30.

[Feng and Guo 2015] X. Feng and S. Guo, "A novel method of determining the sole configuration of tensegrity structures", *Mech. Res. Commun.* **69** (2015), 66–78.

[Feng and Guo 2017] X. Feng and S. Guo, "Geometrical nonlinear elasto-plastic analysis of tensegrity systems via the corotational method", *Mech. Res. Commun.* **79** (2017), 1–11.

[Guest 2006] S. Guest, "The stiffness of prestressed frameworks: a unifying approach", *Int. J. Solids Struct.* **43** (2006), 842–854.

[Juan and Tur 2008] S. H. Juan and J. M. M. Tur, "Tensegrity frameworks: Static analysis review", *Mech. Mach. Theory* **43**:7 (2008), 859–881.

[Kahla and Kebiche 2000] N. B. Kahla and K. Kebiche, "Nonlinear elastoplastic analysis of tensegrity systems", *Eng. Struct.* **22** (2000), 1552–1566.

[Kebiche and Kahla 2000] K. Kebiche and N. B. Kahla, "Nonlinear elastoplastic analysis of tensegrity systems", *Eng. Struct.* **23** (2000), 1552–1566.

[Kebiche et al. 1999] K. Kebiche, M. N. Kazi-Aoual, and R. Motro, "Geometrical non-linear analysis of tensegrity systems", *Eng. Struct.* **21** (1999), 864–876.

[Kim and Yong 2001] J. H. Kim and H. K. Yong, "A predictor-corrector method for structural nonlinear analysis", *Comput. Methods Appl. Mech. Eng.* **191** (2001), 959–974.

[Koohestani and Guest 2013] K. Koohestani and S. D. Guest, "A new approach to the analytical and numerical form-finding of tensegrity structures", *Int. J. Solids Struct.* **50** (2013), 2995–3007.

[Korkmaz 2011] S. Korkmaz, "A review of active structural control: challenges for engineering informatics", *Comput. Struct.* **89** (2011), 2113–2132.

[Le et al. 2011] T. N. Le, J. M. Battini, and M. Hjiaj, "Efficient formulation for dynamics of corotational 2D beams", *Comput. Mech.* **48** (2011), 153–161.

[Le et al. 2012] T. N. Le, J. M. Battini, and M. Hjiaj, "Dynamics of 3D beam elements in a corotational context: a comparative study of established and new formulations", *Finite Elem. Anal. Des.* **61** (2012), 97–111.

[Lee and Lee 2014] S. Lee and J. Lee, "Form-finding of tensegrity structures with arbitrary strut and cable members", *Int. J. Mech. Sci.* **85** (2014), 55–62.

[Luo et al. 2008] Y. Luo, X. Xu, T. Lele, S. Kumar, and D. E. Ingber, "A multi-modular tensegrity model of an actin stress fiber", *J. Biomech.* **41** (2008), 2379–2387.

[Masic and Skelton 2006] M. Masic and R. E. Skelton, "Selection of prestress for optimal dynamic/control performance of tensegrity structures", *Int. J. Solids Struct.* **43** (2006), 2110–2125.

[Murakami 2001] H. Murakami, "Static and dynamic analyses of tensegrity structures. Part 1. Nonlinear equation of motion", *Int. J. Solids Struct.* **38** (2001), 3599–3613.

[Oliveto and Sivaselvan 2011] N. D. Oliveto and M. V. Sivaselvan, "Dynamic analysis of tensegrity structures using a complementarity framework", *Comput. Struct.* **89** (2011), 2471–2483.

[Paul et al. 2006] C. Paul, F. Valero-Cuevas, and H. Lipson, "Design and control of tensegrity robots for locomotion", *IEEE Trans. Robot.* **22** (2006), 944–957.

[Raja and Narayanan 2007] M. G. Raja and S. Narayanan, "Active control of tensegrity structures under random excitation", *Smart Mater. Struct.* **16** (2007), 809–817.

[Rovira and Tur 2009] A. G. Rovira and J. M. M. Tur, "Control and simulation of a tensegrity-based mobile robot", *Robot. Auton. Syst.* **57** (2009), 526–535.

[Shekastehband and Abedi 2013] B. Shekastehband and K. Abedi, "Collapse behavior of tensegrity systems due to cable rupture", *Int. J. Struct. Stab. Dyn.* **13** (2013), 1250079.

[Shekastehband et al. 2012] B. Shekastehband, K. Abedi, N. Dianat, and M. R. Chenaghlou, "Experimental and numerical studies on the collapse behavior of tensegrity systems considering cable rupture and strut collapse with snap-through", *Int. J. Non-Linear Mech.* **47** (2012), 751–768.

[Skelton et al. 2014] R. E. Skelton, F. Fraternali, G. Carpentieri, and A. Micheletti, "Minimum mass design of tensegrity bridges with parametric architecture and multiscale complexity", *Mech. Res. Commun.* **58** (2014), 124–132.

[Sultan and Skelton 2003] C. Sultan and R. Skelton, "Deployment of tensegrity structures", *Int. J. Solids Struct.* **40** (2003), 4637–4657.

[Tibert and Pellegrino 2003] A. G. Tibert and S. Pellegrino, "Review of form-finding methods for tensegrity structures", *Int. J. Space Struct.* **18** (2003), 209–223.

[Tran and Lee 2010] H. C. Tran and J. Lee, "Self-stress design of tensegrity grid structures with exostresses", *Int. J. Solids Struct.* **47** (2010), 2660–2671.

[Tran and Lee 2011] H. C. Tran and J. Lee, "Geometric and material nonlinear analysis of tensegrity structures", *Acta Mech. Sinica* **27**:6 (2011), 938–949.

[Wroldsen et al. 2009] A. S. Wroldsen, M. C. de Oliveira, and R. E. Skelton, "Modelling and control of non-minimal non-linear realisations of tensegrity systems", *Int. J. Control* **82** (2009), 389–407.

[Xu and Luo 2010] X. Xu and Y. Luo, "Form-finding of nonregular tensegrities using a genetic algorithm", *Mech. Res. Commun.* **37** (2010), 85–91.

[Zhang et al. 2013] L. Zhang, Q. Gao, and H. W. Zhang, "An efficient algorithm for mechanical analysis of bimodular truss and tensegrity structures", *Int. J. Mech. Sci.* **70** (2013), 57–68.

[Zhang et al. 2014] L.-Y. Zhang, Y. Li, Y.-P. Cao, and X.-Q. Feng, "Stiffness matrix based form-finding method of tensegrity structures", *Eng. Struct.* **58** (2014), 36–48.

[Zhang et al. 2015] L. Zhang, M. K. Lu, H. W. Zhang, and B. Yan, "Geometrically nonlinear elasto-plastic analysis of clustered tensegrity based on the co-rotational approach", *Int. J. Mech. Sci.* **93** (2015), 154–165.

[Ziegler 2005] F. Ziegler, "Computational aspects of structural shape control", *Comput. Struct.* **83** (2005), 1191–1204.

XIAODONG FENG: `xiaodong.feng@csu.edu.cn`
School of Civil Engineering, Shaoxing University, Shaoxing, 312000, China

∎msp

■
■■msp

SHAFT-HUB PRESS FIT SUBJECTED TO COUPLES AND RADIAL FORCES: ANALYTICAL EVALUATION OF THE SHAFT-HUB DETACHMENT LOADING

ENRICO BERTOCCHI, LUCA LANZONI, SARA MANTOVANI, ENRICO RADI AND ANTONIO STROZZI

A shaft-hub press fit subjected to two non-axisymmetric loading conditions is examined and the situation of incipient detachment between the shaft and the hub is determined. The first condition consists of a central radial load P applied to the hub, balanced by two lateral forces $P/2$ applied to the shaft at a distance d from the hub lateral walls. In the second condition, a central couple C is applied to the hub, and it is balanced by two lateral opposite loads withstood by the shaft at a distance d from the hub lateral walls. The shaft-hub contact is modelled in terms of two elastic Timoshenko beams connected by distributed elastic springs (Winkler foundation), whose constant is analytically evaluated. Based upon this enhanced beam-like modelling, the loading inducing an undesired shaft-hub incipient detachment is theoretically determined in terms of the shaft-hub geometry, of the initial shaft-hub interference, and of the elastic constants. Finite element forecasts are presented to quantify the error of this beam-like approximate analytical approach.

1. Introduction

Press fit between a hub and a shaft is a widely employed clamping method, but it can lead to problems of fretting fatigue if the clamping pressure generated by interference is insufficient to prevent slip. A limit situation in which slip inevitably occurs is when the loading applied to the shaft-hub assembly causes an appreciable shaft bending that in turn produces incipient detachment between the shaft and the hub. This incipient detachment situation is an indicator of poor mechanical design, and it may be assumed as a reference condition against the outcome of fretting.

The title problem bears some similarity with the press fit of the bush into a connecting rod small end [Marmorini et al. 2012]. The undesired event is bush loosening, since it favours bush rotation, which would occlude the lubrication hole; the load that produces bush loosening is assumed as a reference loading, and the admissible force must exhibit a safety factor with respect to the reference load threshold.

The available models of the shaft-hub press fit possess an extensive literature spread over various decades, which may be classified into three main groups. The first category collects the classical, axisymmetric, plane solution of a shaft-hub interference fit. This solution neglects the possible outcome of pressure peaks at the contact extremities, and it ignores loadings that produce shaft bending. The second group addresses the evaluation, for an axisymmetric loading, of the pressure bumps occurring at the contact extremities. The third set considers both the presence of lateral pressure peaks and of shaft bending, caused by a non axisymmetric loading. Extended literature review on these three topics is available in [Strozzi et al. 2011; 2016; Croccolo et al. 2012; Smetana 2001; Radi et al. 2017].

Keywords: press fit, incipient detachment, analytical solution, Winkler foundation, finite elements.
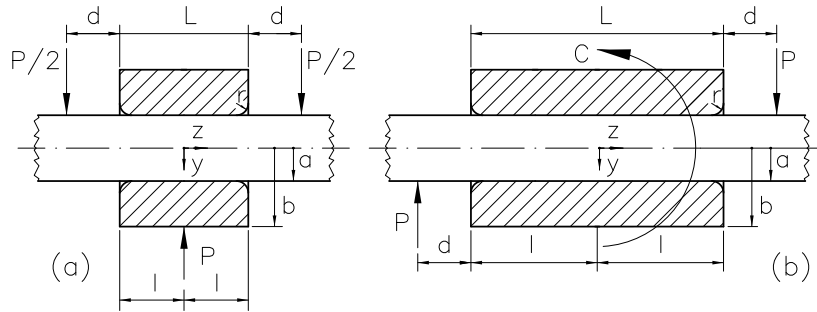
Figure 1. The two loading conditions (a) and (b) in terms of the forces P and the couple C, and the meaning of the symbols a, b, d, l, L, r, y, z.

This paper presents both analytical and numerical investigations on the mechanical response of a shaft-hub press fit subjected to an external, non axisymmetric loading. Two loading conditions of practical interest are addressed:

(i) A central radial load P is sustained by the hub, and it is equilibrated by two lateral forces $P/2$ applied to the shaft at a distance d from the hub lateral walls (Figure 1a).

(ii) A central couple C applied to the hub is equilibrated by two lateral loads $P = C/[2(l+d)]$, sustained by the shaft at a distance d from the hub lateral walls (the hub length being L), and having opposite directions (Figure 1b).

Figure 1 also clarifies the meaning of the symbols a, b, d, l, L, r, y, z.

This practically oriented paper complements a previous work addressing a press-fit, in which the shaft was deflected by two equal bending couples applied to the shaft extremities [Strozzi et al. 2016; Radi et al. 2017]. The above loading together with the two additional loadings illustrated in Figure 1 constitute three loading conditions considered in the DIN standards discussed in the two papers cited.

The main aim of this paper is to determine the intensity of the bending loading that locally annihilates the initial contact pressure due to the shaft-hub press fit alone, and it begins the detachment between the shaft and the hub. As already noted, the occurrence of a shaft-hub separation constitutes an indicator of poor mechanical design, since it promotes undesired phenomena of wear and fretting fatigue [Ciavarella et al. 1998]. Such observations justify this return to the analysis of situations of incipient detachment.

A rigorous three-dimensional analytical modelling of the detachment condition being prohibitively complex, the modelling of the shaft-hub contact is approximated in terms of two elastic Timoshenko beams connected by distributed elastic springs (Winkler model), see [Radi et al. 2017]; the classical Lamé solution is employed to simulate the press-fit stresses in the absence of external loading. The analytical evaluation of the intensity of the loading that locally begins the detachment between the shaft and the hub is achieved by separately evaluating the frictionless contact pressure due to the press-fit alone, and the contact pressure imputable to the shaft bending alone. The corresponding solutions are briefly considered in the following sections; further details can be found in [Radi et al. 2017].

The authors are aware of the availability of alternative approaches for describing the incipient detachment between two bodies; see, e.g., [Deseri and Owen 2003; 2010]. However, the two-beam model already employed in [Radi et al. 2017] was found to be suitable for our purposes.

The analytical prediction of the detachment loading when the shaft is loaded by couples at its extremities, presented in [Radi et al. 2017], indicates that the unavoidably approximate beam-like modelling favoured in this paper to describe this contact detachment problem supplies an indicative value rather than an accurate threshold of the critical loading. It is therefore expected that for the two loading conditions illustrated in Figure 1 the analytical solution be approximate, although still technically significant. Various three-dimensional finite element (FE) forecasts are included in this paper, that provide an accurate prediction of the detachment loading, albeit only for a selection of press-fit geometries, and they permit the evaluation of the error incurred in the approximate analytical approach.

The FE forecasts of [Strozzi et al. 2016] indicate that, if the hub bore edges are rounded, the couple that produces the shaft-hub detachment is higher than its counterpart valid for sharp hub bore edges. In practical situations, this increase may be of, say, 20 per cent. A thorough modelling of the shaft-hub detachment problem should therefore incorporate the hub bore fillet radius effect. However, since the main aim of this paper is to determine an indicative value of the detachment loading rather than its accurate threshold, the effect of the hub bore rounded edges is not explored in this paper, and reference is made to a sharp bore edge both in the analytical and in the FE studies.

In [Radi et al. 2017] the press fits subjected to bending have been classified into two main categories. The first group collects problems in which the shaft laterally protrudes from both the hub sides, and the shaft projecting portions are subjected to bending, as in the two couplings of Figure 1. Bearing mounting often belongs to this category. The second group embraces situations where the shaft protrudes from only one side of the hub, whereas the remaining shaft extremity is aligned with one of the two hub lateral faces; in this case, the external loading is applied to the shaft protrusion and to the hub. The crankpin press-fitting into a crankweb in a composite crankshaft [Smetana 2001; Strozzi and Vaccari 2003] belongs to this second group. This paper addresses the first category by examining in detail two detachment problems whose geometries and loadings are illustrated in Figure 1, and it is organized as follows. Section 2 considers the contact pressure due to press fit alone, whereas Section 3 addresses the contact pressure caused by the shaft bending alone; Section 4 analytically evaluates the Winkler constant; Section 5 imposes the incipient detachment condition; Section 6 reports fundamental solutions in the FE study; Section 7 compares analytical and FE forecasts.

2. Press-fit contact pressure

The shaft-hub contact pressure due to the press-fit alone is axisymmetric, and it stays reasonably constant in its central part, whereas it exhibits localized pressure bumps at the shaft-hub contact extremities, where the hub bore edges are rounded. Overall, the pressure profile is camel backed [Strozzi et al. 2011; Croccolo et al. 2012]. The analytical value of the elastic flattish central contact pressure p_{pf} (the index pf denotes "press fit") is correctly forecast by the Lamé plane modelling, e.g. [Strozzi et al. 2011]:

$$p_{pf} = \frac{E\delta}{2a}(1 - \alpha^2),$$ (1)

where a denotes the nominal value of both the shaft radius (the shaft is assumed to be solid) and of the hub inner radius, $\alpha = a/b$, and b represents the hub outer radius, Figure 1. In addition, δ denotes the radial interference, and E is the Young's modulus of the material of both the above components.

No simple expression is available that quantifies the lateral pressure bumps [Strozzi et al. 2011; Croccolo et al. 2012]. Since the shaft detaches from the hub starting from their contact extremities, at a first sight the detachment loading is expected to be appreciably influenced by such pressure bumps, whose presence cannot therefore be ignored. However, since the pressure bumps are extremely localized, when the loading produces an axial extent of the shaft-hub detachment higher than that of the pressure bump, the pressure bumps disappear, and the contact pressure smoothly decays from its flattish central value to zero [Strozzi et al. 2016]. It may therefore be concluded that, when computing the loading that initiates the shaft-hub separation, it is acceptable to refer to the flattish central contact pressure of formula (1) and to neglect the lateral pressure bumps; see [Strozzi et al. 2016] for additional details.

3. Contact pressure due to the shaft bending

This section addresses the analytical evaluation of the frictionless contact pressure bilaterally exerted between the shaft and the hub in the presence of a perfect fit, i.e., in the absence of interference or clearance, as a result of the external loading alone, see Figure 1. The shaft-hub contact is assumed as bilateral, since this paper addresses and incipient detachment condition rather than a partially detached contact. Following [Radi et al. 2017], the shaft and the hub are described in terms of two Timoshenko beams according to a shear-deformable modelling, endowed with a Winker foundation to account for the deformations of the shaft and hub cross sections due to the in-plane stresses. The analytical approach follows the same lines as those detailed in [Radi et al. 2017] for the shaft loading constituted by two couples, to which the interested reader is referred; attention is paid in Sections 3.1 and 3.2 to the boundary conditions to be applied to the two beams for the two loadings detailed in Figure 1, whereas only a perfunctory description of the analytical solution of the two contact problems of Figure 1 is reported in this paper.

The governing equation of this beam contact problem is the fourth order ODE [Radi et al. 2017]:

$$\frac{d^4\Phi}{dz^4} - \frac{4\varepsilon\lambda^2}{l^2}\frac{d^2\Phi}{dz^2} + \frac{4\lambda^4}{l^4}\Phi = 0, \tag{2}$$

where the non-dimensional constants λ and ε have been introduced together with the auxiliary constant γ:

$$\lambda^4 = \frac{Kl^4}{4}\left(\frac{1}{EI_1} + \frac{1}{EI_0}\right), \quad \gamma^2 = \frac{Kl^2}{4}\left(\frac{\chi_1}{GA_1} + \frac{\chi_0}{GA_0}\right). \tag{3}$$

$$\varepsilon = \frac{\gamma^2}{\lambda^2} = \left(\frac{\chi_1}{GA_1} + \frac{\chi_0}{GA_0}\right)\sqrt{\frac{KEI_0I_1}{4(I_0+I_1)}} = \frac{1+\nu}{2}\sqrt{\frac{K}{\pi E}\frac{1+\alpha^2}{1-\alpha^2}}\left[(1-\alpha^2)\chi_1 + \alpha^2\chi_0\right]. \tag{4}$$

In (2), Φ denotes the relative rotation between two cross sections of the two beams describing the shaft and the hub, respectively, at the same axial coordinate z, Figure 1, and l is the hub half length. In addition, K is the Winkler constant, E is the Young's modulus, G is the shear modulus, A_0 and A_1 are the areas of the cross sections of the two beams, I_0 and I_1 are their moments of inertia, and χ_0 and χ_1 are their shear factors, see [Radi et al. 2017], respectively. A discussion on the evaluation of the Winkler constant K is postponed to Section 4.

The general solution of the ODE (2) in terms of Φ is:

$$\Phi(z) = \left[c_1 \sin\left(\lambda\sqrt{1-\varepsilon}\,\frac{z}{l}\right) + c_2 \cos\left(\lambda\sqrt{1-\varepsilon}\,\frac{z}{l}\right)\right] \cosh\left(\lambda\sqrt{1+\varepsilon}\,\frac{z}{l}\right)$$
$$+ \left[c_3 \sin\left(\lambda\sqrt{1-\varepsilon}\,\frac{z}{l}\right) + c_4 \cos\left(\lambda\sqrt{1-\varepsilon}\,\frac{z}{l}\right)\right] \sinh\left(\lambda\sqrt{1+\varepsilon}\,\frac{z}{l}\right), \tag{5}$$

where c_i ($i = 1, 2, 3, 4$) are non-dimensional constants to be determined by imposing the boundary conditions at $z = 0, l$.

The contact force q between the two beams is obtained by repeatedly differentiating Φ according to formula (6) [Strozzi et al. 2016]. Since it has been ascertained that, for the cases examined, the shaft-hub separation always initiates from the hub extremities defined by $z = l$ [Radi et al. 2017], and not at the hub centre, it is important to evaluate therein the value of the contact force q. Finally, the corresponding maximum contact pressure $p_{\max}$ has been estimated in formula (6) by assuming a cosinusoidal distribution of the contact pressure in the circumferential direction; see [Radi et al. 2017] for additional details:

$$q = K \frac{l^4}{4\lambda^4} \frac{d^3\Phi}{dz^3}, \quad q(l) = \frac{Kl^4}{4\lambda^4} \frac{d^3\Phi(l)}{dz^3}, \quad p_{\max} = \frac{Kl^4}{4\pi r_i \lambda^4} \frac{d^3\Phi(l)}{dz^3}. \tag{6}$$

The boundary conditions for the two loadings of Figures Figure 1a and 1b are separately treated in Sections 3.1 and 3.2.
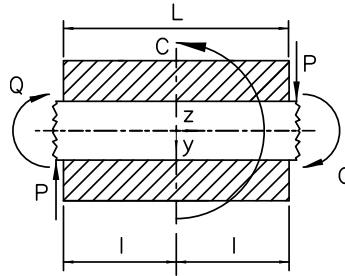
3.1. *Boundary conditions for the loading constituted by a central force and by two lateral equilibrating forces.* In this Section the loading condition is examined in which a central radial force P applied to the hub is equilibrated by two lateral forces $P/2$ applied to the shaft at a distance d from the hub lateral walls, Figure 1a. The aim of this Section is to formulate the corresponding boundary conditions for the beam modelling.

It is convenient to refer to the statically equivalent loading detailed in Figure 2, in which the two forces $P/2$ applied to the shaft at a distance d from the hub lateral walls, Figure 1a, are substituted by two forces $P/2$ applied to the shaft section aligned with the hub lateral walls, and by two couples $C = Pd/2$ applied to the shaft. Figure 2 also clarifies the origin of the z coordinate.

The four unknown constants c_i of the general solution expressed by (5) are evaluated by imposing four boundary conditions, expressing that a) at the shaft-hub contact midpoint, i.e., for $z = 0$, the unknown function Φ vanishes, whereas the shear force assumes the value $P/2$, consistent with the presence of the central force P applied to the hub, and that b) at the shaft-hub contact extremity, i.e. for $z = l$, the
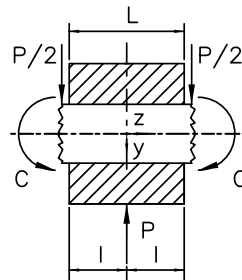
Figure 2. The boundary conditions to be applied to the beam for the loading of Figure 1a.

Figure 3. The boundary conditions to be applied to the beam and to the hub for the loading of Figure 1b.

bending moment M_i and the shear force T_i (indices 0 and 1 denote the hub and the shaft, respectively) equal the applied moment $C = Pd/2$ and the force P, within the respect of the sign conventions of Figure 4 of [Radi et al. 2017]:

$$\Phi(0) = 0, \quad \frac{d^2\Phi}{dz^2}(0^+) = -\frac{P}{2EI_0}, \quad \frac{d\Phi}{dz}(l) = -\frac{C}{EI_1} = -\frac{Pd}{2EI_1}, \quad \frac{d^2\Phi}{dz^2}(l) = \frac{P}{2EI_1}. \qquad (7)$$

The expressions of the four unknown constants c_i are too long to be reported here.

3.2. *Boundary conditions for the loading constituted by a central couple and by two lateral equilibrating forces of opposite directions.* In this section the loading condition is examined in which a central couple applied to the hub is balanced by two lateral, opposite forces $P = C/[2(l + d)]$ exerted on the shaft at a distance d from the hub lateral walls, Figure 1b. The aim of this Section is to formulate the corresponding boundary conditions for the beam modelling.

It is advantageous to refer to the statically equivalent loading detailed in Figure 3, in which the two forces P applied to the shaft at a distance d from the hub lateral walls are substituted by two forces P exerted on the shaft section aligned with the hub lateral walls, and by two couples $Q = Pd$ withstood by the shaft.

The four unknown constants c_i of (5) are evaluated by imposing four boundary conditions, expressing that a) at the shaft-hub contact midpoint, i.e., for $z = 0$, the loading is skew-symmetric, and, therefore, the bending moment assumes the value reported in (8), whereas the contact force q is null, thus implying that $d^3/dz^3 = 0$ according to (6); b) the shear force and the bending moment at the shaft-hub contact extremity, i.e. for $z = l$, assume the values reported in (8), within the respect of the sign conventions of Figure 4 of [Radi et al. 2017]:

$$\frac{d\Phi}{dz}(0^+) = \frac{C}{2EI_0}, \quad \frac{d^3\Phi}{dz^3}(0) = 0, \quad \frac{d\Phi}{dz}(l) = -\frac{Cd}{[2(l+d)]EI_1}, \quad \frac{d^2\Phi}{dz^2}(l) = \frac{C}{[2(l+d)]EI_1}. \qquad (8)$$

4. Evaluation of the Winkler constant

It has been observed in [Radi et al. 2017] that the introduction of a Winkler model in the analytical description of the contact interaction between the shaft and the hub is physically advantageous, since it avoids the outcome of stress singularities at the contact extremities.

In [Radi et al. 2017] various models proposed for evaluating the Winkler constant have been compared, and it has been shown that its numerical value noticeably varies according to the approach employed. In particular, in formula (12) of [Lundberg 1958] the deformability of the shaft-hub cross section has been estimated by adopting a plane model formed by a hollow disk surrounded by a ring, and by adopting a simplified loading. A closed form expression has been obtained for the Winkler constant K:

$$\frac{K}{2G} = \frac{\pi(1+\nu)}{(1-\nu)}\Big[1+\Big(\frac{a_i}{a}\Big)^2\Big]\Big[1+\Big(\frac{a}{b}\Big)^2\Big]\Big[1-\Big(\frac{a_i}{a}\Big)^2\Big(\frac{a}{b}\Big)^2\Big]^{-1}, \tag{9}$$

where a_i, a, and b are the inner, intermediate, and outer radii, respectively. For $\nu = 0.3$, for a solid shaft ($a_i = 0$), and for the reference configuration $b = 2a$, $K/(2G) = 7.29$.

The radial compliance of a solid circular cross section surrounded by a ring is analytically examined in [Strozzi et al. 2016]. Following the approach of [Castillo and Barber 1997], the differences between the shear stresses acting on the two plane cross sections of a thin shaft slice are replaced by body forces. The exact distribution of the shear stresses τ_{rz} and $\tau_{\theta z}$ due to a shear force is analytically available both for a solid disk and a ring, [Love 1944, p. 335]. The analytical expression of the Winkler constant has been evaluated in [Radi et al. 2017] with an energy approach based on the Clapeyron theorem. Within this model, for the above reference geometry $\alpha = a/b = 1/2$ and for $\nu = 0.3$ and adopting plane strain, the normalized Winkler constant $K/(2G)$ is 1.90.

An alternative model for evaluating the Winkler constant assumes that the body forces representative of the shear stresses be uniformly distributed according to a gravitational field within both the solid disk and the ring, see Figure 2a of [Castillo and Barber 1997]. In this case, the analytical solution provides $K/(2G) = 3.68$ for $\alpha = a/b = 1/2$ and for $\nu = 0.3$ in plane strain.

In the present work we propose an alternative procedure for evaluating the Winkler constant, based on the virtual work theorem. We assume indeed a uniform distribution of shear stress, whose resultants are a unit shear force in the shaft and an opposite unit shear force in the hub, as the virtual stress field working for the actual distribution of shear strain provided in [Radi et al. 2017] as τ_{rz}/G and $\tau_{\theta z}/G$ and due to the opposite shear forces Q acting on shaft and hub. The latter work is then compared to that carried out by the unit shear forces acting on shaft and hub for the actual relative displacement between shaft and hub, namely Q/K. In this case, the analytical expression of $K/(2G)$ becomes:

$$\frac{K}{2G} = \frac{48\pi}{D}(1-\alpha^4)^2(1-\nu^2), \tag{10}$$

where

$$D = \big\{(1-\alpha^2)[15-33\nu-20\nu^2+64\nu^3+\alpha^2(34-46\nu-72\nu^2+80\nu^3)+\alpha^4(35-77\nu-4\nu^2+48\nu^3)]$$
$$- 12(1+\alpha^2)[3-\nu-4\nu^2+2\alpha^2(3-\nu-2\nu^2)]\ln\alpha\big\}. \tag{11}$$

With this model, for $\alpha = a/b = 1/2$ and for $\nu = 0.3$, $K/(2G) = 2.6933$ under plane strain conditions.

The Winkler constant derived from the application of the principle of virtual work does not need to be strictly positive. In fact, for $\nu \cong -0.9$ the normalized Winkler constant exhibits an unphysical singular behavior. However, the press-fit problem examined in this paper deals with classical elastic materials whose Poisson's ratio is positive and, therefore, this anomaly has not been examined further.

Figure 4 reports the normalized Winkler constant $K/(2G)$ versus $\alpha = a/b$ for the three above models, i.e., for the body forces according to the exact shear stress distribution, referred to as "Love", for the
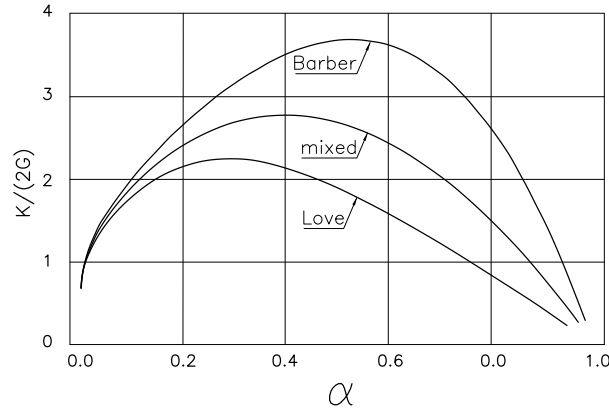
Figure 4. Three normalized Winkler constants $K/(2G)$ in terms of $\alpha = a/b$, for $\nu = 0.3$, in plane strain.

shear stresses distributed according to a gravitational loading, named "Barber", and for the proposed combination of the two above stress distributions, denoted "mixed". Plane strain is assumed, and $\nu = 0.3$. The corresponding values are reasonably comparable; the foundation of (9) supplies considerably higher values and, therefore, it has not been included in Figure 4. Note that the limit of $K/(2G)$ for $\alpha = 0, 1$ vanishes, according to its physical meaning.

In [Radi et al. 2017] it has been noted that, in the region where the shaft-hub separation begins, the shaft protrudes from the hub, so that the cross section of the shaft projecting part, being no longer directly compressed by the contact pressure, but being only deflected by the bending moment, remains reasonably undeformed with respect to its counterpart directly compressed by the hub. The above observation suggests that the Winkler constant may be more realistically evaluated by considering only the in-plane deformability of the hub cross section, whereas the deformability of the shaft cross section is neglected. This assumption produces an increase of the Winkler constant, albeit moderate. For $\alpha = a/b = 1/2$ and for $\nu = 0.3$ under plane strain conditions, the normalized Winkler constant increases to 2.31 for the "Love" model, to 4.81 for the "Barber" model, and to 3.39 for the "mixed" model. The above assumption for the evaluation of the Winkler constant has been adopted in this paper in the compilation of the detachment diagrams; see Figures 6 and 7.

5. Incipient detachment condition

The condition of shaft-hub incipient detachment requires that the contact pressure p_{if} due to the press fit alone and expressed by (1) equals the opposite of the maximum contact pressure p_{max} caused by the shaft bending alone, and expressed by (6):

$$p_{\text{if}} = p_{\text{max}} \Rightarrow \frac{E\delta}{2a}(1 - \alpha^2) = -\frac{Kl^4}{4\pi r_i \lambda^4} \frac{d^3 \Phi(l)}{dz^3}. \tag{12}$$

Equation (12) allows the evaluation of the analytical value of the loading that initiates the shaft-hub detachment. For the loading of Figure 1a, Equation (12) supplies the critical value of the force P, whereas for the loading of Figure 1b it provides the critical value of the couple C.

6. Finite element study

The approximate beam-like modelling developed in this paper supplies an indicative, although still technically significant, value of the incipient detachment loading. To quantify the error incurred by the beam-like approach, various three-dimensional finite element (FE) forecasts have been presented in Section 7, that supply an accurate prediction of the detachment loading, albeit only for a selection of press-fit geometries.

The commercial FE program MSC Marc 2013 has been employed in this study. The 3D mesh is formed by about 23000 biquadratic quadrilateral elements adopting a Fourier formulation. The element size grades smoothly from 0.016 times the shaft radius a at the indenting edge, to 0.1 times in the zones far from the stress singularity. For all the test cases, a refined mesh with halved element sides was employed to assess the numerical convergence. The relative error of the coefficient H defining the radial stress singular term, see below, was found to be 0.14 per cent. A similar mesh is displayed in Figure 3 of [Strozzi et al. 2016].

The FE solutions for the two problems described in Figure 1 express the normalized detachment loading for the following three normalized geometries, namely a) the ratio a/b between the hub inner and outer radii; b) the ratio a/L between the shaft radius and the hub axial length; c) the ratio d/a of the distance of the lateral loadings from the hub lateral faces, to the shaft radius.

To limit the computational effort, fundamental FE loadcases have been identified in Figure 5, whose superposition provides the detachment loading for a general d/a value, although for prescribed values of a/b and a/L. Figure 5(a) addresses the frictionless stress field due to the interference alone, whereas the remaining Figs consider various loadings for a shaft-hub perfect fit, bilateral, frictionless contact pressure. For the loading of Figure 1(a), the three suitable fundamental loadcases are presented in Figures 5(a), 5(b), 5(c), whereas for the loading of Figure 1(b), the three fundamental loadcases are those of Figures 5(a), 5(d), 5(e).

For instance, suitable combinations of the loadings of Figures 5(b) and 5(c) allow various distances d of the lateral forces P from the hub sides to be modelled for a perfect fit. Consequently, for a prescribed d, the relative weights of the solutions of Figures 5(b) and 5(c) may be determined. The weight of the solution of Figure 5(a), supplying the shaft-hub press-fit stresses, may be evaluated by numerically imposing, similar to the analytical condition of Section 5, the incipient detachment condition through the vanishing of the contact pressure where detachment begins. In other words, the correct combination of the previous fundamental solutions must annihilate the radial stress at the sharp edge at the hub bore side.

Unfortunately, it is difficult to robustly implement the above procedure in a FE analysis. In fact, for a general loading, the sharp edge produces a theoretically unbounded contact pressure. To circumvent this numerical difficulty, an incipient detachment condition has been adopted that is based on the non-singular displacement field, see Appendix 4 of [Strozzi et al. 2015]. In more detail, according to the dominant term of the Williams asymptotic expansion, the stress tensor singularly behaves as $H \times f_{ij}(\varphi) \times s^{-0.226}$, whereas the displacement vector non singularly behaves as $H \times g_i(\varphi) \times s^{1-0.226}$, where (s, φ) is a local polar coordinate system along the meridional plane of Figure 1, whose origin falls at the sharp edge of the hub bore. The expressions of the f_{ij}, and g_i functions are known, and they are independent of the loading. In [Yosibash and Szabó 1995] it is shown that the singularity strength is the same for a plane
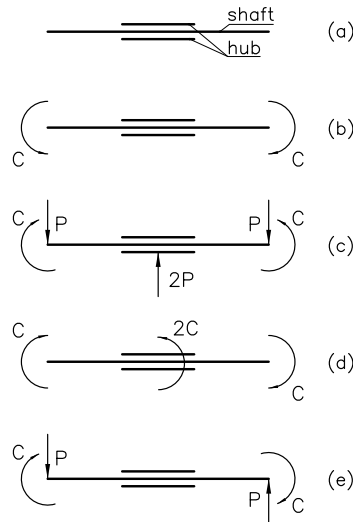
Figure 5. Five basic solutions.

and for an axisymmetric domain, see also [Huang and Leissa 2007]. The incipient detachment condition requires that σ_r vanishes at the sharp edge, which in turn demands that H too be null.

It is numerically convenient to compute H by sampling the FE radial displacement component moving along the hub lateral face, rather than the radial stress component moving along the contact interface. A best fitting procedure is then employed to extract the multiplying coefficient H of $u_r = H \times g_r(0) \times s^{1-0.226}$.

The coefficient H has been evaluated for all the loadcases of Figure 5. Returning to the above example, the relative weights of the two loadcases of Figure 5(b) and 5(c) may be determined by imposing the value of the distance d, Figure 1(a). Such weights depend on the external loading, on the coupling geometry, and on the Poisson ratio. The weight of the loadcase of Figure 5(a) depends on the initial interference, on the coupling geometry, on the Poisson ratio, and linearly on the Young's Modulus; it may be determined by imposing that the superposition of the three above loadcases produces a null coefficient H. It is concluded that this numerical procedure determines the relationship between the initial interference and the external loading, for a prescribed press-fit geometry and for given elastic constants.

7. Comparison between analytical and FE forecasts

As noted in the Introduction, the unavoidably approximate beam-like modelling of the two contact problems (a) and (b) of Figure 1 supplies the order of magnitude of the critical loading rather than an accurate forecast of its threshold. For this reason, various FE forecasts have been enclosed in this paper, that supply accurate predictions of the detachment loading, although only for selected press fit geometries, and they permit the error incurred by the simplified analytical approach to be quantified. The comparison between analytical and FE forecasts for the two press-fit loadings detailed in Figures 1(a) and 1(b) is separately presented in the following two Sections 7.1 and 7.2. As discussed in the Introduction, reference is made for simplicity to hub bore sharp edges, and the effect of a fillet radius is not explored.
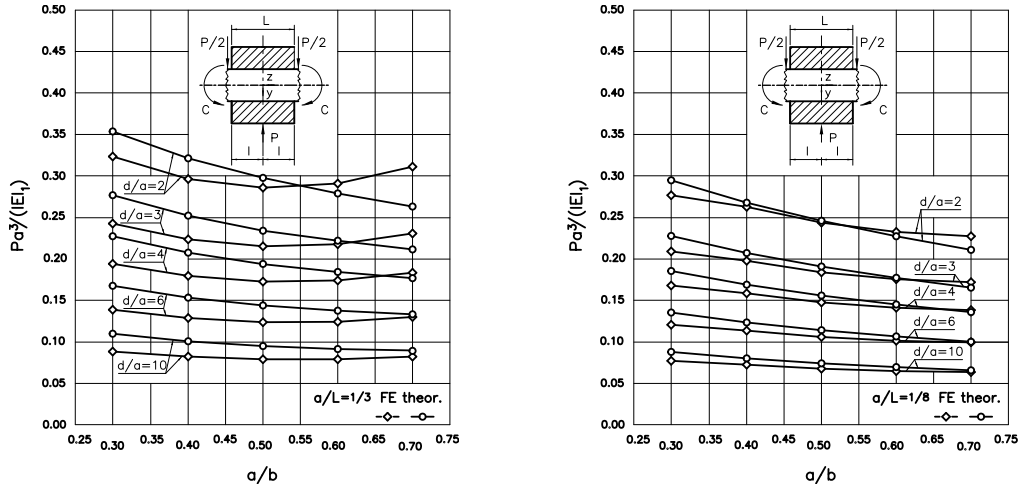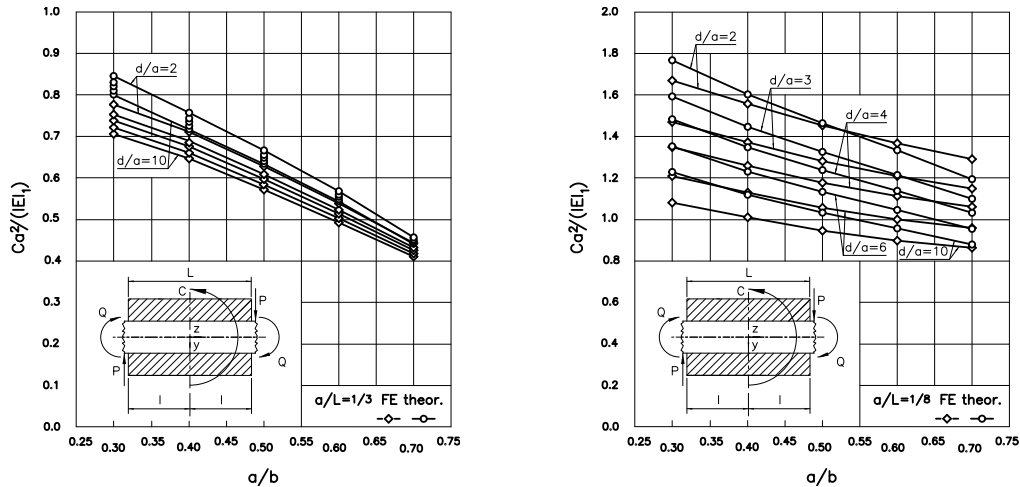
Figure 6. The value of the normalized detachment force $Pa^3/(IEI_1)$ versus a/b for $a/L = 1/3$ (left) and $a/L = 1/8$ (right), in the situation of incipient shaft-hub detachment, for $\nu = 0.3$.

7.1. *Comparison between analytical and FE forecasts for the loading of Figure 1(a).* For the non axisymmetric press-fit loading constituted by three radial forces, Figure 1(a), a suitable expression of the normalized force describing the detachment initiation derives from the analytical solution (5) of the ODE (2) within the respect of the boundary conditions (7). The analytical solution suggests that a proper normalized detachment force is $Pa^3/(IEI_1)$, where P represents the central load, a denotes the shaft radius, I is the diametric interference, E is the Young's modulus, and I_1 is the shaft moment of inertia. The detachment initiation force $Pa^3/(IEI_1)$ depends upon the three aspect ratios $a/b = \alpha$, d/a, a/L. The ranges explored with FE in Figure 6 for the three aspect ratios are $2 \le d/a \le 10$, $0.3 \le \alpha \le 0.7$, $1/8 \le a/L \le 1/3$. To limit the computational effort, only the two extreme values $1/3$ and $1/8$ of the variable a/L have been considered. The corresponding analytical and FE forecasts are presented in Figure 6, in which the abscissa variable is $a/b = \alpha$, the family of curves refers to five a/d values, and the ordinate variable is the normalized detachment force $Pa^3/(IEI_1)$.

The agreement between analytical and FE forecasts is on the whole acceptable, especially for $a/L = 1/8$, a coupling, this, whose geometry is better identifiable in terms of a beam.

In the following, the FE normalized detachment force $Pa^3/(IEI_1)$ of Figure 4 referring to $a/L = 1/8$ and to $d/a = 10$ is compared to the FE normalized detachment couple $Ca^2/(IEI_1)$ of Figure 5 of [Strozzi et al. 2016], also referring to $a/L = 1/8$. In fact, according Figure 4, the shaft extremity is loaded by a force $P/2$ acting at a distance d from the shaft section aligned with the hub lateral walls. For high values of d/a, the deforming effect of the bending couple $Pd/2$ acting on the shaft section aligned with the hub lateral walls is deemed to prevail over that of the shear force $P/2$. Consequently, $Ca^2/(IEI_1) = Pda^2/2/(IEI_1) = 5Pa^3/(IEI_1)$. In conclusion, the normalized couple of Figure 5 of [Strozzi et al. 2016] evaluated for $a/L = 1/8$, is expected to be about five times the normalized force of Figure 6, right, computed for $a/L = 1/8$ and for $d/a = 10$. For $a/b = 0.5$, the above ratio extracted from the FE forecasts of the two above diagrams is about 6, thus confirming the validity of the FE study.

Figure 7. The value of the normalized detachment couple $Ca^2/(IEI_1)$ versus a/b for $a/L = 1/3$ (left) and $a/L = 1/8$ (right), in the situation of incipient shaft-hub detachment, for $\nu = 0.3$.

7.2. Comparison between analytical and FE forecasts for the loading of Figure 1(b).

In the case of the loading of Figure 1(b), constituted by the couple C and by two equilibrating radial forces, a suitable normalized parameter that describes the press-fit incipient detachment is $Ca^2/(IEI_1)$. The detachment initiation couple $Ca^2/(IEI_1)$ depends upon the three aspect ratios $a/b = \alpha$, d/a, a/L. The ranges explored with FE for the three aspect ratios in Figure 7 coincide with those adopted for Figure 6. The agreement between analytical and FE forecasts is on the whole acceptable.

For $a/L = 1/3$, both the analytical and the FE curves referring to $d/a = 2, 3, 4, 6, 10$ are very similar. To avoid confusion in the diagram of Figure 5, only the analytical curves referring to the extremal d/a values 2 and 10 have been drawn. This essential independence of the normalized detachment couple of the parameter d/a suggests the rule of thumb according to which detachment occurs when $Ca^2/(IEI_1) \approx 0.4 \div 0.7$ for $2 \leq d/a \leq 10$ and $0.3 \leq a/b \leq 0.7$. A similar situation in which curves referring to various geometries are essentially superimposed occurs in Figure 5 of [Strozzi et al. 2016].

The reasonably favourable comparisons between analytical and FE predictions indicate that additional situations of incipient detachment may confidently be examined on the basis of the analytical predictions alone, without the need for a FE assessment. For instance, situations mentioned in the Introduction may analytically be examined in which, in a composite crankshaft, the shaft protrudes from only one side of the hub, whereas the remaining shaft extremity is aligned with one of the two hub lateral faces [Strozzi and Vaccari 2003].

8. Conclusions

A shaft-hub press fit subjected to two non-axisymmetric loading conditions has been examined, and the loading producing a situation of incipient detachment between the shaft and the hub has been determined. The first loading condition consists in a central radial load P sustained by the hub, equilibrated by

two lateral forces $P/2$ applied to the shaft at a distance d from the hub lateral walls. In the second loading condition a central couple C applied to the hub is equilibrated by two lateral loads withstood by the shaft at a distance d from the hub lateral walls, and exhibiting opposite directions. The shaft-hub contact has been modelled in terms of two elastic Timoshenko beams [Lanzoni and Radi 2016] connected by distributed elastic springs, whose constant has been analytically evaluated. Based upon this beam-like modelling, the loading inducing an undesired shaft-hub incipient detachment has been theoretically determined in term of the shaft-hub geometry, of the initial shaft-hub interference, and of the elastic constants. The analytical predictions of the incipient detachment loading have been compared to selected finite element forecasts, and the agreement has been found to be technically acceptable.

Acknowledgements

References

[Castillo and Barber 1997] J. Castillo and J. R. Barber, "Lateral contact of slender prismatic bodies", *Proc. Royal Soc. Lond. A Math. Phys. Engng. Sci.* **453** (1997), 2397–2412.

[Ciavarella et al. 1998] M. Ciavarella, D. A. Hills, and G. Monno, "The influence of rounded edges on indentation by a flat punch", *Proc. Inst. Mech. Engs., Part C: J. Mech. Eng. Sci.* **212**:4 (1998), 212–319.

[Croccolo et al. 2012] D. Croccolo, M. D. Agostinis, and N. Vincenzi, "Normalization of the stress concentrations at the rounded edges of a shaft-hub interference fit: extension to the case of a hollow shaft", *J. Strain Anal. Eng. Des.* **47** (2012), 131–139.

[Deseri and Owen 2003] L. Deseri and D. R. Owen, "Toward a field theory for elastic bodies undergoing disarrangements", *J. Elasticity* **70**:1-3 (2003), 197–236.

[Deseri and Owen 2010] L. Deseri and D. R. Owen, "Submacroscopically stable equilibria of elastic bodies undergoing disarrangements and dissipation", *Math. Mech. Solids* **15**:6 (2010), 611–638.

[Huang and Leissa 2007] C. S. Huang and A. W. Leissa, "Three-dimensional sharp corner displacement functions for bodies of revolution", *J. Appl. Mech.* (*ASME*) **74** (2007), 41–46.

[Lanzoni and Radi 2016] L. Lanzoni and E. Radi, "A loaded Timoshenko beam bonded to an elastic half plane", *Int. J. Solids Struct.* **92** (2016), 76–90.

[Love 1944] A. E. H. Love, *A treatise on the mathematical theory of elasticity*, vol. 1, Dover Publications, New York, 1944.

[Lundberg 1958] G. Lundberg, "Spannungen in pressverbänden bei belastung", *Die Kugellager Zeitschrift SKF* **3** (1958), 55–63.

[Marmorini et al. 2012] L. Marmorini, A. Baldini, E. Bertocchi, M. Giacopini, R. Rosi, and A. Strozzi, "On the loosening mechanism of a bush press-fitted in the small end of a connecting rod", *Proc. Ints. Mech. Eng. D: J. Automobile Eng.* **226**:3 (2012), 312–324.

[Radi et al. 2017] E. Radi, L. Lanzoni, A. Strozzi, and E. Bertocchi, "Shaft-hub press fit subjected to bending couples: analytical evaluation of the shaft-hub detachment couple", *Appl. Math. Model.* **50** (2017), 135–160.

[Smetana 2001] T. Smetana, *Untersuchungen zum Übertragungsverhalten biegebelasteter Kegel- und Zylinderpressverbindungen*, Shaker Verlag, 2001.

[Strozzi and Vaccari 2003] A. Strozzi and P. Vaccari, "On the press fit of a crankpin into a circular web in pressed-up crankshafts", *J. Strain Anal. Engng. Des.* **38** (2003), 189–199.

[Strozzi et al. 2011] A. Strozzi, A. Baldini, M. Giacopini, E. Bertocchi, and L. Bertocchi, "Normalization of the stress concentrations at the rounded edges of a shaft-hub interference fit", *J. Strain Anal. Eng. Des.* **46** (2011), 478–491.

[Strozzi et al. 2015] A. Strozzi, E. Bertocchi, A. Baldini, and M. Giacopini, "On the applicability of the Boussinesq influence function in modelling the frictionless elastic contact between a rectangular indenter with rounded edges and a half-plane", *Proc. Inst. Mech. Eng. C J. Mech. Engng. Sci.* **229** (2015), 987–1001.

[Strozzi et al. 2016] A. Strozzi, E. Bertocchi, A. Baldini, and S. Mantovani, "Normalization of the stress concentrations at the rounded edges of an interference fit between a solid shaft subjected to bending and a hub", *Mech. Based Des. Struct. Mach.* **44**:4 (2016), 405–425.

[Yosibash and Szabó 1995] Z. Yosibash and B. Szabó, "The solution of axisymmetric problems near singular points and computation of stress intensity factors", *Finite Elem. Anal. Des.* **19** (1995), 115–129.

ENRICO BERTOCCHI: enrico.bertocchi@unimore.it
DIEF-Dipartimento di Ingegneria Enzo Ferrari, Università di Modena e Reggio Emilia, Via Pietro Vivarelli 10, 41125 Modena, Italy

LUCA LANZONI: luca.lanzoni@unimo.it
DIEF-Dipartimento di Ingegneria Enzo Ferrari, Università di Modena e Reggio Emilia, Via Pietro Vivarelli 10, 41125 Modena, Italy

SARA MANTOVANI: sara.mantovani@unimore.it
DIEF-Dipartimento di Ingegneria Enzo Ferrari, Università di Modena e Reggio Emilia, Via Pietro Vivarelli 10, 41125 Modena, Italy

ENRICO RADI: enrico.radi@unimore.it
DISMI-Dipartimento di Scienze e Metodi dell'Ingegneria, Università di Modena e Reggio Emilia, Via Amendola, 2, 42122 Reggio Emilia, Italy

ANTONIO STROZZI: antonio.strozzi@unimore.it
DIEF-Dipartimento di Ingegneria Enzo Ferrari, Università di Modena e Reggio Emilia, Via Pietro Vivarelli 10, 41125 Modena, Italy

APPROXIMATE ANALYSIS OF SURFACE WAVE-STRUCTURE INTERACTION

NIHAL EGE, BARIŞ ERBAŞ, JULIUS KAPLUNOV AND PETER WOOTTON

Surface wave-structure interaction is studied starting from a specialised approximate formulation involving a hyperbolic equation for the Rayleigh wave along with pseudostatic elliptic equations over the interior of an elastic half-space. The validity of the proposed approach for modelling a point contact is analysed. Explicit dispersion relations are derived for smooth contact stresses arising from averaging the effect of a regular array of spring-mass oscillators and also of elastic rods attached to the surface. Comparison with the exact solution of the associated plane time-harmonic problem in elasticity for the array of rods demonstrates a high efficiency of the developed methodology.

1. Introduction

Dynamic soil-structure interaction was investigated in great detail in numerous publications (for examples, see the widely cited book [Wolf 1985] and general reference work [Luco 1982]) with the emphasis usually placed on the effect of bulk waves, in particular in the insightful papers by Boutin and Roussillon [2004; 2006]. Seemingly surface wave-structure interaction has not been studied until very recently when it has been motivated by seismic metasurfaces design, see [Colombi et al. 2016; Colquitt et al. 2017], in which an array of rods attached to the surface of an elastic half-space is analysed starting from full dynamic equations in linear elasticity.

In this paper, a specialized surface wave model, e.g., see [Kaplunov and Prikazchikov 2013; 2017], is adapted for a broad range of soil-structure interaction problems. The mathematical formulation consists of an explicit wave equation on the surface along with pseudostatic elliptic equations governing the decay over the interior. Although the model has been previously implemented to a variety of dynamic scenarios, including 3D moving load problems [Kaplunov et al. 2013; Erbaş et al. 2017], its validity for studying soil-structure interaction is not immediately obvious. The point is that the asymptotic theory exposed in [Kaplunov and Prikazchikov 2013; 2017] is oriented to near-resonance excitation in the form of a prescribed wave disturbance with the phase speed close to the Rayleigh wave one. Thus, for soil-structure interaction problems involving unknown contact stresses, the assumption of near-resonance behaviour always has to be verified *a posteriori*.

The paper is organized as follows: 3D equations governing transient surface wave-structure interaction are presented in Section 2. For the sake of simplicity, structure dynamics is modelled by a scalar partial differential equation in vertical displacement, which is specified in what follows. In Section 3, a plane

point time-harmonic contact is considered. It is demonstrated that the approximate surface wave model is not applicable due to presence of a spurious localized component. At the same time, the sought after Rayleigh wave contribution predicted by this model is identical to that within the exact solution of the plane time-harmonic problem given in the Appendix.

The effect of smooth contact surface stresses coming from homogenizing regular arrays of resonators attached to the surface of a half-space is studied in Sections 4 and 5. The simplest spring-mass resonators are considered in Section 4, while the next section deals with an array of elastic rods. Explicit dispersion relations are readily derived in both cases. Comparison of the approximate solution in Section 5 with the exact solution presented in [Colquitt et al. 2017] shows a remarkable similarity.

2. Statement of the problem

Let us study dynamic interaction of an elastic structure and a homogeneous isotropic half-space, see Figure 1, starting from the earlier proposed asymptotic model for surface wave fields, e.g., see [Kaplunov and Prikazchikov 2017]. According to this model, we have for the longitudinal wave potential φ the hyperbolic equation

$$\Delta_2 \varphi - \frac{1}{c_R^2} \varphi_{tt} = \frac{(1 + k_2^2)}{2\mu B} P \tag{2-1}$$

at the contact surface $x_3 = 0$ along with the elliptic equation

$$\frac{\partial^2 \varphi}{\partial x_3^2} + k_1^2 \Delta_2 \varphi = 0 \tag{2-2}$$

over the interior $(-\infty < x_1, \ x_2 < \infty, \ 0 < x_3 < \infty)$, where

$$k_i^2 = 1 - \frac{c_R^2}{c_i^2}, \quad i = 1, 2,$$

and

$$B = \frac{k_1}{k_2}(1 - k_2^2) + \frac{k_2}{k_1}(1 - k_1^2) - (1 - k_2^4).$$

In the formulae above, t is time, c_1, c_2, and c_R are the longitudinal, shear, and Rayleigh wave speeds, respectively, μ is the Lamé constant, $P = P(x_1, x_2, t)$ is the unknown normal contact stress, $\Delta_2 = \partial^2/\partial x_1^2 + \partial^2/\partial x_2^2$. The displacement vector is expressed through the longitudinal and shear potentials φ
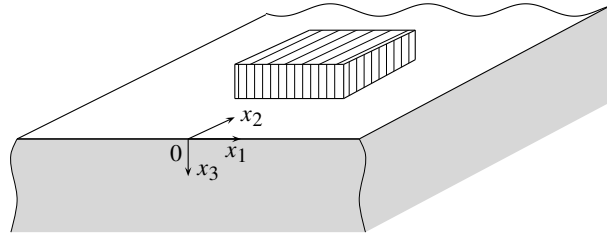
Figure 1. Elastic solid-structure interaction.

$$P = e^{-i\omega t}$$
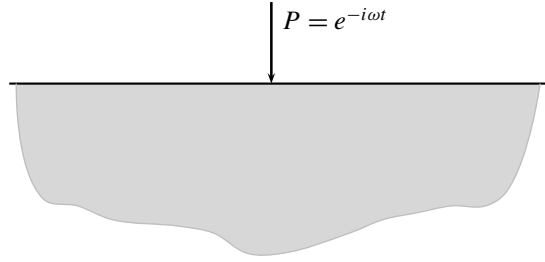
Figure 2. Point time-harmonic force.

and $\boldsymbol{\psi}$ as

$$\boldsymbol{u} = (u_1, u_2, u_3) = \operatorname{grad} \varphi + \operatorname{curl} \boldsymbol{\psi}, \tag{2-3}$$

where

$$\boldsymbol{\psi} = (-\psi_2, \psi_1, 0),$$

with its components satisfying the equations

$$\frac{\partial^2 \psi_i}{\partial x_3^2} + k_2^2 \Delta_2 \psi_i = 0, \quad i = 1, 2, \tag{2-4}$$

over the surface $x_3 > 0$ and the conditions

$$\frac{\partial \psi_i}{\partial x_3} = \frac{1 + k_2^2}{2} \frac{\partial \varphi}{\partial x_i} \tag{2-5}$$

at the interface $x_3 = 0$.

For the sake of simplicity, we model the dynamic behaviour of an elastic structure, see Figure 1, by the following scalar equation:

$$Lv = m v_{tt} \tag{2-6}$$

over the region $-\infty < x_1, x_2 < \infty, -\infty < x_3 < 0$, where $v(x_k, t), k = 1, 2, 3$ is the vertical displacement, m is the mass, and L is a symbolic notation for a differential operator in the variables x_k. The contact conditions at $x_3 = 0$ are taken in the form

$$P = lv \quad \text{and} \quad v = u_3, \tag{2-7}$$

where l also denotes a differential operator in x_k. The presented formulation is oriented to the scenario with a dominant contribution of surface waves to the overall dynamic response. In this case, the effect of bulk waves is neglected; see [Achenbach 1976; Ewing et al. 1957] for more detail. The ranges of validity of such assumptions are evaluated in what follows.

3. Point contact

Consider first a plane time-harmonic problem in cartesian coordinates (x_1, x_3). For a point contact, we get from (2-1) at $P = -P_0\delta(x_1)e^{-i\omega t}$ in its right-hand side

$$\frac{\partial^2\varphi}{\partial x_1^2} - \frac{1}{c_R^2}\frac{\partial^2\varphi}{\partial t^2} = -\frac{1+k_2^2}{2\mu B}P_0\delta(x_1)e^{-i\omega t}, \tag{3-1}$$

where ω is angular frequency, P_0 is constant amplitude of normal stress, and $\delta(x_1)$ denotes the Dirac-delta function. The solution of this equation is

$$\varphi(x_1, 0, t) = i\frac{1+k_2^2}{4\mu B}\frac{P_0 c_R}{\omega}e^{i\omega(|x_1|/c_R-t)}, \tag{3-2}$$

corresponding to propagating surface Rayleigh wave patterns.

Next, we apply a Fourier transform in x_1 to the 2D counterpart of the elliptic equation (2-2) over the interior, having

$$\frac{d^2\varphi^F}{dx_3^2} - k_1^2 k^2 \varphi^F = 0, \tag{3-3}$$

where φ^F denotes the transformed potential and k is Fourier transform parameter. Its solution can be written as

$$\varphi^F(k, x_3, t) = \frac{1+k_2^2}{2\mu B}\frac{P_0}{k^2 - \omega^2/c_R^2}e^{-k_1|k|x_3-i\omega t}. \tag{3-4}$$

As a result,

$$\varphi(x_1, x_3, t) = \frac{(1+k_2^2)P_0 e^{-i\omega t}}{4\pi\mu B}\int_{-\infty}^{\infty}\frac{e^{-k_1|k|x_3}}{k^2 - \omega^2/c_R^2}e^{-ikx_1}\,dk. \tag{3-5}$$

Let us now split the integral in (3-5) into two parts as

$$\int_{-\infty}^{\infty}\frac{e^{-k_1|k|x_3}}{k^2 - \omega^2/c_R^2}e^{-ikx_1}\,dk = I_1 + I_2, \tag{3-6}$$

where

$$I_1 = \frac{c_R}{2\omega}\int_{-\infty}^{\infty}\left(\frac{e^{-k_1\omega x_3/c_R}}{k-\omega/c_R} - \frac{e^{-k_1\omega x_3/c_R}}{k+\omega/c_R}\right)e^{-ikx_1}\,dk \tag{3-7}$$

and

$$I_2 = \frac{c_R}{\omega}\int_0^{\infty}\left(\frac{e^{-k_1kx_3} - e^{-k_1\omega x_3/c_R}}{k-\omega/c_R} - \frac{e^{-k_1kx_3} - e^{-k_1\omega x_3/c_R}}{k+\omega/c_R}\right)\cos(kx_1)\,dk. \tag{3-8}$$

The integral I_2 has no poles and can be readily evaluated numerically. As for the integral I_1, it accounts for the contribution of the Rayleigh wave poles and takes the form

$$I_1(x_1, x_3) = \frac{i\pi c_R}{\omega}e^{(i|x_1|-k_1x_3)\omega/c_R}. \tag{3-9}$$

It is worth noting that the last formula, due to the presence of $|x_1|$, demonstrates a discontinuity of the derivative with respect to x_1 at $x_1 = 0$ not only at the surface $x_3 = 0$ but also over the interior $x_3 > 0$. However, this is also a feature of the Rayleigh pole contribution to the exact solution of the
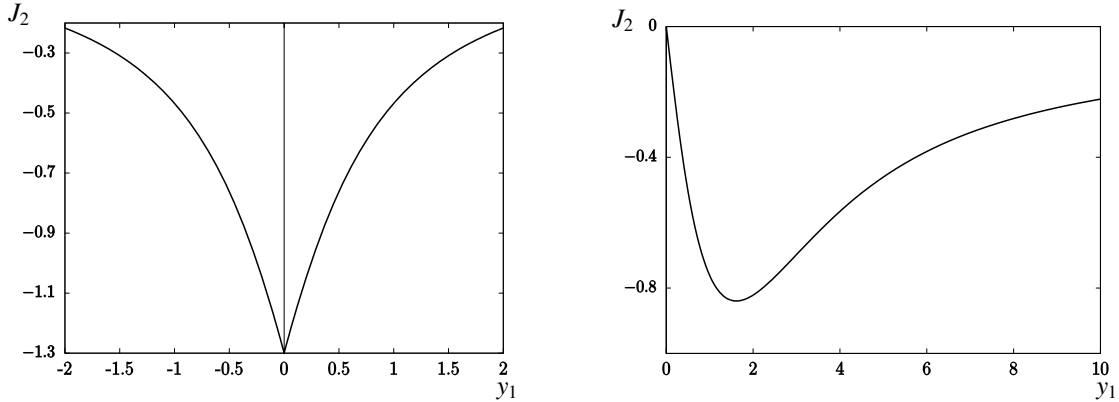
Figure 3. Variation of the integral J_2 along the horizontal and vertical axes for $\nu = 0.25$ and $c_R = 0.914 c_2$. Left: $y_3 = 1$. Right: $y_1 = 0$.

associated plane problem in elasticity presented in the Appendix. In fact, calculating the aforementioned contribution φ_1 to integral (A-5), we have

$$\varphi_1(x_1, x_3, t) = \frac{(1 + k_2^2) P_0}{\pi \mu R'(c_R/c_2)} \frac{c_2}{c_R} I_1(x_1, x_3) e^{-i\omega t}, \tag{3-10}$$

where the Rayleigh denominator is defined by (A-10). It can easily be verified that

$$R'(c_R/c_2) = 4B \, c_2/c_R, \tag{3-11}$$

with constant B from (2-1). Thus, the approximation of the surface wave field given by formulae (3-5) with (3-9) and (3-10) coincide.

At the same time, the integral I_2 is a spurious product of the utilized model for the surface Rayleigh wave, which does not appear in the exact solution of the problem. It corresponds to a pattern localized near a point contact and arises in the model due to neglecting the integrals over the branch cuts characteristic of the exact formulation, e.g., see [Achenbach 1976; Ewing et al. 1957]. This integral may be rewritten in the form

$$I_2 = \frac{\omega}{c_R} J_2 \tag{3-12}$$

with

$$J_2 = \int_0^\infty \left(\frac{e^{-k_1 \zeta y_3} - e^{-k_1 c_2/c_R y_3}}{\zeta - c_2/c_R} - \frac{e^{-k_1 \zeta y_3} - e^{-k_1 c_2/c_R y_3}}{\zeta + c_2/c_R} \right) \cos(\zeta y_1) \, d\zeta, \tag{3-13}$$

where $y_i = \omega/c_2 \, x_i$, $i = 1, 3$. It is plotted in Figure 3 for the Poisson ratio $\nu = 0.25$ and consequently with the Rayleigh wave speed $c_R = 0.914 c_2$ for $y_1 = 0$ (Figure 3, left) and $y_3 = 1$ (Figure 3, right).

The spurious component of the solution related to the integral J_2 makes more problematic the applicability of the promoted surface wave model for tackling a point contact. Moreover, the latter cannot also be treated in the general framework of linear elasticity. In the latter case, the vertical displacement u_3 does not take a finite value at the origin $x_1 = x_3 = 0$ because of the divergence of a Fourier integral following from (A-5), (A-6), and (2-5); see [Ewing et al. 1957] for more detail. In literature, the problem is usually overcome by distributing a point contact, e.g., see [Satto and Wada 1977].

4. Array of mass-spring oscillators

Consider now a plane strain problem for a regular array of mass-spring oscillators attached to the surface of the half-space $x_3 = 0$; see Figure 4. Let m represent mass, χ the spring stiffness, and a the distance between the oscillators. Then, we have from the general equation (2-1),

$$\frac{\partial^2 \varphi}{\partial x_1^2} - \frac{1}{c_R^2} \frac{\partial^2 \varphi}{\partial t^2} = -\frac{1 + k_2^2}{2\mu B} \sum_{n=-\infty}^{\infty} p(x_1, t)\delta(x_1 + na), \tag{4-1}$$

where p is a contact force. In this case, the original 3D elliptic equations for the interior in Section 2 become

$$\frac{\partial^2 \varphi}{\partial x_3^2} + k_1^2 \frac{\partial^2 \varphi}{\partial x_1^2} = 0, \tag{4-2}$$

$$\frac{\partial^2 \psi}{\partial x_3^2} + k_2^2 \frac{\partial^2 \psi}{\partial x_1^2} = 0, \tag{4-3}$$

where $\varphi = \varphi(x_1, x_3, t)$ and $\psi = \psi(x_1, x_3, t)$ with $\psi_i = \psi$, $i = 1, 2$. The relation between the potentials now takes the form

$$\frac{\partial \psi}{\partial x_3} = \frac{1 + k_2^2}{2} \frac{\partial \varphi}{\partial x_1}. \tag{4-4}$$

We also need the formula for the vertical displacement:

$$u_3 = \frac{\partial \varphi}{\partial x_3} + \frac{\partial \psi}{\partial x_1}. \tag{4-5}$$

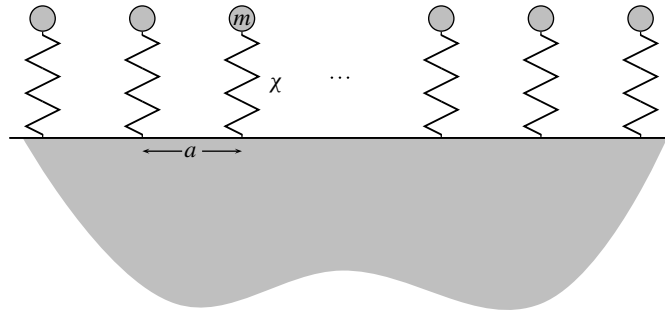Let the vibration of each of the oscillators be governed by

$$m v_{tt} + \chi v = p. \tag{4-6}$$

In addition, we impose the continuity of vertical displacements; see (2-7)$_2$.

First, we distribute the contact stress in the right-hand side of (4-1), setting

$$\sum_{n=-\infty}^{\infty} p(x_1, t)\delta(x_1 + na) \approx \frac{1}{a} p(x_1, t). \tag{4-7}$$

Figure 4. Array of mass-spring oscillators.

Thus, a typical wavelength is assumed to be much greater than the distance between the oscillators. A more sophisticated homogenization technique for a regular array of oscillators is reported in [Boutin and Roussillon 2006].

For a time-harmonic wave in the form $p = p_0 \exp i(kx_1 - \omega t)$, where p_0 is a constant, k is the wavenumber, and ω is the frequency, we readily obtain from equations (4-2)–(4-5)

$$\varphi = -\frac{A}{kk_1} e^{i(kx_1-\omega t)-kk_1x_3} \tag{4-8}$$

and

$$\psi = \frac{2iA}{k(1+k_2^2)} e^{i(kx_1-\omega t)-kk_2x_3}, \tag{4-9}$$

where A is an unknown amplitude. As a result, (4-6) yields

$$v = \frac{p_0}{m(\omega_0^2 - \omega^2)} e^{i(kx_1-\omega t)} \tag{4-10}$$

with

$$\omega_0 = \sqrt{\chi/m}. \tag{4-11}$$

We also have from (4-5)

$$u_3 = A\left(e^{-kk_1x_3} - \frac{2e^{-kk_2x_3}}{1+k_2^2} \right) e^{i(kx_1-\omega t)}. \tag{4-12}$$

On substituting formulae (4-8), (4-10), and (4-12) into the wave equation (4-1) and the continuity condition (2-7)$_2$, we arrive at linear algebraic equations with unknowns A and p_0. They are

$$(k^2 - \omega^2/c_R^2)A = \frac{(1+k_2^2)kk_1}{2\mu a B} p_0, \tag{4-13}$$

$$\frac{1-k_2^2}{1+k_2^2}A = \frac{1}{m(\omega^2 - \omega_0^2)} p_0. \tag{4-14}$$

The associated dispersion relation can be presented as

$$K^2 - \Omega^2 = r(s^2\Omega^2 - 1)K, \tag{4-15}$$

where the dimensionless wave number and frequency are given by

$$K = ka, \quad \Omega = \frac{\omega a}{c_R} \tag{4-16}$$

and

$$s = \frac{c_R}{\omega_0 a}, \quad r = \frac{(1-k_2^2)k_1\chi}{2\mu B}. \tag{4-17}$$

The zero of the left-hand side in (4-15), $K = \Omega$, corresponds to the Rayleigh surface wave, whereas its right-hand side zero, $\Omega_0 = s^{-1}$, coincides with the eigenfrequency of the considered oscillator. The exploited surface wave model is formally valid near the left-hand side zero, e.g., see [Kaplunov and Prikazchikov 2017], and it becomes exact at $K_0 = s^{-1}$.
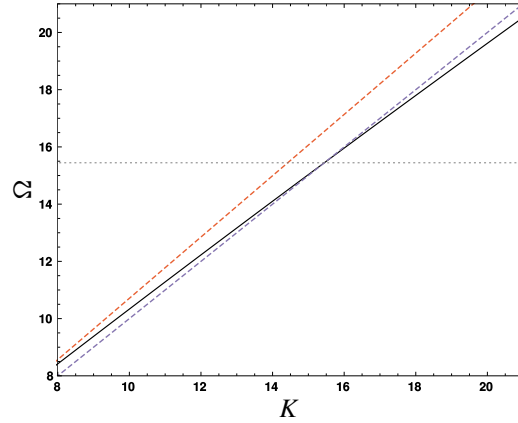
Figure 5. Dispersion curve for an array of mass-spring oscillators. The dispersion equation (4-18) is plotted by a black line, the shear wave ($K = \Omega$) is plotted by the red dotted line, and the Rayleigh wave ($K = c_2/c_R \, \Omega$) is plotted by the blue dotted line.

Numerical results are presented in Figure 5, where the dispersion curve calculated by the formula

$$K = \frac{r(s^2\Omega^2 - 1) + \sqrt{r^2(s^2\Omega^2 - 1)^2 + 4\Omega^2}}{2} \tag{4-18}$$

is plotted by solid line. In this figure, $m = 1000 \, \text{kg/m}$, $a = 2 \, \text{m}$, $\mu = 325 \, \text{MPa}$, $\chi = 4\mu$, $c_1 = 232.379 \, \text{m/s}$, $c_2 = 158.114 \, \text{m/s}$, and $c_R = 140.109 \, \text{m/s}$. The Rayleigh wave $K = c_2/c_R \, \Omega$ (blue dotted line) and shear wave $K = \Omega$ (red dotted line) are also shown along with the eigenfrequency Ω_0 (horizontal line). The figure demonstrates that the validity range of the model is located near the point with coordinates (K_0, Ω_0).

5. Array of elastic rods

In this section, we study a more elaborate plane time-harmonic problem for an array of elastic rods of height H and width h; see Figure 6. We start from the relations in the previous sections using, instead of (4-6), the boundary value problem for longitudinal vibration of a rod over the interval $-H \leq x_3 \leq 0$. This is given by the equation
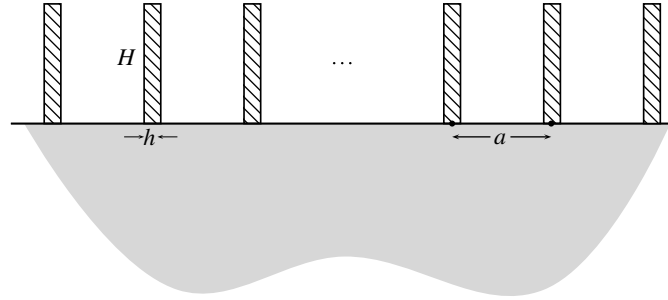
$$E\frac{\partial^2 v}{\partial x_3^2} - m\frac{\partial^2 v}{\partial t^2} = 0, \tag{5-1}$$

subject to the boundary conditions

$$\frac{\partial v}{\partial x_3} = \frac{p}{Eh}, \quad x_3 = 0, \tag{5-2}$$

$$\frac{\partial v}{\partial x_3} = 0, \quad x_3 = -H, \tag{5-3}$$

where m and E are the mass density and Young's modulus, respectively.

Figure 6. Array of elastic rods.

The solution of the problem (5-1)–(5-3) is

$$v = -\frac{c_0 p}{Eh\omega} \frac{\cos(\omega(x_3 + H)/c_0)}{\sin(\omega H/c_0)}, \tag{5-4}$$

with

$$c_0 = \sqrt{E/m}. \tag{5-5}$$

The continuity of the displacements at $x_3 = 0$, see (2-7), taking into account (4-12), results in

$$\frac{c_0}{\omega} \cot \frac{\omega H}{c_0} p_0 = \frac{1 - k_2^2}{1 + k_2^2} A. \tag{5-6}$$

The compatibility of the linear homogeneous equations (5-6) and (4-13) leads to the dispersion relation

$$K^2 - \Omega^2 = q\theta_h K\Omega \tan(\theta_H \Omega), \tag{5-7}$$

where K and Ω are given by (4-16) as above and

$$\theta_h = \frac{c_R h}{c_0 a}, \quad \theta_H = \frac{c_R H}{c_0 a}, \quad q = \frac{E k_1 (1 - k_2^2)}{2\mu B}. \tag{5-8}$$

The zeros of the right-hand side in (5-7),

$$\Omega_m = \frac{\pi m}{\theta_H}, \quad m = 1, 2, 3, \ldots, \tag{5-9}$$

correspond to the eigenfrequencies of a rod with free ends, for which $p = 0$ in (5-2). At the same time, its poles,

$$\Omega_m = \frac{\pi}{2\theta_H} (2m - 1), \quad m = 1, 2, 3, \ldots, \tag{5-10}$$

are related to a rod with a clamped end at $x_3 = 0$. In this case we have to impose the boundary condition $v = 0$ instead of (5-2).

The exact solution of the studied problem in [Colquitt et al. 2017] rewritten in the notation of the present paper becomes

$$R\left(\frac{c_R}{c_2} \frac{\Omega}{K}\right) = -\frac{2Bq\theta_h}{k_1} \left(\frac{\Omega}{K}\right)^3 \sqrt{1 - \frac{c_R^2}{c_1^2} \frac{\Omega^2}{K^2}} \tan(\theta_H \Omega), \tag{5-11}$$
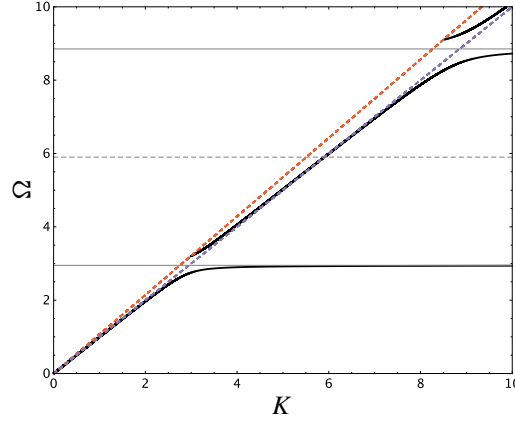
Figure 7. Dispersion curves for the array of rods. Black solid lines correspond to the approximate dispersion equation (5-14) with eigenfrequencies (5-9) and (5-10) indicated by the horizontal dashed and solid lines respectively.

where the Rayleigh denominator R is defined in the Appendix; see (A-10). Its one-term Taylor expansion around $\Omega = K$ is given by

$$R\left(\frac{c_R}{c_2}\frac{\Omega}{K}\right) \approx \frac{c_R}{c_2}\frac{R'(c_R/c_2)}{2K^2}(\Omega^2 - K^2). \tag{5-12}$$

Then, on substituting the latter into the exact dispersion relation (5-11) and taking into consideration identity (3-11), we arrive at

$$K^2 - \Omega^2 = \frac{q\theta_h}{k_1}\frac{\Omega^3}{K}\sqrt{1 - \frac{c_R^2}{c_1^2}\frac{\Omega^2}{K^2}}\,\tan(\theta_H\Omega). \tag{5-13}$$

As might be expected, the right-hand sides of dispersion relations (5-7) and (5-13) are identical at $\Omega = K$, i.e., for the Rayleigh wave.

Numerical data are given in Figures 7 and 8 for the parameters of rods $E = 1.7\,\text{GPa}$, $m = 450\,\text{kg}\cdot\text{m}^{-3}$, $H = 14\,\text{m}$, and $h = 0.3\,\text{m}$ with the same distance between the oscillators and the same parameters of the half-space as in the previous section. For the surface wave model, the dispersion curves are calculated starting from the explicit formula

$$K = \frac{q\theta_h\Omega\tan(\theta_H\Omega) + \sqrt{q^2\theta_h^2\Omega^2\tan^2(\theta_H\Omega) + 4\Omega^2}}{2}, \tag{5-14}$$

while the curves originating from the exact solution are plotted from the transcendental equation (5-11). Since the curves corresponding to (5-11) and (5-14) are virtually identical, in Figure 7, only the approximate dispersion equation is plotted by solid black lines. Eigenfrequency (5-9) and (5-10) are shown in this figure by dashed and solid horizontal lines, respectively. As before, the Rayleigh and shear waves are also displayed. In Figure 8, the curves by (5-11) and (5-14) are depicted by blue and black lines, respectively. It is worth noting that the adapted approximate model also demonstrates a reasonable accuracy near the
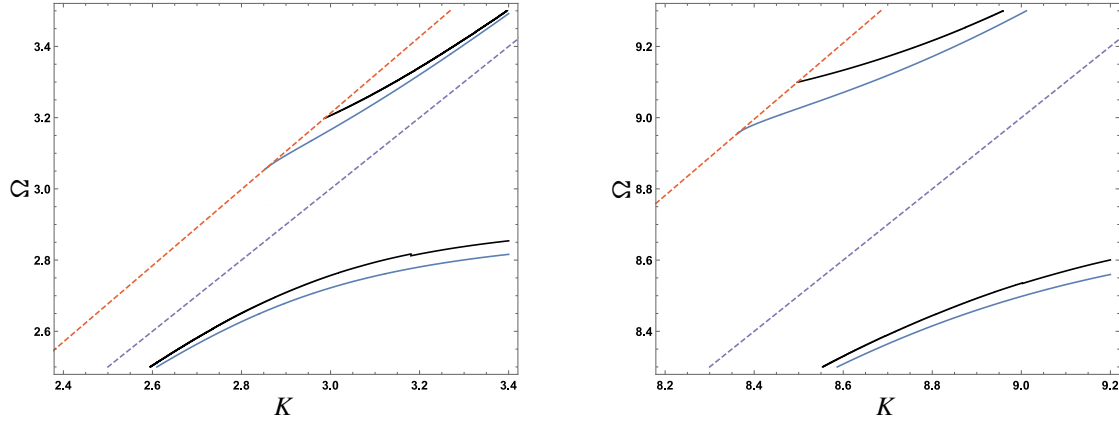
Figure 8. Comparison of the formula (5-14) and the dispersion relation (5-11), corresponding to black and blue solid lines respectively, near the first (left) and second (right) band-gaps.

band-gaps centred around frequencies (5-10) related to a clamped surface of the half-space, which does not support Rayleigh wave propagation.

6. Concluding remarks

An approximate scheme starting from the explicit model for the Rayleigh wave, e.g., see [Kaplunov and Prikazchikov 2017], has been developed for surface wave-structure interaction problems. This scheme is proven not valid for analysing a point harmonic contact. As a result, its various extensions aimed at taking into consideration contact stresses distributed over small surface regions, for example using the methodology in [Muravskii 2008], seem to be of obvious interest.

Comparison with the exact solution of the plane time-harmonic problem for an array of elastic rods attached to the surface demonstrates an acceptable accuracy of the scheme, see Figures 7 and 8, which gives a notable prediction even near band-gaps. In this case, there is also a potential for applying advanced homogenization techniques, as has been done in [Boutin and Roussillon 2006]. Overall, a very promising outcome of the presented comparison indicates clear prospects for implementing the scheme in more elaborated problems of surface wave-structure interaction inspired by the modelling of seismic metasurfaces [Colombi et al. 2016; Colquitt et al. 2017] and also calculating the seismic response of wind turbines and farms, e.g., see [Saccorotti et al. 2011; Westwood et al. 2015].

Appendix

A.1. *Plane problem in elasticity for a half-space.* Consider the plane time-harmonic problem in elasticity for a half-space $-\infty < x_1, x_2 < \infty, 0 < x_3 < \infty$ subject to the following boundary conditions at $x_3 = 0$:

$$\sigma_{13} = \mu\left(2\frac{\partial^2\varphi}{\partial x_1 \partial x_3} + \frac{\partial^2\psi_1}{\partial x_1^2} - \frac{\partial^2\psi_2}{\partial x_3^2}\right) = 0, \tag{A-1}$$

$$\sigma_{33} = \lambda\left(\frac{\partial^2 \varphi}{\partial x_1^2} + \frac{\partial^2 \varphi}{\partial x_3^2}\right) + 2\mu\left(\frac{\partial^2 \varphi}{\partial x_3^2} + \frac{\partial^2 \psi}{\partial x_1 x_3}\right) = -P_0\delta(x_1)e^{-i\omega t}, \tag{A-2}$$

where λ and μ are Lamé parameters, and the wave potentials φ and ψ satisfy the equations

$$\frac{\partial^2 \varphi}{\partial x_1^2} + \frac{\partial^2 \varphi}{\partial x_3^2} - \frac{1}{c_1^2}\frac{\partial^2 \varphi}{\partial t^2} = 0, \tag{A-3}$$

$$\frac{\partial^2 \psi}{\partial x_1^2} + \frac{\partial^2 \psi}{\partial x_3^2} - \frac{1}{c_2^2}\frac{\partial^2 \psi}{\partial t^2} = 0. \tag{A-4}$$

The solution of the formulated problem expressed through Fourier integrals takes the form, e.g., see [Achenbach 1976],

$$\varphi(x_1, x_3, t) = -\frac{P_0 e^{-i\omega t}}{2\pi\mu}\int_{-\infty}^{\infty}\frac{2k^2 - \omega^2/c_2^2}{F}e^{-ikx_1 - \alpha_1 x_3}\,dk, \tag{A-5}$$

and

$$\psi(x_1, x_3, t) = -\frac{P_0 e^{-i\omega t}}{2\pi\mu}\int_{-\infty}^{\infty}\frac{2ik\alpha_1}{F}e^{-ikx_1 - \alpha_2 x_3}\,dk, \tag{A-6}$$

where

$$F = (2k^2 - \omega^2/c_2^2)^2 - 4k^2\alpha_1\alpha_2 \tag{A-7}$$

and

$$\alpha_i = \sqrt{k^2 - \omega^2/c_i^2}, \quad i = 1, 2. \tag{A-8}$$

The function F can be written as

$$F(k, \omega) = k^4 R(c), \tag{A-9}$$

where R is the well-known Rayleigh denominator given by

$$R(c) = (2 - c^2)^2 - 4\sqrt{1 - c^2}\sqrt{1 - \gamma^2 c^2}, \tag{A-10}$$

where $c = \omega/(kc_2)$ and

$$\gamma = \sqrt{\frac{c_2}{c_1}} = \sqrt{\frac{1 - 2\nu}{2 - 2\nu}}, \tag{A-11}$$

with ν denoting the Poisson's ratio.

References

[Achenbach 1976] J. D. Achenbach, *Wave propagation in elastic solids*, 1st ed., North-Holland Series in Applied Mathematics and Mechanics **16**, North-Holland Publishing Co., Amsterdam, 1976.

[Boutin and Roussillon 2004] C. Boutin and P. Roussillon, "Assessment of the urbanization effect on seismic response", *Bull. Seismol. Soc. Am.* **94**:1 (2004), 251–268.

[Boutin and Roussillon 2006] C. Boutin and P. Roussillon, "Wave propagation in presence of oscillators on the free surface", *Int. J. Eng. Sci.* **44**:3-4 (2006), 180–204.

[Colombi et al. 2016] A. Colombi, P. Roux, S. Guenneau, P. Gueguen, and R. V. Craster, "Forests as a natural seismic metamaterial: Rayleigh wave bandgaps induced by local resonances", *Scientific Reports* **6** (2016), art. id. 19238.

[Colquitt et al. 2017] D. J. Colquitt, A. Colombi, R. V. Craster, P. Roux, and S. R. L. Guenneau, "Seismic metasurfaces: sub-wavelength resonators and Rayleigh wave interaction", *J. Mech. Phys. Solids* **99** (2017), 379–393.

[Erbaş et al. 2017] B. Erbaş, J. Kaplunov, D. A. Prikazchikov, and O. Şahin, "The near-resonant regimes of a moving load in a three-dimensional problem for a coated elastic half-space", *Math. Mech. Solids* **22**:1 (2017), 89–100.

[Ewing et al. 1957] W. M. Ewing, W. S. Jardetzky, and F. Press, *Elastic waves in layered media*, McGraw-Hill, 1957.

[Kaplunov and Prikazchikov 2013] J. Kaplunov and D. A. Prikazchikov, "Explicit models for surface, interfacial and edge waves", pp. 73–114 in *Dynamic Localization Phenomena in Elasticity, Acoustics and Electromagnetism*, edited by R. V. Craster and J. Kaplunov, Springer, 2013.

[Kaplunov and Prikazchikov 2017] J. Kaplunov and D. A. Prikazchikov, "Asymptotic theory for Rayleigh and Rayleigh-type waves", pp. 1–106 Advances in Applied Mechanics **50**, Elsevier, 2017.

[Kaplunov et al. 2013] J. Kaplunov, D. A. Prikazchikov, B. Erbaş, and O. Şahin, "On a 3D moving load problem for an elastic half space", *Wave Motion* **50**:8 (2013), 1229–1238.

[Luco 1982] J. E. Luco, "Linear soil-structure interaction: a review", pp. 41–57 in *Earthquake ground motion and its effects on structures: Proc. of the Winter Annu. Meet. of the ASME* (Phoenix, AZ, 1982), edited by S. K. Datta, Applied Mechanics Division **53**, ASME, 1982.

[Muravskii 2008] G. B. Muravskii, "On simplified solutions of contact problems for elastic foundations", *Arch. Appl. Mech.* **78**:2 (2008), 149–162.

[Saccorotti et al. 2011] G. Saccorotti, D. Piccinini, L. Cauchie, and I. Fiori, "Seismic noise by wind farms: a case study from the Virgo gravitational wave observatory, Italy", *Bull. Seismol. Soc. Am.* **101**:2 (2011), 568–578.

[Satto and Wada 1977] H. Satto and H. Wada, "Forced vibrations of a mass connected to an elastic half-space by an elastic rod or a spring", *J. Sound Vib.* **50**:4 (1977), 519–532.

[Westwood et al. 2015] R. F. Westwood, P. Styles, and S. M. Toon, "Seismic monitoring and vibrational characterization of small wind turbines: a case study of the potential effects on the Eskdalemuir International Monitoring System Station in Scotland", *Near Surface Geophysics* **13**:2 (2015), 115–126.

[Wolf 1985] J. Wolf, *Dynamic soil-structure interaction*, Prentice-Hall, Englewood Cliffs, NJ, 1985.

NIHAL EGE: nsahin@anadolu.edu.tr
Department of Mathematics, Anadolu University, Eskisehir, Turkey

BARIŞ ERBAŞ: erbas.baris@gmail.com
Department of Mathematics, Anadolu University, Yunusemre Campus, Eskisehir, Turkey

JULIUS KAPLUNOV: j.kaplunov@keele.ac.uk
School of Computing and Mathematics, Keele University, Keele, United Kingdom

PETER WOOTTON: p.t.wootton@keele.ac.uk
School of Computing and Mathematics, Keele University, Keele, United Kingdom

■msp

TUNING STRESS CONCENTRATIONS THROUGH EMBEDDED FUNCTIONALLY GRADED SHELLS

Xiaobao Li, Yiwei Hua, Chenyi Zheng and Changwen Mi

In this work, we explore the possibility of tuning stress concentrations in materials by judiciously designing embedded functionally graded shells. Specifically, we choose thick-walled cylinders to illustrate our central idea. We specifically consider the boundary value problem of a radially varying graded shell bonded to a thick-walled cylinder. We obtain closed-form solutions and our parametric numerical studies suggest that a graded soft shell can effectively drive the stress concentration from the inner surface of the shell to the shell-cylinder interface. For any boundary loading, an optimal inhomogeneity index that balances the stress concentrations along the inner surface and the interface can be identified. Using the solution to a completely homogeneous cylinder as a benchmark, the stress concentration factor can be reduced by more than 40%. The results of this work suggest the significant potential of functionally graded materials for tailoring the stress concentrations of engineering structures by bonding a properly designed inhomogeneous layer to the perimeter of geometric defects.

1. Introduction

Stresses may be significantly amplified around regions with geometric discontinuities and abrupt changes in material properties or load intensities. This phenomenon is known as stress concentrations. It is often responsible for structural failure, e.g., damage and fracture, and is generally measured by the use of stress concentration factors (SCFs). Consequently, reducing the stress concentration factor of engineering elements and structures is of significant interest and importance in practice. In other words, optimization of stress distribution is desired for those structures with stress concentrations, in particular, for plates and cylinders containing holes. Since the 1960s, many studies have been continuously devoted to the stress analysis of plates with holes of various shapes under different loading conditions [Savin 1961; Theocaris and Petrou 1986; Ukadgaonker and Rao 1999; Rezaeepazhand and Jafari 2010]. More recently, Wu and Mu [2003] developed a computational method to estimate the SCFs of isotropic and orthotropic plates as well as cylinders with a circular cutout. Later, Yang et al. [2008; 2010b] investigated the stress and strain concentrations of a plate containing a circular hole. By the use of the complex variable method, Batista [2011] calculated the stress concentration around a hole with complex geometry in an infinite elastic plate. Patel and Sharma [2017] proposed a numerical approach to study the stress field around polygonal cutouts with complex geometries in an orthotropic media. On the basis of these literature studies, Nagpal et al. [2012] presented a complete analysis and overview on techniques focusing on the relief of stress concentrations in materials and structures with cavities.

The above studies all focused on homogeneous materials with geometric defects. Functionally graded material (FGM) is a class of composite materials that possess continuous variation of material properties along certain spatial dimensions. This distinguishing feature eliminates the sharp discontinuity in material properties that naturally arise when bridging materials with drastically different properties. FGMs may thus help regulate the stress distribution and function performance of composite structures. Due to this, FGMs have received considerable attention in the past two decades and found a number of applications in aerospace engineering [Marin 2005] and biomedical engineering [Watari et al. 2004], among others [Kawasaki and Watanabe 2002; Müller et al. 2003; Chen et al. 2012].

Up to the present, numerous studies have reported applications of FGMs in engineering structures, and in particular, their effect on stress reduction in structures with geometric defects [Jin and Batra 1996; Chi and Chung 2006a; 2006b; Birman and Byrd 2007; Yang et al. 2015]. Kubair and Bhanu-Chandar [2008] solved the SCFs due to a circular hole in a functionally graded panel and found that the stress concentrations can be reduced when the Young's modulus is allowed to progressively increase away from the center of the hole. Yang et al. [2010a] also analyzed the stress distribution of a functionally graded plate with a circular hole and reported significant stress relief as the Young's modulus is allowed to radially increase. Later, Mohammadi et al. [2011] revisited the stress concentration problem around a circular hole in an infinite FGM plate subjected to different loading conditions. More recently, Yang et al. [2015] further studied the three-dimensional equilibrium problem of a voided transversely isotropic FGM plate subjected to loading applied on the remote boundary of the plate. Several other studies on the stress concentration analysis of FGM plates under different conditions include [Kubair 2013; Sburlati et al. 2014; Gouasmi et al. 2015; Mohammadi et al. 2016]. Jha et al. [2013] supplied a comprehensive review on various theories of FGM plates and their applications.

In addition to plates, stress concentrations in another important engineering structure, i.e., graded cylinders, under various loading conditions have also been studied [Pan and Roy 2006; Chen and Lin 2010; Batra and Nie 2010; Nie and Batra 2010; Nie et al. 2011; Sadeghi et al. 2012; Ghannad et al. 2013; Chen 2015]. Horgan and Chan [1999] solved the stress field in a pressure vessel with radially graded Young's modulus. By comparing with a completely homogeneous vessel, they showed the significant difference in stress distribution. Tutuncu [2007] further investigated the stress distribution in cylindrical vessels with exponentially varying modulus along radial axis. Oral and Anlas [2005] derived a closed-form stress solution for an orthotropic cylindrical pressure vessel with inhomogeneous material properties. By treating either the elastic stiffness or Poisson's ratio as a constant, but not both, Dryden and Batra [2013] studied the axisymmetric plane strain problem of a graded cylinder under hydrostatic loading. They also successfully designed an equivalent homogeneous vessel with the same stress concentration level as that of a graded one. Xin et al. [2014] further considered the possible effects of Poisson's ratio on stresses and displacements and presented a theoretical formulation for graded thick-walled cylinders.

Although many studies have been devoted to reducing stress concentrations in pressure vessels, most of them focus on geometric defects embedded in infinite domains under hydrostatic boundary loads. Nonetheless, it has been shown that graded materials work best as a coating or a transitional layer bridging two components with drastically different material properties. When employed this way, an FGM component is able to significantly improve the mechanical behavior of the original structure, including the conventionally undesired stress concentrations [Kashtalyan and Menshykova 2007; Sburlati 2012; Sburlati et al. 2013; Chu et al. 2015].

By the use of a thin FGM ring, Sburlati [2013] explored the possibility to relieve the stress concentration around the circular hole in a homogeneous plate under far-field uniaxial tension. They demonstrated that the SCF around the hole perimeter can be significantly reduced by a proper choice of the grading parameter of the annular ring. Shortly thereafter, they extended their model to take into account both a perfect bonding and a pure sliding condition at the ring/plate interface [Sburlati et al. 2014]. Analytical solutions due to four types of simple far-field loads are presented. Yang and Gao [2016] also confirmed that by using a properly graded thin shell around an elliptic hole in an infinite plate, the SCFs may be effectively reduced.

Motivated by these studies, the primary goal of the present study is to propose a solution to mitigating stress concentrations in a thick-walled cylinder subjected to an arbitrary boundary load. We believe that it is a promising way to improve the stress distribution in thick-walled cylinders by introducing an inhomogeneous annular shell, treated as a thin coating perfectly bonded to the inner surface of a circular cylinder. The Young's modulus of the inhomogeneous shell is allowed to vary along its radial dimension by following a power-law function, whereas the Poisson's ratio of the shell is kept as a constant without any gradation. The problem is formulated with the method of Airy stress function. For the case of inhomogeneous material properties, the conventional biharmonic equation that must be satisfied by the stress function of a homogeneous medium becomes a general fourth-order differential equation of Euler-type. Successful tackling of this differential equation renders us an analytical solution to the stresses and displacements of the proposed problem.

The remainder of this paper is organized as follows. Section 2 presents the Airy stress function formulation of the proposed problem and its analytical solutions due to both an all-around traction and an arbitrary biaxial load. In Section 3, extensive parametric studies are performed to illustrate the effects of the inhomogeneity index of the embedded shell and the traction ratio along perpendicular directions on the stress distribution and stress concentrations. Whenever possible, the benchmark solution to a completely homogeneous cylinder is computed and used as a comparison basis. Finally, in Section 4, a few concluding remarks that were informed from both the analytical solutions and numerical studies are drawn.

2. Formulation and method of solution

As shown in Figure 1, the problem under consideration is composed of a thick-walled cylinder reinforced by a perfectly bonded thin shell, both of finite thickness. The Young's modulus of the cylinder is assumed to be homogeneous while that of the inner shell is treated as a radially graded quantity, i.e.,

$$E^{(i)} = E^{(o)}\left(\frac{r}{r_0}\right)^m, \tag{1}$$

where m represents the inhomogeneity index of the grade shell and therefore should be a real number. The superscripts (i) and (o) are used to denote the quantities that belong to the inner shell and the outer cylinder, respectively. The inhomogeneity index serves as a governing parameter for tuning the relative stiffness between the shell and the cylinder. The power law function (1) was specialized so that the material properties at the shell-cylinder interface $(r = r_0)$ remain continuous. Since the effect of Poisson's ratio (ν) has proven to be very marginal when compared to that of the elastic modulus, see for example [Sburlati et al. 2014, Table 3], it seems reasonable to fix it as an equal constant in both domains. The combination deforms under the application of a uniform boundary loading: $\sigma_x = p$ and $\sigma_y = q$ at the
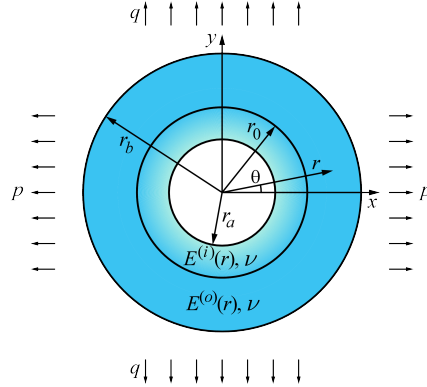
Figure 1. Geometry and loading configuration of the problem.

outer boundary of the cylinder. Such a loading condition is general in the sense that an arbitrary uniform boundary traction can always be converted into this form, with a proper rotation of coordinates.

Due to the axial symmetry of the structure, polar coordinates become a natural choice to formulate and solve the problem. In the absence of body forces, the two-dimensional equations of equilibrium are thus given by

$$\frac{\partial \sigma_r}{\partial r} + \frac{1}{r}\frac{\partial \sigma_{r\theta}}{\partial \theta} + \frac{\sigma_r - \sigma_\theta}{r} = 0, \quad \frac{\partial \sigma_{r\theta}}{\partial r} + \frac{1}{r}\frac{\partial \sigma_\theta}{\partial \theta} + \frac{2}{r}\sigma_{r\theta} = 0, \tag{2}$$

where σ_r, σ_θ, and $\sigma_{r\theta}$ are the normal and shear stress components, respectively. The strain-displacement relations read

$$\varepsilon_r = \frac{\partial u_r}{\partial r}, \quad \varepsilon_\theta = \frac{1}{r}\left(u_r + \frac{\partial u_\theta}{\partial \theta}\right), \quad \varepsilon_{r\theta} = \frac{1}{2}\left(\frac{1}{r}\frac{\partial u_r}{\partial \theta} - \frac{u_\theta}{r} + \frac{\partial u_\theta}{\partial r}\right). \tag{3}$$

The present problem is more reasonable to be modeled as a plane strain one. Nonetheless, it is well known that plane strain formulation generally results in more complicated mathematical expressions when compared to those of plane stress formulation. For simplicity, we have chosen to first formulate the present problem in terms of the plane stress constitutive law:

$$\varepsilon_r = \frac{1}{E(r)}(\sigma_r - \nu\sigma_\theta), \quad \varepsilon_\theta = \frac{1}{E(r)}(\sigma_\theta - \nu\sigma_r), \quad \varepsilon_{r\theta} = \frac{2(1+\nu)}{E(r)}\sigma_{r\theta}. \tag{4}$$

Later in the numerical analysis and discussion (Section 3), the plane strain version of these equations are obtained by the change of material properties: $E \rightarrow E/(1-\nu^2)$ and $\nu \rightarrow \nu/(1-\nu)$.

For problems formulated in terms of stresses, it is well known that in addition to the above equations, the strain compatibility condition must also be satisfied:

$$\frac{\partial^2 \varepsilon_\theta}{\partial r^2} + \frac{1}{r^2}\frac{\partial^2 \varepsilon_r}{\partial \theta^2} + \frac{2}{r}\frac{\partial \varepsilon_\theta}{\partial r} - \frac{1}{r}\frac{\partial \varepsilon_r}{\partial r} = \frac{1}{r}\frac{\partial^2 \varepsilon_{r\theta}}{\partial r\partial \theta} + \frac{1}{r^2}\frac{\partial \varepsilon_{r\theta}}{\partial \theta}. \tag{5}$$

Since the present problem is formulated within the framework of the linearized theory of elasticity, the biaxial boundary tractions shown in Figure 1 can safely be superposed from the two uniaxial tractions along individual coordinate axes. As a result, it would be sufficient to develop a solution due to the traction load $\sigma_x = p$. The solution due to $\sigma_y = q$ can readily be obtained by making the replacements $p \rightarrow q$ and $\theta \rightarrow \theta + \frac{1}{2}\pi$.

With the help of the transformation matrix between the regular Cartesian and polar coordinates, it is easy to find the polar components for the uniaxial traction $\sigma_x = p$:

$$\sigma_r = \tfrac{1}{2}p(1 + \cos 2\theta), \quad \sigma_{r\theta} = -\tfrac{1}{2}p \sin 2\theta. \tag{6}$$

The boundary conditions (6) can further be decomposed into an axial symmetric component,

$$\sigma_r = \tfrac{1}{2}p, \tag{7a}$$

$$\sigma_{r\theta} = 0, \tag{7b}$$

and an antisymmetric component,

$$\sigma_r = \tfrac{1}{2}p \cos 2\theta, \quad \sigma_{r\theta} = -\tfrac{1}{2}p \sin 2\theta. \tag{8}$$

Irrespective of the traction conditions applied at the outer boundary of the cylinder, the inner surface of the embedded shell is always free of tractions:

$$\sigma_r(r_a, \theta) = 0, \tag{9a}$$

$$\sigma_{r\theta}(r_a, \theta) = 0. \tag{9b}$$

The perfect bonding condition between the two material components requires that both the displacements and the stress tractions must be continuous across the shell-cylinder interface:

$$[\sigma_r(r_0, \theta)] = 0, \tag{10a}$$

$$[\sigma_{r\theta}(r_0, \theta)] = 0, \tag{10b}$$

$$[u_r(r_0, \theta)] = 0, \tag{10c}$$

$$[u_\theta(r_0, \theta)] = 0, \tag{10d}$$

where the square brackets denote the jumps of displacements and stress tractions.

To solve the problem we use the Airy stress function in the general form $\varphi = \varphi(r, \theta)$, with the polar stress components written as

$$\sigma_r = \frac{1}{r}\frac{\partial \varphi(r, \theta)}{\partial r} + \frac{1}{r^2}\frac{\partial^2 \varphi(r, \theta)}{\partial \theta^2}, \quad \sigma_\theta = \frac{\partial^2 \varphi(r, \theta)}{\partial r^2}, \quad \sigma_{r\theta} = \frac{1}{r^2}\frac{\partial \varphi(r, \theta)}{\partial \theta} - \frac{1}{r}\frac{\partial^2 \varphi(r, \theta)}{\partial r \partial \theta}. \tag{11}$$

In the remainder of this section, we aim to develop analytical solutions to both the symmetric (7) and the antisymmetric (8) boundary conditions.

2.1. *Axial symmetric solution.*
When the structure shown in Figure 1 is subjected to an all-around traction of magnitude $\tfrac{1}{2}p$, i.e., (7), the Airy stress function becomes azimuthally independent: $\varphi = \varphi_0(r)$. For this case, the compatibility condition can be reformulated in terms of the Airy stress function by combining equations (11), (4), and (5):

$$\frac{d^4\varphi_0(r)}{dr^4} + \frac{2(1-m)}{r}\frac{d^3\varphi_0(r)}{dr^3} + \frac{(m^2 + vm - m - 1)}{r^2}\frac{d^2\varphi_0(r)}{dr^2} - \frac{(m+1)(mv-1)}{r^3}\frac{d\varphi_0(r)}{dr} = 0. \tag{12}$$

This equation is an ordinary differential equation of Euler type whose solution is

$$\varphi_0^{(o)}(r) = z_1 \ln(r) + z_2 r^2 \tag{13}$$

for the outer cylinder and

$$\varphi_0^{(i)}(r) = C_1 r^{m/2+\rho/2+1} + C_2 r^{m/2-\rho/2+1} \tag{14}$$

for the inner shell, where z_1, z_2, C_1, C_2 represent unknown coefficients to be determined by imposing the boundary conditions and $\rho = \sqrt{m^2 + 4 - 4\nu m}$. It is easy to show for the practical range of Poisson's ratio, e.g., $0 < \nu < 0.5$, the parameter ρ is always a real number. Substituting (13) and (14) back into (11) yields

$$\sigma_r^{(o)} = 2z_2 + \frac{z_1}{r^2}, \quad \sigma_\theta^{(o)} = 2z_2 - \frac{z_1}{r^2}, \tag{15a}$$

$$\sigma_r^{(i)} = \frac{(m+\rho+2)r^{m/2+\rho/2}C_1 + (m-\rho+2)r^{m/2-\rho/2}C_2}{2r}, \tag{15b}$$

$$\sigma_\theta^{(i)} = \frac{(m+\rho)(m+\rho+2)r^{m/2+\rho/2}C_1 + (m-\rho)(m-\rho+2)r^{m/2-\rho/2}C_2}{2r}. \tag{15c}$$

The four unknown coefficients (z_1, z_2, C_1, C_2) are determined by the boundary conditions (7a), (9a), (10a), and (10c)

$$z_1 = -\frac{mr_b^2 r_0^2 p}{2\Omega}\left(r_a^\rho(m-2\nu-\rho)(2+m+\rho) - r_0^\rho(m-2\nu+\rho)(2+m-\rho)\right),$$

$$z_2 = \frac{r_b^2 r_a^\rho p}{4\Omega}(2+m+\rho)(m^2+m(2-2\nu-\rho)+2(2-\rho))$$

$$\qquad\qquad - \frac{r_b^2 r_0^\rho p}{4\Omega}(2+m-\rho)(m^2+m(2-2\nu+\rho)+2(2+\rho)), \tag{16}$$

$$C_1 = -\frac{2r_b^2 r_0^{1-m/2+\rho/2}(2+m-\rho)p}{\Omega}, \quad C_2 = -\frac{2r_b^2 r_a^\rho r_0^{1-m/2+\rho/2}(2+m+\rho)p}{\Omega},$$

where

$$\Omega = r_a^\rho(2+m+\rho)(mr_0^2(\rho-m+2\nu)+r_b^2(m^2+m(2-2\nu-\rho)+2(2-\rho)))$$
$$\qquad + r_0^\rho(2+m-\rho)(mr_0^2(\rho+m-2\nu)-r_b^2(m^2+m(2-2\nu+\rho)+2(2+\rho))). \tag{17}$$

2.2. Antisymmetric solution. Given the antisymmetric boundary conditions (8), the Airy stress function for both domains must assume the form $\varphi = \varphi_2(r)\cos 2\theta$. In view of (11) and (4), the strain compatibility (5) can now be recast in terms of the function $\varphi_2(r)$. For the outer cylinder and the inner shell, the compatibility condition becomes

$$\left(\frac{d^2}{dr^2} + \frac{1}{r}\frac{d}{dr} - \frac{4}{r^2}\right)\left(\frac{d^2}{dr^2} + \frac{1}{r}\frac{d}{dr} - \frac{4}{r^2}\right)\varphi_2^{(o)}(r) = 0 \tag{18}$$

and

$$\frac{d^4\varphi_2^{(i)}(r)}{dr^4} + \frac{2(1-m)}{r}\frac{d^3\varphi_2^{(i)}(r)}{dr^3} + \frac{(m^2+\nu m-m-9)}{r^2}\frac{d^2\varphi_2^{(i)}(r)}{dr^2}$$

$$\qquad - \frac{(m+1)(m\nu-9)}{r^3}\frac{d\varphi_2^{(i)}(r)}{dr} + \frac{4m(m\nu+\nu m-3)}{r^4}\varphi_2^{(i)}(r) = 0, \tag{19}$$

respectively. Benefitting from the constant material properties in the cylinder, (18) is easy to solve and the corresponding stress function is found to be

$$\varphi_2^{(o)}(r, \theta) = \left(z_{24} + \frac{z_{23}}{r^2} + z_{21}r^2 + z_{22}r^4 \right) \cos 2\theta. \tag{20}$$

Although the differential equation (19) is much more complicated, it is a fourth-order Euler equation, whose solution can be put in the form

$$\varphi_2^{(i)}(r, \theta) = r^{m+1}\left(D_1 A_1(r) + D_2 A_2(r) + D_3 B_1(r) + D_4 B_2(r) \right) \cos 2\theta. \tag{21}$$

The eight coefficients $(D_1, D_2, D_3, D_4, z_{21}, z_{22}, z_{23}, z_{24})$ are all unknown constants to be evaluated from the boundary conditions (8), (9), and (10). The four functions (A_1, A_2, B_1, B_2) depend solely on the radial coordinate:

$$A_1(r) = r^{-m/2-\alpha/2}, \quad A_2(r) = r^{-m/2+\alpha/2}, \quad B_1(r) = r^{-m/2-\beta/2}, \quad B_2(r) = r^{-m/2+\beta/2}, \tag{22}$$

where

$$\alpha = \sqrt{m^2 + 2m - 2vm + 20 - 2\sqrt{m^2 + v^2 m^2 - 14 v m^2 - 32 v m + 32 m + 64}}, \tag{23a}$$

$$\beta = \sqrt{m^2 + 2m - 2vm + 20 + 2\sqrt{m^2 + v^2 m^2 - 14 v m^2 - 32 v m + 32 m + 64}}. \tag{23b}$$

For real α and β, the inhomogeneity index m has to fall in the interval $[0, 8(2 - \sqrt{3})/(v + 4\sqrt{3} - 7)]$. Given the Airy stress functions (20) and (21), it is straightforward to find the stress components from (11):

$$\sigma_r^{(o)} = -2\left(z_{21} + \frac{2z_{24}}{r^2} + \frac{3z_{23}}{r^4} \right) \cos 2\theta, \tag{24a}$$

$$\sigma_\theta^{(o)} = 2\left(z_{21} + 6z_{22}r^2 + \frac{3z_{23}}{r^4} \right) \cos 2\theta, \tag{24b}$$

$$\sigma_{r\theta}^{(o)} = 2\left(z_{21} + 3z_{22}r^2 - \frac{z_{24}}{r^2} - \frac{3z_{23}}{r^4} \right) \sin 2\theta, \tag{24c}$$

$$\sigma_r^{(i)} = \frac{(m - \alpha - 6)A_1(r)D_1 + (m - \beta - 6)B_1(r)D_3}{2r^{1-m}} \cos 2\theta$$
$$+ \frac{(m + \alpha - 6)A_2(r)D_2 + (m + \beta - 6)B_2(r)D_4}{2r^{1-m}} \cos 2\theta, \quad \text{(24d)}$$

$$\sigma_\theta^{(i)} = \frac{(m - \alpha)(m - \alpha + 2)A_1(r)D_1 + (m - \beta)(m - \beta + 2)B_1(r)D_3}{4r^{1-m}} \cos 2\theta$$
$$+ \frac{(m + \alpha)(m + \alpha + 2)A_2(r)D_2 + (m + \beta)(m + \beta + 2)B_2(r)D_4}{4r^{1-m}} \cos 2\theta, \quad \text{(24e)}$$

$$\sigma_{r\theta}^{(i)} = \frac{(m - \alpha)A_1(r)D_1 + (m - \beta)B_1(r)D_3 + (m + \alpha)A_2(r)D_2 + (m + \beta)B_2(r)D_4}{r^{1-m}} \sin 2\theta. \tag{24f}$$

Simultaneously enforcing the boundary conditions at the inner surface of the shell (9), at the shell-cylinder interface (10), and at the outer boundary of the cylinder (8) solves the eight unknown coefficients

$$z_{21} = \frac{r_b^2 p \sum_{i=1}^{4} \sum_{j>i} (\xi_i - \xi_j) \eta_{ij} a_i a_j}{4 \sum_{i=1}^{4} \sum_{j>i} (\xi_i - \xi_j) \psi_{ij} a_i a_j}, \tag{25a}$$

$$z_{22} = \frac{p \sum_{i=1}^{4} \left(2 r_b^2 r_0^2 (4 z_{21} + 1) \lambda_{i4} - 4 z_{21} r_0^4 \lambda_{i1} - (4 z_{21} + 1) r_b^4 \lambda_{i3} \right) a_i}{4 \sum_{i=1}^{4} (r_0^6 \lambda_{i2} + 2 r_b^6 \lambda_{i3} - 3 r_b^4 r_0^2 \lambda_{i4}) a_i}, \tag{25b}$$

$$z_{23} = \frac{r_b^4 r_0^4 p \sum_{i=1}^{4} \sum_{j>i} (\xi_i - \xi_j) \mu_{ij} a_i a_j}{4 \sum_{i=1}^{4} \sum_{j>i} (\xi_i - \xi_j) \psi_{ij} a_i a_j}, \tag{25c}$$

$$z_{24} = \frac{r_b^2 p \sum_{i=1}^{4} (12 z_{21} r_b^2 r_0^4 \lambda_{i1} - 2(4 z_{21} + 1) r_0^6 \lambda_{i2} + (4 z_{21} + 1) r_b^6 \lambda_{i3}) a_i}{4 \sum_{i}^{4} (r_0^6 \lambda_{i2} + 2 r_b^6 \lambda_{i3} - 3 r_b^4 r_0^2 \lambda_{i4}) a_i}, \tag{25d}$$

$$D_i = p \sum_{j=1}^{4} \zeta_j z_{2j} \lambda_{ij}, \quad i, j = 1, 2, 3, 4, \tag{25e}$$

where λ_{ij}, η_{ij}, μ_{ij}, and ψ_{ij} are elements of 4×4 matrices while ξ_i, a_i, and ζ_i are those of vectors possessing four components. Although the solution procedure was straightforward, the mathematical expressions for these parameters are quite lengthy. For brevity, they are documented in the Appendix.

At this point, the complete solution to the uniaxial traction load $\sigma_x = p$ applied at the outer boundary of the cylinder can readily be obtained by superposing the axial symmetric (15) and the antisymmetric (24a) stresses. For the case of $\sigma_y = q$, stresses can be adapted by making the replacements $\theta \to \theta + \frac{1}{2}\pi$, $\cos 2\theta \to -\cos 2\theta$, and $\sin 2\theta \to -\sin 2\theta$, without affecting the axial symmetric part.

In summary, we solved the boundary value problem presented in Figure 1 by the method of Airy stress function. The solution algorithm follows closely to typical plane elasticity problems as explained in the classical theory of elasticity [Barber 2010]. First, the governing equations of plane elasticity (2)–(5) were combined to construct the compatibility condition on stress components. Second, by the introduction of Airy stress function (11), the condition was further transformed into a fourth-order differential equation whereas both equilibrium equations in (2) are found to be identically satisfied. Third, the compatibility equation in terms of Airy stress function was analytically solved for both axial symmetric and antisymmetric uniform boundary loading. For the two cases, the solutions contain four and eight integration constants, respectively. Finally, they were uniquely determined by implementing the traction boundary conditions at the inner and outer surfaces of the cylinder and the perfect bonding assumption at the graded shell-cylinder interface.

3. Numerical results and discussion

Although we have obtained the analytical solution to the present problem it is mathematically lengthy and therefore inconvenient to demonstrate the effect of the embedded FGM shell. The numerical studies that will be presented in this section are for two purposes. The first of which is to compare the differences in stress concentrations of a thick-walled cylinder, if any, due to an FGM inner shell and a completely homogeneous one. The other is to explore the mechanism of mitigating stress concentrations and thus to enhance the structural integrity of pressure vessels.
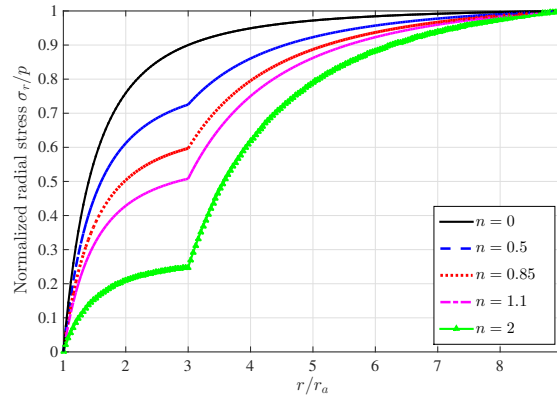
Figure 2. Variation of the normalized radial stress as a function of the radial coordinate for five homogeneous shells.

Calculations require specific values for material properties, geometric parameters, and mechanical loads. We assume that the Poisson's ratio of both the cylinder and the shell is $\nu = 0.3$, because of its very limited impact on stress concentrations [Sburlati 2013]. Due to the absence of the size-dependent effect, it is sufficient to assign just two radii ratios $r_0/r_a = 3$ and $r_b/r_a = 9$ for the geometric parameters. All stress values are normalized with respect to the applied boundary traction. In addition, for comparison purposes the case of a homogeneous inner shell that possesses the same material properties as those of the outer cylinder is also calculated whenever necessary. As aforementioned in Section 2, all analysis and discussion to be presented in this section were performed against the plane strain condition. In the remainder of this section, we first consider the case of a uniform all-around boundary loading, followed by the more general case of an arbitrary biaxial traction.

3.1. *Axial symmetric traction loading.*

3.1.1. *A homogeneous inner shell with different properties from those of the outer cylinder.* For comparison purposes, let us first consider a completely homogeneous inner shell but with a different Young's modulus than that of the outer cylinder

$$E^{(i)} = \left(\frac{r_a}{r_0}\right)^n E^{(o)}, \tag{26}$$

where n is an arbitrary constant representing the relative stiffness between the shell and the cylinder. For nonzero n, it is seen that there is a discontinuity in material properties across the shell-cylinder interface. This simplified case may be treated as a degeneracy of the solution developed for an FGM shell. The Airy stress function of the shell thus takes the same form as that of the cylinder (13). As a result, the stress fields in both domains share the same distribution pattern; see (15a) and (15b). The four constants of integration can subsequently be determined by imposing the boundary conditions at the material's surfaces (r_a, r_b) and the shell-cylinder interface (r_0). For the special case of a completely homogeneous cylinder, the stress field can be obtained by further setting the index n as zero.

Figure 2 shows the normalized radial stress distribution for different values of n ($n = 0, 0.5, 0.85, 1.1, 2$). It is seen that for positive n, the radial stress is always smaller than that of a completely homogeneous
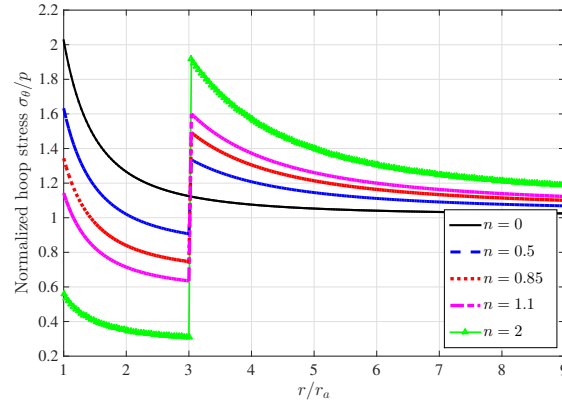
Figure 3. Variation of the normalized hoop stress as a function of the radial coordinate for five homogeneous shells.

cylinder ($n = 0$ or $E^{(i)} = E^{(o)}$). In particular, the radial stress is significantly reduced at the shell-cylinder interface. Because in this case the Young's modulus of the embedded shell is smaller than that of the outer cylinder, the slope of the radial stress curve becomes smaller in the shell and larger in the cylinder, when compared to the case of $n = 0$. With increasing n, both the slope and general level of the radial stress in the shell decrease. For the outer cylinder, an opposite trend can be confirmed. It is also noticed that at the shell-cylinder interface the radial stress is not differentiable, although the stress value remains continuous. For all values of n, the maximum stress always appears on the outer surface of the cylinder and is equal to the applied all-around tension, indicating that stress concentrations are not of a concern for the radial stress component.

Figure 3 shows the variation of the normalized hoop stress for the same five cases that were studied in Figure 2. It is seen that for the case of a completely homogeneous cylinder ($n = 0$), the stress concentration factor reads $\sigma_\theta / p = 2.025$. For $n \neq 0$ the hoop stress experiences a sharp discontinuity across the shell-cylinder interface. The softer the inner shell is the larger the stress discontinuity becomes. Moreover, the stress level becomes lower in the embedded shell but higher in the outer cylinder. In both domains, the hoop stress component decays with the radial coordinate. Furthermore, it is interesting to note the trade-off pattern between the stress levels at the rim of the inner shell and at the shell-cylinder interface. With increasing n, the stress concentration factor at $r = r_a$ monotonically decreases. The opposite is true for the stress concentration factor at the shell-cylinder interface. This behavior suggests an optimized value of the relative stiffness parameter ($n = 0.725$, $E^{(i)}/E^{(o)} \approx 0.451$) such that the stress concentration factors at the shell surface and at the shell-cylinder interface become an equal value ($\sigma_\theta / p = 1.446$). The stress concentration level has reduced by 27.7% when compared with a completely homogeneous thick-walled cylinder.

3.1.2. *A graded thin shell perfectly bonded to a thick-walled cylinder.* In this subsection, we aim to analyze the stress distribution inside an FGM shell perfectly bonded to the inner surface of a thick-walled cylinder. The combination is still subjected to an axisymmetric all-around tension at the outer surface of the cylinder $r = r_b$. The Young's modulus of the FGM shell is allowed to vary along its radial dimension, by following the power-law function (1). To investigate the variation of stresses, the four constants of

m	z_1/p	z_2/p	C_1/p	C_2/p
0.5	-1.692	0.510	0.366	-2.417
0.85	-2.176	0.513	0.272	-1.216
1.1	-2.521	0.516	0.212	-0.819
2	-3.698	0.523	0.071	-0.233

Table 1. Numerical values of the four constants of integration in (16) that are used for plotting Figures 4 and 5, left. The other parameters are set as $v = 0.3$, $r_0/r_a = 3$, and $r_b/r_a = 9$.
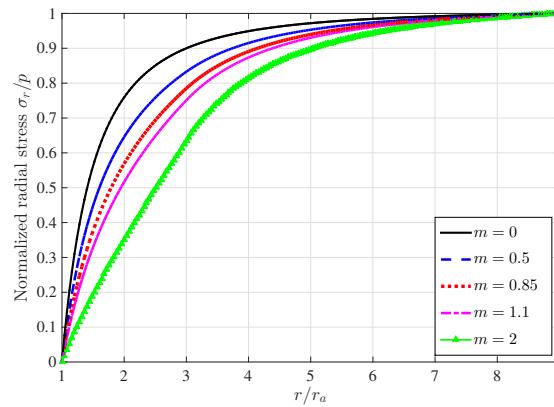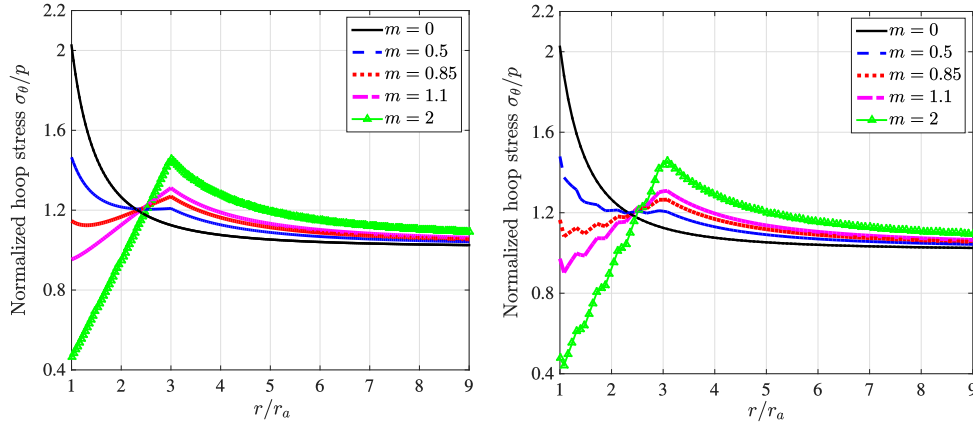

Figure 4. Variation of the normalized radial stress along the radial dimension for five inhomogeneous shells.

integration in (16) must first be determined. Table 1 tabulates numerical values of these coefficients for four representative inhomogeneity indices. Values of other parameters are already given at the beginning of Section 3. It is also worth mentioning that, since the Young's modulus remains continuous across the shell-cylinder interface, its value does not enter into the determination of stress components.

Figure 4 shows the normalized radial stress along the thickness dimension of the structure for five inhomogeneity indices. It is found that the radial stress level can be effectively reduced by the use of an FGM shell. In particular, the radial stress at the graded shell-cylinder interface is significantly lower than that of an integral cylinder of constant stiffness. The larger the inhomogeneity index is the more effective the stress reduction becomes. Benefitting from the continuity of material properties across the graded shell-cylinder interface ($r = r_0$), no sharp corners in the radial stress curves were observed. For all five cases, the maximum radial stress always appears at the outer surface of the cylinder and thus implies the absence of concentration.

To validate the accuracy of the developed analytical solution, finite element modelings of the exactly same model were also performed. Figure 5 shows the analytical solution and finite element results of the hoop stress distribution for five values of the inhomogeneity index. It can be seen that these two independent solutions agree with each other very well. In the finite element approach, the biggest challenge involves the modeling of the inhomogeneous shell. In this work, we closely followed a discretization

Figure 5. Variation of the normalized hoop stress along the radial dimension for five inhomogeneous shells. Left: analytical solution. Right: finite element modeling.

scheme recently proposed by Liu et al. [2018]. Readers who are interested in the numerical modeling of inhomogeneous materials may refer to the article for more details.

When compared with the radial stress, the distribution pattern of the hoop stress becomes more complicated. In the graded shell, three trends can be clearly observed. First, when m is small the hoop stress decreases all the way through the thickness of the shell. Second, as the value of the inhomogeneity index increases the hoop stress curve shows a parabolic behavior and a local minimum can be found somewhere between the shell rim and the shell-cylinder interface. Third, when the inhomogeneity index reaches a critical value (e.g., $m \approx 1.1$) the point of inflection of the hoop stress curve disappears and the hoop stress monotonically increases all the way through the thickness of the shell.

Similar to the case of a homogeneous inner shell, the hoop stress at the shell surface $r = r_a$ decreases with increasing inhomogeneity index. However, the opposite trend is found at the shell-cylinder interface. On the other hand, the hoop stress within the outer cylinder decays all the way along the radial axis for any inhomogeneity index. Soft shells result in higher hoop stresses in the cylinder. Unlike the case of a homogeneous shell, the hoop stress across the shell-cylinder interface now becomes continuous but is still not differentiable. The sharpness of the corner at $r = r_0$ behaves a positive function of the inhomogeneity index. It is clear that the maximum hoop stress for the case of an inhomogeneous shell may occur either at the shell rim or at the shell-cylinder interface, depending on the value of the inhomogeneity index. It can be inferred that there must exist an optimized inhomogeneity index ($m = 0.731$) to make the hoop stress equal ($\sigma_\theta / p = 1.248$) at the shell surface and at the shell-cylinder interface. It becomes obvious that the use of a graded inner shell is more effective than a homogeneous one when the stress reduction is of primary concern. In this case, the stress concentration factor has reduced by 38.4% when compared with a completely homogeneous thick-walled cylinder.

3.2. *An arbitrary biaxial traction load.* We now consider a thick-walled cylinder reinforced by a graded inner shell and subjected to a general biaxial traction load applied at the outer boundary of the cylinder. Since there are many possible combinations of the applied tractions p and q, we here introduce another parameter $\gamma = q/p$. In the numerical examples, several typical values of γ are taken, e.g., $\gamma = 1, 0.5, 0, -0.5,$ and -1. It is noted that when $\gamma = 1$ the solution degenerates to the special case of

z_{21}/p	z_{22}/p	z_{23}/p	z_{24}/p	D_1/p	D_2/p	D_3/p	D_4/p
-0.272	$1.320 \cdot 10^{-04}$	-1.361	0.899	0.365	-0.189	-0.177	$3.485 \cdot 10^{-04}$

Table 2. Numerical values of the eight constants of integration in (25) that are used for plotting the various figures in Section 3.2. The other parameters are set as $m = 0.5$, $v = 0.3$, $r_0/r_a = 3$, and $r_b/r_a = 9$.
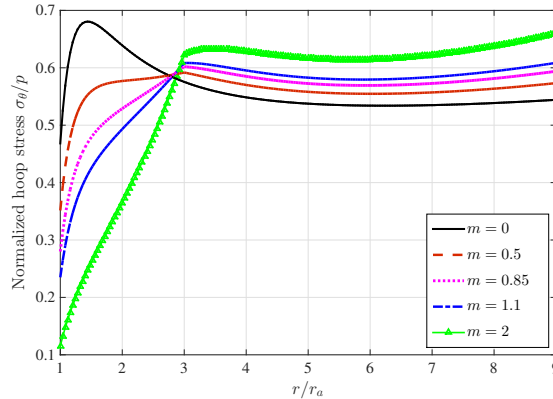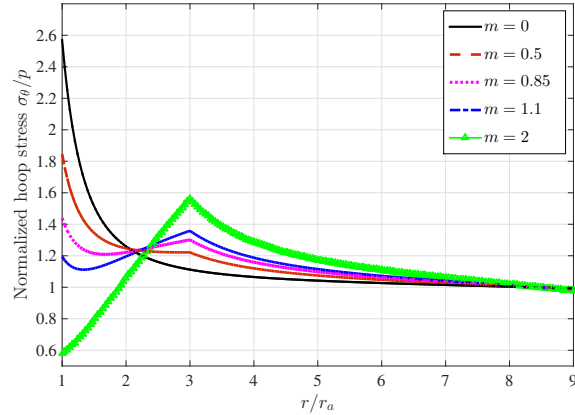

Figure 6. Variation of the normalized hoop stress along x-axis ($\theta = 0$) for five inhomogeneity indices. The traction ratio was fixed as a constant $\gamma = 0.5$.

an axial symmetric traction load that was studied in the previous subsection. A uniaxial tension ($\sigma_x = p$) is represented by $\gamma = 0$ whereas the antisymmetric/pure shear load ($\sigma_x = p, \sigma_y = -p$) is equivalent to $\gamma = -1$. Moreover, it is sufficient to consider the loading case of $q \leq p$, since all solutions due to $q \geq p$ can be obtained by a simple coordinate rotation of $\frac{1}{2}\pi$ around the axis of symmetry.

In addition to Table 1, calculation of stresses due to an arbitrary biaxial load also requires the eight constants of integration given by (25). For the representative inhomogeneity index $m = 0.5$, the numerical values of these coefficients are tabulated in Table 2. Again, stresses are independent on the Young's modulus $E^{(o)}$, benefitting from its continuity across the shell-cylinder interface. In the next two subsections, we explore separately the effects of the inhomogeneity index m and the loading parameter γ on the stress reduction in the thick-walled cylinder.

3.2.1. *Effect of the inhomogeneity index.* In this subsection, we study the effect of the inhomogeneity index m. Several specific values of the index were considered in the subsequent numerical calculations, e.g., $m = 0, 0.5, 0.85, 1.1$, and 2. To exclude the undesired coupling effect of the traction ratio, it was fixed as a constant, i.e., $\gamma = 0.5$, in this subsection.

Figures 6 and 7 show the hoop stress distribution along x and y directions, respectively. Along the radial direction $\theta = 0$, the behavior of the hoop stress has been significantly affected by the introduction of the inhomogeneous shell. For all cases with $m \neq 0$, the hoop stress now increases within the inner shell and then approximately stays constant in the cylinder. The location of the maximum hoop stress has changed from close to the inner surface of the shell toward to the shell-cylinder interface. Moreover, with increasing inhomogeneity the hoop stress value decreases at the inner surface of the shell. Slight fluctuations in the hoop stress level were found at the shell-cylinder boundary, with the highest stress
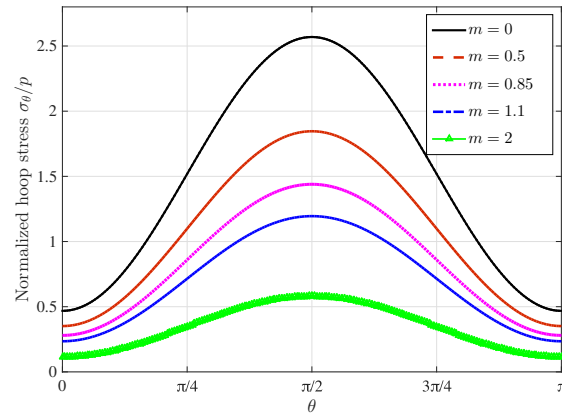
Figure 7. Variation of the normalized hoop stress along y-axis ($\theta = \frac{1}{2}\pi$) for five inhomogeneity indices. The traction ratio was fixed as a constant $\gamma = 0.5$.

value given by the largest inhomogeneity $m = 2$. An intersection among the stress curves was found near the shell-cylinder interface, approaching from the shell side.

Along the other radial direction $\theta = \frac{1}{2}\pi$, the distribution of the hoop stress shows quite similar behavior as that of the case due to an all-around boundary traction (Figure 7). In the inhomogeneous shell, the hoop stress decreases when the shell inhomogeneity is small. In particular, for the special case of zero inhomogeneity ($m = 0$), the stress concentration factor is the highest ($\sigma_\theta / p = 2.556$). For large inhomogeneity indices, e.g., $m \geq 1.1$, the trend has been reversed. Roughly in the interval $0.85 < m < 1.1$, the hoop stress curve behaves as a parabola with positive curvature and the maximum value of the hoop stress could occur on either boundary of the shell, or on both. In contrast, the hoop stresses in the outer cylinder monotonically decay for all values of the inhomogeneity index.

Referring to both Figure 6 and Figure 7, it can be concluded that the maximum hoop stress exists on either the inner surface of the shell or the shell-cylinder interface. Therefore, there must exist a critical inhomogeneity index, $\hat{m}$, which makes the hoop stress equal at $r = r_a$ and $r = r_0$. A numerical search is performed for such an optimized inhomogeneity level. A close examination of Figures 6 and 7 reveals that the optimum inhomogeneity index must lie within the interval $(0.85, 1.1)$. The search can start from either the lower or the upper bound. For the given inhomogeneity index, the stress concentration factor at the inner surface of the shell is compared with that at the shell-cylinder interface. If the two factors are found to be unequal, the inhomogeneity index is updated by an increment of 0.001. The stress concentration factors are subsequently recalculated. The search stops until the difference between the two factors is less than a predefined degree of accuracy, e.g., 0.001. The final result was found to be $\hat{m} \approx 0.961$. It is clear that when $m < \hat{m}$, the maximum hoop stress occurs on the inner surface of the shell, the same situation as that of a completely homogeneous thick-walled cylinder. On the other hand, when $m > \hat{m}$ the most severe stress concentration shifts to the shell-cylinder interface. The concentration factor of the hoop stress component reaches its minimum value ($\sigma_\theta / p = 1.327$) when $m = \hat{m}$. This represents a reduction of 48.1% in the stress concentration factor when compared with a completely homogeneous cylinder under the exact same loading condition.
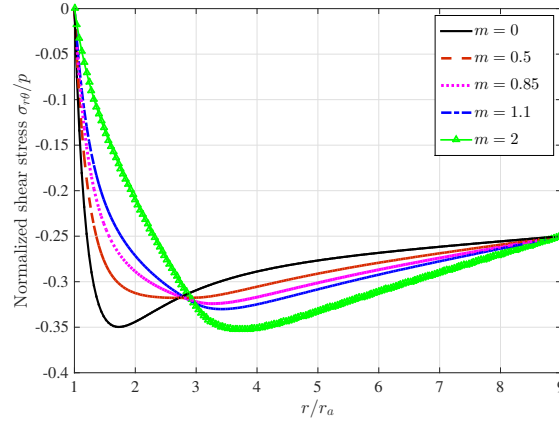
Figure 8. Variation of the normalized hoop stress along the inner surface of the inhomogeneous shell ($r = r_a$) for five inhomogeneity indices. The traction ratio was fixed as a constant $\gamma = 0.5$.
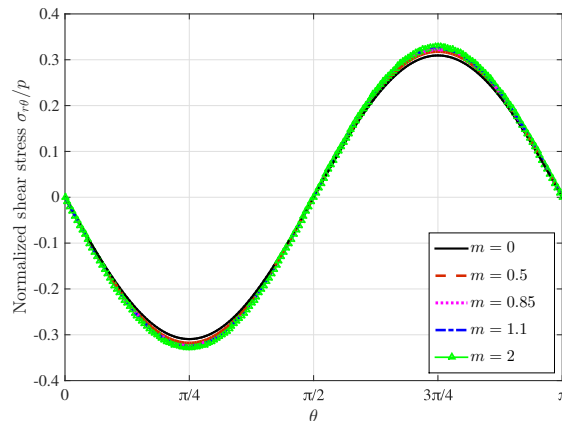
Figure 9. Variation of the normalized hoop stress along the shell-cylinder interface ($r = r_0$) for five inhomogeneity indices. The traction ratio was fixed as a constant $\gamma = 0.5$.

Since the stress concentration always occurs on the inner surface for a cylinder subjected to far-field boundary loading, it is enlightening to examine the hoop stress distribution along $r = r_a$, as shown in Figure 8. It is seen that no matter how the inhomogeneity index changes, the hoop stress curve follows a complete period of sine-wave within $\theta \in [0, \pi]$. The minimum and the maximum hoop stresses are found at $\theta = 0$ and $\theta = \frac{1}{2}\pi$, respectively. The general level of the hoop stress decreases with increasing inhomogeneity index.

Figure 9 shows the shear stress distribution along the shell-cylinder interface ($r = r_0$). It is seen that the effect of the inhomogeneity index m is quite marginal. In the interval $\theta \in [0, \pi]$, all shear stress curves follow a complete sine-wave. The extremes of the shear stress appear at $\theta = \frac{1}{4}\pi$ and $\frac{3}{4}\pi$. It is therefore instructive to examine the shear stress distribution along either of these two directions. Figure 10 shows the variation of the shear stress component through the wall thickness of the structure along $\theta = \frac{1}{4}\pi$. It is found that along this dimension all shear stresses are negative. A point of inflection exists for
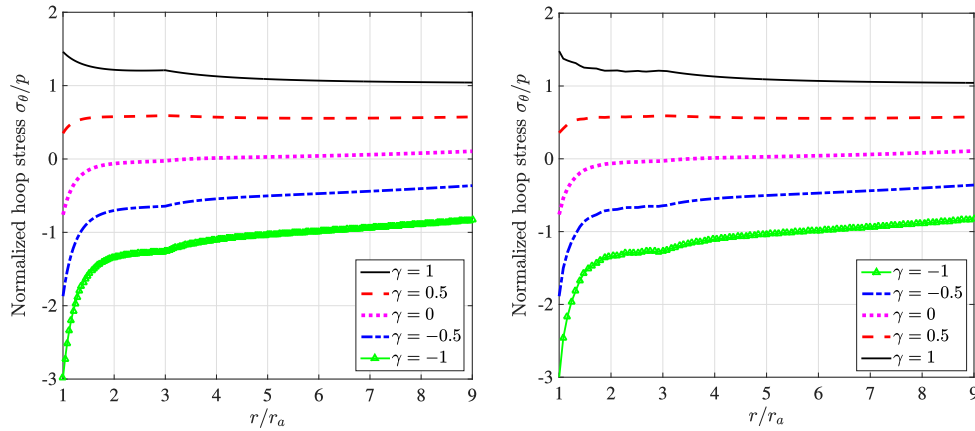
Figure 10. Variation of the normalized hoop stress along the radial direction ($\theta = \frac{1}{4}\pi$) for five inhomogeneity indices. The traction ratio was fixed as a constant $\gamma = 0.5$.

all inhomogeneity indices, with the exact location clearly depending on the value of m. With increasing inhomogeneity index, the location of the shear stress extreme shifts from inside the inner shell to the outer cylinder. More importantly, the magnitude of the shear stress extreme decreases with the inhomogeneity index when m is small and subsequently increases when it becomes large. This observation implies that there exists an optimal inhomogeneity index $\hat{m}$ at which the magnitude of the shear stress extreme assumes its lowest value. Numerical search suggests that the optimal inhomogeneity index is $\hat{m} \approx 0.504$, occurring at $r \approx 2.767 r_a$. In this case, the corresponding concentration factor of the shear stress is the lowest ($\sigma_{r\theta}/p = 0.318$).

3.2.2. *Effect of the traction ratio.* To investigate the effect of the traction ratio $\gamma = q/p$, in this subsection we fix the inhomogeneity index as a constant, i.e., $m = 0.5$. As expected, for all loading cases ($|\gamma| \leq 1$) no stress concentrations were found for the radial stress component. The absolute value of the maximum radial stress is never greater than p. It is therefore only necessary to examine the hoop and shear stresses.

The hoop stress distribution along the radial dimension $\theta = 0$ is shown in Figure 11. It is seen that for positive γ, the hoop stress varies smoothly through the thickness of the structure. For negative γ, the hoop stress depends more sensitively on the radial coordinate. Very high compressive values are found near the inner surface of the graded shell whereas the stress curve varies quite smoothly in the outer cylinder. As γ switches from positive to negative, the hoop stress also switches from tension to compression. Again, excellent agreements have been achieved between the results predicted by the analytical approach and the finite element approach.

On the other hand, the distribution of the hoop stress along the radial direction $\theta = \frac{1}{2}\pi$ behaves quite differently, as shown by both the analytical (Figure 12, left) and the finite element (Figure 12, right) solutions. In this direction, the hoop stress remains positive irrespective of the sign of the traction ratio γ. It is obvious that the hoop stress continuously decays in both domains, with a blunt corner found across the shell-cylinder interface. The level of σ_θ in the inner shell is inversely proportional to γ. Although an opposite trend shows in the outer cylinder, the stress levels due to all loading conditions are actually quite close to $\sigma_x = p$. From Figure 12 it is clear that high stress concentrations appear near the inner surface of the embedded shell and the concentration factor increases with decreasing traction ratio γ.

Figure 11. Variation of the normalized hoop stress along the x direction ($\theta = 0$) for five boundary loads. The inhomogeneity index of the inner shell was fixed as a constant $m = 0.5$. Left: analytical solution. Right: finite element modeling.
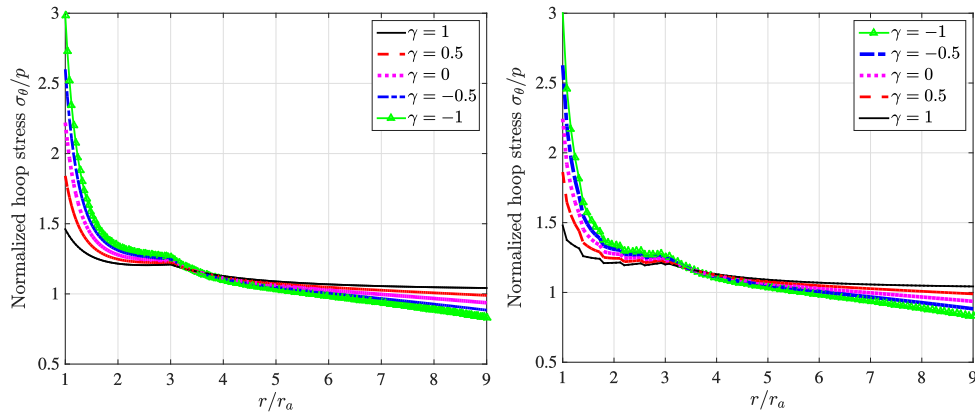
Figure 12. Variation of the normalized hoop stress along the y direction ($\theta = \frac{1}{2}\pi$) for five boundary loads. The inhomogeneity index of the inner shell was fixed as a constant $m = 0.5$. Left: analytical solution. Right: finite element modeling.

Informed by Figures 11 and 12, high stress values are always found at the surface of the inner shell. As a result, in Figure 13, we present the distribution of the hoop stress along the inner surface of the shell $r = r_a$. Due to symmetry, only a half interval of the surface was taken into account. In general, for $\theta \in [0, \pi]$, the hoop stress varies by following a sine pattern for each traction ratio γ. It is found that stress extremes always appear along the x or y direction. For all traction ratios considered in the numerical study ($|\gamma| \leq 1$), the maximum compressive and tensile hoop stresses happen along the x and y direction, respectively. Among them, the antisymmetric traction load results in the highest stress concentration factor ($\sigma_\theta/p = 3$), the same value as that of a voided homogeneous plate subjected to a uniaxial tensile load. Nonetheless, it should be recalled that such a stress distribution is obtained by fixing the inhomogeneity index of the inner shell as a constant ($m = 0.5$).
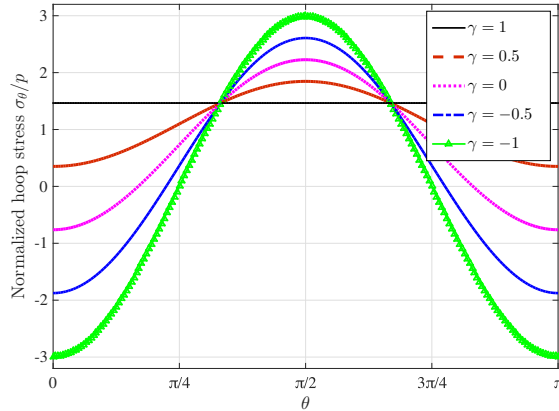
Figure 13. Variation of the normalized hoop stress along the inner surface of the shell ($r = r_a$) for five boundary loads. The inhomogeneity index of the inner shell was fixed as a constant $m = 0.5$.
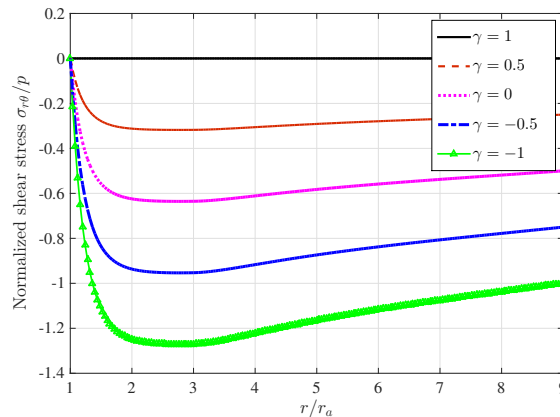

Figure 14. Variation of the normalized shear stress along the radial direction ($\theta = \frac{1}{4}\pi$) for five boundary loads. The inhomogeneity index of the inner shell was fixed as a constant $m = 0.5$.

Enlightened by the stress distribution in an axially loaded structural member, the maximum shear stress should occur along the radial direction $\theta = \frac{1}{4}\pi$, as shown in Figure 14. The magnitude of the shear stress increases with decreasing γ, as the boundary loading shifts from an all-around tension to an antisymmetric load. For the case of $\gamma = -1$, slight stress concentration in the shear stress component was found near the shell-cylinder interface. Along the radial direction, the absolute value of the shear stress rapidly increases in the inner half of the shell and remains nearly constant in the outer half. No significant variations of the shear stress occur in the cylinder.

Figure 15 shows the distribution of the shear stress component along the shell-cylinder interface ($r = r_0$). As can be expected, the maximum values are found along directions that are $\frac{1}{4}\pi$ from the two loading axes ($\theta = 0, \frac{1}{2}\pi$). The shear stress extremes behave a negative function of the traction ratio γ, with the maximum values occurring in the case of the antisymmetric load.
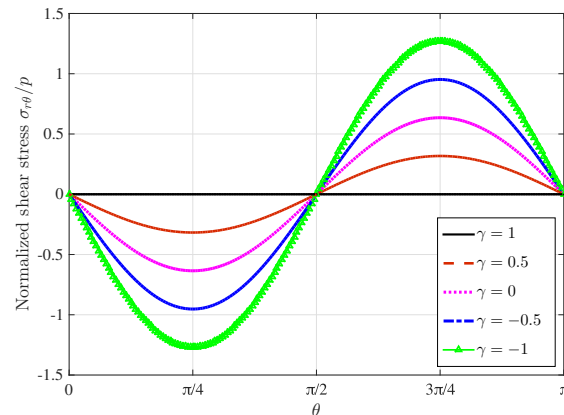
Figure 15. Variation of the normalized shear stress along the shell-cylinder interface $(r = r_0)$ for five boundary loads. The inhomogeneity index of the inner shell was fixed as a constant $m = 0.5$.

4. Conclusions

In this work, we solved the stress distribution and stress concentration in a homogeneous thick-walled cylinder, reinforced by either a radially graded or a homogeneous inner shell. An arbitrary biaxial traction load applied at the outer boundary of the cylinder was taken into consideration. Closed-form analytical solutions were obtained with the method of Airy stress function. On the basis of the analytical solutions and extensive numerical experiments, a few summaries and conclusions can be made as follows:

- We show that the stress concentration that is commonly encountered in thick-walled cylinders can be significantly mitigated by introducing a graded inner shell with a proper distribution in elastic modulus.

- With reference to the elastic stiffness of a thick-walled cylinder, a graded soft shell tends to decrease the conventional stress concentration occurring at the inner boundary of the structure. Nonetheless, stresses at the interface separating the shell and the cylinder increase inevitably due to the softening of the inner layer of the hollow structure.

- An optimal inhomogeneity index in the power-law gradation can be found for which the stress concentrations at the inner boundary of the structure and at the shell-cylinder interface are well balanced.

- In addition to the inhomogeneity index of the embedded shell, we also investigated the effect of the biaxial traction ratio. For all loading cases, no significant concentrations in the radial and shear stress components are found. The hoop stress concentration is therefore of the primary concern. In analogy to the classical solution of a thick-walled cylinder, the concentration factor in the hoop stress component increases with growing difference (including sign) between the boundary loads along perpendicular directions. In this sense, an all-around uniform load is most desired.

Despite the completeness of this work in the context of an idealized plane elasticity problem, future work in this line of research could entail more practical engineering conditions:

(1) the incorporation of more realistic bonding conditions across the embedded shell-cylinder interface,

(2) grading functions different than the power-law, and

(3) three-dimensional structures.

Appendix: Expressions for the various parameters defined in (25)

The parameters λ_{ij}, η_{ij}, μ_{ij}, and ψ_{ij} are elements of four 4×4 matrices:

$$
\begin{aligned}
\lambda_{11} = \frac{1}{\Lambda A_1(r_0)} \Big(& 4(1+\nu)\beta M_{22} + 2(1+\nu)(\alpha-\beta)M_{23} - 2(1+\nu)(\alpha+\beta)M_{24} \\
& + M_{14}\big(2(1+\nu)(\alpha-\beta) + (2-m+\beta)M_{22} + (-2+m+\alpha)M_{23}\big) \\
& + M_{13}\big(-2(1+\nu)(\alpha-\beta) + (-2+m+\beta)M_{22} + (2-m-\alpha)M_{24}\big) \\
& + M_{12}\big(-4(1+\nu)\beta + (2-m-\beta)M_{23} + (-2+m-\beta)M_{24}\big) \Big),
\end{aligned}
$$

$$
\begin{aligned}
\lambda_{12} = \frac{1}{\Lambda A_1(r_0)} \Big(& 8\nu\beta M_{22} + 4\nu(\alpha-\beta)M_{23} - 4\nu(\alpha+\beta)M_{24} \\
& + M_{14}\big(2(3+\nu)(\alpha+\beta) + (6-m+\beta)M_{22} + (m-6+\alpha)M_{23}\big) \\
& + M_{13}\big(-2(3+\nu)(\alpha-\beta) + (m-6+\beta)M_{22} + (6-m-\alpha)M_{24}\big) \\
& + M_{12}\big((6-m-\beta)M_{23} - 4(3+\nu)\beta + (m-6-\beta)M_{24}\big) \Big),
\end{aligned}
$$

$$
\begin{aligned}
\lambda_{13} = \frac{1}{\Lambda A_1(r_0)} \Big(& 2(1+\nu)(\alpha+\beta)M_{24} - 4(1+\nu)\beta M_{22} - 2(1+\nu)(\alpha-\beta)M_{23} \\
& + M_{14}\big(2(1+\nu)(\alpha+\beta) + (\beta-6-m)M_{22} + (6+m+\alpha)M_{23}\big) \\
& + M_{13}\big((6+m+\beta)M_{22} - 2(1+\nu)(\alpha-\beta) - (6+m+\alpha)M_{24}\big) \\
& + M_{12}\big((6+m-\beta)M_{24} - 4(1+\nu)\beta - (6+m+\beta)M_{23}\big) \Big),
\end{aligned}
$$

$$
\begin{aligned}
\lambda_{14} = \frac{1}{\Lambda A_1(r_0)} \Big(& 4(\alpha+\beta)M_{24} - 8\beta M_{22} + 4(\beta-\alpha)M_{23} \\
& + M_{14}\big(2(\nu-1)(\alpha+\beta) + (\beta-2-m)M_{22} + (2+m+\alpha)M_{23}\big) \\
& + M_{13}\big(2(1-\nu)(\alpha-\beta) + (2+m+\beta)M_{22} - (2+m+\alpha)M_{24}\big) \\
& + M_{12}\big(4(1-\nu)\beta - (2+m+\beta)M_{23} + (2+m-\beta)M_{24}\big) \Big),
\end{aligned}
$$

$$
\begin{aligned}
\lambda_{21} = \frac{1}{\Lambda A_2(r_0)} \Big(& 2(1+\nu)(\alpha+\beta)M_{23} - 4(1+\nu)\beta M_{21} - 2(1+\nu)(\alpha-\beta)M_{24} \\
& + M_{14}\big(2(1+\nu)(\alpha-\beta) + (m-2-\beta)M_{21} + (2-m+\alpha)M_{23}\big) \\
& + M_{13}\big((2-m-\beta)M_{21} - 2(1+\nu)(\alpha+\beta) + (m-2-\alpha)M_{24}\big) \\
& + M_{11}\big(4(1+\nu)\beta + (m-2+\beta)M_{23} + (2-m+\beta)M_{24}\big) \Big),
\end{aligned}
$$

$$
\begin{aligned}
\lambda_{22} = \frac{1}{\Lambda A_2(r_0)} \Big(& 4\nu(\alpha+\beta)M_{23} - 8\nu\beta M_{21} - 4\nu(\alpha-\beta)M_{24} \\
& + M_{14}\big(2(3+\nu)(\alpha-\beta) + (m-6-\beta)M_{21} + (6-m+\alpha)M_{23}\big) \\
& + M_{13}\big((6-m-\beta)M_{21} - 2(3+\nu)(\alpha+\beta) + (m-6-\alpha)M_{24}\big) \\
& + M_{11}\big(4(3+\nu)\beta + (m-6+\beta)M_{23} + (6-m+\beta)M_{24}\big) \Big),
\end{aligned}
$$

$$\lambda_{23} = \frac{1}{\Lambda A_2(r_0)}\Big(4(1+\nu)\beta M_{21} - 2(1+\nu)(\alpha+\beta)M_{23} + 2(1+\nu)(\alpha-\beta)M_{24}$$
$$+ M_{14}\big(2(1+\nu)(\alpha-\beta) + (6+m-\beta)M_{21} + (\alpha-6-m)M_{23}\big)$$
$$+ M_{13}\big((6+m-\alpha)M_{24} - 2(1+\nu)(\alpha+\beta) - (6+m+\beta)M_{21}\big)$$
$$+ M_{11}\big(4(1+\nu)\beta + (6+m+\beta)M_{23} + (\beta-6-m)M_{24}\big)\Big),$$

$$\lambda_{24} = \frac{1}{\Lambda A_2(r_0)}\Big(8\beta M_{21} - 4(\alpha+\beta)M_{23} + 4\nu(\alpha-\beta)M_{24}$$
$$+ M_{14}\big(2(\nu-1)(\alpha-\beta) + (2+m-\beta)M_{21} + (\alpha-2-m)M_{23}\big)$$
$$+ M_{13}\big(2(1-\nu)(\alpha+\beta) - (2+m+\beta)M_{21} + (2+m-\alpha)M_{24}\big)$$
$$+ M_{11}\big(4(\nu-1)\beta + (2+m+\beta)M_{23} + (2-m+\beta)M_{24}\big)\Big),$$

$$\lambda_{31} = \frac{1}{\Lambda B_1(r_0)}\Big(-2(1+\nu)(\alpha-\beta)M_{21} + 2(1+\nu)(\alpha+\beta)M_{22} + 4(1+\nu)\alpha M_{24}$$
$$+ M_{14}\big((2-m-\alpha)M_{21} - 4(1+\nu)\alpha + (m-2-\alpha)M_{22}\big)$$
$$+ M_{12}\big(2(1+\nu)(\alpha+\beta) + (m-2+\beta)M_{21} + (2-m+\alpha)M_{24}\big)$$
$$+ M_{11}\big(2(1+\nu)(\alpha-\beta) + (2-m-\beta)M_{22} + (m-2+\alpha)M_{24}\big)\Big),$$

$$\lambda_{32} = \frac{1}{\Lambda B_1(r_0)}\Big(8\nu\alpha M_{24} - 4\nu(\alpha-\beta)M_{21} - 4\nu(\alpha+\beta)M_{22}$$
$$+ M_{14}\big((6-m-\alpha)M_{21} - 4(3+\nu)\alpha + (m-6-\alpha)M_{22}\big)$$
$$+ M_{12}\big(2(3+\nu)(\alpha+\beta) + (m-6+\beta)M_{21} + (6-m+\alpha)M_{24}\big)$$
$$+ M_{11}\big(2(3+\nu)(\alpha-\beta) + (6-m-\beta)M_{22} + (m-6+\alpha)M_{24}\big)\Big),$$

$$\lambda_{33} = \frac{1}{\Lambda B_1(r_0)}\Big(2(1+\nu)(\alpha-\beta)M_{21} + 2(1+\nu)(\alpha+\beta)M_{22} + 4(1+\nu)\alpha M_{24}$$
$$+ M_{14}\big((6+m-\alpha)M_{22} - 4(1+\nu)\alpha - (6+m+\alpha)M_{21}\big)$$
$$+ M_{12}\big(2(1+\nu)(\alpha+\beta) + (6+m+\beta)M_{21} + (\alpha-6-m)M_{24}\big)$$
$$+ M_{11}\big(2(1+\nu)(\alpha-\beta) - (6+m+\beta)M_{22} + (6+m+\alpha)M_{24}\big)\Big),$$

$$\lambda_{34} = \frac{1}{\Lambda B_1(r_0)}\Big(4(\alpha-\beta)M_{21} + 4(\alpha+\beta)M_{22} - 8\alpha M_{24}$$
$$+ M_{14}\big(4(1-\nu)\alpha - (2+m+\alpha)M_{21} + (2+m-\alpha)M_{22}\big)$$
$$+ M_{12}\big(2(\nu-1)(\alpha+\beta) + (2+m+\beta)M_{21} + (\alpha-2-m)M_{24}\big)$$
$$+ M_{11}\big(2(\nu-1)(\alpha-\beta) - (2+m+\beta)M_{22} + (2+m+\alpha)M_{24}\big)\Big),$$

$$\lambda_{41} = \frac{1}{\Lambda B_2(r_0)}\Big(2(1+\nu)(\alpha+\beta)M_{21} + 2(1+\nu)(\alpha-\beta)M_{22} - 4(1+\nu)\alpha M_{23}$$
$$+ M_{13}\big(4(1+\nu)\alpha + (m-2+\alpha)M_{21} + (2-m+\alpha)M_{22}\big)$$
$$+ M_{11}\big((m-2-\beta)M_{22} - 2(1+\nu)(\alpha+\beta) + (2-m-\alpha)M_{23}\big)$$
$$+ M_{12}\big((2-m+\beta)M_{21} - 2(1+\nu)(\alpha-\beta) + (m-2-\alpha)M_{23}\big)\Big),$$

$$
\begin{aligned}
\lambda_{42} = \frac{1}{\Lambda B_2(r_0)} \Big(& 4\nu(\alpha + \beta)M_{21} + 4\nu(\alpha - \beta)M_{22} - 8\nu\alpha M_{23} \\
& + M_{13}\big(4(3+\nu)\alpha + (m-6+\alpha)M_{21} + (6-m+\alpha)M_{22}\big) \\
& + M_{11}\big((m-6-\beta)M_{22} - 2(3+\nu)(\alpha + \beta) + (6-m-\alpha)M_{23}\big) \\
& + M_{12}\big((6-m+\beta)M_{21} - 2(3+\nu)(\alpha - \beta) + (m-6-\alpha)M_{23}\big)\Big),
\end{aligned}
$$

$$
\begin{aligned}
\lambda_{43} = \frac{1}{\Lambda B_2(r_0)} \Big(& 4(1+\nu)\alpha M_{23} - 2(1+\nu)(\alpha + \beta)M_{21} - 2(1+\nu)(\alpha - \beta)M_{22} \\
& + M_{13}\big(4(1+\nu)\alpha + (6+m+\alpha)M_{21} + (\alpha - 6 - m)M_{22}\big) \\
& + M_{11}\big((6+m-\beta)M_{22} - 2(1+\nu)(\alpha + \beta) - (6+m+\alpha)M_{23}\big) \\
& + M_{12}\big((\beta - 6 - m)M_{21} - 2(1+\nu)(\alpha - \beta) + (6+m-\alpha)M_{23}\big)\Big),
\end{aligned}
$$

$$
\begin{aligned}
\lambda_{44} = \frac{1}{\Lambda B_2(r_0)} \Big(& 8\alpha M_{23} - 4(\alpha + \beta)M_{21} - 4\nu(\alpha - \beta)M_{22} \\
& + M_{13}\big(4(\nu - 1)\alpha + (2+m+\alpha)M_{21} + (\alpha - 2 - m)M_{22}\big) \\
& + M_{11}\big(2(1-\nu)(\alpha + \beta) + (2+m-\beta)M_{22} - (2+m+\alpha)M_{23}\big) \\
& + M_{12}\big(2(1-\nu)(\alpha - \beta) + (\beta - 2 - m)M_{21} + (2+m-\alpha)M_{23}\big)\Big),
\end{aligned}
$$

$$
\eta_{ij} = r_b^2 r_0^4(\lambda_{i3}\lambda_{j2} - \lambda_{j3}\lambda_{i2}) + 2r_0^6(\lambda_{i2}\lambda_{j4} - \lambda_{j2}\lambda_{i4}) + r_b^6(\lambda_{i3}\lambda_{j4} - \lambda_{j3}\lambda_{i4}),
$$

$$
\mu_{ij} = r_0^4(\lambda_{i2}\lambda_{j1} - \lambda_{j2}\lambda_{i1}) + r_b^4(\lambda_{i4}\lambda_{j1} - \lambda_{j4}\lambda_{i1}),
$$

$$
\begin{aligned}
\psi_{ij} = r_0^8(\lambda_{i2}\lambda_{j1} - \lambda_{j2}\lambda_{i1}) + 2r_b^2 r_0^6(\lambda_{i4}\lambda_{j2} - \lambda_{i2}\lambda_{j4}) + r_b^4 r_0^4(3(\lambda_{i1}\lambda_{j4} - \lambda_{i4}\lambda_{j1}) + \lambda_{i2}\lambda_{j3} - \lambda_{i3}\lambda_{j2}) \\
+ 2r_b^6 r_0^2(\lambda_{i3}\lambda_{j1} - \lambda_{i1}\lambda_{j3}) + r_b^8(\lambda_{i4}\lambda_{j3} - \lambda_{j4}\lambda_{i3}),
\end{aligned}
$$

where

$$
M_{11} = \frac{(m^2 + 2(1-\alpha)m - \alpha(2-\alpha))\nu}{2(m+\alpha)} - \frac{m-\alpha-6}{m+\alpha},
$$

$$
M_{12} = \frac{(m^2 + 2(1+\alpha)m + \alpha(2+\alpha))\nu}{2(m-\alpha)} - \frac{m+\alpha-6}{m-\alpha},
$$

$$
M_{13} = \frac{(m^2 + 2(1-\beta)m - \beta(2-\beta))\nu}{2(m+\beta)} - \frac{m-\beta-6}{m+\beta},
$$

$$
M_{14} = \frac{(m^2 + 2(1+\beta)m + \beta(2+\beta))\nu}{2(m-\beta)} - \frac{m+\beta-6}{m-\beta},
$$

$$
\begin{aligned}
M_{21} = \tfrac{1}{96}\big(& m^2(4\nu - 28) + m(\beta^2 - \alpha^2 + 28\beta - 4\beta\nu - 24\nu - 88) \\
& - \beta^3 - 6\beta^2 + 6\alpha^2 + \alpha^2\beta + 64\beta - 192\nu - 192\big),
\end{aligned}
$$

$$
\begin{aligned}
M_{22} = \tfrac{1}{96}\big(& m^2(4\nu - 28) + m(\alpha^2 - \beta^2 - 28\alpha - 4\alpha\nu - 24\nu - 88) \\
& + \alpha^3 - 6\alpha^2 + 6\beta^2 - \beta^2\alpha - 64\alpha - 192\nu - 192\big),
\end{aligned}
$$

$$M_{23} = \frac{1}{96}\big(m^2(4\nu - 28) - m(\alpha^2 - \beta^2 + 28\beta - 4\beta\nu + 24\nu + 88)$$
$$+ \beta^3 - 6\beta^2 + 6\alpha^2 - \alpha^2\beta - 64\beta - 192\nu - 192\big),$$

$$M_{24} = \frac{1}{96}\big(m^2(4\nu - 28) - m(\beta^2 - \alpha^2 - 28\alpha + 4\alpha\nu + 24\nu + 88)$$
$$+ \alpha^3 + 6\alpha^2 - 6\beta^2 - \beta^2\alpha - 64\alpha + 192\nu + 192\big),$$

and

$$\Lambda = M_{11}(-2\beta M_{22} - (\alpha - \beta)M_{23} + (\alpha + \beta)M_{24}) + M_{12}(2\beta M_{21} - (\alpha + \beta)M_{23} + (\alpha - \beta)M_{24})$$
$$+ M_{13}((\alpha - \beta)M_{21} + (\alpha + \beta)M_{22} - 2\alpha M_{24}) + M_{14}(-(\alpha + \beta)M_{21} - (\alpha - \beta)M_{22} + 2\alpha M_{23}).$$

The parameters ξ_i, a_i, and ζ_i are elements of three four-component vectors

$$\xi_i = \{\alpha \quad -\alpha \quad \beta \quad -\beta\},$$
$$a_i = \{A_1(r_a) \quad A_2(r_a) \quad B_1(r_a) \quad B_2(r_a)\},$$
$$\zeta_i = \{r_0^{1-m} \quad r_0^{3-m} \quad r_0^{-3-m} \quad r_0^{-1-m}\}.$$

Acknowledgements

References

[Barber 2010] J. R. Barber, *Elasticity*, 3rd ed., Solid Mechanics and Its Applications **172**, Springer, 2010.

[Batista 2011] M. Batista, "On the stress concentration around a hole in an infinite plate subject to a uniform load at infinity", *Int. J. Mech. Sci.* **53**:4 (2011), 254–261.

[Batra and Nie 2010] R. C. Batra and G. J. Nie, "Analytical solutions for functionally graded incompressible eccentric and non-axisymmetrically loaded circular cylinders", *Compos. Struct.* **92**:5 (2010), 1229–1245.

[Birman and Byrd 2007] V. Birman and L. W. Byrd, "Modeling and analysis of functionally graded materials and structures", *Appl. Mech. Rev. (ASME)* **60**:5 (2007), 195–216.

[Chen 2015] Y. Z. Chen, "A novel solution for thick-walled cylinders made of functionally graded materials", *Smart Struct. Syst.* **15**:6 (2015), 1503–1520.

[Chen and Lin 2010] Y. Z. Chen and X. Y. Lin, "An alternative numerical solution of thick-walled cylinders and spheres made of functionally graded materials", *Comput. Mater. Sci.* **48**:3 (2010), 640–647.

[Chen et al. 2012] X. Chen, L. Gu, B. Zou, Y. Wang, and X. Cao, "New functionally graded thermal barrier coating system based on LaMgAl$_{11}$O$_{19}$/YSZ prepared by air plasma spraying", *Surf. Coat. Technol.* **206**:8-9 (2012), 2265–2274.

[Chi and Chung 2006a] S.-H. Chi and Y.-L. Chung, "Mechanical behavior of functionally graded material plates under transverse load, I: Analysis", *Int. J. Solids Struct.* **43**:13 (2006), 3657–3674.

[Chi and Chung 2006b] S.-H. Chi and Y.-L. Chung, "Mechanical behavior of functionally graded material plates under transverse load, II: Numerical results", *Int. J. Solids Struct.* **43**:13 (2006), 3675–3691. Correction in **44**:5 (2007), 1691.

[Chu et al. 2015] P. Chu, X.-F. Li, J.-X. Wu, and K. Y. Lee, "Two-dimensional elasticity solution of elastic strips and beams made of functionally graded materials under tension and bending", *Acta Mech.* **226**:7 (2015), 2235–2253.

[Dryden and Batra 2013] J. Dryden and R. C. Batra, "Optimum Young's modulus of a homogeneous cylinder energetically equivalent to a functionally graded cylinder", *J. Elasticity* **110**:1 (2013), 95–110.

[Ghannad et al. 2013] M. Ghannad, G. H. Rahimi, and M. Z. Nejad, "Elastic analysis of pressurized thick cylindrical shells with variable thickness made of functionally graded materials", *Compos. B Eng.* **45**:1 (2013), 388–396.

[Gouasmi et al. 2015] S. Gouasmi, A. Megueni, A. S. Bouchikhi, K. Zouggar, and A. Sahli, "On the reduction of stress concentration factor around a notch using a functionally graded layer", *Mater. Res.* **18**:5 (2015), 971–977.

[Horgan and Chan 1999] C. O. Horgan and A. M. Chan, "The pressurized hollow cylinder or disk problem for functionally graded isotropic linearly elastic materials", *J. Elasticity* **55**:1 (1999), 43–59.

[Jha et al. 2013] D. K. Jha, T. Kant, and R. K. Singh, "A critical review of recent research on functionally graded plates", *Compos. Struct.* **96** (2013), 833–849.

[Jin and Batra 1996] Z.-H. Jin and R. C. Batra, "Some basic fracture mechanics concepts in functionally graded materials", *J. Mech. Phys. Solids* **44**:8 (1996), 1221–1235.

[Kashtalyan and Menshykova 2007] M. Kashtalyan and M. Menshykova, "Three-dimensional elastic deformation of a functionally graded coating/substrate system", *Int. J. Solids Struct.* **44**:16 (2007), 5272–5288.

[Kawasaki and Watanabe 2002] A. Kawasaki and R. Watanabe, "Thermal fracture behavior of metal/ceramic functionally graded materials", *Eng. Fract. Mech.* **69**:14-16 (2002), 1713–1728.

[Kubair 2013] D. V. Kubair, "Stress concentration factors and stress-gradients due to circular holes in radially functionally graded panels subjected to anti-plane shear loading", *Acta Mech.* **224**:11 (2013), 2845–2862.

[Kubair and Bhanu-Chandar 2008] D. V. Kubair and B. Bhanu-Chandar, "Stress concentration factor due to a circular hole in functionally graded panels under uniaxial tension", *Int. J. Mech. Sci.* **50**:4 (2008), 732–742.

[Liu et al. 2018] Z. Liu, J. Yan, and C. Mi, "On the receding contact between a two-layer inhomogeneous laminate and a half-plane", *Struct. Eng. Mech.* **66**:3 (2018), 329–341.

[Marin 2005] L. Marin, "Numerical solution of the Cauchy problem for steady-state heat transfer in two-dimensional functionally graded materials", *Int. J. Solids Struct.* **42**:15 (2005), 4338–4351.

[Mohammadi et al. 2011] M. Mohammadi, J. R. Dryden, and L. Jiang, "Stress concentration around a hole in a radially inhomogeneous plate", *Int. J. Solids Struct.* **48**:3-4 (2011), 483–491.

[Mohammadi et al. 2016] M. Mohammadi, G. C. Saha, and A. H. Akbarzadeh, "Elastic field in composite cylinders made of functionally graded coatings", *Int. J. Eng. Sci.* **101** (2016), 156–170.

[Müller et al. 2003] E. Müller, Č. Drăsar, J. Schilz, and W. A. Kaysser, "Functionally graded materials for sensor and energy applications", *Mater. Sci. Eng. A* **362**:1-2 (2003), 17–39.

[Nagpal et al. 2012] S. Nagpal, N. Jain, and S. Sanyal, "Stress concentration and its mitigation techniques in flat plate with singularities: a critical review", *Eng. J.* **16**:1 (2012), 1–16.

[Nie and Batra 2010] G. J. Nie and R. C. Batra, "Exact solutions and material tailoring for functionally graded hollow circular cylinders", *J. Elasticity* **99**:2 (2010), 179–201.

[Nie et al. 2011] G. J. Nie, Z. Zhong, and R. C. Batra, "Material tailoring for functionally graded hollow cylinders and spheres", *Compos. Sci. Technol.* **71**:5 (2011), 666–673.

[Oral and Anlas 2005] A. Oral and G. Anlas, "Effects of radially varying moduli on stress distribution of nonhomogeneous anisotropic cylindrical bodies", *Int. J. Solids Struct.* **42**:20 (2005), 5568–5588.

[Pan and Roy 2006] E. Pan and A. K. Roy, "A simple plane-strain solution for functionally graded multilayered isotropic cylinders", *Struct. Eng. Mech.* **24**:6 (2006), 727–740.

[Patel and Sharma 2017] N. P. Patel and D. S. Sharma, "On the stress concentration around a polygonal cut-out of complex geometry in an infinite orthotropic plate", *Compos. Struct.* **179** (2017), 415–436.

[Rezaeepazhand and Jafari 2010] J. Rezaeepazhand and M. Jafari, "Stress concentration in metallic plates with special shaped cutout", *Int. J. Mech. Sci.* **52**:1 (2010), 96–102.

[Sadeghi et al. 2012] H. Sadeghi, M. Baghani, and R. Naghdabadi, "Strain gradient elasticity solution for functionally graded micro-cylinders", *Int. J. Eng. Sci.* **50**:1 (2012), 22–30.

[Savin 1961] G. N. Savin, *Stress concentration around holes*, International Series of Monographs on Aeronautics and Astronautics, Division I: Solid and Structural Mechanics **1**, Pergamon, New York, 1961.

[Sburlati 2012] R. Sburlati, "Analytical elastic solutions for pressurized hollow cylinders with internal functionally graded coatings", *Compos. Struct.* **94**:12 (2012), 3592–3600.

[Sburlati 2013] R. Sburlati, "Stress concentration factor due to a functionally graded ring around a hole in an isotropic plate", *Int. J. Solids Struct.* **50**:22-23 (2013), 3649–3658.

[Sburlati et al. 2013] R. Sburlati, S. R. Atashipour, and S. Hosseini-Hashemi, "Study on the effect of functionally graded coating layers on elastic deformation of thick circular plates: a closed-form elasticity solution", *Compos. Struct.* **99** (2013), 131–140.

[Sburlati et al. 2014] R. Sburlati, S. R. Atashipour, and S. A. Atashipour, "Reduction of the stress concentration factor in a homogeneous panel with hole by using a functionally graded layer", *Compos. B Eng.* **61** (2014), 99–109.

[Theocaris and Petrou 1986] P. S. Theocaris and L. Petrou, "Stress distributions and intensities at corners of equilateral triangular holes", *Int. J. Fract.* **31**:4 (1986), 271–289.

[Tutuncu 2007] N. Tutuncu, "Stresses in thick-walled FGM cylinders with exponentially-varying properties", *Eng. Struct.* **29**:9 (2007), 2032–2035.

[Ukadgaonker and Rao 1999] V. G. Ukadgaonker and D. K. N. Rao, "Stress distribution around triangular holes in anisotropic plates", *Compos. Struct.* **45**:3 (1999), 171–183.

[Watari et al. 2004] F. Watari, A. Yokoyama, M. Omori, T. Hirai, H. Kondo, M. Uo, and T. Kawasaki, "Biocompatibility of materials and development to functionally graded implant for bio-medical application", *Compos. Sci. Technol.* **64**:6 (2004), 893–908.

[Wu and Mu 2003] H.-C. Wu and B. Mu, "On stress concentrations for isotropic/orthotropic plates and cylinders with a circular hole", *Compos. B Eng.* **34**:2 (2003), 127–134.

[Xin et al. 2014] L. Xin, G. Dui, S. Yang, and J. Zhang, "An elasticity solution for functionally graded thick-walled tube subjected to internal pressure", *Int. J. Mech. Sci.* **89** (2014), 344–349.

[Yang and Gao 2016] Q. Yang and C.-F. Gao, "Reduction of the stress concentration around an elliptic hole by using a functionally graded layer", *Acta Mech.* **227**:9 (2016), 2427–2437.

[Yang et al. 2008] Z. Yang, C.-B. Kim, C. Cho, and H. G. Beom, "The concentration of stress and strain in finite thickness elastic plate containing a circular hole", *Int. J. Solids Struct.* **45**:3-4 (2008), 713–731.

[Yang et al. 2010a] Q. Yang, C.-F. Gao, and W. Chen, "Stress analysis of a functional graded material plate with a circular hole", *Arch. Appl. Mech.* **80**:8 (2010), 895–907.

[Yang et al. 2010b] Z. Yang, C.-B. Kim, H. G. Beom, and C. Cho, "The stress and strain concentrations of out-of-plane bending plate containing a circular hole", *Int. J. Mech. Sci.* **52**:6 (2010), 836–846.

[Yang et al. 2015] B. Yang, W. Q. Chen, and H. J. Ding, "3D elasticity solutions for equilibrium problems of transversely isotropic FGM plates with holes", *Acta Mech.* **226**:5 (2015), 1571–1590.

XIAOBAO LI: xiaobaoli@hfut.edu.cn
School of Civil Engineering, Hefei University of Technology, Hefei, China

YIWEI HUA: 107653759@qq.com
Jiangsu Key Laboratory of Engineering Mechanics, School of Civil Engineering, Southeast University, Nanjing, China

CHENYI ZHENG: 594040623@qq.com
Jiangsu Key Laboratory of Engineering Mechanics, School of Civil Engineering, Southeast University, Nanjing, China

CHANGWEN MI: mi@seu.edu.cn
Jiangsu Key Laboratory of Engineering Mechanics, School of Civil Engineering, Southeast University, Nanjing, China

∎
∎∎
∎msp

CIRCULAR-HOLE STRESS CONCENTRATION ANALYSIS ON
GLASS-FIBER-COTTON REINFORCED MC-NYLON

You Rui Tao, Ning Rui Li and Xu Han

The influence of geometrical discontinuities on the stress distribution is critical for design applications. A novel type of composite, named glass-fiber-cotton reinforced monomer casting nylon (GFCR MC-nylon), is prepared, and the circular-hole stress concentration of a GFCR MC-nylon plate is investigated via the digital image correlation technique (DIC). The experimental results show that the stress concentration factor (SCF) of the composite varies with the diameter of the circular hole and stress intensity. A novel finite element model is established to investigate the influence of glass-fiber (GF) length on SCF. The simulation results show high agreement with the experimental results. The findings provide the basis for the structure design of fiber-cotton reinforced composite.

1. Introduction

For a homogeneous thin panel with a circular hole subjected to uniaxial loading, the distribution of stress is not monotonic around the circular hole. The stress concentration factor (SCF) is defined as the stress around the circular hole divided by the average stress. Generally, the maximum SCF is located at the hole edge.

Nowadays, fiber-reinforced composites have been widely applied in industry. The stress concentration of fiber-reinforced composites has attracted attention in the recent past. If the fiber under consideration is an isotropic material with a circular hole, Cheng and Chen [1988] have provided equations to solve the SCF for plane-stress analysis. The equations show that the distribution of stress is determined by the proportion and elastic modulus of the fiber and resin. Maximyuk et al. [2014] studied the nonlinear deformation of flexible composite shells with a reinforced curved hole under static loading. Pandita and Nishiyabu [Pandita et al. 2003] investigated the tensile strain field of woven fabric composites with digital photogrammetry technology. The experimental results revealed the strain concentrations near the singularity and that the strain concentrations were influenced by the tensile loading direction and the hole dimension relative to the size of the unit cell of the plain woven fabrics. Ghasemi and Razavian [2012] advocated that the influence of specimen dimension, notch size, lay ups, and material properties were important to the residual strength and stress concentration factor of laminated composite materials. Defense hole systems are used to redistribute the stresses around the main hole by introducing an auxiliary hole in the low-stress area near the main hole. Jadee and Othman [2015] investigated the effect of the defense hole system on the stress distribution around the bolt-hole in a GF reinforced polymer composite bolted joint, showing that adding an auxiliary hole near the bolt-hole reduces the stresses in the vicinity of the bolt hole. Toubal et al. [2005] investigated the stress concentration characterization of a laminate carbon epoxy with an electronic speckle pattern interferometer, which were compared with the predictions of a

theoretical model previously developed by Lekhnitskii [Lekhnitskii et al. 1968] and a finite element study. Liu and Huang [2014] thought that the SCF with transversely isotropic fibers involved can be sufficiently approximated by a much simpler stress concentration factor formula derived upon isotropic fiber rein-forcement. Liu and Tang [2016] studied the stress concentration in notched cross-ply laminates under tensile loading. Some other researchers focused on the influence of ply cluster thickness and location on matrix cracking evolution in open-hole composite laminates [Moure et al. 2016], progressive failure analysis on scaled open-hole tensile composite laminates [Bao and Liu 2016], gradient model [Khoroshun and Kabysh 2007], and a unified approach to problems of stress concentration near V-shaped notches [Savruk and Kazberuk 2007]. The above references show that reduced stress concentration in composites has been studied widely and applied in engineering. However, there are few studies or experiments available in the literature that explain the stress concentration of long GF cotton reinforced composites.

Finite element simulation has been adopted in the stress concentration analysis of composites. For example, Wu and Mu [2003] compared the SCF in isotropic and orthotropic finite-width panels by performing systematic finite element simulations. Finite element modeling also has been applied in the stress-analysis of laminated composite plates containing circular holes under transverse loading [Paul and Rao 1995]. Hao et al. [2015] investigated the notch effects and crack propagation on kenaf/polypropylene nonwoven composites. However, the finite element modeling used in the above references was based on commercial finite element method (FEM) code, such as the Discrete Damage Mechanics model, which is not suited to analyze the influence of length and proportion of fibers on stress concentration.

New measurement technologies have been applied in the investigation of stress concentration, such as digital photogrammetry technology [Maximyuk et al. 2014], electronic speckle pattern interferometry [Toubal et al. 2005], and digital image correlation (DIC) [Aparna et al. 2015]. The DIC technique uses high-speed, high-resolution, and accurate charge-coupled device cameras for measuring displacement components on the surface of the testing material having speckle patterns. Images are captured at the time of testing at every stress cycle and these deformed patterns are correlated with a reference pattern and determining the displacements of the so-called subsets.

In this paper, the authors prepared a novel type of long GF cotton reinforced nylon through casting. The ultimate strength of the composite is more than 140 MPa. Therefore, this composite may be manufactured as a structural part in which a circular hole is always used to connect the other parts. The present study is hence aimed at investigating the stress concentration on the composite plate using the DIC technique. The arrangement of this paper is summarized as follows. The preparation of the composite and tensile samples and experimental procedure are introduced in Section 2. The experimental results of stress concentration are discussed in Section 3. Then, a novel finite element model is established and the finite element analysis results are compared with experimental results in Section 4. At last, in Section 5, the authors give the conclusions of this study.

2. Preparation of GFCR MC-nylon specimen

As a type of engineering plastic with high molecular weight, high mechanical advantages, and excellent self-lubricating performance, monomer casting nylon (MC-nylon) has been widely used for the produc-tion of gears, bearings, and slide blocks [Xu et al. 2013]. Many attempts have been made to improve the properties of MC-nylon [Zhang et al. 2012; Wang et al. 2013], such as incorporating GF into the plastic

resin. However, in the above researches, the mechanical properties of the composite were not improved significantly because the length of the GFs was too short.

As shown in Figure 1 (left), GF cotton is a new reinforcing material in composites. GF cotton is not a mixture of GF and cotton, but is instead gossypine long GF. In other word, GF cotton is made up nondirectional long GFs, which is loosened from a GF bundle, shown in Figure 1 (center) by a garnetting machine. In the GF bundle, the orientation of the GFs is directional. After loosening, the GF bundle is dispersed as single one. The orientation of single GF is nondirectional, as shown in Figure 1 (left). To illustrate the orientation of the GFs, a microscopic image of the fibers in a composite is shown in Figure 1 (right). It is clear that the fibers are nondirectional. In this investigation, the length of the GFs is 60 mm, which is much longer than that of short GF-reinforced composites. This novel composite is isotropic because the orientation of the GFs in the composite is nondirectional in three-dimensional space.

The raw materials in this composite include caprolactam monomer, a main catalyst, an auxiliary catalyst, and reinforced material. The caprolactam monomer was supplied by China Petroleum and Chemical Co. Sodium hydroxide (NaOH), the main catalyst, was purchased from Genert Chemical Reagent Co. (Tianjin, China). Toluene-2,4-diisocyanate (TDI), the auxiliary catalyst, was purchased from Kelong Chemical Reagent Factory (Chengdu, China). GF cotton, which acts as reinforced material, was manufactured by Nanjing GF Co. The length of monofilament of GF is 60 mm.

The preparation of the GF-cotton reinforced MC-nylon is in Figure 2. Firstly, an appropriate amount of GF cotton was put in mold preheated to 170 °C. A proper quantity of caprolactam and a small quantity of carbon powder were put into a three-necked flask, and then were heated to about 130 °C. To remove water in the caprolactam, the melting caprolactam was refluxed under vacuum for about 30 min. Then a proper amount of NaOH was added into the melting caprolactam to promote the ring-opening reaction. After refluxing the melt for another 30 min, TDI (0.6 wt% of the melting caprolactam) was added to the caprolactam. Thirdly, the melt was cast into the mold filled with GF cotton, Figure 2 (left and center), and the mold cavity was enclosed with a punch, Figure 2 (right). The caprolactam was polymerized for 20 min. The composite was then obtained and ejected from the mold. A composite plate prepared by this technology is shown in Figure 2 (bottom).

Cut from the composite plate, the specimen is shown in Figure 3 (right). The width (D) and length of the specimen is respectively 50 mm and 80 mm, and the thickness of this plate is 1 mm, as shown in Figure 3 (left). The ends of the specimens act as gripped ends. The hole is drilled in the center of the specimens by a drilling machine. To investigate the effect of hole diameter on the SCF, the hole diameter is drilled as 2 mm, 3 mm, 4 mm, 5 mm, 6 mm, 7 mm, 8 mm, 9 mm, 10 mm, and 12 mm, respectively. All the holes are not drilled in different composite plates, but are successively drilled in the same plate. Therefore, the influence of the composite property on SCF may be avoided. Due to

Figure 1. GF cotton and nondirectional fibers. Left: GF cotton. Center: GF bundle. Right: GF in composite.
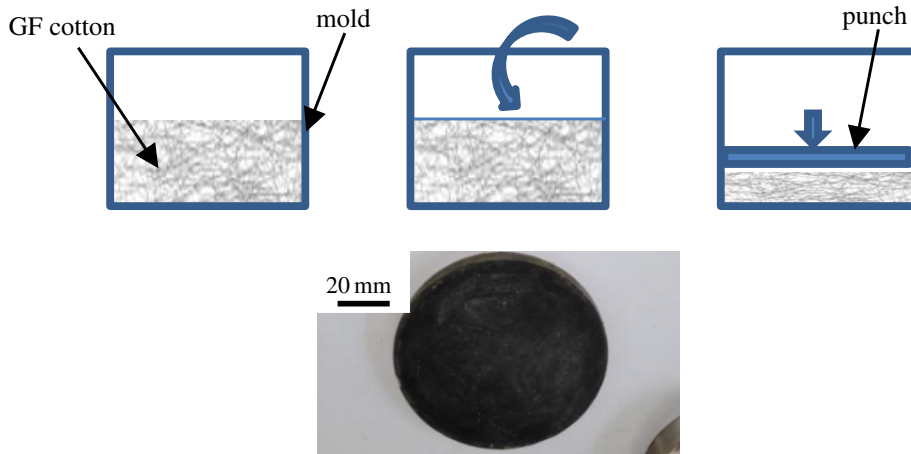
Figure 2. Preparation of GF cotton reinforced MC-nylon. Top: GF cotton in mold, pouring MC-nylon, and polymerizing. Bottom: GFCR MC-nylon plate.
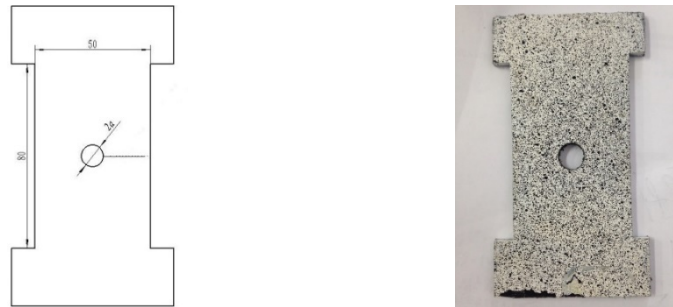
Figure 3. Experimental specimen. Left: specimen size (mm). Right: painted specimen.

the plate's thickness being 1 mm, and the fact that the minimum diameter of circular hole is 2 mm, the state of stress is approximately plane stress under simple tension conditions. Certainly, the state of stress is close to plane stress while the diameter of the circular hole increases. The DIC technique relies on contrasting patterns on the surface of the measured specimen. The color of the composite plate is black, therefore, the specimens should be painted with white and black paint subsequently, and this is shown in Figure 3 (center). The specimen preparation is as follows. Firstly, white paint is painted on the surface of the specimen. Then, tiny black paint-drops are evenly painted on the surface of the specimen. The maximum diameter of the black paint-drops is less than 0.2 mm.

In general, the SCF of a circular hole in an infinite plate is different from that in a finite plate. In other words, SCF is influenced by the ratio of plate width to circular hole diameter ($D/2a$). However, for an isotropic plate, the research reveals that the finite plate can be viewed as an infinite plate on the condition that $D/2a$ is more than 4 [Tan 1988]. In this study, the minimum $D/2a$ of the specimen is 4.16. Therefore, the specimen with a circular hole can be viewed as an infinite plate and it is not necessary to take the effect of $D/2a$ on SCF into account.
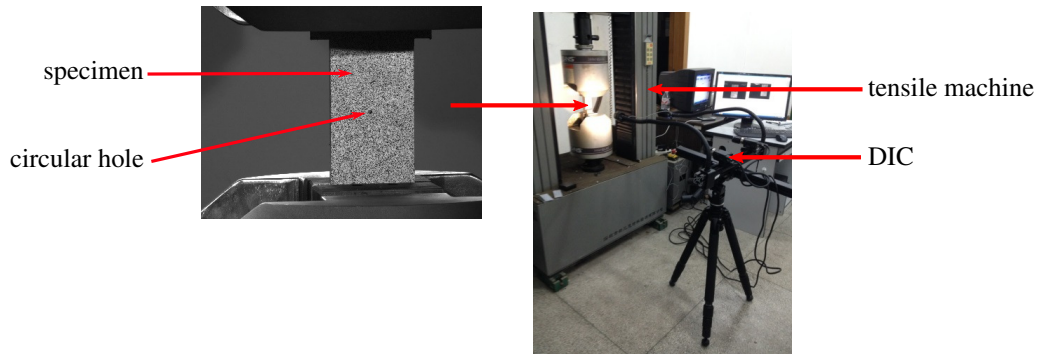
Figure 4. Experimental equipment.

3. Experimental equipment and procedure

DIC has been applied in many industrial areas, such as the automobile and aviation industries. DIC uses video cameras to record images on the surface of the testing specimen, stores them in digital form, and performs image analysis to extract the full-field shape, deformation, and motion measurements with the help of many types of object-based patterns, including lines, grids, dots, and random arrays. In this work, the authors use DIC to measure the strain field of a composite plate. The DIC system used in this investigation is named noncontacting full-field strain measurement system-VIC3D, which is manufactured by Correlated Solutions Inc. of the United States. The measuring length range of this DIC system is from 0.8 mm to 50 m, and the measuring strain range is from 0.001 to 20.

The DIC equipment and the specimens are shown in Figure 4. The composite specimen is clamped in the clamping chuck of the testing machine. The aim of this article is to investigate the SCF of the composite plate under elastic conditions. Therefore, the maximum stress loaded on the specimen is no more than 15 MPa, which is much less than the yield stress of 80 MPa for this composite. Moreover, the tensile loading applied to the specimen is adjusted according to the diameter of circular hole to ensure that the maximum stress in all experiments is identical. In this experiment, the frequency of taking pictures for DIC is set as 120 pictures per minute and the loading rate is set as 40 N/s, which indicates that loading is nearly quasistatic.

4. Experimental results and discussion

4.1. *Effect of diameter of circular hole on SCF.* A strain nephogram indicates the value of strain by color. Two strain nephograms of the composite specimen are shown in Figure 5, in which the strain along the loading direction ε_y is indicated by a different color. The maximum and minimum strains are displayed in red and burgundy, respectively. It can be seen from Figure 5 (left) that the strain of the specimen has approximate bilateral symmetry in space. Both the right and left sides of the circular hole in the strain nephogram are colored by red, especially near the edge of hole, which indicates that the deformation concentration is high in this area. In other words, the stress concentration first emerges near the edge of circular hole, while the strain concentration gradually disappears far away from the edge of hole. To evaluate the stress concentration of the circular hole, the strain values are extracted along the
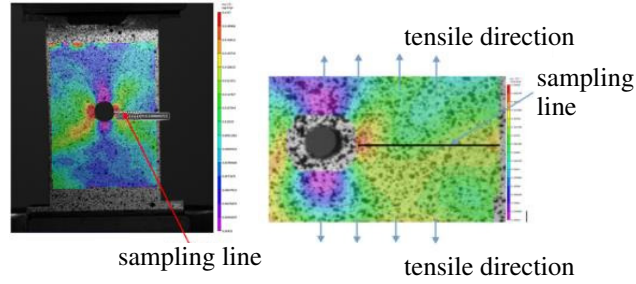
Figure 5. Strain nephogram around hole. Left: strain nephogram. Right: local strain nephogram.
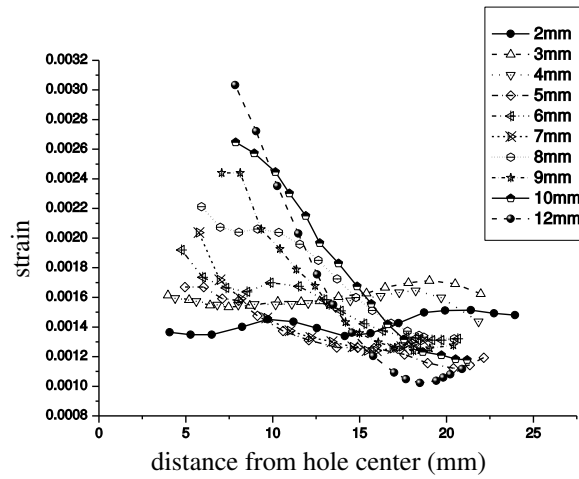

Figure 6. Strain distribution around circular hole.

horizontal sampling line shown in Figure 5, and are listed in Figure 6, in which the x-axis represents the distance from the central point to the sampling point and the y-axis indicates the corresponding strain. Intuitively, the fluctuation of strain curves is small when the diameter of the circular hole is less than 4 mm. In other words, the strain along the sampling line is almost even and the stress concentration is inapparent in this case. As the diameter of the whole increases, the strain near the hole edge increases, which leads to the slope of the strain curve to increase. Therefore, the stress concentration becomes more and more obvious.

Hole-edge stress concentration may be represented by SCF, which is the maximum stress of the hole edge divided by the average stress. For isotropic metal materials, the tangential direction tensile-stress distribution around the hole edge may be represented by

$$\sigma_\rho^m = \frac{\sigma^0}{2}\left(1 + A\frac{a^2}{\rho^2} + \left(1 + B\left(\frac{4a^2}{\rho^2} - \frac{3a^4}{\rho^4}\right)\right)\cos 2\varphi\right), \tag{1}$$

where σ_ρ^m represents the tangential direction tensile-stress, σ^0 stands for the nominal stress, a is the radius of the circular hole, ρ represents the distance from the measured point to the center of the hole, and φ is the deviation angle from tensile direction. In (1), σ_ρ^m reaches its maximum value when φ is $90°$.
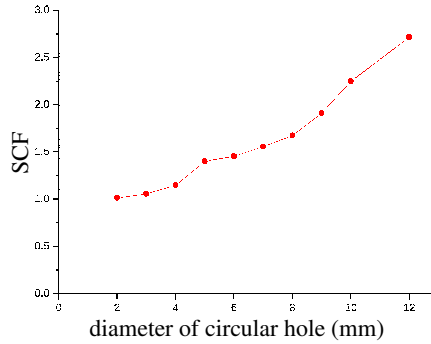
Figure 7. Experimental SCF of the composite.

In (1), A and B are determined by

$$A = \frac{(1 - v^m - 2(v^m)^2)E^f - (1 - v^f - 2(v^f)^2)E^m}{E^f(1 + v^m) + E^m(1 - v^f - 2(v^f)^2)}, \tag{2}$$

$$B = \frac{E^m(1 + v^f) - E^f(1 + v^m)}{-E^m(1 + v^f) + E^f(-3 + v^m + 4(v^m)^2)}, \tag{3}$$

in which E^m and E^f are respectively the elastic modulus of the resin and the fiber, and v^m and v^f are the volume fraction of the resin and the fiber, respectively. Therefore, (1) shows that the SCF is not only determined by the constituent original properties, but also by the composite geometric parameters such as the fiber volume fraction.

For the GF cotton reinforced MC-nylon, E^m and E^f are 3 GPa and 80 GPa respectively; v^m and v^f are 0.85 and 0.15 respectively. Therefore, while a is equal to ρ, the maximum SCF calculated from (1) is about 1.9.

In this paper, we define the maximum SCF for the composite just as in an isotropic plate; namely, as the maximum stress of the hole edge divided by the average stress. Then we calculate the maximum SCF of the composite from Figure 6 and list the SCF in Figure 7, which shows that the maximum SCF of the composite increases as the diameter of the circular hole increases. The maximum SCF is between 1.012 and 2.726, which is different from 1.9, as calculated by (1). Therefore, the experimental results show that (1) is not suitable for calculating the SCF of this composite. This may be caused by the influence of the diameter of circular hole and the length of GF.

As shown in Figure 1 and Figure 8 (left), the GF in this composite is bent and tangled up, which constitutes a fiber network. Under tension stress, the GF around the circular hole acts as "rebar". The GF network reinforces the matrix and transmits the strain far away from the hole edge. Compared to the stiffness of matrix, the stiffness of GF is higher. Therefore, the GF network in the composite acts as "anchoring" and "tangling", which alleviates the strain concentration near the hole edge and decreases the SCF. Moreover, the experimental results show that the maximum SCF of this composite is more than that calculated by (1).

Unidirectional fiber-reinforced composites have been widely applied in industries, and it's maximum SCF of a circular hole may be much more than that in the isotropic case. For example, the maximum SCF of a typical unidirectional carbon-fiber-reinforced composite is 9.37 [Liu and Tang 2016], which
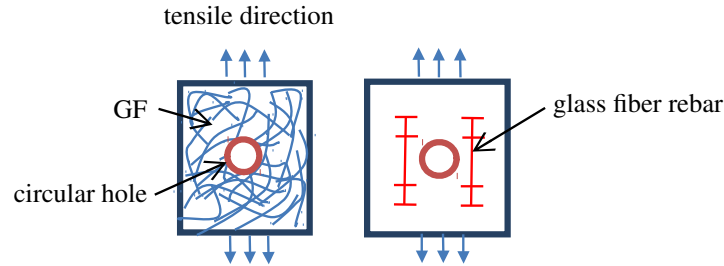
Figure 8. Anchoring (left) and tangling (right) of fiber network.

indicates that the stress concentrates around the hole edge seriously. Although the length and strength of the carbon fiber in [Liu and Huang 2014] is much higher than that of the GF in this composite, the SCF of the carbon-fiber-reinforced composite is much higher than that of this composite. The cause may lie in that the unidirectional fiber in composite can be viewed as "round steel" and the fibers network in composite act as rebar. It is evident that the anchoring and tangling of the fiber network alleviate the stress concentration. Therefore, the conclusion may be drawn that the length and strength of the fiber is not the sole factor in influencing the SCF of circular hole. Sometimes the distribution of fibers plays a more important role in alleviating stress concentration.

Figure 8 indicates that the maximum SCF of the composite is determined by hole size and microstructure size. On the one hand, the bigger the hole, the higher the SCF. For example, when the diameter is 2 mm, the corresponding SCF is close to 1, and the maximum SCF is 2.726 when the diameter is 12 mm. All experimental results are obtained from the same specimen and the center of all the circular holes are identical. Therefore, the influence of the material properties on the SCF can be excluded. The factors that affect the SCF are hole size and microstructure size. Microstructure size, namely the average GF length around the hole, also influences the SCF. A sketch of the distribution of GFs and the circular hole are shown in Figure 9. The length of all GFs are identical and the orientation of GFs is random. The average length of fibers around the circular hole is determined by the diameter of the circular hole. The authors developed a program to calculate the average length of the GFs around the hole, which is shown in Figure 10. It can be found from Figure 10 that the larger the diameter, the smaller the average length of GF. While the diameter of hole is 12 mm, the average length of the GF decreases from 60 mm to 55 mm. The average length of GF is approximately negative linear with the diameter of circular hole.
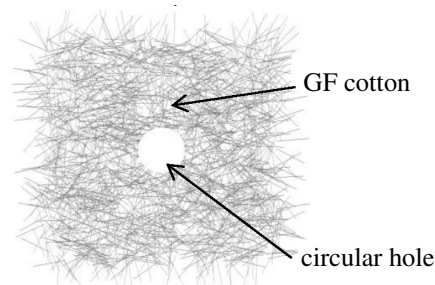
Figure 9. Circular hole and random distribution of GFs.
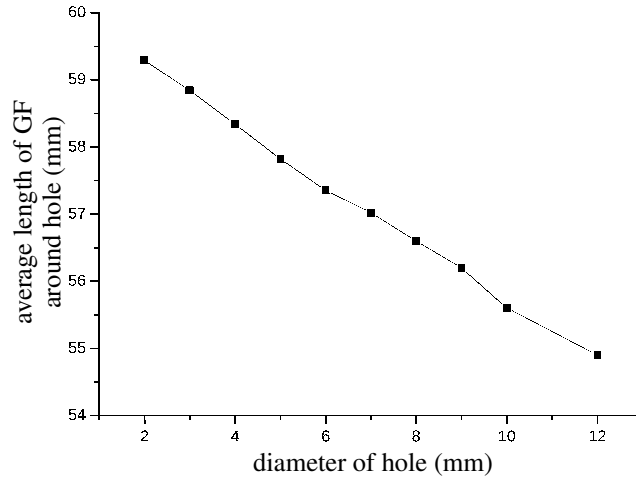
Figure 10. The average length of fibers around the circular hole.

As the average length of the GFs reduce, the effect of anchoring and tangling weakens. Therefore, the stress concentrates near the hole edge and the SCF increases. Moreover, the integrity of the GF network weakens as the diameter of the circular hole increases. In a word, the integrity of the GF network and the average length of the GF around circular hole influence the SCF, and the SCF of the composite is determined by hole size and GF size.

4.2. *Effect of stress intensity on SCF.* Generally, SCF is unrelated to the stress σ^0, as shown in (1). However, the experimental results show that the SCF of this composite is related to the stress σ^0. With the help of the DIC system, the authors recorded the strain around circular hole under different stress intensities (3 MPa, 5.5 MPa, 8 MPa, and 10 MPa). The SCF under different stress intensities and different diameters of the circular hole is shown in Figure 11. On the whole, for all circular holes, the higher the stress, the lesser the SCF. For example, the SCF of the 10 mm circular hole decreased from 2.92 to 2.34 (about 20%), while the stress increased from 3 MPa to 10 MPa.
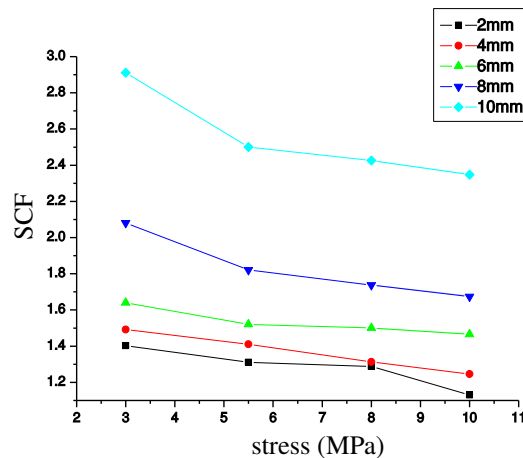
Figure 11. SCF under different nominal stresses.

In our knowledge, the SCF of the circular hole edge is unrelated to the nominal stress under static loads for isotropic composites. The authors advocate that both the material construction of the composite and the distribution of the GF influence the SCF under static load. As opposed to a single phase material such as metal, the composite consists of two phases: the matrix phase MC-nylon and the reinforced phase GF. The mechanical properties of the reinforcing material GF is much different from that of MC-nylon. For example, the modulus of elasticity of MC-nylon is about 3 GPa, which is much less than that of GF, which is 80 GPa. Therefore, under the same stress, the deformation of the soft matrix phase is much larger than that of rigid GF. Under the action of axial loading, the MC-nylon around the bilateral of the circular hole deforms first, and then the stress is transmitted to the reinforced phase. At the same time, the reinforced phase works faintly under low stress intensity. In other words, the concentrated strain of the matrix around the hole edge is hardly transmitted from the hole edge. Therefore, the strain concentrates around the hole edge and the SCF is high. When the nominal stress increases, the reinforced phase works and the strain concentration around the hole edge weakens, which leads to a decrease of SCF.

Also, Figure 11 shows that the reduction of SCF varies with the diameter of the hole. The reduction ratios of the SCF for 2 mm, 4 mm, 6 mm, and 8 mm circular holes are 19.2%, 16.8%, 14.9%, 19.7%, respectively. The average GF length and the integrality of GF network around the circular hole may play an important role in the reduction of the SCF. The smaller the diameter of circular hole, the longer the average GF length and the better the integrality of the GF network. In other words, the reinforced phase works effectively regardless of the nominal stress. Therefore, the SCF of the 2 mm circular hole is the minimum regardless the stress intensity.

5. Finite element analysis

5.1. *Finite element model.* The reason why the commercial FEM code is not suited to analyze the influence of the length and proportion of the fibers on stress concentration is illustrated in Section 1. It is necessary to suggest a novel method to simulate the stress concentration of a circular hole for this composite. The core idea of this simulation model is that the matrix phase and reinforced phase in this composite are assigned different material properties respectively. Moreover, the GF is simplified as a bar and its distribution is random. In this composite, the diameter of the GF is 13 microns and the number of GFs is massive, which may lead to the number of elements in the simulation model being extremely massive. Therefore, the authors simplify the GF as a bar with a square cross section. The side length of the square cross section is 0.8 mm, and the length of the bar is identical to the GF length. It is noted that the volume fraction of the GF in this simulation model is identical to that of the 21% composite. In this FEM model, the Solid185-type element is applied to mesh the MC-nylon and the GF. First, the GF is meshed with the element size 0.4 mm. Then the MC-nylon is meshed with the adaptive element, and the interface elements between the MC-nylon and GF are coincided.

The geometric modeling is as follows. The first step is to construct the geometric model of GF through the loop statement in the APDL language. The GF bars are confined within a cuboid. Length, width, and thickness of the cuboid are respectively 80 mm, 50 mm, and 5 mm, which is identical to the dimensions of the specimen. The distribution of the GF is random and uniform in the matrix. To investigate the influence of GF length on the SCF, the GF length are 13 mm, 26 mm, 38 mm, and 60 mm, respectively. For example, the GF length in Figure 13 is 13 mm. The number of GF bars depends on the volume of
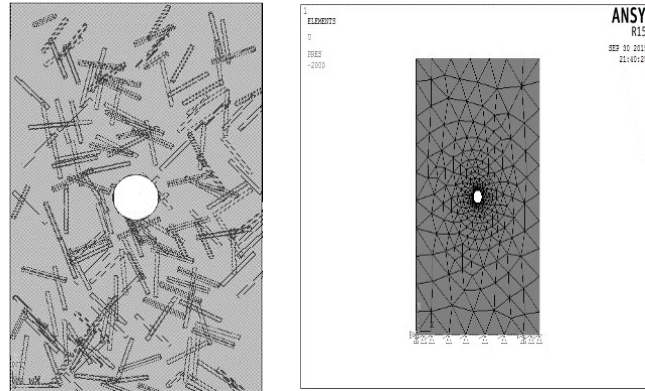
Figure 12. The geometric model (left) and finite element model (right).

a single GF bar and the volume fraction of the GF in the composite. The second step is to construct the geometric model of the matrix, and the volume of GF bars is removed from the cuboid by Boolean operation. It is noted that the dimension of the cuboid is the same as that of the specimen, and the diameter of the circular hole varies from 2 mm to 12 mm. Figure 12 (left) shows this model and the random distribution of GFs.

The matrix and GF are meshed sequentially by the element type Solid185. The element size for the GF is 0.4 mm. Then the matrix elements and the GF elements are combined with the linkage of nodes, shown in Figure 12 (right). The bottom edge of the model is fixed, and a load of 2000 N is applied to the upper side nodes. The boundary condition and load applied on the finite model is identical to that in the experiment.

5.2. *Results and discussion.* The simulation results obtained from the above simulation model are shown in Figure 13. Firstly, the simulated SCF and the experimental SCF are compared when the GF length is
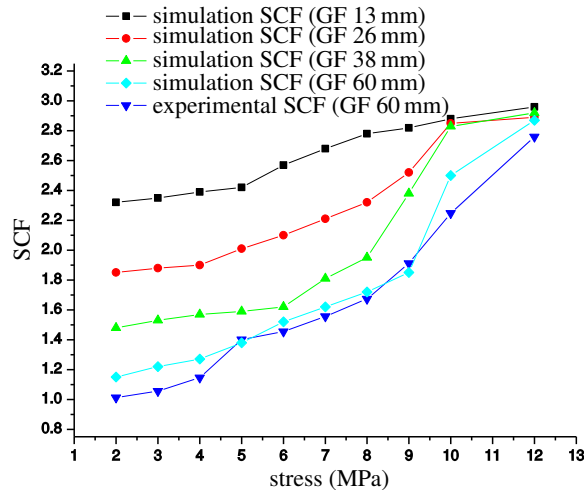
Figure 13. Simulation results.

60 mm. Although the former value is a bit more than the latter one as a whole, the average difference between the two SCFs is only 5.6%. Therefore, it is consistent between the experimental SCF and the simulation results. Figure 13 also shows that the shorter the GF in the composite, the larger the SCF. The average SCF for the composite with 38 mm, 26 mm, and 13 mm long GFs is 1.97, 2.25, and 2.62 respectively. Moreover, Figure 13 indicates that the gradient of SCF curves decreases as the GF shortens. For example, when the GF length is 13 mm, the SCF increases from 2.32 to 2.96 and the corresponding variation of the SCF is 21.6%. For 60 mm GF, the SCF raises from 1.14 to 2.76 and the corresponding variation of the SCF reaches 58.6%. It may be that the "anchoring" and "tangling" of the fiber network weakens as the GF shortens, and the strain concentrates around the edge of circular hole. Moreover, it can be easily seen that the SCF is close to 3 while the diameter of circular hole is 12 mm regardless of GF length. This may be induced by the decrease in the average length of the GF and the weakening of anchoring and tangling, which has been discussed in Section 2.

For the isotropic plate without fiber reinforcement, the SCF of the circular hole is 3 and is unrelated to the diameter of the circular hole. In other words, the corresponding SCF curve is a horizontal line because there is no anchoring or tangling of fiber network. When the GF length in this composite is close to zero, the composite is similar to the isotropic plate without fiber reinforcement. It is obvious that the simulation results shown in Figure 13 are rational. Therefore, the SCF of the circular hole of the composite is related to both the diameter of the circular hole and the GF length.

6. Conclusion

In this paper, a novel composite named as glass-fiber-cotton reinforced MC-nylon is prepared and the stress concentration of a circular hole of this composite is investigated with the digital image correlation technique. The experimental results show that the maximum SCF of the composite increases as the diameter of circular hole increases. Also, the higher the stress intensity, the lesser the SCF. Moreover, a novel simulation model to investigate the SCF of this material is suggested, showing that the shorter the GF in composite, the larger the SCF. In a word, the SCF of this composite is influenced by the GF length, the stress intensity, and the diameter of the circular hole.

References

[Aparna et al. 2015] M. L. Aparna, G. Chaitanya, K. Srinivas, and J. A. Rao, "Fatigue testing of continuous GFRP composites using digital image correlation (DIC) technique a review", *Materials Today: Proceedings* **2**:4-5 (2015), 3125–3131.

[Bao and Liu 2016] H. Bao and G. Liu, "Progressive failure analysis on scaled open-hole tensile composite laminates", *Compos. Struct.* **150** (2016), 173–180.

[Cheng and Chen 1988] S. Cheng and D. Chen, "On the stress distribution in laminae", *J. Reinf. Plast. Compos.* **7**:2 (1988), 136–144.

[Ghasemi and Razavian 2012] A. R. Ghasemi and I. Razavian, "Measurement of variation in fracture strength and calculation of stress concentration factor in composite laminates with circular hole", *J. Solid Mech.* **4**:3 (2012), 226–236.

[Hao et al. 2015] A. Hao, L. Yuan, and J. Chen, "Notch effects and crack propagation analysis on kenaf/polypropylene nonwoven composites", *Compos. A Appl. Sci. Manuf.* **74** (2015), 11–19.

[Jadee and Othman 2015] K. Jadee and A. R. Othman, "Analysis of stress mitigation through defence hole system in GFRP composite bolted joint", *Am. J. Mech. Eng.* **3**:4 (2015), 126–134.

[Khoroshun and Kabysh 2007] L. P. Khoroshun and Y. M. Kabysh, "Gradient model in the problem of stress-concentration around a circular hole in two-component stochastic composites", *Int. Appl. Mech.* **43**:12 (2007), 1336–1346.

[Lekhnitskii et al. 1968] S. G. Lekhnitskii, W. S. Tsai, and T. Cheron, *Anisotropic plates*, Gordon and Breach Science Publishers, New York, 1968.

[Liu and Huang 2014] L. Liu and Z. Huang, "Stress concentration factor in matrix of a composite reinforced with transversely isotropic fibers", *J. Compos. Mater.* **48**:1 (2014), 81–98.

[Liu and Tang 2016] G. Liu and K. Tang, "Study on stress concentration in notched cross-ply laminates under tensile loading", *J. Compos. Mater.* **50**:3 (2016), 283–296.

[Maximyuk et al. 2014] V. A. Maximyuk, E. A. Storozhuk, and I. S. Chernyshenko, "Stress state of flexible composite shells with reinforced holes", *Int. Appl. Mech.* **50**:5 (2014), 558–565.

[Moure et al. 2016] M. M. Moure, S. K. García-Castillo, S. Sánchez-Sáez, E. Barbero, and E. J. Barbero, "Influence of ply cluster thickness and location on matrix cracking evolution in open-hole composite laminates", *Compos. B Eng.* **95** (2016), 40–47.

[Pandita et al. 2003] S. Pandita, K. Nishiyabu, and I. Verpoest, "Strain concentrations in woven fabric composites with holes", *Compos. Struct.* **59**:3 (2003), 361–368.

[Paul and Rao 1995] T. K. Paul and K. M. Rao, "Finite element stress analysis of laminated composite plates containing two circular holes under transverse loading", *Comput. Struct.* **54**:4 (1995), 671–677.

[Savruk and Kazberuk 2007] M. P. Savruk and A. Kazberuk, "A unified approach to problems of stress concentration near V-shaped notches with sharp and rounded tip", *Int. Appl. Mech.* **43**:2 (2007), 182–197.

[Tan 1988] S. C. Tan, "Finite-width correction factors for anisotropic plate containing a central opening", *Compos. Mater* **22** (1988), 1080–1097.

[Toubal et al. 2005] L. Toubal, M. Karama, and B. Lorrain, "Stress concentration in a circular hole in composite plate", *Compos. Struct.* **68**:1 (2005), 31–36.

[Wang et al. 2013] S. B. Wang, B. Teng, and S. Zhang, "Torsional wear behavior of monomer casting nylon composites reinforced with GF: effect of content of GF", *Tribology Trans.* **56** (2013), 178–186.

[Wu and Mu 2003] H.-C. Wu and B. Mu, "On stress concentrations for isotropic/orthotropic plates and cylinders with a circular hole", *Compos. B Eng.* **34**:2 (2003), 127–134.

[Xu et al. 2013] S. Xu, X. Zhao, and L. Ye, "Mechanical and crystalline properties of monomer casting Nylon-6/SiO_2 composites prepared via in situ polymerization", *Polym. Eng. Sci.* **53**:9 (2013), 1809–1822.

[Zhang et al. 2012] S. Zhang, C. Cui, and G. Chen, "Tribological behavior of MC Nylon6 composites filled with glass fiber and fly ash", *J. Wuhan Univ. Technol.-Mat. Sci. Edit.* **27**:2 (2012), 290–295.

YOU RUI TAO: taoyourui@hebut.edu.cn
State Key Laboratory of Reliability and Intelligence of Electrical Equipment, Hebei University of Technology, Tianjin, China

NING RUI LI: 316470923@qq.com
College of Mechanical Engineering, Hebei University of Technology, tianjin, China

XU HAN: xhan@hebut.edu.cn
College of Mechanical Engineering, Hebei University of Technology, Tianjin, China

ELASTIC MODULI OF BORON NITRIDE NANOTUBES BASED ON FINITE ELEMENT METHOD

HOSSEIN HEMMATIAN, MOHAMMAD REZA ZAMANI AND JAFAR ESKANDARI JAM

Boron nitride nanotubes (BNNTs) possess superior thermal conductivity and mechanical/electrical properties, and are a suitable and favourable reinforcement for binanocomposites. Experimental studies on nanoscale materials are time-consuming, costly, and require accurate implementation. Therefore, a three-dimensional finite element (FE) model of a space-frame structure is proposed for BNNTs, which is based on molecular structural mechanics. The effects of length, chirality, diameter, and defect on the elastic moduli of BNNTs are investigated. The results show that defects in the nanotubes decrease the mechanical properties. The values of the Young's modulus and shear modulus of BNNTs without defects change from 1.022 TPa to 1.042 TPa and from 0.33 TPa to 0.536 TPa, respectively. It is found that, with increasing chirality and radius of BNNTs, the Young's modulus and shear modulus increase. As the length of zigzag and armchair BNNTs increases, the Young's modulus increases and the shear modulus decreases. Also, it was observed that by using the finite element method (FEM) based on molecular dynamics, one can accurately determine the mechanical properties of BNNTs. The results demonstrate that the proposed FE model is a valuable tool for studying the mechanical behaviour of BNNTs.

1. Introduction

Rubio et al. [1994] theoretically predicted boron nitride nanotube (BNNT). Then, Chopra et al. [1995] synthesized double-walled boron nitride nanotube (DWBNNT), and afterwards single-walled boron nitride nanotube (SWBNNT) was produced by arc discharge [Loiseau et al. 1996] and chemical substitution reactions [Golberg et al. 1999]. Over the past two decades, BNNTs have attracted researchers attention in different fields due to their novelty and superlative mechanical [Chen et al. 2004b; Griebel and Hamaekers 2007; Vaccarini et al. 2000], electrical [Khoo et al. 2004; Chen et al. 2004a; Ishigami et al. 2005; Terrones et al. 1996], and chemical properties [Golberg et al. 2001].

Similar to carbon nanotubes (CNTs), a BNNT can be imagined as rolled up hexagonal BN layers and have different types chirality, as well as zigzag and armchair configurations [Chopra et al. 1995]. BNNTs, like CNTs, have extraordinary mechanical properties [Hernández et al. 1998; Chopra and Zettl 1998], high thermal conductivity along the nanotube length [Chang et al. 2005], and good resistance to oxidation at high temperature [Chen et al. 2004b]. Despite their similar structures, BNNTs have different properties because of their different atoms [Fereidoon et al. 2015]. CNTs show a metallic, semiconductor, or insulator characteristic depending on chirality and diameter, while BNNTs, independent of their chirality, diameter, and number of walls, behave as an insulator for low electric fields [Khaleghian and Azarakhshi 2016; Molani 2017].

In addition, BNNTs are better able to store hydrogen compared to CNTs and have found many applications in hydrogen storage [Wu et al. 2004]. BNNTs are also nontoxic to health and environment due to their chemical inertness and structural stability. Therefore, BNNTs are particularly suitable for biological employment [Zhi et al. 2005].

The elastic properties of BNNTs have theoretically and experimentally been investigated. Slightly different results were presented, but all calculated values indicate a very high Young's modulus (note that it is slightly smaller than for CNTs), which has led to their use as a structural reinforcement of matrix materials [Zhi et al. 2010]. Polymer nanocomposites combining polymers and nanofiller components have attracted research attention from the academic and industrial communities due to their diverse functional applications, good processing, and relatively low cost [Mehar et al. 2017b; 2018].

First-principles [Bahrami Panah and Vaziri 2015], tight-binding [Hernández et al. 1998], density functional [Mirzaei and Salamat Ahangari 2016], and classical molecular mechanics [Li and Chou 2006] approaches have been performed to characterize the properties of BNNTs. By using thermal vibration amplitude analysis, Chopra and Zettl [1998] estimated 1.22 TPa ± 0.24 TPa for the Young's modulus of multiwalled boron nitride nanotubes (MWBNNTs). Hernández et al. [1999] employed the tight-binding method to obtain 862 GPa–940 GPa for the axial Young's modulus of BNNTs. Verma et al. [2007] obtained the axial Young's modulus of the zigzag and armchair BNNTs using the tight-binding method. They also observed that the Young's modulus of zigzag tubes is higher than for armchair ones.

Akdim et al. [2003] indicated that the Young's modulus of BNNTs is in range of 0.71 TPa–0.83 TPa and is slightly dependent on the tube diameter. Also, theoretically, Young's modulus has been predicted to be 1.2 TPa [Hernández et al. 1998; 1999].

The Young's modulus of DWBNNT was calculated by Fakhrabad and Shahtahmassebi [2013] using the ab initio calculations based on density functional theory (DFT), and their estimated value is 821 GPa and 764 GPa for (2, 2) @ (7, 7) and (2, 2) @ (9, 9), respectively. The Young's modulus of SWBNNTs with vacancy and functionalization defects was calculated by Gerieble and Hamaekers [Griebel et al. 2009] using a molecular dynamics (MD) simulation. They found that Young's modulus decreases with increasing defect concentration. Furthermore, for functionalized BNNTs, they reported no significant decrease with increasing functionalization [Santosh et al. 2009].

The experimental value of Young's modulus of BNNTs is reported to be 1.1 TPa–1.3 TPa [Bettinger et al. 2002]. In another experimental effort, Wei et al. [2010] obtained the value of 895 GPa for the Young's modulus of MWBNNT. Suryavanshi et al. [2004] applied the electric-field-induced resonance method and specified the Young's modulus as 0.8 TPa. Golberg et al. [2007] used an integrated TEM-atomic force microscope (AFM) piezodriven holder to directly test the elastic modulus. The values of 0.5 TPa–0.6 TPa were found for MWBNNTs grown by the BOCVD method.

Experimental studies on nanoscale materials are time-consuming, costly, and require accurate implementation. Therefore, analytical, computational, and theoretical approaches are applied to predict the mechanical properties of nanoscale materials [Mehar et al. 2017a; 2017c; 2017d; Mehar and Panda 2017]. Two main classes of theoretical methods are the atomistic-based methods [Yakobson et al. 1996; Lu 1997; Sánchez-Portal et al. 1999] and the continuum mechanics-based ones [Li and Chou 2003; Chang and Gao 2003; Odegard et al. 2002]. A three-dimensional finite element (FE) model, named as the space-frame model, is used to study the mechanical behaviour of BNNTs. Ansari et al. [2015] used DFT calculations to obtain accurate force constants which are employed when determining element properties.

Fundamental to these approaches, BNNTs are considered as geometrical space-frame structures. Therefore, BNNTs can be analysed by classical structural mechanics. In this paper, the effects of length, chirality, diameter, and defect on the elastic moduli of BNNTs are studied. While this method is conceptually simple and computationally efficient, our results indicate that its computational accuracy is comparable to that of more refined methods such as first-principle and tight-binding methods. Our study has clearly demonstrated the dependency of Young's modulus and shear modulus of BNNTs on tube length, chirality, and radius.

2. FE modelling

2.1. *Atomic structure of BNNTs.* The atomic structure of BNNTs depends on chirality, which is defined by the chiral vector $\vec{C}_h$ and the chiral angle θ. The chiral vector $\vec{C}_h$ can be defined in terms of the lattice translation indices (n, m) and the basic vectors $\vec{a}_1$ and $\vec{a}_2$ of the hexagonal lattice as [Hemmatian et al. 2014]

$$\vec{C}_h = n\vec{a}_1 + m\vec{a}_2. \tag{1}$$

The chiral angle θ is the angle between the chiral vector $\vec{C}_h$ with respect to the zigzag direction $(n, 0)$ where $\theta = 0°$. For the chiral angles of 0° and 30°, the armchair and zigzag nanotubes are formed, respectively. In terms of the roll-up vector, the armchair nanotubes are defined by (n, n) and the zigzag nanotubes by $(n, 0)$. For chiral angles different from 0° and 30°, the chiral nanotubes, which are defined by a pair of indices (n, m), where $n \neq m$, are formed. Schematic representations of the three types of nanotubes are shown in Figure 1.

2.2. *Modelling.* BNNTs atoms are bonded together with covalent bonds forming a hexagonal lattice. These bonds have a characteristic bond length and bond angle in the 3D space. The displacement of individual atoms under an external force is constrained by the bonds. Therefore, the total deformation of the nanotube is the result of the interactions between the bonds. By considering the bonds as connecting load-carrying elements, and the atoms as joints of the connecting elements, BNNTs may be simulated as space-frame structures and their mechanical behaviour can be analysed using classical structural mechanics. The 3D FE model is developed using the ANSYS commercial code to assess the mechanical properties of BNNTs.

(10, 0)   (10, 10)   (10, 5)
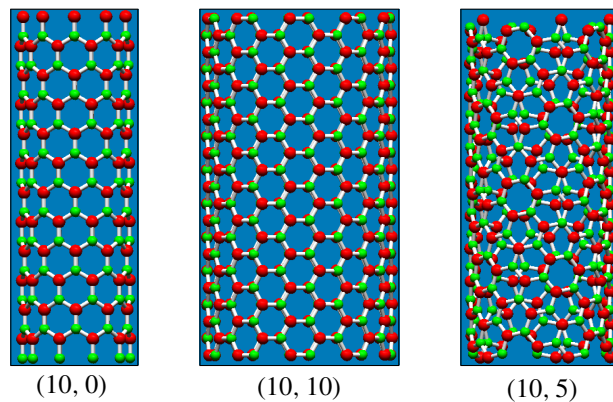
Figure 1. Schematic diagram of zigzag (10, 0), armchair (10, 10), and chiral (10, 5) nanotubes.

nanotube diameter, d	$1.648\,\text{Å}$
cross-sectional area, A	$2.132\,\text{Å}^2$
length of boron-nitrogen bond, l	$1.45\,\text{Å}$
polar inertia momentum, I_{xx}	$0.7250\,\text{Å}^4$
inertia momentum, $I_{zz} = I_{yy} = I$	$0.3625\,\text{Å}^4$
Young's modulus, E	$4.2155 \cdot 10^{-8}\,\text{N/Å}^2$
shear modulus, G	$4.9437 \cdot 10^{-9}\,\text{N/Å}^2$

Table 1. The properties of beam elements for a real BNNT [Ansari et al. 2015].

To model a BNNT, it is necessary to create atomic coordinates in the form of a keypoint or node and connecting atoms by a line or element. One of the possible outputs of the Nanotube Modeller software is the PDB, which specifies the coordinates of each atom as x, y, and z, and also identifies the connected atoms. But this output is not understandable for ANSYS, which is an APDL programming language. To convert the output file of the PDB format into an APDL language, Python interface programming software is used. A brief program in Python is written for each atom of carbon, a point with coordinates x, y, and z, and for each atomic connection, which creates a line between the two points. The 3D elastic BEAM4 element is used for meshing linens and modelling bonds. This element is a uniaxial element with tension, compression, torsion, and bending capabilities. It has six degrees of freedom at each node: translations in the nodal x-, y-, and z-directions and rotations about the nodal x-, y-, and z-axes. The element is defined by two or three nodes as well as its cross-sectional area, two moments of inertia, two dimensions, and the material properties. For the automatic generation of the BN bonds elements, a routine was created using the ANSYS macrolanguage.

2.3. *Atomic properties of beam elements.* Molecular structural mechanics (MSM) along with FEM is used for modelling. MSM is a moderately new technique for the mechanical modelling of nanostructures [Li and Chou 2003]. Covalent bonds are modelled with beam elements as they form only at certain intervals among atoms and act linearly. The properties of these elements are obtained by linking the potential energy of bonds (from a chemical point of view) and the strain energy of mechanical elements (from a mechanical point of view). To represent the covalent bond between boron and nitrogen atoms, a circular beam of length l, diameter d, Young's modulus E, and shear modulus G was considered. To obtain the properties of this model, a linkage between the molecular mechanics and the density functional theory is constructed [Ansari et al. 2015]. The required properties of the beam element are given in Table 1.

3. Calculation of elastic moduli

3.1. *Young's modulus.* The Young's modulus of a material is the ratio of normal stress to normal strain as obtained from a uniaxial tension test ($E = \sigma/\varepsilon$). Therefore, the Young's modulus of BNNT is calculated using the following equation:

$$E = \frac{FL}{\delta L\, A_0},\tag{2}$$

where F is applied force to nanotube, A_0 is the cross-sectional area, and L is the initial length. The longitudinal displacement of the nanotube δL is determined from FE analysis. A_0 is equal to πDt,
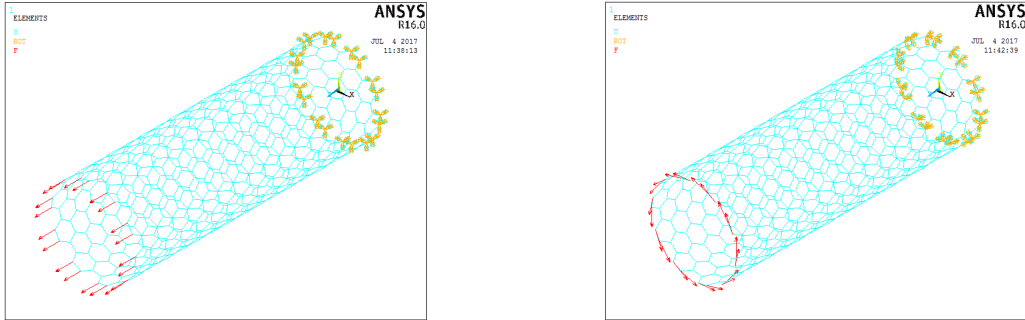
Figure 2. FE meshes of the (10, 10) nanotube with length $40\,\text{Å}$ along with the applied loading and boundary conditions: (left) tension, (right) torsion.

where D is the mean diameter of the tube and t is the nanotube thickness. The wall thickness of BNNTs has not yet been clearly specified. The wall thickness is selected as $0.34\,\text{nm}$ [Zhi et al. 2005] and the centre of the BNNT wall is placed at the midsection of the tube thickness.

In order to apply the conditions of tension, the nodes of the upper end of the BNNT have been fully built-in (zero displacement and rotation conditions), while the nodes of the bottom end, are subjected to tensile forces [Fereidoon et al. 2014]; see Figure 2 (left).

3.2. *Shear modulus.* The following relation is used for calculating the shear modulus of BNNTs:

$$G = \frac{TL}{J\theta}, \tag{3}$$

where T stands for the torque acting at the one end of the nanotube and applied by tangential forces. Here, θ and J are torsional angle and polar moment of inertia of the cross-sectional area of the BNNT, respectively. The torsional angle θ is calculated by FE analysis. J is computed by (4), considering the BNNT as a hollow tube with middiameter D and thickness t:

$$J = \tfrac{1}{32}\pi[(D+t)^4 - (D-t)^4]. \tag{4}$$

In order to apply the conditions of torsion, the nodes of the upper end of the BNNT are fully built-in (zero displacement and rotation conditions), while the nodes of the bottom end are subjected to tangential forces; see Figure 2 (right).

4. Results and discussions

The mechanical properties of BNNTs depend on their length, chirality, diameter, and defect. Several works investigated the dependence of the elastic moduli of BNNTs on their diameter and chirality. Armchair and zig-zag nanotubes are included in the investigation.

4.1. *Elastic moduli of BNNT and defected BNNT.* The elastic properties of BNNTs depend on their size and chirality. In this section, the FE model is applied to investigate the effect of chirality on the elastic moduli of regular BNNTs and defected ones. For modelling defective nanotubes, three bonds of each nanotube are omitted. Loading and boundary conditions of defected (10, 10) BNNTs with length of $40\,\text{Å}$ in tension and torsion states are shown in Figure 3 (left) and Figure 3 (right), respectively.
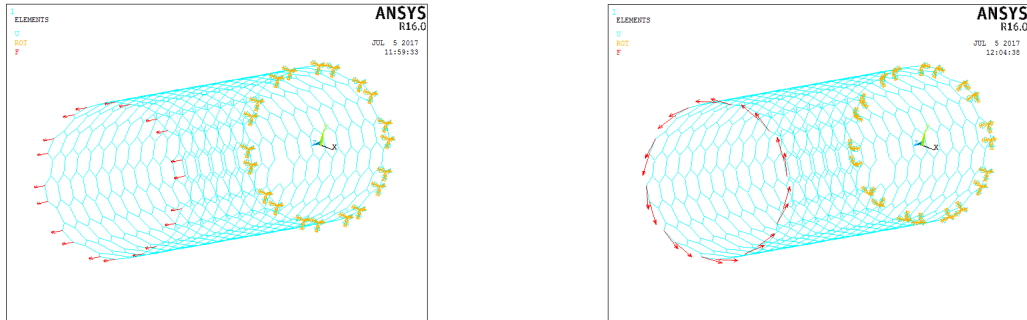
Figure 3. FE meshes of the (10, 10) defected nanotube with length 40 Å along with the applied loading and boundary conditions: (left) tension, (right) torsion.
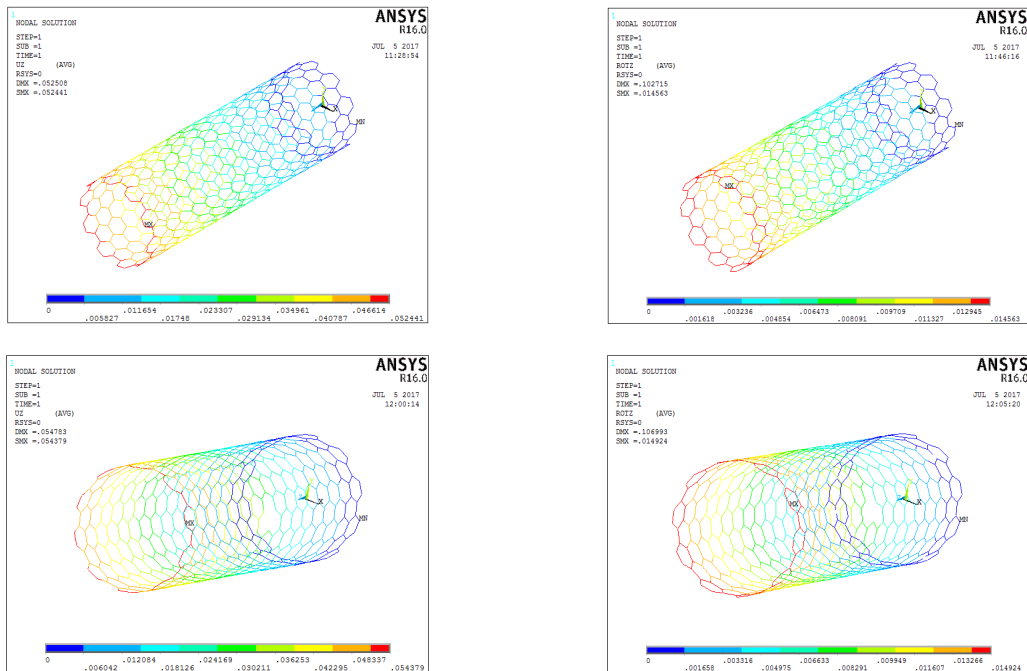
Figure 4. Deformations of a regular nanotube (top) and a defected one (bottom) under tension (left column) and torsion (right column) loading.

Deformations of nanotubes and defected nanotubes under tension and torsion loading are represented in Figure 4. As shown in Figure 4, the longitudinal and angular deformations of defected nanotubes were more pronounced than in regular nanotubes. Figure 5 shows the comparisons of the Young's and shear moduli of regular BNNTs and defected ones with length 40 Å in terms of chirality. Results show that as the chirality increases, the Young's modulus and shear modulus of the BNNT increases but the increase in Young's modulus is not considerable. The mechanical properties of the defected nanotube were lower than the nanotube with the same chirality. Also, as the chirality increases, the elastic moduli of defected BNNT increases.
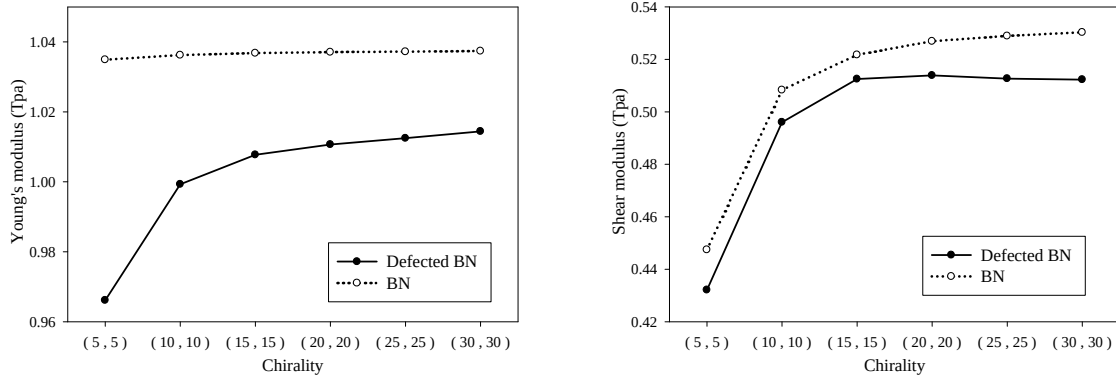
Figure 5. The elastic moduli of a regular nanotube and a defected one plotted against the chirality for $L = 40\,\text{Å}$.

elastic moduli	(TPa)	reference
Young's modulus	1.22 ± 0.24	[Chopra and Zettl 1998]
	1.022–1.112	[Fereidoon et al. 2015]
	0.71–0.83	[Zhi et al. 2010]
	0.862–0.94	[Verma et al. 2007]
	0.982–1.11	[Hernández et al. 1999]
	0.895	[Fakhrabad and Shahtahmassebi 2013]
	0.7–1.2	[Santosh et al. 2009]
	0.7–1.2	[Bettinger et al. 2002]
	1.1–1.3	[Wei et al. 2010]
	0.764–0.821	[Suryavanshi et al. 2004]
	0.7–0.9	[Zhong et al. 2001]
	1	[Chowdhury et al. 2010]
	1.034–1.037	current work
shear modulus	0.42	[Chowdhury et al. 2010]
	0.44–0.53	current work

Table 2. Elastic moduli of BNNTs from simulation and experimental works.

The Young's and shear moduli of BNNTs are archived by tension and torsion loading in the range of 1.039 TPa–1.041 TPa and 0.44 TPa–0.52 TPa, respectively. Elastic moduli of BNNT from simulation and experimental works are given in Table 2. The current results are in good agreement with simulated and experimental values.

4.2. *Young's modulus.* Zigzag nanotubes with chirality $(5, 0)$, $(10, 0)$, $(15, 0)$, $(20, 0)$, $(25, 0)$, and $(30, 0)$ and armchair nanotubes with chirality $(5, 5)$, $(10, 10)$, $(15, 15)$, $(20, 20)$, $(25, 25)$, and $(30, 30)$ were analysed under tension forces. The BNNTs have lengths of 40 Å, 60 Å, 80 Å, and 100 Å. The effects of chirality, length, and radius on the Young's moduli of BNNTs are investigated in the following:
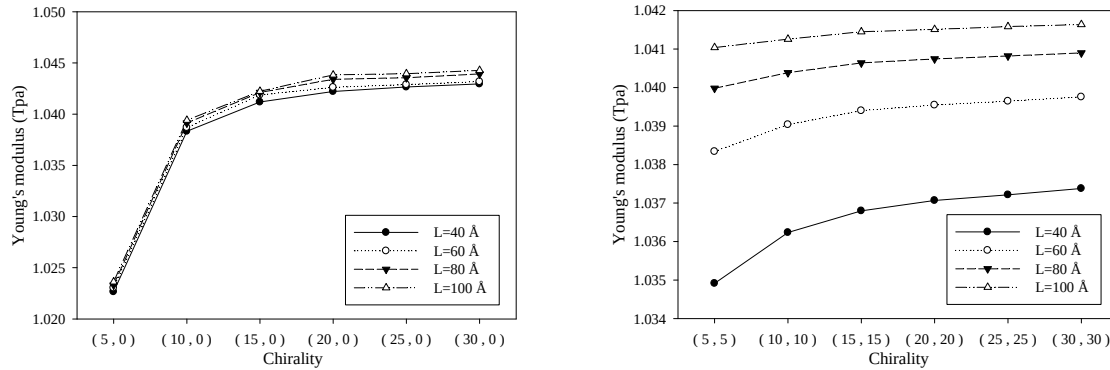
Figure 6. Young's modulus of BNNTs as a function of chirality: (left) zigzag, (right) armchair.
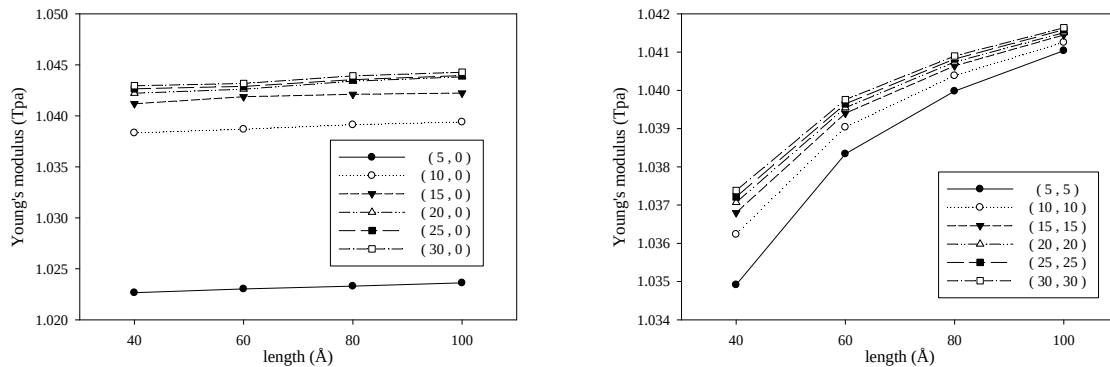
Figure 7. Young's modulus of BNNTs as a function of length: (left) zigzag, (right) armchair.

Chirality. Figures 6 (left) and 6 (right) indicate the variation of Young's modulus of zigzag and armchair nanotubes (respectively) with lengths of 40 Å, 60 Å, 80 Å, and 100 Å as a function of chirality. For armchair and zigzag nanotubes, with increasing chirality and consequently radius, the Young's modulus increases. The gradients of variations are greater in small radii, and with increasing radius, the Young's modulus tends to constant values. Moreover, the Young's moduli of zigzag nanotubes with different lengths are very close, but in armchair nanotubes, the differences are significant.

Length. Variations of Young's modulus of zigzag and armchair nanotubes with respect to length are plotted in Figures 7 (left) and 7 (right), respectively. For armchair and zigzag nanotubes, with increasing length, the Young's modulus increases. The gradients of variations become smaller as the length increases, and tend to constant values. Furthermore, the changes of Young's moduli of zigzag BNNTs with respect to lengths aren't considerable when compared to armchair ones.

Radius. Armchair and zigzag nanotubes are arranged in terms of increasing nanotube radius and are represented in Table 3. Young's moduli of armchair and zigzag nanotubes in terms of radius for different lengths is shown in Figure 8. Generally, with an increase in radius, the Young's modulus of BNNTs increases. But for roughly similar radii, the Young's moduli of zigzag nanotubes are larger than for armchair nanotubes. For example, the radius of the nanotube (10, 10) lies between the radii of the nanotubes (15, 0) and (20, 0), but its Young's modulus is less than the two other BNNTs.

chirality	radius	chirality	radius
(5, 0)	1.999	(25, 0)	9.993
(5, 5)	3.462	(15, 15)	10.385
(10, 0)	3.997	(30, 0)	11.991
(15, 0)	5.996	(20, 20)	13.846
(10, 10)	6.923	(25, 25)	17.308
(20, 0)	7.994	(30, 30)	20.77

Table 3. Arranging armchair and zigzag nanotubes in terms of increasing radius.

Figure 8. Young's modulus of zigzag and armchair BNNTs as a function of radius.

4.3. *Shear modulus.* Zigzag nanotubes with chirality (5, 0), (10, 0), (15, 0), (20, 0), (25, 0), and (30, 0) and armchair nanotubes with chirality (5, 5), (10, 10), (15, 15), (20, 20), (25, 25), and (30, 30) were analysed under torsion forces (torque). BNNTs with different lengths of 40 Å, 60 Å, 80 Å, and 100 Å were studied. The influences of chirality, length, and radius on the shear modulus of BNNTs were studied and results are given in the following:

Chirality. Figures 9 (left) and 9 (right) illustrate the variations of shear moduli of zigzag and armchair nanotubes with lengths of 40 Å, 60 Å, 80 Å, and 100 Å in terms of chirality. As the chirality increases, and subsequently as the radii of the zigzag and armchair nanotubes increase, their shear moduli increase. The slope of the changes in the smaller radii is greater and reaches a constant value as the radius increases. Furthermore, the shear moduli of armchair-type nanotubes are larger than the zigzag and increase as the chirality increases. As chirality increases, the shear moduli of armchair and zigzag nanotubes approximately reach equal constant value.

Length. Shear moduli of zigzag and armchair nanotubes with respect to length are plotted in Figure 10, left and right, respectively. Figure 10 indicates that as the length of zigzag and armchair BNNTs increases, the shear modulus decreases. The gradients of variations reduce with increasing length and tend to constant values. The results show that the mechanical properties of BNNTs depend on chirality and the length of the nanotubes.

Radius. Shear moduli of armchair and zigzag nanotubes in terms of radius for different lengths is plotted in Figure 11. In general, with increasing radius, the BNNT shear modulus increases. But for roughly similar radii, the moduli of zigzag nanotubes is larger than the armchair ones.

Figure 9. Shear modulus of BNNTs as a function of chirality: (left) zigzag, (right) armchair.

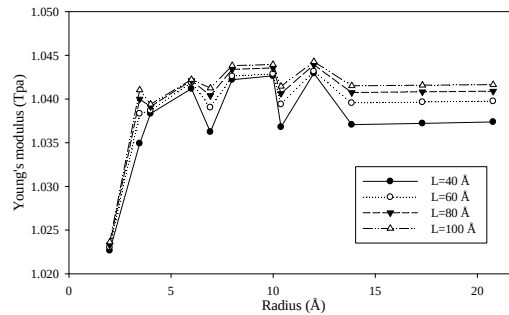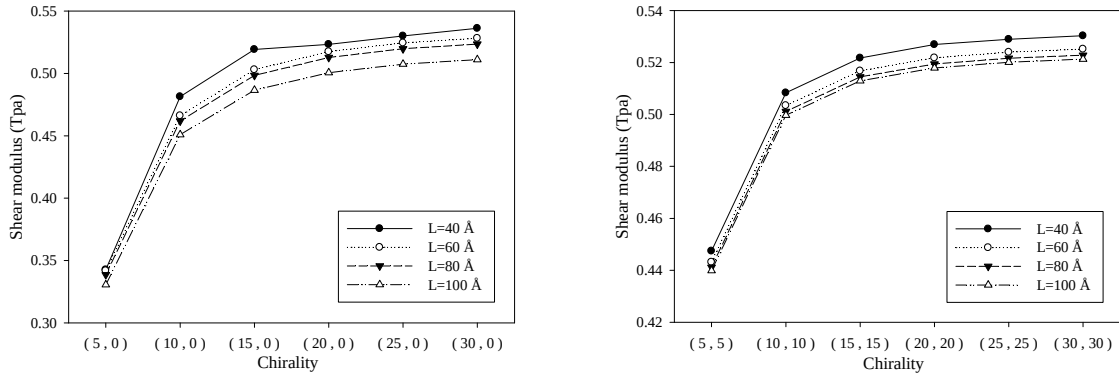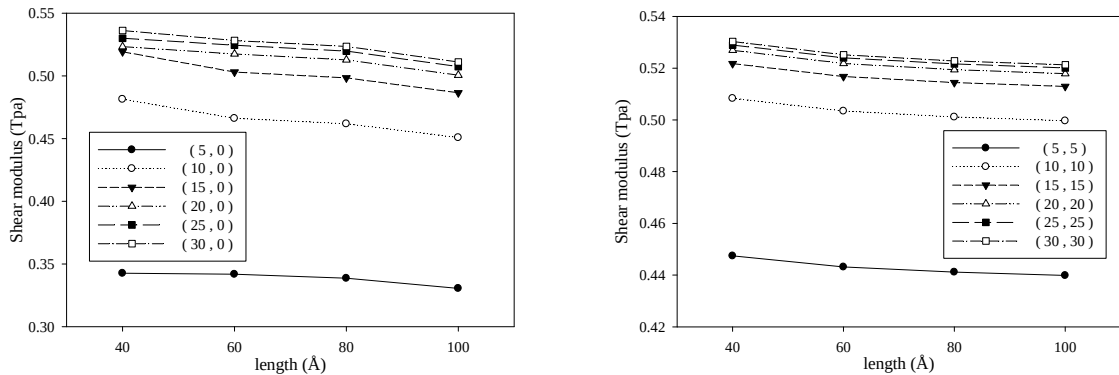**Figure 10.** Shear modulus of BNNTs as a function of length: (left) zigzag, (right) armchair.
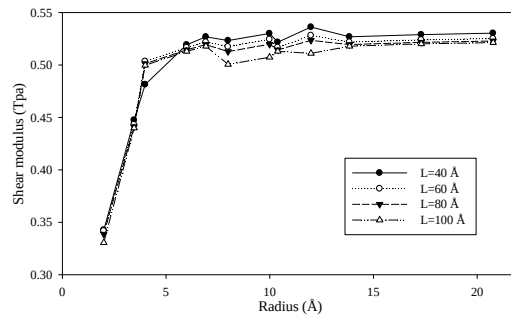
Figure 11. Shear modulus of zigzag and armchair BNNTs as a function of radius.

5. Conclusions

Three-dimensional finite element (FE) models for BNNTs have been proposed. To create the FE models, nodes are placed at the locations of atoms and the bonds between them are modelled using three-dimensional elastic beam elements via considering a linkage between molecular and continuum mechanics. The FE model comprises a small number of elements and performs with minimal computational time

and minimal computational power. This advantage, in combination with the modelling abilities of the FE method, extends the model applicability to all kinds of nanotubes with very large numbers of atoms.

The results showed that defection of nanotube decreases the mechanical properties. The effects of chirality, length, and radius on Young's modulus and shear modulus of armchair and zigzag BNNTs were investigated based on the FE model. The values of the Young's modulus and shear modulus of BNNTs without defects have changed from 1.022 TPa to 1.042 TPa and from 0.33 TPa to 0.536 TPa, respectively.

Results show that with increasing chirality, and consequently radius, the Young's modulus and shear modulus increase. As the length of zigzag and armchair BNNTs increases, the Young's modulus increases and the shear modulus decreases. Generally, as the radius increases, the Young's modulus and shear modulus increase. Furthermore, in a roughly similar radius, generally, the elastic moduli of zigzag nanotubes are larger than the armchair ones. Hence, the elastic moduli of BNNTs, especially at low radii and lengths, depend on the chirality (atomic arrangement) and the length of the nanotubes.

Also, it was observed that by using the FEM based on molecular dynamics, one can accurately determine the mechanical properties of the BNNTs. Due to the mechanical properties, BNNTs can be applied as a suitable substitute for CNTs in combination with polymers to produce specific nanocomposites.

References

[Akdim et al. 2003] B. Akdim, R. Pachter, X. Duan, and W. W. Adams, "Comparative theoretical study of single-wall carbon and boron-nitride nanotubes", *Phys. Rev. B* **67**:24 (2003), 245404.

[Ansari et al. 2015] R. Ansari, S. Rouhi, M. Mirnezhad, and M. Aryayi, "Stability characteristics of single-walled boron nitride nanotubes", *Archiv. Civil Mech. Eng.* **15** (2015), 162–170.

[Bahrami Panah and Vaziri 2015] N. Bahrami Panah and R. Vaziri, "Structure and electronic properties of single-walled zigzag BN and $B_3C_2N_3$ nanotubes using first-principles methods", *Int. J. Nano Dimen.* **6**:2 (2015), 157–165.

[Bettinger et al. 2002] H. F. Bettinger, T. Dumitrică, G. E. Scuseria, and B. I. Yakobson, "Mechanically induced defects and strength of BN nanotubes", *Phys. Rev. B* **65**:4 (2002), 041406.

[Chang and Gao 2003] T. C. Chang and H. J. Gao, "Size-dependent elastic properties of a single-walled carbon nanotube via a molecular mechanics model", *J. Mech. Phys. Solids* **51** (2003), 1059.

[Chang et al. 2005] C. W. Chang, W. Q. Han, and A. Zettl, "Thermal conductivity of B-C-N and BN nanotubes", *Appl. Phys. Lett.* **86** (2005), 173102.

[Chen et al. 2004a] C.-W. Chen, M.-H. Lee, and S. J. Clark, "Band gap modification of single-walled carbon nanotube and boron nitride nanotube under a transverse electric field", *Nanotechnology* **15**:12 (2004), 1837.

[Chen et al. 2004b] Y. Chen, J. Zou, S. J. Campbell, and G. L. Caer, "Boron nitride nanotubes: pronounced resistance to oxidation", *Appl. Phys. Lett.* **84** (2004), 2430–2432.

[Chopra and Zettl 1998] N. G. Chopra and A. Zettl, "Measurement of the elastic modulus of a multi-wall boron nitride nanotube", *Solid State Comm.* **105**:5 (1998), 297–300.

[Chopra et al. 1995] N. G. Chopra, R. J. Luyken, K. Cherrey, V. H. Crespi, M. L. Cohen, S. G. Louie, and A. Zettl, "Boron nitride nanotubes", *Science* **269**:5226 (1995), 966–967.

[Chowdhury et al. 2010] R. Chowdhury, C. Y. Wang, S. Adhikari, and F. Scarpa, "Vibration and symmetry-breaking of boron nitride nanotubes", *Nanotechnology* **21**:36 (2010), 365702.

[Fakhrabad and Shahtahmassebi 2013] D. V. Fakhrabad and N. Shahtahmassebi, "First-principles calculations of the Young's modulus of double wall boron-nitride nanotubes", *Mater. Chem. Phys.* **138**:2 (2013), 963–966.

[Fereidoon et al. 2014] A. Fereidoon, M. Rajabpour, and H. Hemmatian, "Elastic moduli of carbon nanotubes with new geometry based on FEM", *J. Theor. Appl. Mech. (Warsaw)* **52**:1 (2014), 235–245.

[Fereidoon et al. 2015] A. Fereidoon, M. Mostafaei, M. D. Ganji, and F. Memarian, "Atomistic simulations on the influence of diameter, number of walls, interlayer distance and temperature on the mechanical properties of BNNTs", *Superlatt. Microstruct.* **86** (2015), 126–133.

[Golberg et al. 1999] D. Golberg, Y. Bando, W. Han, K. Kurashima, and T. Sato, "Single-walled B-doped carbon, B/N-doped carbon and BN nanotubes synthesized from single-walled carbon nanotubes through a substitution reaction", *Chem. Phys. Lett.* **208**:3 (1999), 337–342.

[Golberg et al. 2001] D. Golberg, Y. Bando, K. Kurashima, and T. Sato, "Synthesis and characterization of ropes made of BN multiwalled nanotubes", *Scr. Mater.* **44**:8 (2001), 1561–1565.

[Golberg et al. 2007] D. Golberg, P. M. F. J. Costa, O. Lourie, M. Mitome, X. Bai, K. Kurashima, C. Zhi, C. Tang, and Y. Bando, "Direct force measurements and kinking under elastic deformation of individual multiwalled boron nitride nanotubes", *Nano Lett.* **7**:7 (2007), 2146–2151.

[Griebel and Hamaekers 2007] M. Griebel and J. Hamaekers, "Molecular dynamics simulations of boron-nitride nanotubes embedded in amorphous Si-BN", *Comput. Mater. Sci.* **39**:3 (2007), 502–517.

[Griebel et al. 2009] M. Griebel, J. Hamaekers, and F. Heber, "A molecular dynamics study on the impact of defects and functionalization on the Young modulus of boron-nitride nanotubes", *Comput. Mater. Sci.* **45**:4 (2009), 1097–1103.

[Hemmatian et al. 2014] H. Hemmatian, A. Fereidoon, and M. Rajabpour, "Mechanical properties investigation of defected, twisted, elliptic, bended and hetero-junction carbon nanotubes based on FEM", *Fullerenes, Nanotubes and Carbon Nanostructures* **22** (2014), 528–544.

[Hernández et al. 1998] E. Hernández, C. Goze, P. Bernier, and A. Rubio, "Elastic properties of C and $B_x C_y N_z$ composite nanotubes", *Phys. Rev. Lett.* **80**:20 (1998), 4502–4505.

[Hernández et al. 1999] E. Hernández, C. Goze, P. Bernier, and A. Rubio, "Elastic properties of single-wall nanotubes", *Appl. Phys. A* **68** (1999), 287–292.

[Ishigami et al. 2005] M. Ishigami, J. D. Sau, S. Aloni, M. L. Cohen, and A. Zettl, "Observation of the giant Stark effect in boron-nitride nanotubes", *Phys. Rev. Lett.* **94**:5 (2005), 056804.

[Khaleghian and Azarakhshi 2016] M. Khaleghian and F. Azarakhshi, "Electronic properties studies of benzene under boron nitride nano ring field", *Int. J. Nano Dimen.* **7**:4 (2016), 290–294.

[Khoo et al. 2004] K. H. Khoo, M. S. C. Mazzoni, and S. G. Louie, "Tuning the electronic properties of boron nitride nanotubes with transverse electric fields: a giant dc Stark effect", *Phys. Rev. B* **69**:20 (2004), 201401.

[Li and Chou 2003] C. Li and T.-W. Chou, "A structural mechanics approach for the analysis of carbon nanotubes", *Int. J. Solids Struct.* **40**:10 (2003), 2487–2499.

[Li and Chou 2006] C. Li and T.-W. Chou, "Static and dynamic properties of single-walled boron nitride nanotubes", *J. Nanosci. Nanotechnol.* **6**:1 (2006), 54–60.

[Loiseau et al. 1996] A. Loiseau, F. Willaime, N. Demoncy, G. Hug, and H. Pascard, "Boron nitride nanotubes with reduced numbers of layers synthesized by arc discharge", *Phys. Rev. Lett.* **76**:25 (1996), 4737–4740.

[Lu 1997] J. P. Lu, "Elastic properties of carbon nanotubes and nanoropes", *Phys. Rev. Lett.* **97**:7 (1997), 1297.

[Mehar and Panda 2017] K. Mehar and S. K. Panda, "Elastic bending and stress analysis of carbon nanotube-reinforced composite plate: experimental, numerical, and simulation", *Adv. Polym. Technol.* (2017), 1–15.

[Mehar et al. 2017a] K. Mehar, S. K. Panda, T. Q. Bui, and T. R. Mahapatra, "Nonlinear thermoelastic frequency analysis of functionally graded CNT-reinforced single/doubly curved shallow shell panels by FEM", *J. Therm. Stresses* **40**:7 (2017), 899–916.

[Mehar et al. 2017b] K. Mehar, S. K. Panda, and T. R. Mahapatra, "Theoretical and experimental investigation of vibration characteristic of carbon nanotube reinforced polymer composite structure", *Int. J. Mech. Sci.* **133** (2017), 319–329.

[Mehar et al. 2017c] K. Mehar, S. K. Panda, and B. K. Patle, "Stress, deflection, and frequency analysis of CNT reinforced graded sandwich plate under uniform and linear thermal environment: a finite element approach", *Polym. Compos.* (2017).

[Mehar et al. 2017d] K. Mehar, S. K. Panda, and B. K. Patle, "Thermoelastic vibration and flexural behavior of FG-CNT reinforced composite curved panel", *Int. J. Appl. Mech.* **9**:4 (2017), 1750046.

[Mehar et al. 2018] K. Mehar, S. K. Panda, and T. R. Mahapatra, "Large deformation bending responses of nanotube-reinforced polymer composite panel structure: numerical and experimental analyses", *Proceedings of the Institution of Mechanical Engineers, Part G: Journal of Aerospace Engineering* (2018), 0954410018761192.

[Mirzaei and Salamat Ahangari 2016] M. Mirzaei and R. Salamat Ahangari, "Density functional explorations of quadrupole coupling constants for BN, BP, AlN, and AlP graphene-like structures", *Int. J. Nano Dimen.* **7**:4 (2016), 284–289.

[Molani 2017] F. Molani, "The effect of C, Si, N, and P impurities on structural and electronic properties of armchair boron nanotube", *J. Nanostruct. Chem.* **7**:3 (2017), 243–248.

[Odegard et al. 2002] G. M. Odegard, T. S. Gates, L. M. Nicholson, and K. E. Wise, "Equivalent continuum modelling of nano-structured materials", *Compos. Sci. Technol.* **62** (2002), 1869.

[Rubio et al. 1994] A. Rubio, J. L. Corkill, and M. L. Cohen, "Theory of graphitic boron nitride nanotubes", *Phys. Rev. B* **49**:7 (1994), 5081–5084.

[Sánchez-Portal et al. 1999] D. Sánchez-Portal, E. Artacho, J. M. Soler, A. Rubio, and P. Ordejón, "Ab initio structural, elastic, and vibrational properties of carbon nanotubes", *Phys. Rev. B* **59**:19 (1999), 12678–12688.

[Santosh et al. 2009] M. Santosh, P. K. Maiti, and A. Sood, "Elastic properties of boron nitride nanotubes and their comparison with carbon nanotubes", *J. Nanosci. Nanotechnol.* **9**:9 (2009), 5425–5430.

[Suryavanshi et al. 2004] A. P. Suryavanshi, M. Yu, J. Wen, C. Tang, and Y. Bando, "Elastic modulus and resonance behaviour of boron nitride nanotubes", *Appl. Phys. Lett.* **84**:14 (2004), 2527–2529.

[Terrones et al. 1996] M. Terrones, W. K. Hsu, H. Terrones, J. P. Zhang, S. Ramos, J. P. Hare, R. Castillo, K. Prassides, A. K. Cheetham, H. W. Kroto, and D. R. M. Walton, "Metal particle catalysed production of nanoscale BN structures", *Chem. Phys. Lett.* **259**:5 (1996), 568–573.

[Vaccarini et al. 2000] L. Vaccarini, C. Goze, L. Henrard, E. Hernández, P. Bernier, and A. Rubio, "Mechanical and electronic properties of carbon and boron-nitride nanotubes", *Carbon* **38**:11-12 (2000), 1681–1690.

[Verma et al. 2007] V. Verma, V. Jindal, and K. Dharamvir, "Elastic moduli of a boron nitride nanotube", *Nanotechnology* **18**:43 (2007), 435711.

[Wei et al. 2010] X. Wei, M. S. Wang, Y. Bando, and D. Golberg, "Tensile tests on individual multi-walled boron nitride nanotubes", *Adv. Mater.* **22**:43 (2010), 4895–4899.

[Wu et al. 2004] X. Wu, J. Yang, J. G. Hou, and Q. Zhu, "Deformation-induced site selectivity for hydrogen adsorption on boron nitride nanotubes", *Phys. Rev. B* **69**:15 (2004), 153411.

[Yakobson et al. 1996] B. I. Yakobson, C. J. Brabec, and J. Bernholc, "Nanomechanics of carbon tubes: instabilities beyond linear range", *Phys. Rev. Lett.* **76** (1996), 2511.

[Zhi et al. 2005] C. Zhi, Y. Bando, C. Tang, and D. Golberg, "Immobilization of proteins on boron nitride nanotubes", *J. Am. Chem. Soc.* **127**:49 (2005), 17144–17145.

[Zhi et al. 2010] C. Zhi, Y. Bando, C. Tang, and D. Golberg, "Boron nitride nanotubes", *Mater. Sci. Eng. R* **70** (2010), 92–111.

[Zhong et al. 2001] D. Y. Zhong, S. Liu, G. Y. Zhang, and E. G. Wang, "Large-scale well aligned carbon nitride nanotube films: low temperature growth and electron field emission", *J. Appl. Phys.* **89** (2001), 5939.

HOSSEIN HEMMATIAN: hoseinhemmatian@gmail.com
Department of Mechanical Engineering, Semnan Branch, Islamic Azad University, Semnan, Iran

MOHAMMAD REZA ZAMANI: a_mrzamani@mut.ac.ir
Faculty of Mechanical Engineering, Malek-Ashtar University of Technology, Tehran, Iran

JAFAR ESKANDARI JAM: eskandari@mut.ac.ir
Faculty of Mechanical Engineering, Malek-Ashtar University of Technology, Tehran, Iran

∎msp

EFFECT OF INTERCONNECT LINEWIDTH ON THE EVOLUTION OF INTRAGRANULAR MICROCRACKS DUE TO SURFACE DIFFUSION IN A GRADIENT STRESS FIELD AND AN ELECTRIC FIELD

LINYONG ZHOU, PEIZHEN HUANG AND QIANG CHENG

Based on the weak formulation for combined surface diffusion and evaporation/condensation, we derive the governing equation of the finite-element induced both by stressmigration and electromigration. The corresponding program is developed for simulating the evolution of the intragranular microcracks caused by surface diffusion in copper interconnect lines under a gradient stress field and an electric field. Unlike previously published works, this paper is focused on how the interconnect linewidth influences the microcrack evolution. Numerical analysis results show that there exists a critical value of the linewidth $\hat{h}_c$. When $\hat{h} > \hat{h}_c$, the microcrack will drift along the direction of the electric field by a stable form. When $\hat{h} \leq \hat{h}_c$, it will split into two small microcracks and the decrease of the linewidth is beneficial for the microcrack splitting. Besides, the critical linewidth increases with the increase of the electric field and the aspect ratio, and the critical linewidth first increases and then decreases with the increase of the stress gradient. That is, the increase of the electric field and the aspect ratio is beneficial for the microcrack to split. In addition, all of the critical values of the electric field, the aspect ratio and the stress gradient decrease with the decrease of the linewidth. The microcrack has a stronger dependence on the linewidth when $\hat{h} < 25$.

1. Introduction

Interconnect lines are widely used in micro-devices. With the trend of miniaturization and integration of microelectronic systems, the feature size on the integrated circuit chip continues to decrease, following the sharp increase in current density and the sharp decrease in interconnect linewidth. Interconnect lines are usually subjected to severe mechanical and electrical load [Bower and Craft 1998]. In addition, interconnect lines inevitably exist some drawbacks, such as voids and microcracks. If the voids or microcracks grow and change their shape, they could affect the reliability of interconnects [Bower and Shankar 2007]. Therefore, it is significant to understand the effect of linewidth on the evolution of microcracks in a stress field and an electric field [Krug and Dobbs 1994; Schimschak and Krug 1997].

Over the last forty years, the behavior of electromigration and stressmigration has been studied extensively because it can seriously affect the reliability of the conductor lines. Due to the technological need in microelectronic industry, measurement (see [Cho and Thompson 1989; Dreyer and Varker 1992], for instance) and prediction of time-to-failures (see [Bower and Craft 1998; Giroux et al. 1995; Zhang et al. 2010], for example) and their distributions have dominated electromigration testing and modelling in the past. And the mass transport mainly occurs through interfacial diffusion and grain boundary diffusion.

The results also indicate that growth, drift, and accumulation of existing voids lead to the observed strong linewidth dependence. Furthermore, in situ observations of the damage development have shown that failure of interconnect lines is a complicated process including nucleation, growth, motion and shape changes of voids [Vairagar et al. 2004]. There are some voids within a grain [Kraft et al. 1993] except on a grain boundary. The evolution of voids within a grain changes its shape only through surface diffusion. And the morphology of voids within a grain due to surface diffusion induced by electromigration or by stressmigration has been investigated in detail.

There have been a number of analytical studies on the electromigration-induced void morphological evolution under high current density [Wang and Yao 2017a; 2017b], on predicting finger-shaped void propagation speed in solder interconnects [Yao et al. 2009], and on the steady motion velocity of an elliptical inclusion and voids under electromigration and a gradient stress field [Dong and Li 2009; Li et al. 2010]. In addition, Gungor and Maroudas [1999] showed a theoretical analysis for electromigration-induced failure of metallic interconnect lines and predicted that prevention of failure is possible by adjusting the grain orientation with respect to the applied electric field.

Experimental studies have revealed that the current density, the stress field and the self-diffusion coefficient can significantly affect the failure mechanism of the interconnect lines [Huntington and Grone 1961; Black 1969; Blech and Herring 1976; Blech 1998; Zschech et al. 2010; Vanstreels et al. 2014; Lin et al. 2017]. In addition, when the electric current passing through the interconnect lines, the metal atoms flow out from the cathode of the interconnect line into the anode induced by electromigration. And they deposit at the anode, forming a linear gradient stress field [Dong and Li 2009]. The gradient stress, in its turn, motivates atoms to diffuse on the microcrack surface, changing its shape and position. This coupling effect has never been quantitatively analyzed.

There are also many numerical analyses on stressmigration and electromigration due to diffusion processes [Bower and Craft 1998; Bower and Shankar 2007; Bower and Freund 1993; Kraft and Arzt 1995; Sun and Suo 1997; Sun et al. 1997; Xia et al. 1997; Liu et al. 1998; Dalleau and Weide-Zaage 2001; Fridline and Bower 2002; Liu and Yu 2006]. Several authors [Bower and Craft 1998; Bower and Freund 1993; Xia et al. 1997; Kraft and Arzt 1995] showed two dimensional finite-element simulations of void evolution due to strain and electromigration induced surface diffusion. They discussed the failure mechanisms and the nucleation, growth and evolution of voids in the interconnect lines of microelectronic circuits, including the effect of linewidth on the failure time. Before long, the method was extended to three-dimensional problems [Zhang et al. 1998]. Electromigration induced void nucleation, growth and evolution have been extensively studied by the finite-element method [Dwyer 2010]. The failure analysis of critical-length data from electromigraion was studied [Dwyer 2011], which is corresponding to the experiment results [Blech 1998]. The numerical method mentioned above is on the weak formulation including curvature, electric field and stress field [Bower and Shankar 2007; Xia et al. 1997; Fridline and Bower 1999]. But the finite-element method combined surface diffusion and evaporation/condensation was first built in [Sun and Suo 1997], which has since been applied to a range of problems, such as grain growth [Huang et al. 2003b], faceted crystals and grain boundary grooving [Liu and Yu 2006], the evolution of a bicrystal film and a tricrystal film on a substate, and the morphological evolution of microcracks [Huang et al. 2003a; 2003c; Huang and Sun 2004; Wang et al. 2006]. In recent years, the finite-element method based on the weak formulation combined surface diffusion and evaporation/condensation has

been extended and applied to studied the microcrack evolution caused by surface diffusion induced by stressmigration [He and Huang 2014] and electromigration [He and Huang 2015].

However, the weak formulation incorporating surface diffusion and evaporation/condensation induced both by electromigration and stressmigration has not been reported in the literature up to now. And no report has analyzed the effect of interconnect linewidth on the morphological evolution of intragranular microcrcacks due to surface diffusion in a gradient stress field and an electric field. The aim of the present work reported here is primarily to develop a finite-element program to simulate the morphological evolution of the intragranular microcracks under a gradient stress field and an electric field. And the work is focused on how the interconnect linewidth influences the microcrack evolution.

This paper is organized as follows. In Section 2, we introduce our analysis model of two-dimensional intragranular microcrack, then briefly describe the basic diffusion theory and develop the finite-element method induced both by stressmigration and electromigration in Section 3. In Section 4, the microcrack evolution is simulated under different linewidths, gradient stress fields, electric fields and aspect ratios, and the corresponding effect is discussed. Section 5 presents the main conclusion.

2. Modeling of two-dimensional intragranular microcrack evolution

Interconnect lines are usually under large stress. The stress in an interconnect line arises mainly from two sources: heat and electromigration. Current passes through the interconnect line, causing atoms to migrate in the direction of electron flow. The matter transports on the microcrack surface and it causes the shape change and the motion of the microcrack. The electromigration causes atoms depletion near the cathode and deposition near the anode of the line. It leads to a gradient stress along the interconnect line with a tensile stress near the cathode and compressive stress near the anode as shown in Figure 1. The gradient stress, in its turn, motivates atoms to diffuse on the microcrack surface, changing its shape and position.

Figure 2 shows the model of our analysis. The interconnect line is idealized as a two-dimensional single crystal with a microcrack along the midline and is assumed in a state of plain strain. The line is subjected to an electric field as a voltage V_0 and a linear gradient stress filed with a tensile stress near the cathode and compressive stress near the anode which is induced in the interface between the line and the passivation. We assume that the distribution of the voltage in the boundary is uniform and that
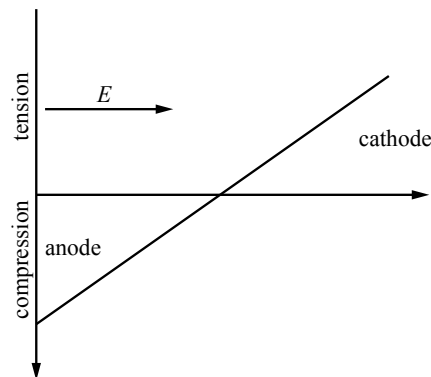
Figure 1. Schematic illustration of the gradient stress induced by electromigration.
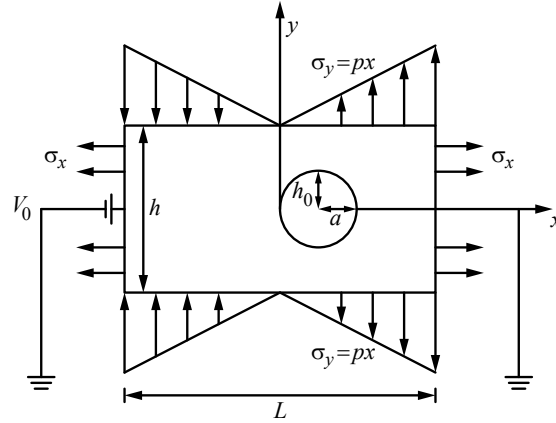
Figure 2. A model of an intragranular microcrack under a gradient stress field and an electric field.

the electric field in the line has no component normal to the plane of the figure. Diffusion through the bulk is assumed to be negligible. Therefore, in the absence of grain boundaries, the only mode of mass transport is diffusion along the microcrack surface. We have assumed that the surface energy is isotropic and that the surface energy does not interfere with the electric field energy and the strain energy.

For simplicity, the microcrack is characterized by the aspect ratio $\beta = a/h_0$, where a is the initial major semiaxis of the microcrack, h_0 is the initial minor semiaxis, L is the length of the interconnect line, and h is the linewidth.

3. Basic theory

3.1. *Surface diffusion equations.* Based on Herring's classical theory Herring 1999, we adopt a kinetic law that, at every point on the grain surface, the flux of the surface diffusion, J, is proportional to the driving force F:

$$J = MF. \tag{1}$$

Here M is the mobility of atoms on the surface; it is related to the self-diffusivity by the Einstein relation, $M = \Omega D\delta/kT$, in which Ω is the volume of the atom, D is the self-diffusivity on the surface, δ is the effective thickness of atoms participating in matter transport, k is Boltzmann's constant, and T is the absolute temperature. The driving force F is defined by the decrease in free energy per unit volume of matter moving per unit distance on the surface.

As matter is deposited onto or removed from a free surface, a normal velocity v_{ns} of the free surface results. Mass conservation requires that

$$v_{ns} = -\nabla \cdot J, \tag{2}$$

where $\nabla \cdot J$ is the surface divergence of the flux vector. Let δr_{ns} be the virtual normal displacement on the surface and δI be the virtual mass displacement; we have

$$\delta r_{ns} = -\nabla \cdot \delta(I). \tag{3}$$

Given a microcrack, the driving force, $\boldsymbol{F}$, according to the kinetic law, drives the flux $\boldsymbol{J}$ to conserve the microcrack mass, the divergence of the flux gives rise to the surface velocity, which then updates the shape for a small time increment. Repeat the procedure for many time increments to trace the evolving microcrack shape. However, a surface diffusion problem that conserves solid mass as formulated above is difficult to implement in a finite-element setting. Once an evaporation/condensation process is introduced into microstructure evolution, the overall mass conservation is easier to treat by a finite-element method [Sun and Suo 1997].

3.2. Weak statement for combined surface diffusion and evaporation/condensation.
Following the principle of virtual work [Sun et al. 1994], we obtain the integral form

$$\int \boldsymbol{F} \cdot \delta \boldsymbol{I} \, dA = -\delta G, \tag{4}$$

where δG is the increment in free energy and dA is the area of the element. Substituting (1) into (4), we have

$$\int \frac{\boldsymbol{J} \cdot \delta \boldsymbol{I}}{M} \, dA = -\delta G. \tag{5}$$

Once $\boldsymbol{J}$ is solved from (5), the surface normal velocity is obtained from (2), which then updates the shape for a small increment.

Imagine two concurrent processes on a microcrack surface: surface diffusion and evaporation/condensation. The kinetic law for evaporation/condensation is similar to the surface diffusion. Let p be the free energy reduction associated with per unit volume of matter added to per unit surface area of the microcrack, and v_{nv} be the volume of matter added to per unit area of the microcrack surface per unit time. They are proportional to each other:

$$v_{nv} = mp, \tag{6}$$

where m is the mobility of evaporation/condensation. The resulting equations of the surface normal velocity v_n and the surface virtual displacement δr_n due to the combined action of evaporation/condensation and surface diffusion are

$$v_n = v_{nv} - \nabla \cdot \boldsymbol{J}, \tag{7}$$

$$\delta r_n = \delta r_{nv} - \nabla \cdot \delta \boldsymbol{I}. \tag{8}$$

Associated with the virtual motion, the free energy changes by δG. According to the two kinds of driving forces, $\boldsymbol{F}$ and p, matter relocation and exchange on the microcrack surface area element, δA, reduce the free energy by $(\boldsymbol{F} \cdot \delta \boldsymbol{I} + p \delta r_{nv}) dA$. Thus, we have the weak formulation for combined surface diffusion and evaporation/condensation:

$$\int (\boldsymbol{F} \cdot \delta \boldsymbol{I} + p \delta r_{nv}) dA = -\delta G. \tag{9}$$

Substituting Equations (1)–(8) into (9), we have

$$\int \left(\frac{\boldsymbol{J} \cdot \delta \boldsymbol{I}}{M} + \frac{(v_n + \nabla \cdot \boldsymbol{J})(\delta r_n + \nabla \cdot \delta \boldsymbol{I})}{m} \right) ds = -\delta G. \tag{10}$$

The finite-element method introduced in [Sun and Suo 1997] is used for solving the above the weak formulation. The difference between references [Sun and Suo 1997; He and Huang 2014; He and Huang 2015] and this paper is that we consider the coupling with a gradient stress field and an electric field. The kinetic and mass conservation laws expressed in the left-hand side of (10) are the same, but the energy term in the right-hand side of (10) has two extra terms, the strain energy and the electric potential.

3.3. *Finite-element method.*

The system consists of two coupled subsystems: the microcrack surface and the solid body (as shown in Figure 2). The motion of the microcrack surface is affected by the strain energy and the electric potential within the solid body, which in turn is affected by the shape changes due to the surface motion. Each subsystem is discretized into finite elements as follow. Following [Sun et al. 1997], we represent the microcrack surface by a set of linear isoparametric finite elements. Each element has four degrees of freedom to describe motion and three degrees of freedom to describe diffusion. These coordinates, together with mass displacement I at all the nodal points, form generalized coordinates

$$q_1, q_2, q_3, \ldots, q_{n-2}, q_{n-1}, q_n,$$

where n is the total number of degrees of freedom. The generalized velocities are

$$\dot{q}_1, \dot{q}_2, \dot{q}_3, \ldots, \dot{q}_{n-2}, \dot{q}_{n-1}, \dot{q}_n,$$

The velocity and virtual motion of any point on the surface can be interpolated by the corresponding values at the nodes. Integrating the weak statement equation (10) element by element, we get a bilinear form in $\dot{q}$ and δq. The right-hand side of (10) is the total free energy change associated with the virtual motion,

$$\delta G = -\sum f_i \delta q_i, \tag{11}$$

which allows us to compute the generalized forces $f_1, f_2, \ldots, f_n$. Collect the coefficient of δq_i, giving

$$\sum_j H_{ij} \cdot q_j = f_i. \tag{12}$$

The matrix H is symmetric and positive-definite, and both H and the force vector f depend on the coordinates of all the nodes. Equation (12) is a set of nonlinear ordinary differential equations and is solved by using the Runge–Kutta method. In this paper, for the sample problem to be simulated as shown in Figure 2, we consider surface energy, strain energy and electric potential. The free energy variation associated with a given element is computed as follows:

$$\delta G = \gamma_s \delta l - \int \omega \delta r_n + \frac{Z^* |e|}{\Omega} \int V \delta r_n \, ds, \tag{13}$$

where ω represents the strain energy density, γ_s is the element surface tension, Z^* is a phenomenological constant known as the effective valence of an atom, e is the charge of the electron and V is the electric potential. This is different from previous works for combining strain energy density and electric potential [He and Huang 2014; 2015]: the force components acting on the two nodes of the element due to the

element surface energy, strain energy and electric potential are

$$
\mathbf{f}^e = \gamma_s
\begin{bmatrix}
\cos\theta \\
\sin\theta \\
0 \\
-\cos\theta \\
-\sin\theta \\
0 \\
0
\end{bmatrix}
- \frac{l}{2}
\begin{bmatrix}
\left(\frac{2}{3}\omega_1 + \frac{1}{3}\omega_2\right)\sin\theta \\
-\left(\frac{2}{3}\omega_1 + \frac{1}{3}\omega_2\right)\cos\theta \\
0 \\
\left(\frac{1}{3}\omega_1 + \frac{2}{3}\omega_2\right)\sin\theta \\
-\left(\frac{1}{3}\omega_1 + \frac{2}{3}\omega_2\right)\cos\theta \\
0 \\
0
\end{bmatrix}
+ \frac{Z^*|e|l}{2\Omega}
\begin{bmatrix}
\left(\frac{2}{3}V_1 + \frac{1}{3}V_2\right)\sin\theta \\
-\left(\frac{2}{3}V_1 + \frac{1}{3}V_2\right)\cos\theta \\
0 \\
\left(\frac{1}{3}V_1 + \frac{2}{3}V_2\right)\sin\theta \\
-\left(\frac{1}{3}V_1 + \frac{2}{3}V_2\right)\cos\theta \\
0 \\
0
\end{bmatrix}.
$$

Here ω_1 and ω_2 represent the strain energy density of nodes 1 and 2, and V_1 and V_2 are the nodal values of the electric potential function.

Both the strain energy density and the electric potential on the microcrack surface affect the surface motion. We choose to discretize the solid body and use the standard finite procedure.

For each time step Δt, the calculations proceed as follows:

  (i) Solve the electric field and the stress field problem on the current configuration, including the computation of the strain energy density, the electric potential and project the results onto the surface nodes.

 (ii) Compute the new surface configuration.

(iii) Update the time.

4. Numerical simulation and discussion

In this section, based on the finite-element method for large change of a solid due to matter diffusion, the behavior of the intragranular microcracks caused by surface diffusion induced both by stressmigration and electromigration is analyzed by the finite-element method developed in this paper. We focus on how the interconnect linewidth influences the microcrack evolution. The reliability of the finite-element method under electric field has been conformed as shown in [He and Huang 2015]. Meanwhile, mass conservation requires that the total area of the microcrack remain constant. The actual change of this area during simulation can therefore be taken as a measure of the computing accuracy. We monitor the total area of a microcrack as a means to verify the accuracy of our numerical results. Large numbers of numerical calculations indicate that the finite-element method used is robust, accurate and efficient. For convenience, we introduce the dimensionless linewidth $\hat{h} = h : h_0$ to reflect the influence of the interconnect linewidth on the evolution of intragranular microcrack through changing the value of h. Additionally, we introduce the nondimensional time $\hat{t} = tM\gamma_s/h_0^4$ and a dimensionless stress gradient $\hat{p} = pLH_0/\gamma_s$. The relative magnitude of the two forces, the electromigration driving force and the surface tension, is given by $\chi = V_0|e|Z^*h_0/\Omega\gamma_s L$.

Figure 3 shows the evolution of intragranular microcracks for $\chi = 0.6$, $\beta = 4$, $\hat{p} = 29$ as the linewidth decreases ($\hat{h} = 80, 50, 20, 15$). As shown in each of the plots, the initial shape of the microcrack is elliptical and the curvature of each point on the microcrack surface is different. The pronounced difference in curvature along the microcrack perimeter induces mass redistribution, with mass being removed from relatively flat microcrack surfaces and depositing in the microcrack tips. From the initial stress
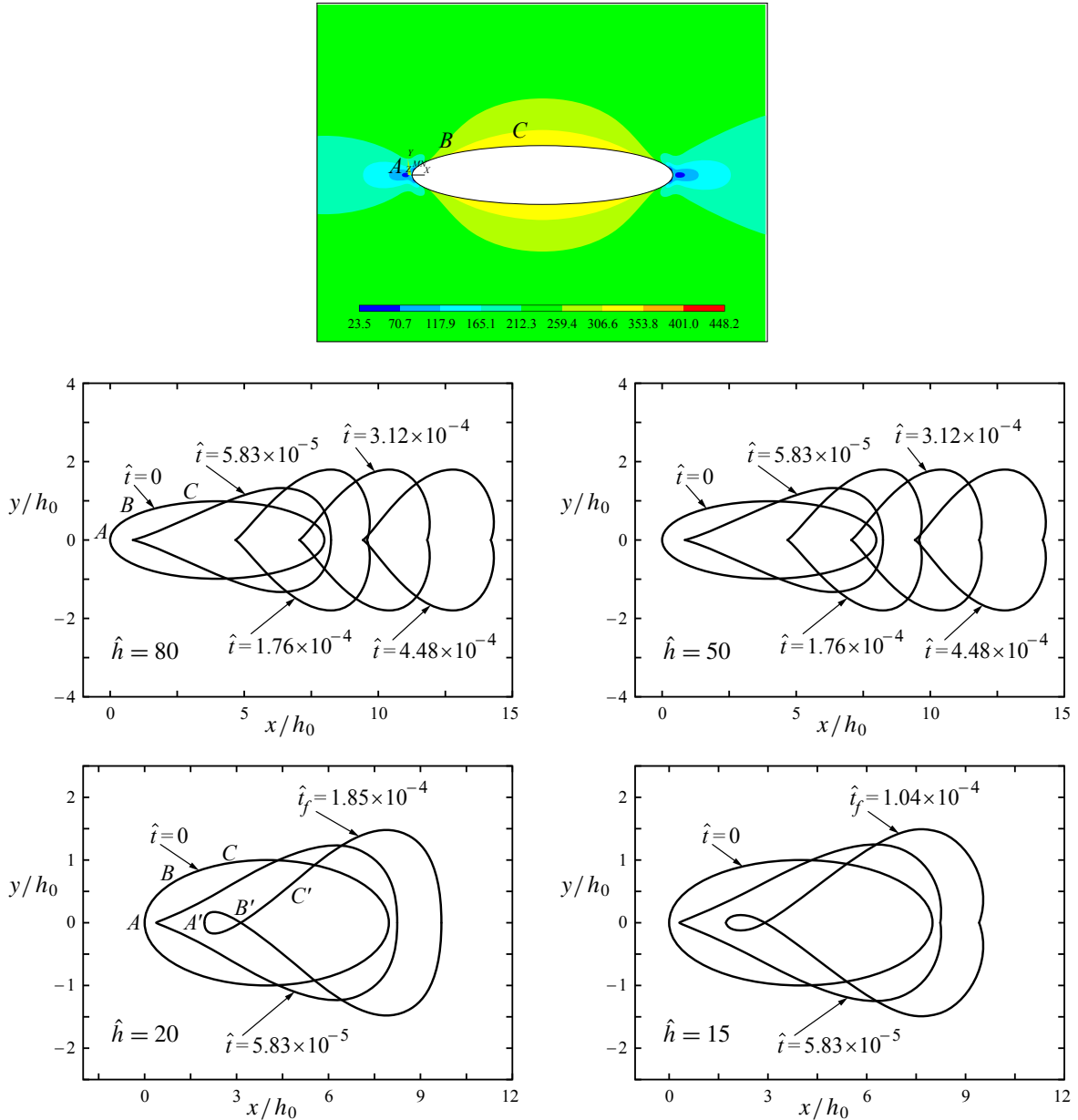
Figure 3. Initial stress nephogram (top; scale values in MPa) and evolution of the intra-granular microcrack for $\chi = 0.6$, $\beta = 4$, $\hat{p} = 29$. Note the different scales between graphs. Four values of $\hat{h}$ are illustrated: 80, 50, 20, 15.

nephogram (Figure 3, top) we see that $\omega_C > \omega_B > \omega_A$, which indicates that atoms in point C would move to point B and point A under the surface diffusion driving force induced by strain energy. Meanwhile, as we know, the electromigration driving force is proportional to the gradient of the electric potential. In the first time plot (middle row, left), we have $(\partial V/\partial s)_C > (\partial V/\partial s)_B > (\partial V/\partial s)_A$ at the initial time. So, the atoms in point C would move to point B, and then from point B to point A under the electromigration

driving force. If the stress field and electric field dominate the microcrack evolution, atoms deposited on point B start to form a bulge at the microcrack surface (seen as a shallow concavity on each side of the tip of the drop-shaped curve). With an increase in the gradient stress field and electric field, atoms continue to gather there.

With a decrease in linewidth, the current density increases and the stress gradient increases sharply. The bulges on the upper and lower surfaces can connect (point B' in bottom right panel), and then the cavity splits into two small microcracks, as shown in the bottom row panels. When the bulge reaches a certain size atoms start to emanate from it because the chemical potential here is enhanced relative to the vicinity. If this process dominates, the bulge will reverse and eventually the energy in the microcrack surface tends to be the same as under surface diffusion, as shown in the middle row of Figure 3. In addition, the driving force of the stress field and the electric field causes material to diffuse from the right side of the microcrack to the left. So the microcrack appears to migrate through the interconnect line. It can be seen that under different linewidths, the intragranular microcraks evolution tends to be two different trends. In other words, there must exist a critical linewidth $\hat{h}_c$. When $\hat{h} > \hat{h}_c$, the microcrack will evolve into a stable shape as it migrates along the interconnect line. In contrast, when $\hat{h} \leq \hat{h}_c$, the microcrack splits into two small parts.

Parts (d) and (e) of Figure 3 show that the splitting time of the microcrack decreases with a decrease in linewidth. Figure 4 shows the relationship of the splitting time $\hat{t}_f$ with the decrease of linewidth under different aspect ratios. It is obvious that the splitting time decreases as the linewidth decreases. This behavior indicates that the decrease in the linewidth accelerates the microcrack splitting process. Besides, it can be seen from the declining trend, when $\hat{h} < 25$ the influence of the size effect is distinct. When $\hat{h} > 25$, the variation of the curve is tardy, which means the effect of the size could almost be neglected. Compare the curves with different aspect ratios in Figure 3; it can be seen that the larger of the aspect ratio, the shorter time of the intragranular microcracks needed to spilt. That is, the increase of the aspect ratio is beneficial to microcrack splitting.

From this analysis, we conclude that the critical linewidth depends not only on the electric field but on the aspect ratio and the stress gradient. Figure 5, left, shows the critical linewidth of the microcrack splitting as a function of the electric field χ for four values of β when $\hat{p} = 15$. This figure indicates that $\hat{h}_c$ increases with the electric field. That is, the increase of the electric field is beneficial to the microcrack
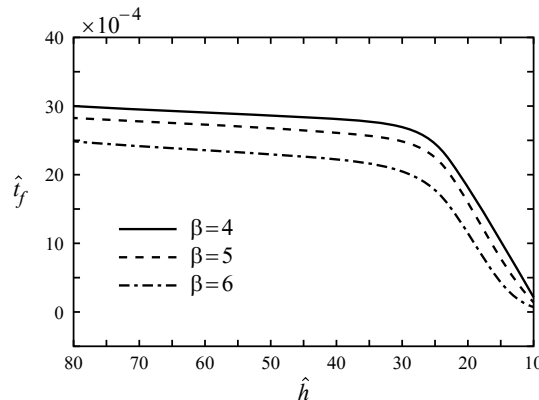
**Figure 4.** Dependence of $\hat{t}_f$ on $\hat{h}$ for $\chi = 0.6$, $\hat{p} = 29$.
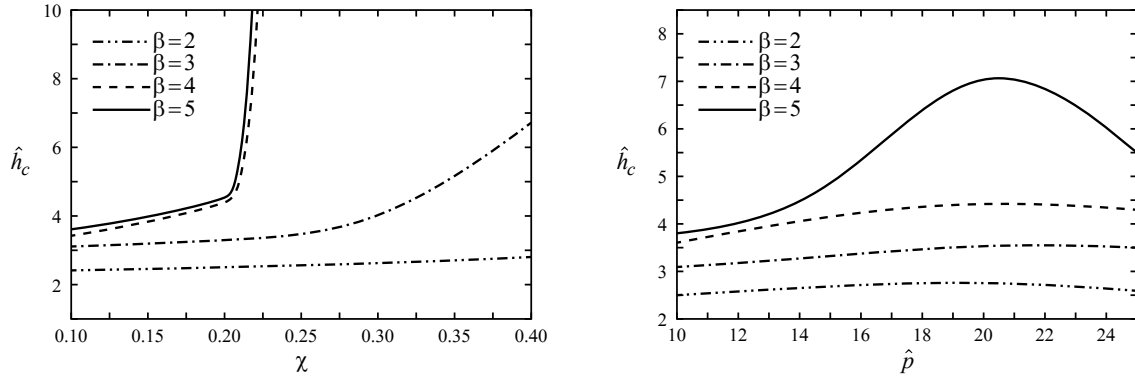
Figure 5. Left: dependence of $\hat{t}_c$ on χ for $\hat{p} = 15$.   Right: dependence of $\hat{t}_c$ on $\hat{p}$ for $\chi = 0.2$.

splitting. The critical linewidth increases as the increase of the aspect ratio for a given gradient stress and an electric field, which also manifests that the increase of the aspect ratio is also beneficial to the microcrack splitting. But its influence to the critical linewidth becomes very week when the aspect ratio exceeds a certain value. All microcracks for $\beta \geq 4$ split into two microcracks when $\chi > 0.22$.

Figure 5, right, shows the critical linewidth of the microcrack splitting as a function of the stress gradient under different aspect ratios for $\chi = 0.2$. For a given electric field and aspect ratio, the critical linewidth first increases and then decrease as the increase of the gradient stress field. When the stress gradient $\hat{p}$ is approximately equal to 20, the critical linewidth reaches its maximum. This feature is highlighted for the large microcrack.

Through a large number of numerical simulations, we also find that there exists a critical electric field χ_c for a given stress gradient $\hat{p}$, aspect ratio β and linewidth $\hat{h}$ and there exists a critical aspect ratio β_c for a given stress gradient $\hat{p}$, electric field χ and linewidth $\hat{p}$. There also exists a critical stress gradient $\hat{p}_c$ for a given electric field χ, aspect ratio β and linewidth $\hat{h}$. When $\chi < \chi_c$, $\beta < \beta_c$ or $\hat{p} < \hat{p}_c$, the microcrack will evolve into a stable shape as it migrates along the line. More interesting results are found that the microcrack splits into two small parts when $\chi > \chi_c$, $\beta > \beta_c$ or $\hat{p} > \hat{p}_c$.

Figure 6 shows the critical electric field χ_c as a function of the linewidth under different aspect ratios for $\hat{p} = 29$. The slope of these curves at any point represents the magnitude of the dependence. It can
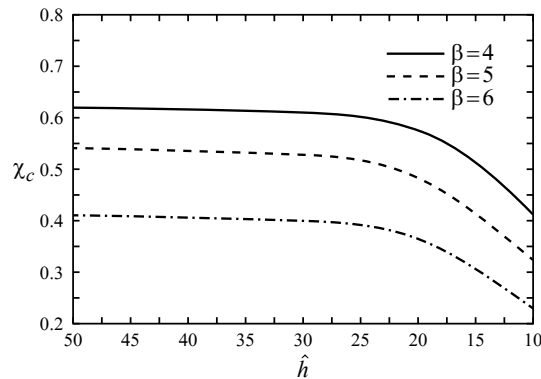
Figure 6. Dependence of χ_c on $\hat{h}$ for $\hat{p} = 29$.
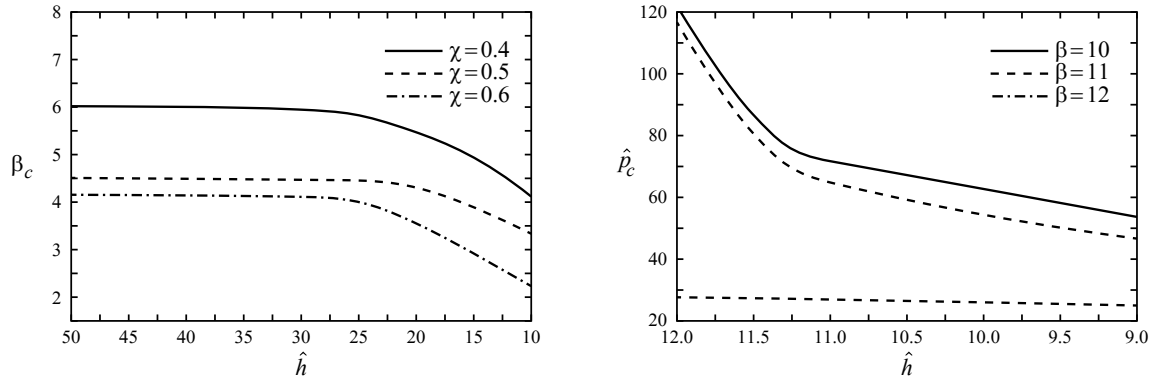
Figure 7. Left: dependence of β_c on $\hat{h}$ for $\hat{p} = 29$.   Right: Dependence of $\hat{p}_c$ on $\hat{h}$ for $\chi = 0.1$.

be seen from the variation tendency of the curve, the critical electric field decrease gradually with the decreases of linewidth, which demonstrates that the increasing current density accelerates the microcrack splitting. Moreover, we can find that the critical electric field dependence of the linewidth is relatively weakened when $\hat{h} \geq 25$. The results indicate that the influence of size effect could be ignored for this situation. Contrasting the three curves in the figure, it can be seen that the larger of the aspect ratio or the electric field of the microcrack, the easier for the microcrack to split. That is, the increase of aspect ratio and electric field are beneficial for the microcrack to split.

We turn to the variation in the critical aspect ratio β_c with $\hat{h}$ and χ. This is shown in Figure 7, left, as a function of the linewidth under different electric field for $\hat{p} = 29$. This figure indicates that the critical aspect ratio of the microcrack splitting decreases with the decrease of linewidth. That is to say, for a given electric field, the microcrack splitting will be much easy to occur with linewidth decreasing. Moreover, β_c decreases with an increase in the electric field, so such an increase is beneficial to microcrack splitting. It also can be seen from the the figure that the influence of size effect can be ignored when $\hat{h} \geq 25$.

Finally, Figure 7, right, shows the critical stress gradient $\hat{p}_c$ as a function of the linewidth under different aspect ratios for $\chi = 0.1$. We see that the critical stress gradient of the microcrack splitting decreases with the linewidth. In other words, for a given electric field and aspect ratio, microcrack splitting will occur more easily as the linewidth decreases. The critical stress gradient $\hat{p}_c$ also decreases with an increase in the aspect ratio. The critical stress gradient dependence on the linewidth is particularly noticeable for the larger microcrack when $\hat{h} > 11.3$.

5. Conclusion

In this paper, we derived the governing equation of the finite-element incorporating surface diffusion and evaporation/condensation induced both by stressmigration and electromigration. Then, the finite-element method was used to simulate the effect of interconnect linewidth on the evolution of microcracks under surface diffusion induced by the gradient stress field and the electric field. The main results obtained are summarized as follows:

(1) There must exist a critical linewidth $\hat{h}_c$. When $\hat{h} > \hat{h}_c$, the microcrack will evolve into a stable shape as it migrates along the interconnect line. When $\hat{h} \leq \hat{h}_c$, the microcrack splits into two small parts. The

splitting time decreases with the linewidth; that is, a decrease in the linewidth accelerates the microcrack splitting process. But the size effect could almost be neglected when $\hat{h} > 25$.

(2) The critical linewidth $\hat{h}_c$ depend not only on the electric field but also on the aspect ratio and the stress gradient. It increases with the electric field and the aspect ratio, while it first increases and then decreases as the stress gradient increases.

(3) There exists a critical electric field χ_c, a critical aspect ratio β_c and a critical stress gradient $\hat{p}_c$. When any of these variables are below those critical values, the microcrack evolves into a a stable shape as it migrates along the line, whereas when they exceed the critical values, the microcrack splits up.

(4) All three critical quantities decrease gradually with the decrease of linewidth. The influence of size effect on χ_c and β_c can be ignored when $\hat{h} \geq 25$, while the influence of size effect on $\hat{p}_c$ is very noticeable for the larger microcrack when $\hat{h} \geq 11.3$.

References

[Black 1969] J. R. Black, "Electromigration: a brief survey and some recent results", *IEEE. Trans. Electron Devices* **16**:4 (1969), 338–347.

[Blech 1998] I. A. Blech, "Diffusional back flows during electromigration", *Acta Mater.* **46**:11 (1998), 3717–3723.

[Blech and Herring 1976] I. A. Blech and C. Herring, "Stress generation by electromigration", *Appl. Phys. Lett.* **29**:3 (1976), 131–133.

[Bower and Craft 1998] A. F. Bower and D. Craft, "Analysis of failure mechanisms in the interconnect lines of microelectronic circuits", *Fatigue Fract. Eng. Mater. Struct.* **21**:5 (1998), 611–630.

[Bower and Freund 1993] A. F. Bower and L. B. Freund, "Analysis of stress-induced void growth mechanisms in passivated interconnect lines", *J. Appl. Phys.* **74**:6 (1993), 3855–3868.

[Bower and Shankar 2007] A. F. Bower and S. Shankar, "A finite element model of electromigration induced void nucleation, growth and evolution in interconnects", *Model. Simul. Mater. Sci. Eng.* **15**:8 (2007), 923–940.

[Cho and Thompson 1989] J. Cho and C. V. Thompson, "Grain size dependence of electromigration-induced failures in narrow interconnects", *Appl. Phys. Lett.* **54**:25 (1989), 2577–2579.

[Dalleau and Weide-Zaage 2001] D. Dalleau and K. Weide-Zaage, "Three-dimensional voids simulation in chip metallization structures: a contribution to reliability evaluation", *Microelectron. Reliab.* **41**:9-10 (2001), 1625–1630.

[Dong and Li 2009] X. Dong and Z. H. Li, "An analytical solution for motion of an elliptical void under gradient stress field", *Appl. Phys. Lett.* **94**:7 (2009), art. id. 071909.

[Dreyer and Varker 1992] M. L. Dreyer and C. J. Varker, "Electromigraton [sic] activation energy dependence on AlCu interconnect linewidth and microstructure", *Appl. Phys. Lett.* **60**:15 (1992), 1860–1862.

[Dwyer 2010] V. M. Dwyer, "An investigation of electromigration induced void nucleation time statistics in short copper interconnects", *J. Appl. Phys.* **107**:10 (2010), art. id. 103718.

[Dwyer 2011] V. M. Dwyer, "Analysis of critical-length data from electromigration failure studies", *Microelectron. Reliab.* **51**:9-11 (2011), 1568–1572.

[Fridline and Bower 1999] D. R. Fridline and A. F. Bower, "Influence of anisotropic surface diffusivity on electromigration induced void migration and evolution", *J. Appl. Phys.* **85**:6 (1999), 3168–3174.

[Fridline and Bower 2002] D. Fridline and A. Bower, "Numerical simulations of stress induced void evolution and growth in interconnects", *J. Appl. Phys.* **91**:4 (2002), 2380–2390.

[Giroux et al. 1995] F. Giroux, H. Roede, C. Gounelle, P. Mortini, and G. Ghibaudo, "Linewidth influence on electromigration tests at wafer level on TiN/AlCu/TiN/Ti metal lines", pp. 114–121 in *Conference on Microelectronic Manufacturing Yield, Reliability, and Failure Analysis* (Austin, TX, 1995), edited by G. Rao and M. Piccoli, Proc. SPIE **2635**, SPIE, Bellingham, WA, 1995.

[Gungor and Maroudas 1999] M. R. Gungor and D. Maroudas, "Nonhydrostatic stress effects on failure of passivated metallic thin films due to void surface electromigration", *Surf. Sci.* **432**:3 (1999), L604–L610.

[He and Huang 2014] D. He and P. Z. Huang, "A finite-element analysis of intragranular microcracks in metal interconnects due to surface diffusion induced by stress migration", *Comput. Mater. Sci.* **87** (2014), 65–71.

[He and Huang 2015] D. He and P. Z. Huang, "A finite-element analysis of in-grain microcracks caused by surface diffusion induced by electromigration", *Int. J. Solids Struct.* **62** (2015), 248–255.

[Herring 1999] C. Herring, "Surface tension as a motivation for sintering", pp. 33–69 in *Fundamental contributions to the continuum theory of evolving phase interfaces in solids*, edited by J. M. Ball et al., Springer, 1999.

[Huang and Sun 2004] P. Z. Huang and J. Sun, "A numerical analysis of intergranular penny-shaped microcrack shrinkage controlled by coupled surface and interface diffusion", *Metall. Mater. Trans. A* **35**:4 (2004), 1301–1309.

[Huang et al. 2003a] P. Z. Huang, Z. H. Li, J. Sun, and H. Gao, "Morphological healing evolution of intragranular penny-shaped microcracks by surface diffusion, I: Simulation", *Metall. Mater. Trans. A* **34**:2 (2003), 277–285.

[Huang et al. 2003b] P. Z. Huang, J. Sun, and Z. H. Li, "Axisymmetric finite-element simulation of grain growth behaviour", *Model. Simul. Mater. Sci. Eng.* **11**:1 (2003), 41–55.

[Huang et al. 2003c] P. Z. Huang, J. Sun, and Z. H. Li, "Evolution of penny-shaped microcracks by interface migration", *Int. J. Solids Struct.* **40**:8 (2003), 1959–1972.

[Huntington and Grone 1961] H. B. Huntington and A. R. Grone, "Current-induced marker motion in gold wires", *J. Phys. Chem. Solids* **20**:1-2 (1961), 76–87.

[Kraft and Arzt 1995] O. Kraft and E. Arzt, "Numerical simulation of electromigration-induced shape changes of voids in bamboo lines", *Appl. Phys. Lett.* **66**:16 (1995), 2063–2065.

[Kraft et al. 1993] O. Kraft, S. Bader, J. E. Sanchez, and E. Arzt, "Observation and modelling of electromigration-induced void growth in Al-based interconnects", *Mater. Res. Soc. Proc.* **309** (1993), 199–204.

[Krug and Dobbs 1994] J. Krug and H. T. Dobbs, "Current-induced faceting of crystal surfaces", *Phys. Rev. Lett.* **73**:14 (1994), 1947–1950.

[Li et al. 2010] Y. Li, Z. Li, X. Wang, and J. Sun, "Analytical solution for motion of an elliptical inclusion in gradient stress field", *J. Mech. Phys. Solids* **58**:7 (2010), 1001–1010.

[Lin et al. 2017] S.-K. Lin, Y.-C. Liu, S.-J. Chiu, Y.-T. Liu, and H.-Y. Lee, "The electromigration effect revisited: non-uniform local tensile stress-driven diffusion", *Sci. Rep.* **7** (2017), art. id. 3082.

[Liu and Yu 2006] Z. Liu and H.-H. Yu, "A numerical study on the effect of mobilities and initial profile in thin film morphology evolution", *Thin Solid Films* **513**:1-2 (2006), 391–398.

[Liu et al. 1998] Y. K. Liu, C. L. Cox, and R. J. Diefendorf, "Finite element analysis of the effects of geometry and microstructure on electromigration in confined metal lines", *J. Appl. Phys.* **83**:7 (1998), 3600–3608.

[Schimschak and Krug 1997] M. Schimschak and J. Krug, "Surface electromigration as a moving boundary value problem", *Phys. Rev. Lett.* **78**:2 (1997), 278–281.

[Sun and Suo 1997] B. Sun and Z. Suo, "A finite element method for simulating interface motion, II: Large shape change due to surface diffusion", *Acta Mater.* **45**:12 (1997), 4953–4962.

[Sun et al. 1994] B. Sun, Z. Suo, and A. G. Evans, "Emergence of cracks by mass transport in elastic crystals stressed at high temperatures", *J. Mech. Phys. Solids* **42**:11 (1994), 1653–1677.

[Sun et al. 1997] B. Sun, Z. Suo, and W. Yang, "A finite element method for simulating interface motion, I: Migration of phase and grain boundaries", *Acta Mater.* **45**:5 (1997), 1907–1915.

[Vairagar et al. 2004] A. V. Vairagar, S. G. Mhaisalkar, A. Krishnamoorthy, K. N. Tu, A. M. Gusak, M. A. Meyer, and E. Zschech, "In situ observation of electromigration-induced void migration in dual-damascene Cu interconnect structures", *Appl. Phys. Lett.* **85**:13 (2004), 2502–2504.

[Vanstreels et al. 2014] K. Vanstreels, P. Czarnecki, T. Kirimura, Y. K. Siew, I. D. Wolf, J. Bömmels, Z. Tőkei, and K. Croes, "In-situ scanning electron microscope observation of electromigration-induced void growth in 30 nm 1/2 pitch Cu interconnect structures", *J. Appl. Phys.* **115**:7 (2014), art. id. 074305.

[Wang and Yao 2017a] Y. Wang and Y. Yao, "A theoretical analysis of the electromigration-induced void morphological evolution under high current density", *Acta Mech. Sinica* **33**:5 (2017), 868–878.

[Wang and Yao 2017b] Y. Wang and Y. Yao, "A theoretical analysis to current exponent variation regularity and electromigration-induced failure", *J. Appl. Phys.* **121**:6 (2017), art. id. 065701.

[Wang et al. 2006] H. Wang, Z. H. Li, and J. Sun, "Effects of stress and temperature gradients on the evolution of void in metal interconnects driven by electric current and mechanical stress", *Model. Simul. Mater. Sci. Eng.* **14**:4 (2006), 607–615.

[Xia et al. 1997] L. Xia, A. F. Bower, Z. Suo, and C. F. Shih, "A finite element analysis of the motion and evolution of voids due to strain and electromigration induced surface diffusion", *J. Mech. Phys. Solids* **45**:9 (1997), 1473–1493.

[Yao et al. 2009] Y. Yao, L. M. Keer, and M. E. Fine, "Electromigration effect on pancake type void propagation near the interface of bulk solder and intermetallic compound", *J. Appl. Phys.* **105**:6 (2009), art. id. 063710.

[Zhang et al. 1998] Y. W. Zhang, A. F. Bower, L. Xia, and C. F. Shih, "Three dimensional finite element analysis of the evolution of voids and thin films by strain and electromigration induced surface diffusion", *J. Mech. Phys. Solids* **47**:1 (1998), 173–199.

[Zhang et al. 2010] L. Zhang, J. P. Zhou, J. Im, P. S. Ho, O. Aubel, C. Hennesthal, and E. Zschech, "Effects of cap layer and grain structure on electromigration reliability of Cu/low-k interconnects for 45 nm technology node", pp. 581–585 in *2010 IEEE International Reliability Physics Symposium* (Anaheim, CA, 2010), IEEE, Piscataway, NJ, 2010.

[Zschech et al. 2010] E. Zschech, R. Hübner, O. Aubel, and P. S. Ho, "EM and SM induced degradation dynamics in copper interconnects studied using electron microscopy and X-ray microscopy", pp. 574–580 in *IEEE International Reliability Physics Symposium* (Anaheim, CA, 2010), IEEE, Piscataway, NJ, 2010.

LINYONG ZHOU: zhouly@nuaa.edu.cn
State Key Laboratory of Mechanics and Control of Mechanical Structures, Nanjing University of Aeronautics and Astronautics, 29 Yudao Street, Nanjing, 210016, China

PEIZHEN HUANG: pzhuang@nuaa.edu.cn
State Key Laboratory of Mechanics and Control of Mechanical Structures, Nanjing University of Aeronautics and Astronautics, 29 Yudao Street, Nanjing, 210016, China

QIANG CHENG: qcheng@nuaa.edu.cn
State Key Laboratory of Mechanics and Control of Mechanical Structures, Nanjing University of Aeronautics and Astronautics, 29 Yudao Street, Nanjing, 210016, China

msp

UNCERTAINTY QUANTIFICATION AND SENSITIVITY ANALYSIS
OF MATERIAL PARAMETERS
IN CRYSTAL PLASTICITY FINITE ELEMENT MODELS

MIKHAIL KHADYKO, JACOB STURDY, STÉPHANE DUMOULIN,
LEIF RUNE HELLEVIK AND ODD STURE HOPPERSTAD

A number of studies have directly compared measurements of polycrystals' deformation to the solution of a crystal plasticity model of the same polycrystal. An accurate representation of the full 3D microstructure and the boundary conditions has been shown to be important to obtain a good correspondence between the behaviour of the real and the simulated polycrystal. However, much less is known about the relationship between the global and the local solutions of crystal plasticity models and the influence of material parameters on the local response of the polycrystal. To address these questions, uncertainty quantification and sensitivity analysis are performed on finite element models of oligocrystals with a crystal plasticity material model. The results show significant variations in the simulated stress and strain fields due to variations in the material parameters. Sensitivity analysis is used to quantify the contribution of crystal orientation, latent hardening and other material model parameters to the variability of the crystal plasticity finite element model solution. The uncertainty in the stress and strain fields and their sensitivities vary between the oligocrystals, but nevertheless, some distinct trends can be identified. The most prominent trend is that, in general, the solution is most sensitive to the variations of the latent hardening description and the crystallographic orientations of the constituent crystals.

1. Introduction

In the last decade, advances in both computational methods and experimental techniques have made it possible to create very detailed and precise finite element (FE) models of real polycrystals and directly compare their simulated responses to experimental observations. Due to current computational limitations, the polycrystals studied are usually either very small [Guery et al. 2014; 2016; Heripre et al. 2007; Musienko et al. 2007; Zhang et al. 2015; Pinna et al. 2015; Lim et al. 2014], or their constituent grains are very big and few in number [Sachtleber et al. 2002; Hoc et al. 2003; Saai et al. 2010; Badulescu et al. 2011; Cuadra et al. 2016; Zhang et al. 2016; Dumoulin et al. 2013]. The small number of grains allows measuring and comparing the local strain fields on the surfaces of the specimens to the simulation results. Results from these kind of experimental studies may be used to calibrate single crystal plasticity (CP) models in a direct and consistent way, and are important for the modelling of localisation and fracture using crystal plasticity finite element methods (CP-FEM), which rely on the accuracy of the local solution of the stress and strain fields. Local measurements of strain fields in polycrystals may also reveal the influence of various microstructural features on the mechanical behaviour of the crystals, such as grain boundaries and inclusions.

The numerical aspects of this type of studies are examined in [Lim et al. 2016]. The role of mesh resolution, grain boundary representation and boundary conditions (BCs) is studied using a microstructure generated with a phase-field model. In [Heripre et al. 2007; Musienko et al. 2007; Zhang et al. 2015], simulations with realistic (obtained from the *in-situ* measurements with e.g. digital image correlation) and simplified BCs were compared, and realistic BCs were shown to be important for the accuracy of the simulation results. Another factor relevant for the accuracy of the predictions of the CP-FEM model is the real 3D microstructure, lying beneath the surface of the specimen, on which the strain measurements are performed. In [Heripre et al. 2007; Musienko et al. 2007; Zeghadi et al. 2007], it was demonstrated that it is not possible to accurately predict the strain field on the surface of a specimen with significant thickness without accounting for the whole structure.

The role of the CP model parameters has only been studied briefly. In [Lim et al. 2014], the way the grain orientations are assigned to the elements of the CP-FEM model was studied. The most often used method is assigning the average orientation to all elements within one grain, which was compared to assigning a locally measured orientation to each corresponding element. The relative influence of work-hardening parameters and BCs was compared in [Zhang et al. 2015]. Yet to the best of the authors' knowledge, no extensive quantitative studies of the sensitivity of the local CP-FEM solutions to the parameters of the constitutive model have been performed. The CP model parameters are usually obtained by comparing the simulated and experimental force-displacement curves. In the fitting procedure, the material parameters are either chosen based on previous studies (usually the case with the latent hardening description), varied within some physically plausible range (as with the dislocation accumulation and annihilation terms in the Kocks–Mecking type models [Teodosiu et al. 1991]), or varied more or less arbitrary (as for the parameters of the Pierce–Asaro–Needleman model [Needleman et al. 1985]). One caveat when using such methods is that different sets of parameters may result in similar global force-displacement responses but different local solutions [Khadyko et al. 2016a]. To address this possibility, the investigation in [Guery et al. 2014] attempted to use both the local and global response of the polycrystal in the fitting procedure and found that obtaining a set of parameters that satisfies both the global force-displacement curve and the local strain field equally well was not possible. Given these limitations, it is desirable to assess the impact of the uncertainty in the CP model parameters through the mathematical framework of uncertainty quantification (UQ) and sensitivity analysis (SA). UQ can quantify the variability of model predictions for given uncertainty about model parameters, while SA evaluates how individual parameters contribute to this variability.

The perspective of UQSA views a computational model as a function that relates inputs, z, to outputs or quantities of interest $y = f(z)$. However, instead of treating z as exactly known, the uncertainty about input values is accounted for by treating them as random variables with a probability distribution that represents the likelihood or plausibility of different values of the inputs, e.g. if an input is known only to be bounded between two values it may be represented as a uniform random variable. Thus the output of the model is not a single deterministic value but a random variable with a probability distribution that may be analysed to quantify the uncertainty and further the contribution of individual inputs to that uncertainty may be quantified by sensitivity analysis.

Various UQ and SA tools have been applied in a wide range of scientific fields including structural analysis [Ghiocel and Ghanem 2002], hydrology [Hall et al. 2009], environmental engineering [Fassò and Cameletti 2010], biomechanics and many more. An overview and guide to the application of UQSA

methods may be found in [Eck et al. 2016]. The methods themselves are not specific to any particular field and may be applied to analyse any kind of model relating uncertain inputs to uncertain outputs. For example a parametric study of the phenomenological plasticity and fracture models was performed in [Pardoen 2006].

The main focus of the UQ studies in crystal plasticity has been the variability of the microstructure (grain morphology and crystallographic texture) and the material processing parameters and their influence on the global response of the polycrystalline materials. A number of studies have been performed by Zabaras and co-authors [Chen and Zabaras 2014; Wen and Zabaras 2012; Kouchmeshky and Zabaras 2010]. These studies develop a methodology, summarized in [Zabaras 2010], which reduces the complexity of a polycrystals' microstructure to a set of functions, which may be treated by the UQ methods. The propagation of uncertainty from the microstructure to the global response of the material is a topic of several other studies [Madrid et al. 2014; Salvati and Korsunsky 2017; Hiriyur et al. 2011; Stevens 2016]. A review of the UQSA methods applied in material science [Chernatynskiy et al. 2013] suggests that this field is still in its nascent stage.

Some attempts to assess the sensitivity of the CP-FEM solution to e.g. uncertainty in the latent hardening matrix were made in [Pham et al. 2017; Renner et al. 2016]. In both studies, each independent component of the matrix was assigned a high value, while all others were held at unity. Then the response of the model for all cases was qualitatively compared. This is a local form of UQSA. Local methods examine the effect of a change around a reference value for one model input while keeping all other inputs fixed. In many cases the dependency of the output on the input parameters may be non-additive, non-monotonic, and non-linear, at least in some locations of the input space. Therefore the results obtained by local methods could be misleading as these effects will not be reflected by the local analysis. Global methods consider the whole input space and can account for non-additive, non-monotonic, and non-linear dependencies of the output on the input and are thus in general more reliable and informative than local methods.

Global methods of UQSA can be categorized as intrusive or non-intrusive. Intrusive approaches require the uncertainty in the model inputs to be substituted into the model to derive new governing equations accounting for uncertainty. On the other hand, non-intrusive methods do not require modification of the existing models. Model outcomes are obtained using the usual (deterministic) solver for a set of different input samples. UQSA is then based on the outputs obtained for each input sample. This approach can be applied to any model with any numerical implementation, and it is therefore much better suited for the present study. In this work the polynomial chaos (PC) method [Sudret 2008] is used. The method consists of the following steps:

(1) Identification of the outputs of interest (in our case some way of representing the stress and strain fields as a convenient set of values is necessary).

(2) Identification and assessment of the distribution of the uncertain inputs (in our case the uncertain inputs are the material model parameters and their distribution should be chosen).

(3) Sampling of the input space to acquire samples (i.e., discrete sets of material parameters should be picked from the chosen distribution).

(4) Evaluation of the deterministic model to obtain the outputs, corresponding to the inputs from the previous step (i.e., CP-FEM simulations with the sampled sets of material parameters are performed).

(5) Calculation of UQSA measures.

(6) Assessment of convergence of UQSA measures.

A more detailed overview of the methods may be found in [Eck et al. 2016].

As the appropriate values of material parameters for a given CP-FEM model are generally quite uncertain, this study investigates the resulting uncertainty of the stress and strain fields of a CP-FEM solution due to the uncertainty in the material parameters. Additionally, sensitivity analysis investigates the relative contributions of each material parameter. The subject of UQSA is a set of 2D and 3D oligocrystals subjected to uniaxial tensile loading. The UQSA method allows performing a global quantitative analysis of the said uncertainties and sensitivities, unlike the local qualitative studies previously performed with CP-FEM. In addition to improving understanding of the effects of material parameters in CP-FEM simulations, the article also aims more broadly to introduce the aforementioned UQSA methods and tools into CP-FEM.

2. Uncertainty quantification and sensitivity analysis

To account for the uncertainty about parameters they are treated as a random vector, $\mathbf{Z}$, where the probability distribution of $\mathbf{Z}$ represents the likelihood or plausibility of different values of the input. Thus the quantity of interest is a random variable defined by applying the function to the random variable $\mathbf{Z}$, i.e., $Y = f(\mathbf{Z})$.[1] The uncertainty about the quantity of interest may be quantified by the expected value and variance of Y:

$$\mathrm{E}(Y) = \int_{-\infty}^{\infty} y \rho_Y(y)\, dy,$$

$$\mathrm{Var}(Y) = \int_{-\infty}^{\infty} \{Y - \mathrm{E}(Y)\}^2 \rho_Y(y)\, dy,$$

(1)

where $\rho_Y(y)$ is simply the probability density function of Y.

Beyond accounting for the inherent uncertainty about the model prediction, sensitivity analysis (SA) can determine the contribution of particular components of $\mathbf{Z}$, i.e., specific inputs, to the uncertainty of Y. Variance based sensitivity analysis decomposes the variance of the model output, $\mathrm{Var}(Y)$, into portions attributable to specific inputs or combinations of inputs. There are two widely used sensitivity indices based on this decomposition of variance. The first is called the first order or main sensitivity index of input Z_i and is given by

$$S_{M,i} = \frac{\mathrm{Var}\{E(Y|Z_i)\}}{\mathrm{Var}(Y)}.$$

(2)

This index measures the fraction of total variance that is attributable to variability of Z_i independent of the variability of all other inputs and if Z_i were known exactly the $\mathrm{Var}(Y)$ would be expected to decrease by that proportion. The main sensitivity index $S_{M,i}$ is useful for prioritizing which parameters may be most influential on the model behaviour as a large value indicates that changes in Z_i alone have

---

[1]Note that deterministic or known values are traditionally denoted with lowercase letters, while uppercase letters represent random variables. Values realized from the random variable $\mathbf{Z}$ or specific points within the range of $\mathbf{Z}$ are denoted by z as their values are known and have no uncertainty.

significant impacts on the model output. The second index is called the total sensitivity index of input Z_i and is defined as

$$S_{T,i} = \frac{\mathrm{E}\{\mathrm{Var}(Y|\mathbf{Z}_{\neg i})\}}{\mathrm{Var}(Y)}, \tag{3}$$

where $\mathbf{Z}_{\neg i}$ is the vector of all inputs except Z_i. This index measures the expected amount of variability remaining if all other variables except Z_i were known exactly. It may be useful for identifying irrelevant parameters as a low value of $S_{T,i}$ suggests that Z_i is not an influential input on the model output, and conversely measurements of Y do not provide significant information about Z_i in the context of parameter estimation and design of experiments, e.g. [Rodriguez-Fernandez et al. 2007]. Thus sensitivity indices may also be used to identify the viability of estimating parameters from particular measurements.

The case where the first order index is quite small while the total index is large indicates that the parameter has strong interactive effects. In other words, the parameter's influence is largely dependent on the values of other parameters, thus the effect of changing its value alone may cause very different responses. For example, a parameter may be important in a component of the model that is activated only for certain levels of other parameters.

A number of methods may be employed to characterize $Y = f(\mathbf{Z})$ or its probability distribution such as Monte Carlo methods or modifying the governing equations to solve the stochastic problem directly [Eck et al. 2016]. In this study we use a nonintrusive method[2] called polynomial chaos which represents the function $f(z)$ as a series of orthogonal polynomials:

$$f_N(z) = \sum_{i=0}^{k(N)} c_i \Phi_i(z), \quad k = \binom{D+N}{N} = \frac{(D+N)!}{N!\,D!}, \tag{4}$$

where N denotes the highest order polynomial, k denotes the number of terms, and D is the number of components in $\mathbf{Z}$. The basis polynomials are chosen to be orthogonal with respect to the probability density $\rho_\mathbf{Z}(z)$ of $\mathbf{Z}$ such that

$$\int_{-\infty}^{\infty} \Phi_i(z)\Phi_j(z)\rho_\mathbf{Z}(z)\,dz = \mathrm{E}(\Phi_i(\mathbf{Z})\Phi_j(\mathbf{Z})) = \gamma_i \delta_{ij} \quad \text{(no sum)}, \tag{5}$$

where E is the expected value, γ_i is a normalisation constant associated with Φ_i, and δ_{ij} is the Kronecker delta. This orthogonality ensures that the probabilistic moments of $Y_N = f_N(\mathbf{Z})$ are simply algebraic combinations of the coefficients, c_i, and thus once the coefficients are obtained the expected value, variance, and sensitivity indices are easily calculated. To evaluate the coefficients a linear least squares problem is formulated by evaluating the model at a number of different points in the parameter space sampled according to the probability distribution of $\mathbf{Z}$ and the output values are regressed on the basis functions. The convergence rate of $Y_N = f_N(\mathbf{Z})$ with respect to the maximum order N is dependent on the smoothness of $f(z)$, but typically only order 4 or 5 is sufficient to achieve converged and accurate estimates of expected value, variance and sensitivity indices. This must be checked by verifying that the estimates are consistent between successive orders of approximation. In this study, it was ensured that the UQSA measures calculated from $f_N(\mathbf{Z})$ and $f_{N-1}(\mathbf{Z})$ have a relative precision within 1%.

---

[2]Nonintrusive means that the underlying deterministic model does not need to be modified.

In this study the Python package *chaospy* [Feinberg and Langtangen 2015] is employed to sample from the distribution of $\boldsymbol{Z}$, generate basis polynomials for specified orders of truncation, solve the regression problem and finally evaluate the variability and sensitivity indices.

3. Numerical models

3.1. *Single crystal plasticity model.* The single crystal plasticity model used in this work is formulated within a finite deformation framework. The total deformation gradient $\boldsymbol{F}$ is multiplicatively decomposed as follows [Needleman et al. 1985]:

$$\boldsymbol{F} = \boldsymbol{F}^e \boldsymbol{F}^p, \tag{6}$$

where $\boldsymbol{F}^e$ and $\boldsymbol{F}^p$ are the elastic and plastic part of $\boldsymbol{F}$, respectively. The plastic part $\boldsymbol{F}^p$ transforms the body from the initial to the intermediate configuration by plastic slip, whereas the elastic part $\boldsymbol{F}^e$ transforms the body from the intermediate to the current configuration by elastic deformation and rigid body rotation. The plastic velocity gradient $\bar{\boldsymbol{L}}^p$ on the intermediate configuration is defined by

$$\bar{\boldsymbol{L}}^p = \dot{\boldsymbol{F}}^p (\boldsymbol{F}^p)^{-1} = \sum_{\alpha=1}^{n} \dot{\gamma}^a \boldsymbol{m}_0^\alpha \otimes \boldsymbol{n}_0^\alpha, \tag{7}$$

where the orthonormal vectors $\boldsymbol{m}_0^\alpha$ and $\boldsymbol{n}_0^\alpha$ are the slip direction and slip plane normal vectors, respectively, for a slip system α in the initial and intermediate configurations, $\dot{\gamma}^\alpha$ is the slip rate on slip system α, and n is the total number of slip systems.

The elastic Green strain tensor $\bar{\bar{\boldsymbol{E}}}^e$ defined with respect to the intermediate configuration is given by

$$\bar{\boldsymbol{E}}^e = \frac{1}{2}(\bar{\boldsymbol{C}}^e - \boldsymbol{I}), \quad \bar{\boldsymbol{C}}^e = (\boldsymbol{F}^e)^T \boldsymbol{F}^e, \tag{8}$$

where $\bar{\boldsymbol{C}}^e$ is the elastic right Cauchy–Green deformation tensor and $\boldsymbol{I}$ is the second-order unity tensor. The second Piola–Kirchhoff stress tensor $\bar{\boldsymbol{S}}$ on the intermediate configuration reads as

$$\bar{\boldsymbol{S}} = J(\boldsymbol{F}^e)^{-1} \boldsymbol{\sigma} (\boldsymbol{F}^e)^{-T}, \tag{9}$$

where $\boldsymbol{\sigma}$ is the Cauchy stress tensor and $J = \det \boldsymbol{F}$ is the Jacobian determinant. A linear hyperelastic relation for small elastic strains is defined by

$$\bar{\boldsymbol{S}} = \bar{\boldsymbol{C}}_{el}^{\bar{S}} : \bar{\boldsymbol{E}}^e \tag{10}$$

where $\bar{\boldsymbol{C}}_{el}^{\bar{S}}$ is the fourth-order tensor of elastic moduli. For the FCC lattice, on which this study focuses, this tensor has three independent components describing the elastic anisotropy of the crystal.

The plastic flow is described by [Hutchinson 1976]:

$$\dot{\gamma}^\alpha = \dot{\gamma}_0 \left(\frac{|\tau^\alpha|}{\tau_c^\alpha} \right)^{\frac{1}{m}} \operatorname{sgn}(\tau^\alpha), \tag{11}$$

where $\dot{\gamma}_0$ is the reference slip rate, m is the instantaneous strain rate sensitivity, τ_c^α is the yield strength of slip system α, and the resolved shear stress τ^α is obtained as

$$\tau^\alpha = \bar{\boldsymbol{C}}^e \bar{\boldsymbol{S}} : (\boldsymbol{m}_0^\alpha \otimes \boldsymbol{n}_0^\alpha). \tag{12}$$

The hardening is defined by

$$\dot{\tau}_c^{\alpha} = \theta(\Gamma) \sum_{\beta=1}^{n} q_{\alpha\beta} |\dot{\gamma}^{\beta}|, \tag{13}$$

where $\theta(\Gamma)$ is the master hardening modulus, $q_{\alpha\beta}$ is the matrix of self-hardening and latent-hardening coefficients, and the accumulated slip Γ is defined by the evolution equation:

$$\dot{\Gamma} = \sum_{\alpha=1}^{n} |\dot{\gamma}^{\alpha}|. \tag{14}$$

The master hardening modulus $\theta(\Gamma)$ is defined as follows [Tome et al. 1984]:

$$\theta(\Gamma) = \theta_1 + \left(\theta_0 - \theta_1 + \frac{\theta_0 \theta_1}{\tau_1} \Gamma \right) \exp\left(-\frac{\theta_0}{\tau_1} \Gamma \right), \tag{15}$$

where θ_0, θ_1 and τ_1 are material parameters. The initial slip resistance τ_0 is assumed equal for all slip systems.

The crystal plasticity material model was implemented as a user-material subroutine, using the explicit integration scheme of [Grujicic and Batchu 2002].

3.2. *CP-FEM models.*

Investigating the effects of uncertainty about CP model parameters requires considering microstructure models that satisfy several constraints. The models should be generic enough such that the results obtained are representative of a range of similar models. Further, the models should be small enough to make running a multitude of simulations feasible. The models should also include enough grains to provide a wide range of interactions between the grains and the resulting inhomogeneous stress and strain fields. Finally, the meshes must be fine enough to resolve these fields in detail yet coarse enough for a fast and efficient simulation.

Therefore the morphology chosen for the study was a generic Voronoi tessellation type structure with ten approximately equiaxed convex grains representing oligocrystals. Both a 2D structure with plane-strain conditions and a 3D structure were used. The structures are shown in Figure 1. The model was subjected to tension by applying a velocity along the x-axis to its right edge (or face in case of 3D model) which smoothly ramps up to a constant value. The left edge (or face) of the model is constrained in displacement in the x-direction and the other edges (faces) are free. The effect of BCs on the local stress and strain fields in polycrystals was studied elsewhere [Heripre et al. 2007; Zhang et al. 2015]. To explore different configurations and interactions of hard/soft orientations, 5 different sets of 10 random crystallographic orientations were assigned to the 10 grains of the 2D and 3D models. This provided 5 models with markedly different stress and strain fields on which the sensitivities could be calculated and compared.

The mesh of the 2D CP-FEM model consists of 3004 two-dimensional plane-strain elements, and that of the 3D model consists of 8000 brick elements. Reduced integration and the Flanagan–Belytschko stiffness-based hourglass control [Flanagan and Belytschko 1981] were used in both cases. The explicit solver of the nonlinear FEM code LS-DYNA [Hallquist 2016] was used in the calculations. Mass-scaling was applied to reduce the computation time and the kinetic energy was controlled at every step to ensure that it was very small compared to the total energy and that the simulation remained quasi-static.
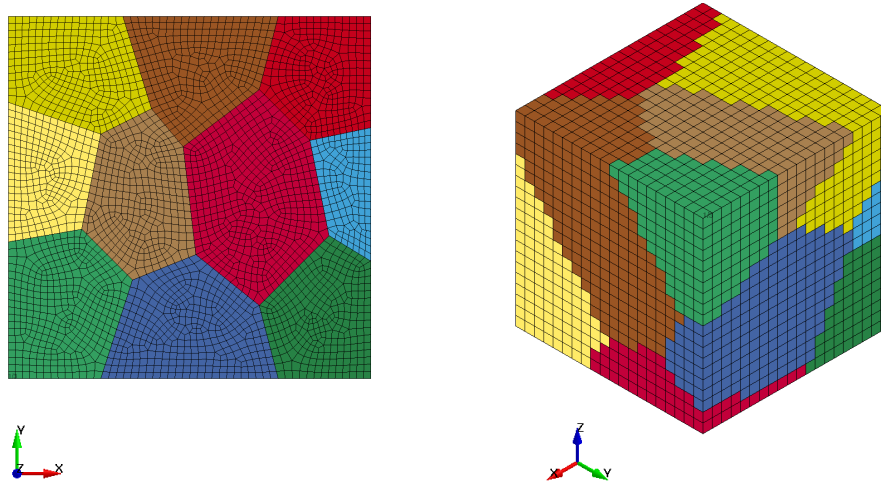
Figure 1. Illustrations of the 2D plane-strain and 3D microstructures.

Parameter	AA6063-T4	AA6063-T7
$\Delta\varphi_1$ (°)	$-2\ldots0\ldots2$	$-2\ldots0\ldots2$
τ_0 (MPa)	$20\ldots30\ldots40$	$40\ldots60\ldots80$
τ_1 (MPa)	$17\ldots26\ldots35$	$6\ldots9\ldots12$
θ_0 (MPa)	$163\ldots244\ldots325$	$129\ldots194\ldots257$
θ_1 (MPa)	$8\ldots12\ldots16$	$1\ldots2\ldots3$
q	$1\ldots1.5\ldots2$	$1\ldots1.5\ldots2$

Table 1. Ranges of the material model parameters for the 2D and 3D structures.

3.3. *Distribution of material parameters.*

In this study, aluminium is used as a model material. The material parameters are therefore based on the parameters of Al alloys studied previously in [Khadyko et al. 2016b]. The baseline values and ranges of the material parameters are summarized in Table 1.

The elastic constants depend on the interatomic potentials, are similar in all Al alloys, and may be measured with high accuracy. Thus, the elastic constants were excluded from the sensitivity study. Crystal plasticity simulations and experiments are often limited to quasi-static cases (very low strain rates), for which rate-independent and rate-dependent single crystal plasticity models produce identical results [Pan and Rice 1983; Gambin 1992]. The choice of the reference slip rate $\dot{\gamma}_0$ and the rate sensitivity m does not affect the solution as long as m is sufficiently small to preserve rate-insensitivity. Thus these parameters were also excluded from the sensitivity study. The values used for the elasticity constants and the constants governing rate dependence are summarized in Table 2.

c_{11} (MPa)	c_{12} (MPa)	c_{44} (MPa)	$\dot{\gamma}_0$ (s^{-1})	m
106430	60350	28210	0.010	0.005

Table 2. Elastic and rate sensitivity parameters of the crystal plasticity model.

The Euler angles describing the orientation of the crystal are parameters that do not appear explicitly in the material model, but are nevertheless crucial. In this work, the Euler angles are defined following the conventions established in [Bunge 1982]. The crystal orientations are usually measured by EBSD on a grid covering a patch of a polycrystal. Errors in the measurements may introduce various sources of random and systematic errors to the orientation. In CP-FEM models, orientations are most often assigned by finding the average of the orientations measured within a crystalline grain and assigning the resulting orientation to all elements within this grain. An alternative approach uses the grid points of the EBSD scan as the centroids of the elements of the CP-FEM model and assigns the orientation measured in each point to the corresponding element. The first approach is the most widespread in CP-FEM models, thus it is utilized in this study. The first Euler angle φ_1 (i.e., the rotation around the z-axis according to the coordinate system defined in Figure 1) is assumed to vary around the base value within a $\pm 2°$ range for all the grains in the model. This may be e.g. representing the error of the specimen positioning in the electronic microscope, or other systematic error.

The next group of parameters includes the initial slip resistance τ_0 and the hardening parameters θ_0, θ_1 and τ_1. These parameters do not have a direct physical connection to the microstructure of the material and can only be derived indirectly from the force-displacement curve and the deformation of the specimen. Considering all the errors associated with experimental and numerical procedures, these parameters are highly uncertain. In this work, we use two different baseline sets of the initial slip resistance and the hardening parameters. One represents a ductile alloy reinforced mainly by solid solution of the alloying elements, with values corresponding to AA6063-T4, and the other represents a stronger but less ductile alloy reinforced mainly by precipitate particles, with values corresponding to AA6063-T7 [Khadyko et al. 2016b]. The material parameters are assumed to vary within a range of $\pm 30\%$ of the baseline value.

The next parameter is the latent hardening coefficient q. This parameter is very difficult to evaluate experimentally, so its value is based on the estimations provided by e.g. [Kocks and Brown 1966; Franciosi et al. 1980] or some geometrical arguments [Liu et al. 2015]. Quite often, it is assumed for simplicity to be unity (i.e., latent hardening equals self-hardening), as in [Erinosho et al. 2013]. The most common value used in CP-FEM simulations is $q = 1.4$, though $q = 1.6$ was also proposed by [Kocks and Brown 1966]. In this work, it is assumed that the latent hardening of the crystal can be described by the latent hardening matrix with one independent parameter, and that the most correct value of this parameter is within the range $q \in [1, 2]$ with $q = 1.5$ as the baseline value.

3.4. *Identification of the outputs of interest.* Simulations with material parameters lying in the centre of the respective ranges (see Table 1) are used as a baseline to which all other simulations are compared by computing the normalized root mean squared deviation (RMSD) of the scalar field variable ϕ, defined by

$$\text{RMSD}(\phi) = \sqrt{\frac{1}{N_e} \sum_{n=1}^{N_e} \left(\frac{\phi_n}{\tilde{\phi}} - \frac{\phi_{0n}}{\tilde{\phi}_0} \right)^2}, \qquad (16)$$

where the local value ϕ_n of the variable ϕ is obtained in the n-th element of the N_e elements of the model, $\tilde{\phi}$ is a normalization factor calculated from the field ϕ. Further, ϕ_0 represents the baseline field and $\tilde{\phi}_0$ the corresponding normalization factor. The particular normalization values $\tilde{\phi}$ and $\tilde{\phi}_0$ used for each scalar field are discussed below. Note that RMSD is identical to root mean squared error, but in this case there is no error per se rather just a metric of the average deviation over the mesh.

The first scalar field variable is the equivalent plastic strain field, ε^p, conjugate with the von Mises norm of the stress field. The value of the equivalent plastic strain ε^p is calculated in each element of the model at different points of the deformation history (at approximately 5%, 10% and 15% global strain). Then, the field produced by the model with varied material parameters is compared to the field produced by the baseline simulation. In this case, ϕ is the equivalent plastic strain ε^p; ϕ_n and ϕ_{0n} are the equivalent plastic strains in the n-th element of the current and the baseline simulation, respectively; $\tilde{\phi}$ and $\tilde{\phi}_0$ are both the global strain (which should be equal to the average of the strain for all elements in this case and also identical for all simulations including the baseline). The $\text{RMSD}(\varepsilon^p)$ is a non-negative scalar that shows how much the normalized strain field in the current simulation with the current set of material parameters differs from the normalized strain field in the baseline case. Minimization of this or a similar function may be used in a material parameters identification procedure, as e.g. in [Guery et al. 2014].

The second field is the equivalent (von Mises) stress field, here denoted σ. Whereas the average plastic strain in all simulations was identical, the average stress varied greatly and depends strongly on the yield strength and work-hardening. In this case, ϕ is the equivalent stress σ; ϕ_n and $\tilde{\phi}$ are the equivalent stress in the n-th element and average equivalent stress in the current simulation; ϕ_{0n} and $\tilde{\phi}_0$ are the corresponding quantities for the baseline simulation. The third and fourth scalar fields applied in the sensitivity study are the hydrostatic pressure field P and the stress triaxiality field $T = -P/\sigma$. The RMSD of these fields is calculated in the same manner as for the equivalent stress field.

The final target of the sensitivity study is the global force-displacement curve. This curve is often used for the material parameter fitting, and as mentioned before, it was used alongside the local strain field for this purpose in [Guery et al. 2014] with little success. A typical fitting procedure would minimize the squared error between the experimental and the simulated force-displacement curve by varying the material parameters. Here the same type of measure is applied. The baseline curve is again used as reference (or provisional "experimental" curve) and the RMSD is defined by

$$\text{RMSD}(F) = \sqrt{\frac{1}{N_d} \sum_{i=1}^{N_d} \left(\frac{F(d_i) - F_0(d_i)}{F_0(d_i)} \right)^2}, \tag{17}$$

where $F(d)$ is the total force at displacement d in the current simulation, $F_0(d)$ is the corresponding force in the baseline simulation, N_d is the number of simulation history points where the force and displacement are obtained, and d_{N_d} is the maximum displacement.

3.5. *Evaluation of polynomial chaos expansions and UQSA measures.* To understand how much the variability of the parameters, denoted by the vector $Z = \begin{pmatrix} \Delta\varphi_1 & \tau_0 & \tau_1 & \theta_0 & \theta_1 & q \end{pmatrix}$, influences CP-FEM simulations, UQSA of the outputs of interests was performed for each of the configurations discussed in Section 3.2. As no statistical evidence was available to characterize the distribution of the parameters considered, each parameter was described as an independent uniform random variable with ranges given in Table 1, i.e., all values in the range are treated as equally valid.

UQSA for each configuration was performed by employing the *chaospy* software package [Feinberg and Langtangen 2015] to generate samples in the input space and basis polynomials, to estimate coefficients of the expansion based on a linear regression of the output value, and finally to estimate measures of uncertainty and sensitivity indices.

For each material type (T4 and T7), a set of sample values was generated according to the Hammersley quasi-random sequence [2013], as this sequence is nested and allows for successively increasing the number of points in the quasi-random sequence by only evaluating the number of additional samples required. The maximum polynomial order was $N = 5$, which requires estimating $k = 462$ coefficients, and thus 924 samples (simulations) for the chosen regression method. This order was chosen to ensure that the estimates of sensitivity indices agreed within 1% between successive orders of polynomials.

Evaluation of the CP-FEM models for each input sample was performed as described in Section 3.2, followed by post processing of each simulation to calculate the outputs of interest (see Section 3.4) corresponding to each input sample. For each post-processed output, the coefficients of a truncated polynomial expansion were estimated by the regression method, and subsequently the expected value, variance, standard deviation, and sensitivity indices were calculated from the coefficients.

3.6. *Averaging of results across orientations.* As discussed in Section 3.1, this analysis considered CP-FEM models based on two generic structures (one 2D and the other 3D as shown in Figure 1). Applying 5 unique combinations of crystallographic orientations to each of these generic structures generated 5 CP-FEM models for both 2D and 3D simulations. For each of these 5 models, uncertainty quantification and sensitivity analysis were conducted once over the range of T4 material parameters and again over the range of T7 material parameters. Thus, uncertainty and sensitivity measures were estimated for 20 distinct cases, i.e., 5 cases for each of 2D-T4, 2D-T7, 3D-T4, and 3D-T7 models.

As the exact sensitivities and uncertainties generally depend on the specific CP-FEM model, the goals of this UQSA were to investigate: (1) how much the quantities outlined in Section 3.2 vary on average over the range of material parameters, (2) if model sensitivities are consistent over the range of crystallographic orientations and structures, and (3) which, if any, parameters are consistently more influential on these quantities. As such, it was necessary to combine and summarize the UQSA results by averaging the results from each of the individual analyses conducted as well as calculating meaningful measures of the variability of these quantities across crystallographic orientations.

In this analysis RMSDs quantified the deviation of global force, equivalent plastic strain, equivalent stress, hydrostatic pressure, and stress triaxiality from a reference value calculated based on the average value of all parameters. This measure provides a convenient measure of the deviation of the model solution from the baseline solution at nominal parameter values. The UQ estimates the expected value and standard deviation of the RMSDs for a given set of crystallographic orientations. The expected values of the RMSDs measure how much the quantities of interest differ on average from the reference values. The standard deviation of the RMSDs quantifies the spread of these deviations over the possible parameter values, i.e., a low standard deviation suggests that most possible parameter sets produce values deviating from the reference values to a similar extent, whereas a large standard deviation of the RMSDs suggests that there are quite different levels of deviation for distinct points in the parameter space. To compare both of these aspects across sets of crystallographic orientations, the average value of the expected RMSDs as well as the average value of the standard deviation of RMSDs across all orientation sets within each group (2D-T4, 2D-T7, 3D-T4, and 3D-T7) were calculated. For each quantity of interest (see Section 3.2), the average RMSD and its associated average standard deviation are reported as

$$\overline{E(X)} \pm \overline{\text{std}(X)} = \frac{1}{n} \sum_{i=1}^{n} E(X_i) \pm \frac{1}{n} \sum_{i=1}^{n} \text{std}(X_i), \qquad (18)$$

where n is the number of sets of crystallographic orientations, X denotes the RMSD of one of the mechanical fields analysed, and X_i denotes the RMSD of the same field calculated for the i-th set of crystallographic orientations.

To summarize the sensitivity analyses for various sets of crystallographic orientations, the average value, $\bar{S}_j$, and sample standard deviation, $s(S_j)$, of each sensitivity index over all sets of crystallographic orientations for a given material and geometry were calculated as

$$\bar{S}_j = \frac{1}{n} \sum_{i=1}^{n} S_{j,i}, \quad s(S_j) = \sqrt{\frac{1}{n} \sum_{i=1}^{n} (S_{j,i} - \bar{S}_j)^2}, \tag{19}$$

where j indicates a specific parameter and i indexes the sets of crystallographic orientations.

4. Results and discussion

The UQ results for the RMSDs are presented in Figure 2 against the global strain level. The RMSD for most of the fields naturally tends to increase with strain, though in some models it remains almost constant.

The RMSD of the global force is almost constant and independent of the strain level. For both the 2D and 3D models and for both materials, the average is around 12% with an average standard deviation
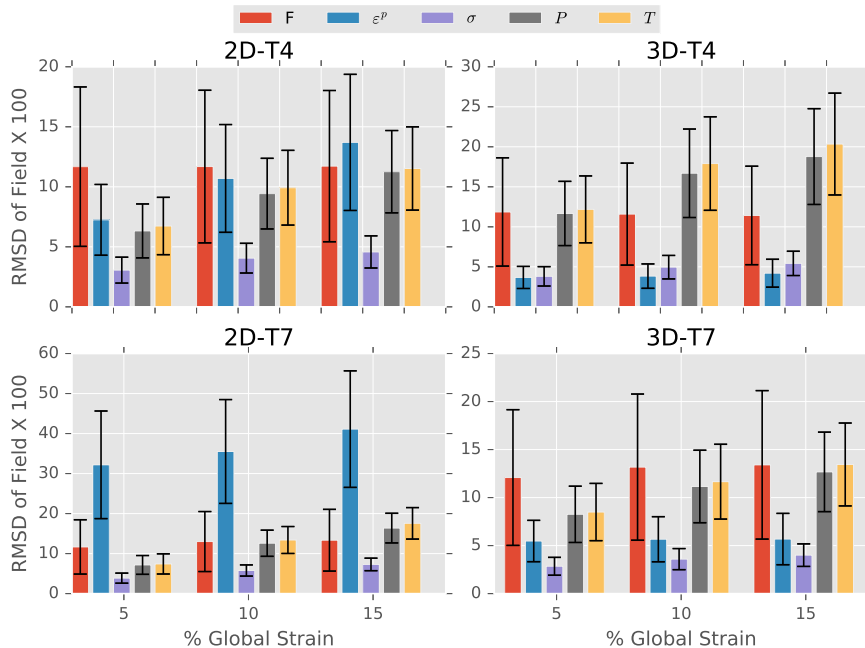
Figure 2. Root mean squared deviation (see (16) and (17)) for the outputs of interest. Bars represent the average expected value of RMSD across the 5 sets of crystallographic orientations considered, and the black error bars represent plus/minus the average standard deviation of RMSD across the orientations.
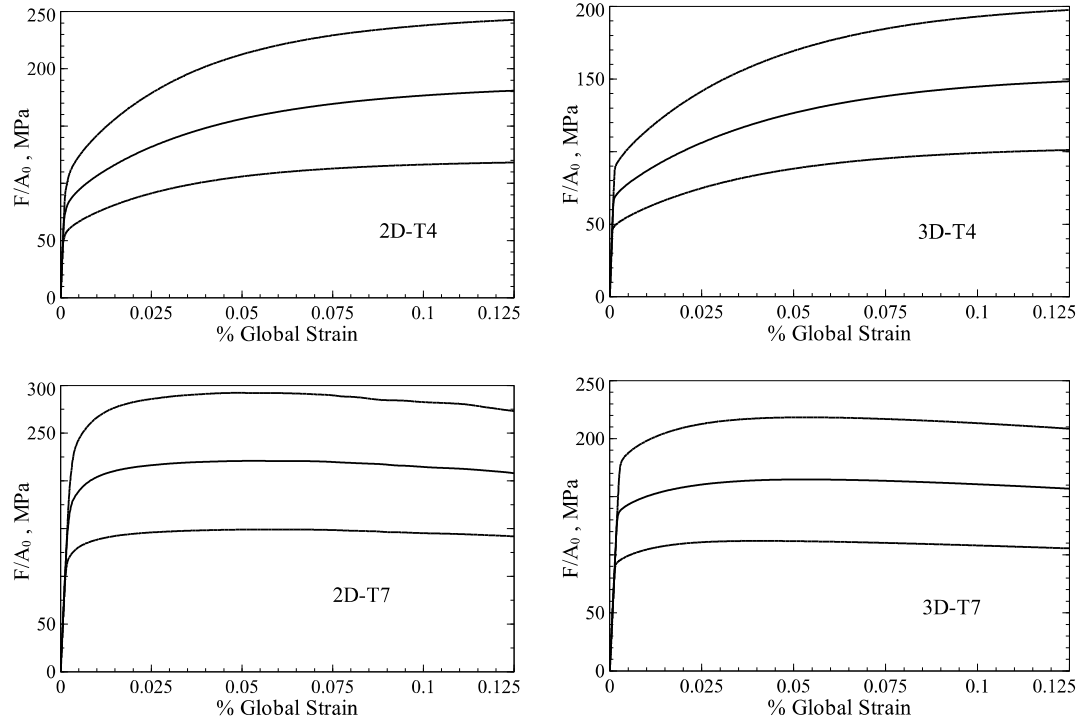
Figure 3. The engineering stress-strain curves of the baseline simulation (middle curve) and the simulations with the highest RMSD(F) (top and bottom curves) for one of the orientation sets.

of 6%. The maximum variation in the force is illustrated by the engineering stress-strain plots for one orientation set for each model type in Figure 3. The plots show the baseline simulation curve as well as the curves with the highest RMSD(F), i.e., the engineering stress-strain curves for all other simulations lie within the area bounded by these two curves. The plot may be compared to the results of the uniaxial tension tests in [Khadyko et al. 2016b]. The material in that reference is extruded and possesses a strong crystallographic texture, therefore its response cannot be directly compared to the response of the model olygocrystals. Nevertheless, the yielding and work-hardening behaviour of the oligocrystals is still quite similar to the results in [Khadyko et al. 2016b].

In the 2D models, the highest average value and average standard deviation are found for RMSD(ε^p). In particular, the average value of RMSD(ε^p) reaches 15% for the T4 material and over 40% for the T7 material, meaning that choosing arbitrary values of material parameters from the nominal ranges results in the level of strain in each element on average differing by 15% and 40%, respectively, from the baseline value in the two cases. The variability of RMSD(ε^p) for the T7 material is also high, reaching 15% at higher strains, indicating that the plastic strain fields obtained from different material parameter sets are not only different from the baseline, but also from each other. The high RMSD(ε^p) for the T7 material is most likely due to its low work-hardening and tendency to localize. The exact position of localization may change, creating large differences between the current and the baseline plastic strain fields. For the T4 material, the plastic strain field is more homogeneous, giving a lower RMSD(ε^p).

For the 3D models, RMSD(ε^p) is much smaller, just below 5% for the T4 material and just above 5% for the T7 material. The average variabilities for the 3D models are also small, on the order of 2%–3%. Considering that the material model is the same, the difference stems from the plane-strain condition and more constrained plastic flow in the 2D model, which makes it more prone to plastic instability and localization. To illustrate the described trends, a collection of equivalent plastic strain contour plots are presented in Figure 4 on the deformed configuration. The equivalent strain contour plots show the baseline simulation and the simulation with the highest RMSD(ε^p) for one of the orientation sets.
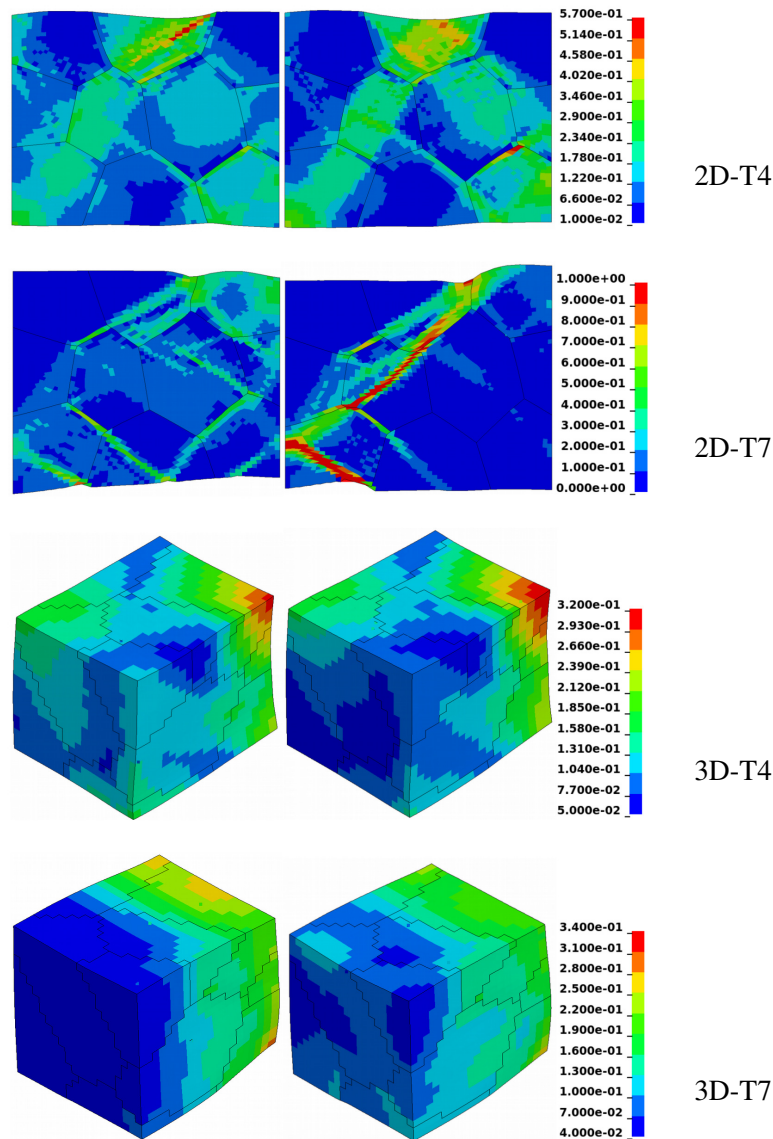
Figure 4. Equivalent plastic strain in the baseline simulation (left) and a simulation with the highest RMSD(ε^p) (right) for the 2D-T4, 2D-T7, 3D-T4 and 3D-T7 models.

The equivalent stress field is very stable, with both low average RMSD(σ) and low average variability, independent of the model and material type. The average RMSD(σ) is less than or equal to around 5%. The RMSDs for the hydrostatic pressure field and the stress triaxiality field show very similar average values and variabilities. This is not surprising when considering the definition of the stress triaxiality and the low RMSD of the von Mises stress. The average values of RMSD(P) and RMSD(T) for the 2D models are 10% for the T4 material and 15% for the T7 material. Notably, the dependence of the RMSDs on material type is reversed for the 3D model, where the average is almost 20% for the T4 material and 15% for the T7. The variability of the RMSDs for the hydrostatic pressure and stress triaxiality is also fairly consistent for all models and is around 5%. These trends may have some consequences in the CP-FEM modelling of ductile fracture. The low variability of the stress field shows that it is possible to obtain a good estimate of the equivalent stress distribution in the oligocrystal even when the material parameters are not known precisely. On the other hand, the stress triaxiality estimation requires a higher accuracy of the estimation of the material parameters.

Calibrating material model parameters based on force-displacement curves raises the question of whether there is a correlation between the RMSD of the force and the plastic strain field. If these quantities vary independently of each other, the correlation will be negligible, and the best fit for the force-displacement curve does not necessarily produce the best fit for the plastic strain field. On the other hand, if there is a correlation, then a better fit of the force-displacement curve should produce a model with better predictions of the local strain field. The correlations of RMSD(F) and RMSD(ε^p) for each set of crystallographic orientations were calculated by

$$\text{corr}(x, y) = \frac{\sum_{i=1}^{n}(x_i - \bar{x})(y_i - \bar{y})}{\sqrt{\sum_{i=1}^{n}(x_i - \bar{x})^2 \sum_{i=1}^{n}(y_i - \bar{y})^2}}, \tag{20}$$

with $x = \text{RMSD}(F)$ and $y = \text{RMSD}(\varepsilon^p)$, $\bar{x}$ and $\bar{y}$ denote the average values of the RMSD for the $n = 928$ simulations of the given set of crystallographic orientations. For each material type the average correlations and their associated standard deviations were also calculated in the same manner as those of the sensitivity indices (19). The resulting values are presented in Figure 5. The correlation coefficients are small in all cases, although they are higher for the 3D models than for the 2D models. Even the highest values are just around 30%. Thus, in the case of the models and orientation sets tested, the force and the strain field varied mostly independently of each other.
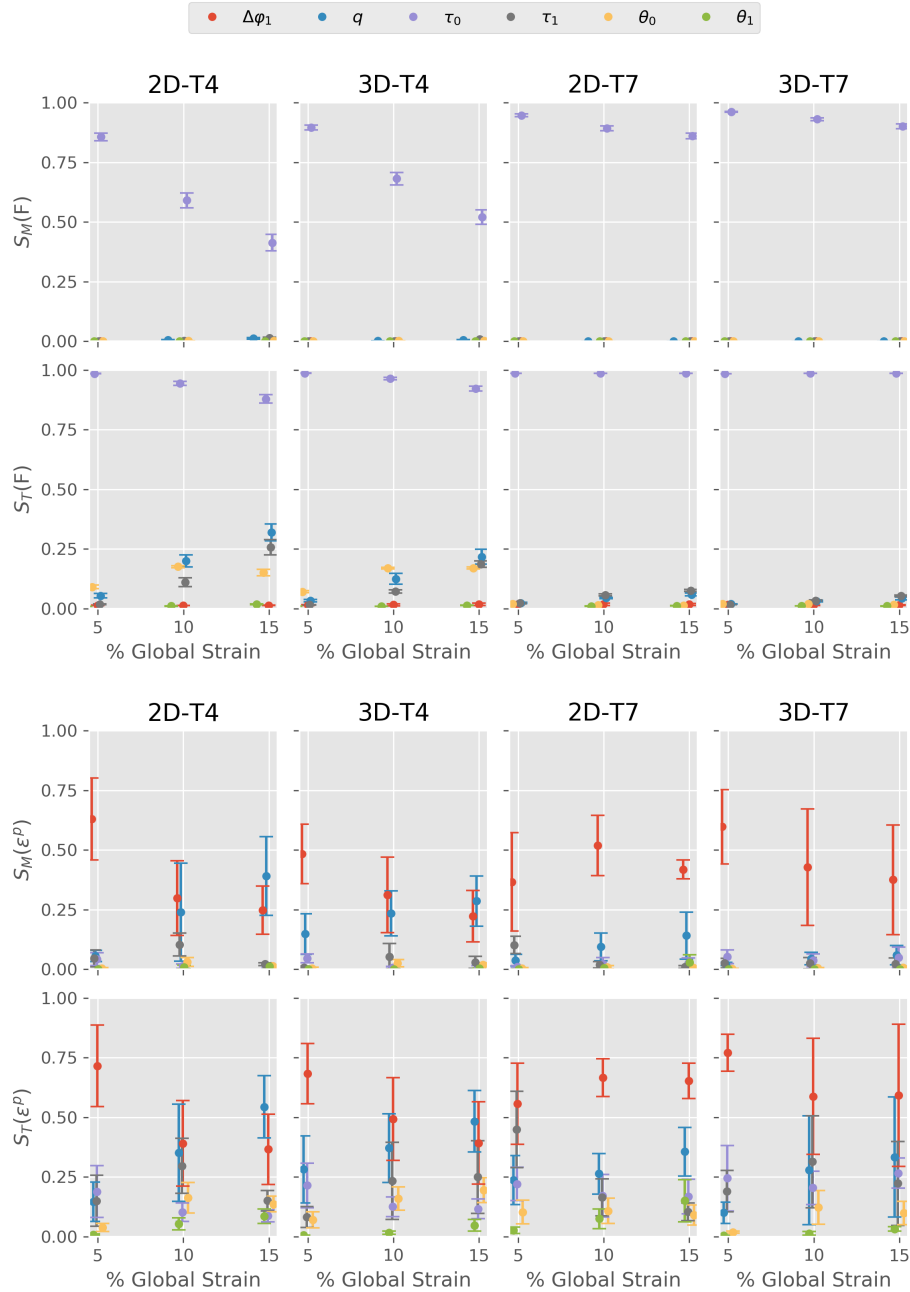
The sensitivity indices for the global force are presented in Figure 6, top. Both 2D and 3D models demonstrate similar trends. In all cases, RMSD(F) is most sensitive to the initial slip resistance τ_0. The main sensitivity indices for all other material parameters are negligible. On the other hand, the total sensitivity indices for the T4 material for both the 2D and 3D models are increasing with strain and become significant for q, τ_1 and θ_0. For the T7 material, the total sensitivities are still negligible for these parameters. Both the main and total sensitivity indices of θ_1 and $\Delta\varphi_1$ are negligible for all models and material types. The trend seen for the total sensitivities is likely the result of the different work-hardening of the T4 and T7 materials. The T4 material has significant work-hardening so the force level has more room for variation, in contrast to the T7 material for which the force level can only moderately deviate from the force at yielding. The work-hardening parameters primarily affect RMSD(F) only in interaction with each other, as only their total sensitivity indices are significant, while their main sensitivity indices
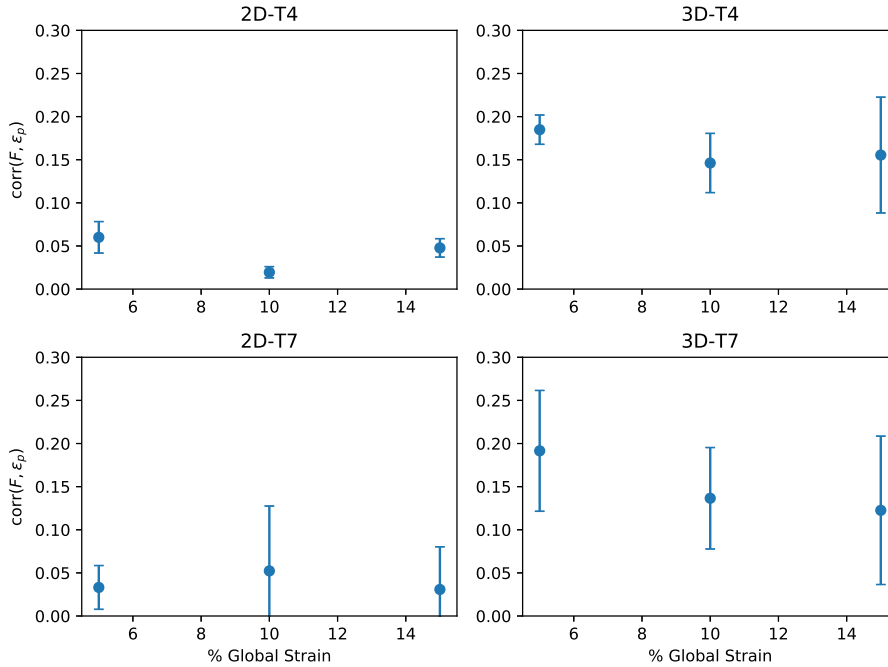
Figure 5. Sample correlation coefficient as defined in (20) of the global force and plastic strain for the 5 models for each case between $\text{RMSD}(F)$ and $\text{RMSD}(\varepsilon^p)$. The points are the average value of the correlations and the error bars represent plus/minus one sample standard deviation of the correlation coefficients. The averages and standard deviations are determined according to (20).

remain negligible. In other words, the effect of the work-hardening parameters is highly dependent on the values of the other parameters. For some values of other parameters they may have high influence, but on average they have no strong independent effect. If the force-displacement curve is used for the material model calibration, then for the T7 material only the initial slip resistance may be determined with certainty, the other parameters do not affect it noticeably within the given ranges. On the other hand, the local fields show very different sensitivities. A conclusion can be made, that for low work-hardening alloys it is not possible to establish the local material parameters of the CP model, based on the global stress-strain curve. In contrast, the calibration of the material model to the force-displacement curve of T4 material allows adjusting the initial slip resistance as well as the hardening parameters, particularly for larger displacements.

The sensitivity indices for $\text{RMSD}(\varepsilon^p)$ are shown in Figure 6, bottom. The plots of main and total indices both show that $\text{RMSD}(\varepsilon^p)$ is most sensitive to the parameters q and $\Delta\varphi_1$. Generally, the sensitivity to q starts from a lower value and rises with increasing strain, while sensitivity to $\Delta\varphi_1$ starts at a higher value and decreases for both T4 and T7 tempers. The most probable explanation is that as deformation develops and crystals rotate, activating multiple distinct slip systems, the interaction between slip systems becomes more important, while the small variation in the initial orientation and possible initial slip system activation becomes less important with increasing deformation. For the T4

Figure 6. Main and total sensitivity indices S_M and S_T of the global force (top) and of the normalized equivalent plastic strain (bottom). Circles represent the average value of the sensitivity indices across the 5 sets of crystallographic orientations considered, and the error bars indicate plus/minus one standard deviation of the sensitivities across the orientations. For ease of viewing the x-position of the points is shifted by a small amount such that the sensitivities may be differentiated.

temper at 15% strain, the sensitivity to q overtakes the sensitivity to $\Delta\varphi_1$. In contrast, for the T7 material the sensitivity to $\Delta\varphi_1$ is so high initially that it is still dominating even at 15% global strain, while the sensitivity to q at this strain level is still relatively small in comparison. The third most important material parameter is τ_1, which almost always has a significantly smaller sensitivity index than the parameter is τ_1, which almost always has a significantly smaller sensitivity index than the first two. The total sensitivity indices of the other parameters are much higher than their main indices, meaning that their effects on the plastic strain field depend on the values of other parameters. The previous study on the latent hardening [Khadyko et al. 2016a] indicates that if a more advanced latent hardening description was used, the variability of the stress-strain fields and their sensitivity to latent hardening could be even higher.

The main and total sensitivity indices for $\text{RMSD}(\sigma)$, $\text{RMSD}(P)$ and $\text{RMSD}(T)$ exhibit the same trends as $\text{RMSD}(\varepsilon^p)$ and are not shown here. The parameters $\Delta\varphi_1$ and q dominate, with $\Delta\varphi_1$ more important at small strains and for the T7 material. The initial slip resistance τ_0 is usually the third most important, except for the T7 material in the 2D model, where the parameter τ_1 sometimes takes its place.

Considering the mesh resolution influence on the uncertainty and sensitivity of the model response, the following argument can be made. The presented CPFEM model type was used extensively in the literature. The convergence studies universally show that increasing mesh density improves the resolution of the mechanical fields but does not change the field "shape" significantly. An example of this may be found in [Khadyko et al. 2016b]. The field gradients will become sharper, which should in principle increase RMSD of the corresponding fields.

5. Conclusions

UQSA methods were applied to study the variability and sensitivity of global and local solutions of a CP-FEM model to the variations in material model parameters. Both a 2D plane-strain model and a 3D model (using Voronoi tessellation) with 10 grains each were created, representing oligocrystals. Five sets of 10 random grain orientations were assigned to each oligocrystal. Two baseline material types were tested: a high work-hardening material based on the AA6063-T4 alloy, and a low work-hardening, high yield stress material based on the AA6063-T7 alloy. To investigate the effects of parameter variability on the predictions of model simulations, polynomial chaos expansions for outputs of interest representing the strain and stress fields and the global force were estimated. UQ measures and sensitivity indices were calculated from the polynomial chaos expansion. The generated stress and strain fields and the global force were analysed by normalizing them and comparing to the baseline fields and force. The results show that the equivalent plastic strain field may have significant variation, mostly due to early onset of strain localization. If the material work-hardening rate is high and the plastic flow is not constrained, then the variation of the plastic strain is quite low. The variation in the von Mises equivalent stress field is typically low, which means that it is possible to obtain a good estimate of the equivalent stress distribution in the oligocrystal even with uncertain values of the material parameters. On the other hand, the variations in the hydrostatic stress and stress triaxiality fields are significant, compared to the equivalent stress field and in some cases also the equivalent plastic strain field. The sensitivity study shows that the mechanical fields are most sensitive to the uncertainty in the crystallographic orientation and the latent hardening. The other parameters are mostly important in combination with each other. For the global force, in contrast, the strongest sensitivity index was obtained for the initial slip resistance. In the case

of the low work-hardening material, the other parameters are almost irrelevant, while for the high work-hardening material they become somewhat more prominent for higher strains and in combination with each other. The correlation between the global force variation and the plastic strain field variation is very low, showing that the relationship between local and global solutions depends heavily on the material parameters. Thus it is, in general, impossible to infer the local behaviour from global measurements without accurate knowledge of the material parameters.

The application of the UQSA to the CP-FEM models is challenging, because of the high computational cost of the CP-FEM models. Therefore, only five sets of orientations and models of oligocrystals were used in this study. Nevertheless, the results show consistent trends for all tested sets of crystallographic orientations, despite the fact that the orientations were all picked randomly from the whole orientation space. The CP-FEM solutions for the mechanical fields, such as the equivalent plastic strain field (which may be calculated by means of digital image correlation and used in various applications, e.g. material model calibration or fracture studies) and the hydrostatic pressure and stress triaxiality fields (which are crucial for advanced fracture predictions) show significant variability, due to uncertainty in the material parameters. The solution is most sensitive to the uncertainty in the Euler orientation angle and the latent hardening description. A similar UQSA study could be performed for specific polycrystal configurations and BCs tailored to a particular problem. Such a study would highlight and evaluate quantitatively the more particular trends relevant for that exact model.

References

[Badulescu et al. 2011] C. Badulescu, M. Grédiac, H. Haddadi, J.-D. Mathias, X. Balandraud, and H.-S. Tran, "Applying the grid method and infrared thermography to investigate plastic deformation in aluminium multicrystal", *Mech. Mater.* **43** (2011), 36–53.

[Bunge 1982] H.-J. Bunge, *Texture analysis in materials science: mathematical methods*, Butterworth-Heinemann, 1982.

[Chen and Zabaras 2014] P. Chen and N. Zabaras, "Uncertainty quantification for multiscale disk forging of polycrystal materials using probabilistic graphical model techniques", *Comput. Mater. Sci.* **84** (2014), 278–292.

[Chernatynskiy et al. 2013] A. Chernatynskiy, S. R. Phillpot, and R. LeSar, "Uncertainty quantification in multiscale simulation of materials: a prospective", *Annu. Rev. Mater. Res.* **43** (2013), 157–182.

[Cuadra et al. 2016] J. Cuadra, K. P. Baxevanakis, A. Loghin, and A. Kontsos, "Validation of a cyclic plasticity computational method using fatigue full-field deformation measurements", *Fatigue Fract. Eng. Mater. Struct.* **39**:6 (2016), 722–736.

[Dumoulin et al. 2013] S. Dumoulin, O. S. Hopperstad, N. A. Sène, P. Balland, R. Arrieux, and J.-M. Moreau, "Numerical modelling of plastic forming of aluminium single crystals", *Int. J. Mater. Form.* **6** (2013), 13–27.

[Eck et al. 2016] V. G. Eck, J. Donders, W. P. Sturdy, J. Feinberg, T. Delhaas, L. R. Hellevik, and W. Huberts, "A guide to uncertainty quantification and sensitivity analysis for cardiovascular applications", *Int. J. Numer. Method. Biomed. Eng.* **32** (2016), e02755–n/a.

[Erinosho et al. 2013] T. O. Erinosho, A. C. F. Cocks, and F. P. E. Dunne, "Texture, hardening and non-proportionality of strain in BCC polycrystal deformation", *Int. J. Plast.* **50** (2013), 170–192.

[Fassò and Cameletti 2010] A. Fassò and M. Cameletti, "A unified statistical approach for simulation, modeling, analysis and mapping of environmental data", *Simulation* **86** (2010), 139–153.

[Feinberg and Langtangen 2015] J. Feinberg and H. P. Langtangen, "Chaospy: An open source tool for designing methods of uncertainty quantification", *J. Comput. Science* **11** (2015), 46–57.

[Flanagan and Belytschko 1981] D. P. Flanagan and T. Belytschko, "A uniform strain hexahedron and quadrilateral with orthogonal hourglass control", *Int. J. Numer. Methods Eng.* **17**:5 (1981), 679–706.

[Franciosi et al. 1980] P. Franciosi, M. Berveiller, and A. Zaoui, "Latent hardening in copper and aluminium single crystals", *Acta Metall.* **28**:3 (1980), 273–283.

[Gambin 1992] W. Gambin, "Refined analysis of elastic-plastic crystals", *Int. J. Solids Struct.* **29**:16 (1992), 2013–2021.

[Ghiocel and Ghanem 2002] D. M. Ghiocel and R. G. Ghanem, "Stochastic finite-element analysis of seismic soil-structure interaction", *J. Eng. Mech.* (*ASCE*) **128** (2002), 66–77.

[Grujicic and Batchu 2002] M. Grujicic and S. Batchu, "Crystal plasticity analysis of earing in deep-drawn OFHC copper cups", *J. Mater. Sci.* **37**:4 (2002), 753–764.

[Guery et al. 2014] A. Guery, F. Latourte, F. Hild, and S. Roux, "Identification of crystal plasticity law parameters using kinematic measurements in polycrystals", pp. 8 pp in *WCCM XI — 11th World Congress on Computational Mechanics* (Barcelona, Spain), 2014.

[Guery et al. 2016] A. Guery, F. Hild, F. Latourte, and S. Roux, "Slip activities in polycrystals determined by coupling DIC measurements with crystal plasticity calculations", *Int. J. Plast.* **81** (2016), 249–266.

[Hall et al. 2009] J. W. Hall, S. A. Boyce, Y. Wang, R. J. Dawson, S. Tarantola, and A. Saltelli, "Sensitivity analysis for hydraulic models", *J. Hydraulic Eng.* **135** (2009), 959–969.

[Hallquist 2016] J. O. Hallquist, *LS–DYNA theory manual*, Livermore Software Technology Corporation, 2016.

[Hammersley 2013] J. Hammersley, *Monte Carlo methods*, Springer, 2013.

[Heripre et al. 2007] E. Heripre, M. Dexet, J. Crepin, L. Gélebart, A. Roos, M. Bornert, and D. Caldemaison, "Coupling between experimental measurements and polycrystal finite element calculations for micromechanical study of metallic materials", *Int. J. Plast.* **23** (2007), 1512–1539.

[Hiriyur et al. 2011] B. Hiriyur, H. Waisman, and G. Deodatis, "Uncertainty quantification in homogenization of heterogeneous microstructures modeled by XFEM", *Int. J. Numer. Methods Eng.* **88**:3 (2011), 257–278.

[Hoc et al. 2003] T. Hoc, J. Crépin, L. Gélébart, and A. Zaoui, "A procedure for identifying the plastic behavior of single crystals from the local response of polycrystals", *Acta Mater.* **51** (2003), 5477–5488.

[Hutchinson 1976] J. W. Hutchinson, "Bounds and self-consistent estimates for creep of polycrystalline materials", *Proc. R. Soc. Lond. A* **348**:1652 (1976), 101–127.

[Khadyko et al. 2016a] M. Khadyko, S. Dumoulin, G. Cailletaud, and O. S. Hopperstad, "Latent hardening and plastic anisotropy evolution in AA6060 aluminium alloy", *Int. J. Plast.* **76** (2016), 51–74.

[Khadyko et al. 2016b] M. Khadyko, S. Dumoulin, and O. S. Hopperstad, "Texture gradients and strain localisation in extruded aluminium profile", *Int. J. Solids Struct.* **97-98** (2016), 239–255.

[Kocks and Brown 1966] U. F. Kocks and T. J. Brown, "Latent hardening in aluminum", *Acta Metall.* **14**:2 (1966), 87–98.

[Kouchmeshky and Zabaras 2010] B. Kouchmeshky and N. Zabaras, "Microstructure model reduction and uncertainty quantification in multiscale deformation processes", *Comput. Mater. Sci.* **48**:2 (2010), 213–227.

[Lim et al. 2014] H. Lim, J. D. Carroll, C. C. Battaile, T. E. Buchheit, B. L. Boyce, and C. R. Weinberger, "Grain-scale experimental validation of crystal plasticity finite element simulations of tantalum oligocrystals", *Int. J. Plast.* **60** (2014), 1–18.

[Lim et al. 2016] H. Lim, F. Abdeljawad, S. J. Owen, B. W. Hanks, J. W. Foulk, and C. C. Battaile, "Incorporating physically-based microstructures in materials modeling: bridging phase field and crystal plasticity frameworks", *Model. Simul. Mater. Sci. Eng.* **24** (2016), 045016.

[Liu et al. 2015] M. Liu, C. Lu, and A. K. Tieu, "Crystal plasticity finite element method modelling of indentation size effect", *Int. J. Solids Struct.* **54** (2015), 42–49.

[Madrid et al. 2014] P. J. Madrid, D. Sulsky, and R. A. Lebensohn, "Uncertainty quantification in prediction of the in-plane Young's modulus of thin films with fiber texture", *J. Microelectromechan. System.* **23**:2 (2014), 380–390.

[Musienko et al. 2007] A. Musienko, A. Tatschl, K. Schmidegg, O. Kolednik, R. Pippan, and G. Cailletaud, "Three-dimensional finite element simulation of a polycrystalline copper specimen", *Acta Mater.* **55** (2007), 4121–4136.

[Needleman et al. 1985] A. Needleman, R. J. Asaro, J. Lemonds, and D. Peirce, "Finite element analysis of crystalline solids", *Comput. Methods Appl. Mech. Eng.* **52**:1 (1985), 689–708.

[Pan and Rice 1983] J. Pan and J. R. Rice, "Rate sensitivity of plastic flow and implications for yield-surface vertices", *Int. J. Solids Struct.* **19**:11 (1983), 973–987.

[Pardoen 2006] T. Pardoen, "Numerical simulation of low stress triaxiality ductile fracture", *Comput. Struct.* **84** (2006), 1641–1650.

[Pham et al. 2017] M. S. Pham, A. Creuziger, M. Iadicola, and A. D. Rollett, "Roles of texture and latent hardening on plastic anisotropy of face-centered-cubic materials during multi-axial loading", *J. Mech. Phys. Solids* **99** (2017), 50–69.

[Pinna et al. 2015] C. Pinna, Y. Lan, M. Kiu, P. Efthymiadis, M. Lopez-Pedrosa, and D. Farrugia, "Assessment of crystal plasticity finite element simulations of the hot deformation of metals from local strain and orientation measurements", *Int. J. Plast.* **73** (2015), 24–38.

[Renner et al. 2016] E. Renner, Y. Gaillard, F. Richard, F. Amiot, and P. Delobelle, "Sensitivity of the residual topography to single crystal plasticity parameters in Berkovich nanoindentation on FCC nickel", *Int. J. Plast.* **77** (2016), 118–140.

[Rodriguez-Fernandez et al. 2007] M. Rodriguez-Fernandez, S. Kucherenko, C. Pantelides, and N. Shah, "Optimal experimental design based on global sensitivity analysis", *Comput. Aided Chem. Eng.* **24** (2007), 63–68.

[Saai et al. 2010] A. Saai, H. Louche, L. Tabourot, and H. J. Chang, "Experimental and numerical study of the thermo-mechanical behavior of Al bi-crystal in tension using full field measurements and micromechanical modeling", *Mech. Mater.* **42** (2010), 275–292.

[Sachtleber et al. 2002] M. Sachtleber, Z. Zhao, and D. Raabe, "Experimental investigation of plastic grain interaction", *Mater. Sci. Eng. A* **336** (2002), 81–87.

[Salvati and Korsunsky 2017] E. Salvati and A. M. Korsunsky, "An analysis of macro- and micro-scale residual stresses of Type I, II and III using FIB-DIC micro-ring-core milling and crystal plasticity FE modelling", *Int. J. Plast.* **98** (2017), 123–138.

[Stevens 2016] G. N. Stevens, *Experiment-based validation and uncertainty quantification of partitioned models: improving predictive capability of multi-scale plasticity models*, dissertation, Clemson University, 2016.

[Sudret 2008] B. Sudret, "Global sensitivity analysis using polynomial chaos expansions", *Reliab. Eng. Syst. Saf.* **93**:7 (2008), 964–979.

[Teodosiu et al. 1991] C. Teodosiu, J. L. Raphanel, and L. Tabourot, "Finite element simulation of the large elastoplastic deformation of multicrystals", pp. 153–168 in *Proceedings of the International Seminar MECAMAT'91* (Fontainebleau, France), 1991.

[Tome et al. 1984] C. Tome, G. R. Canova, U. F. Kocks, N. Christodoulou, and J. J. Jonas, "The relation between macroscopic and microscopic strain hardening in F.C.C. polycrystals", *Acta Metall.* **32**:10 (1984), 1637–1653.

[Wen and Zabaras 2012] B. Wen and N. Zabaras, "A multiscale approach for model reduction of random microstructures", *Comput. Mater. Sci.* **63** (2012), 269–285.

[Zabaras 2010] N. Zabaras, "An information-theoretic multiscale framework with applications to polycrystalline materials", Materials Process, Design and Control Laboratory (MPDC), Cornell University, 2010.

[Zeghadi et al. 2007] A. Zeghadi, S. Forest, A.-F. Gourgues, and O. Bouaziz, "Ensemble averaging stress-strain fields in polycrystalline aggregates with a constrained surface microstructure — Part 2: crystal plasticity", *Philos. Mag.* **87**:8-9 (2007), 1425–1446.

[Zhang et al. 2015] C. Zhang, H. Li, P. Eisenlohr, W. Liu, C. Boehlert, M. Crimp, and T. Bieler, "Effect of realistic 3D microstructure in crystal plasticity finite element analysis of polycrystalline Ti-5Al-2.5Sn", *Int. J. Plast.* **69** (2015), 21–35.

[Zhang et al. 2016] T. Zhang, J. Jiang, B. Britton, B. Shollock, and F. Dunne, "Crack nucleation using combined crystal plasticity modelling, high-resolution digital image correlation and high-resolution electron backscatter diffraction in a superalloy containing non-metallic inclusions under fatigue.", *Proc. Math. Phys. Eng. Sci.* **427** (2016), 20150792.

MIKHAIL KHADYKO: mikhail.khadyko@ntnu.no
Norwegian University of Science and Technology (NTNU), 7491 Trondheim, Norway

JACOB STURDY: jacob.t.sturdy@ntnu.no
Norwegian University of Science and Technology (NTNU), 7491 Trondheim, Norway

STÉPHANE DUMOULIN: stephane.dumoulin@sintef.no
SINTEF Materials and Chemistry, 7941 Trondheim, Norway

LEIF RUNE HELLEVIK: leif.r.hellevik@ntnu.no
Norwegian University of Science and Technology (NTNU), 7491 Trondheim, Norway

ODD STURE HOPPERSTAD: odd.hopperstad@ntnu.no
Norwegian University of Science and Technology (NTNU), 7491 Trondheim, Norway

■msp

INTERACTION OF SHEAR CRACKS IN MICROSTRUCTURED MATERIALS MODELED BY COUPLE-STRESS ELASTICITY

Panos A. Gourgiotis

The interaction of two colinear in-plane shear cracks is investigated within the context of couple-stress elasticity. This theory introduces characteristic material length scales that emerge from the underlying microstructure and has proved to be very effective for modeling complex microstructured materials. An exact solution of the boundary value problem is obtained through integral transforms and singular integral equations. The main goal is to explain the size effects that are experimentally observed in fracture of brittle microstructured materials. Two basic configurations are considered: a micro-macrocrack interaction, and a micro-microcrack interaction. Numerical results are presented illustrating the effects of couple-stresses on the stress intensity factor and the energy release rate. It is shown that significant deviations from the predictions of the standard LEFM occur when the geometrical lengths of the problem become comparable to the characteristic material length of the couple-stress theory revealing that in such cases it is inadequate to analyze fracture problems employing only classical elasticity considerations.

1. Introduction

It is well known that in brittle materials crack growth is accompanied by the formation of microcracks around the main crack [Hoagland et al. 1974; Atkinson 1984; Rice et al. 1994; Nara et al. 2011]. The occurrence of such stress-induced microcracking has been recognized as an important toughening mechanism in many microstructured materials [Kreher and Pompe 1981; Evans and Faber 1984; Noselli et al. 2013]. There are many fracture models that deal with the nucleation and growth of such microcracks (e.g., [Kachanov 1993; Deng and Nemat-Nasser 1994; Shao and Rudnicki 2000]), however the majority of such models are based on the classical theory of linear elastic fracture mechanics (LEFM) which, however, is scale independent and cannot realistically describe the fracture processes in such situations. This deficiency of the classical theory can be circumvented by the use of generalized continuum theories. These theories introduce characteristic material lengths in their formulation and have been successfully employed in many cases to model the experimentally observed size-effects which are closely related to the material microstructure.

  The simplest gradient-type generalized continuum theory that can effectively model size effects in elastic solids is the theory of couple-stress elasticity, also known as constrained Cosserat elasticity [Toupin 1962; Mindlin and Tiersten 1962; Koiter 1964]. In couple-stress elasticity the Euler–Cauchy principle is augmented with a nonvanishing couple traction and the strain-energy density becomes a function of the strain and the gradient of rotation. Such assumptions are appropriate for materials with granular or cellular structure, where the interaction between adjacent elements may introduce internal moments. For

the plane-strain isotropic case, the couple-stress theory introduces one material length scale which can be related to the intrinsic material microstructure [Lakes 1983; Anderson and Lakes 1994; Bigoni and Drugan 2007; Lakes 2016]. The couple-stress theory has been recently employed to model size effects in microstructured materials in, among other areas, fracture [Gourgiotis and Georgiadis 2008; Radi 2008; Piccolroaz et al. 2012; Gourgiotis and Piccolroaz 2014; Morini et al. 2014; Dyskin and Pasternak 2015], contact [Zisis et al. 2014; 2015; Gourgiotis et al. 2016; Karuriya and Bhandakkar 2017; Song et al. 2017; Wang et al. 2018], stress localization [Gourgiotis and Bigoni 2016a; 2016b; Bigoni and Gourgiotis 2016; Zisis 2018; Lakes 2018], and wave propagation problems [Piccolroaz and Movchan 2014; Goodarzi et al. 2016; Wang et al. 2017; Gourgiotis and Bigoni 2017].

The present work examines the interaction problem of two shear cracks in a microstructured material under remote mode II loading. The material microstructure is modeled here by use of the couple-stress theory. For simplicity, the attention here is limited to the case of two colinear finite-length cracks in an infinite body under plane-strain conditions. Of special interest is the case where the geometrical lengths of the problem become comparable to the characteristic material length of the couple-stress theory. In this context, two configurations are examined in detail: the micro-macrocrack interaction; and the micro-microcrack interaction. In the framework of the classical LEFM theory, crack interaction problems were investigated, among others, in [Rubinstein 1985; Rose 1986; Kachanov 1993; Deng and Nemat-Nasser 1994]. Interestingly, the crack interaction problem has not been investigated before in the context of any generalized continuum theory. Regarding works closely related to our problem, we cite first the analyses by Sternberg and Muki [1967] and Atkinson and Leppington [1977] who examined the mode I crack in a couple stress material. The full field solution for the mode II crack problem in couple-stress elasticity was given by Gourgiotis and Georgiadis [2007], while recently Baxevanakis et al. [2017] examined the interaction problem of an in-plane shear crack with a glide dislocation.

A full field exact solution of the mixed boundary value problem is obtained by means of the Fourier transform and singular integral equations. Analytical expressions for the stress intensity factor (SIF) and the energy release rate (ERR) are obtained for both cracks. The dependence of these quantities upon the characteristic material length of the couple-stress theory is then examined in detail in order to assess the effects of the microstructure on the fracture process. A comparison of these quantities in the framework of couple-stress elasticity with the classical elasticity solutions is also provided. The main goal of the present study is to examine the possible deviations from the predictions of classical LEFM with a view towards understanding the mechanisms that govern the fracture of brittle materials on the microscale.

2. Basic equations of plane-strain couple-stress elasticity

In this section, we recall briefly the main features of the plane strain couple-stress elasticity. A detailed presentation of the plane strain anisotropic couple-stress theory can be found in [Gourgiotis and Bigoni 2017].

For a body that occupies a domain in the (x, y)-plane under conditions of plane-strain, the equations of equilibrium in the absence of body forces and body moments reduce to

$$\frac{\partial \sigma_{xx}}{\partial x} + \frac{\partial \sigma_{yx}}{\partial y} = 0, \quad \frac{\partial \sigma_{xy}}{\partial x} + \frac{\partial \sigma_{yy}}{\partial y} = 0, \quad \sigma_{xy} - \sigma_{yx} + \frac{\partial m_{xz}}{\partial x} + \frac{\partial m_{yz}}{\partial y} = 0, \tag{1}$$

where $(\sigma_{xx}, \sigma_{yy}, \sigma_{xy}, \sigma_{yx})$ and (m_{xz}, m_{yz}) are the nonvanishing components of the (asymmetric) stress and couple-stress tensors, respectively. The complete solution of (1) admits the following representation in terms of two sufficiently smooth stress functions $\Phi(x, y)$ and $\Psi(x, y)$ [Mindlin 1963]:

$$
\sigma_{xx} = \frac{\partial^2 \Phi}{\partial y^2} - \frac{\partial^2 \Psi}{\partial x \partial y}, \qquad \sigma_{yy} = \frac{\partial^2 \Phi}{\partial x^2} + \frac{\partial^2 \Psi}{\partial x \partial y},
$$
$$
\sigma_{xy} = -\frac{\partial^2 \Phi}{\partial x \partial y} - \frac{\partial^2 \Psi}{\partial y^2}, \quad \sigma_{yx} = -\frac{\partial^2 \Phi}{\partial x \partial y} + \frac{\partial^2 \Psi}{\partial x^2},
$$

(2)

and

$$
m_{xz} = \frac{\partial \Psi}{\partial x}, \quad m_{yz} = \frac{\partial \Psi}{\partial y}.
$$

(3)

Accordingly, the governing kinematic relations in the framework of the geometrically linear theory become

$$
\varepsilon_{xx} = \frac{\partial u_x}{\partial x}, \quad \varepsilon_{yy} = \frac{\partial u_y}{\partial y}, \quad \varepsilon_{xy} = \varepsilon_{yx} = \frac{1}{2}\left(\frac{\partial u_y}{\partial x} + \frac{\partial u_x}{\partial y}\right),
$$

(4)

$$
\omega = \frac{1}{2}\left(\frac{\partial u_y}{\partial x} - \frac{\partial u_x}{\partial y}\right), \quad \kappa_{xz} = \frac{\partial \omega}{\partial x}, \quad \kappa_{yz} = \frac{\partial \omega}{\partial y},
$$

(5)

where u_q are the displacement components, ε_{pq} are the components of the usual strain tensor, $\omega_z \equiv \omega$ is the rotation, and $(\kappa_{xz}, \kappa_{yz})$ are the nonvanishing components of the curvature tensor (i.e., the gradient of rotation) expressed in dimensions of [length]$^{-1}$.

For a homogeneous centrosymmetric and isotropic couple-stress material the constitutive equations furnish

$$
\sigma_{xx} = (\lambda + 2\mu)\varepsilon_{xx} + \lambda\varepsilon_{yy}, \quad \sigma_{yy} = (\lambda + 2\mu)\varepsilon_{yy} + \lambda\varepsilon_{xx}, \quad \sigma_{xy} + \sigma_{yx} = 4\mu\varepsilon_{xy}
$$

(6)

and

$$
m_{xz} = 4\mu\ell^2\kappa_{xz}, \quad m_{yz} = 4\mu\ell^2\kappa_{yz},
$$

(7)

where (μ, λ) stand for the Lamé moduli, and ℓ is the characteristic material length of couple-stress theory [Mindlin and Tiersten 1962]. Note also that $\lambda = 2\mu\nu(1 - 2\nu)^{-1}$, where ν is the Poisson's ratio.

The Mindlin's stress functions must satisfy the following pair of differential equations that result from the requirement of kinematical compatibility [Muki and Sternberg 1965]:

$$
\frac{\partial}{\partial x}(\Psi - \ell^2\nabla^2\Psi) = -2(1-\nu)\ell^2\nabla^2\left(\frac{\partial \Phi}{\partial y}\right),
$$
$$
\frac{\partial}{\partial y}(\Psi - \ell^2\nabla^2\Psi) = 2(1-\nu)\ell^2\nabla^2\left(\frac{\partial \Phi}{\partial x}\right),
$$

(8)

which, in turn, implies that

$$
\nabla^4\Phi = 0, \quad \nabla^2\Psi - \ell^2\nabla^4\Psi = 0.
$$

(9)

Finally, combining (2)–(7), one can obtain the following relations expressing the displacement gradients in terms of Mindlin's stress functions:

$$\frac{\partial u_x}{\partial x} = \frac{1}{2\mu}\left(\frac{\partial^2 \Phi}{\partial y^2} - \frac{\partial^2 \Psi}{\partial x \partial y} - \nu \nabla^2 \Phi\right), \tag{10}$$

$$\frac{\partial u_y}{\partial y} = \frac{1}{2\mu}\left(\frac{\partial^2 \Phi}{\partial x^2} + \frac{\partial^2 \Psi}{\partial x \partial y} - \nu \nabla^2 \Phi\right), \tag{11}$$

$$\frac{\partial u_x}{\partial y} + \frac{\partial u_y}{\partial x} = -\frac{1}{2\mu}\left(2\frac{\partial^2 \Phi}{\partial x \partial y} - \frac{\partial^2 \Psi}{\partial x^2} + \frac{\partial^2 \Psi}{\partial y^2}\right). \tag{12}$$

3. Formulation of the crack problem

Consider two colinear cracks situated along the x-axis consisting of the segments $\mathcal{L}_1 = (a_1 < x < b_1)$ and $\mathcal{L}_2 = (a_2 < x < b_2)$, with $a_2 > b_1$ (Figure 1). The crack-faces are traction free and the body is subjected to remote mode II loading of magnitude S. For simplicity, the origin of the Cartesian coordinate system coincides with crack-tip a_1.

To facilitate our parametric analysis the following geometric quantities are defined

$$\alpha = \tfrac{1}{2}(b_1 - a_1), \quad \beta = \tfrac{1}{2}(b_2 - a_2), \quad \text{and} \quad \delta = a_2 - b_1, \tag{13}$$
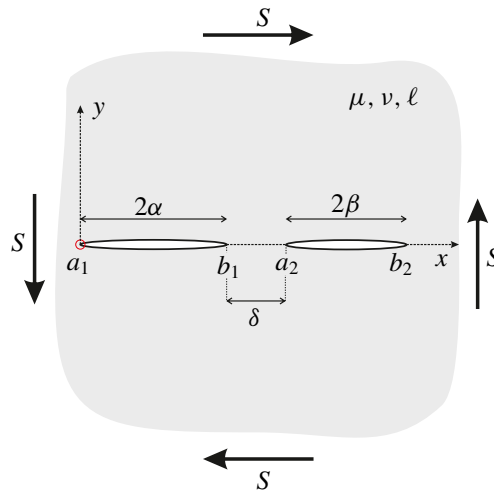
where α and β are the half-lengths of the two colinear cracks, and δ is the distance between them.

Due to the antisymmetry with respect to the $y = 0$ plane, the problem can be viewed as a half-plane problem in the domain $y \geq 0$ under the following boundary conditions:

$$\sigma_{yx}(x, 0) = 0 \quad \text{for} \quad x \in \mathcal{L}, \tag{14}$$

$$\sigma_{yy}(x, 0) = 0 \quad \text{for} \quad -\infty < x < \infty, \tag{15}$$

$$m_{yz}(x, 0) = 0 \quad \text{for} \quad -\infty < x < \infty, \tag{16}$$

Figure 1. Two collinear cracks subjected to remote mode II loading.

accompanied by the antisymmetry condition

$$u_x(x, 0) = 0 \quad \text{for} \quad x \notin \mathcal{L}, \tag{17}$$

and the regularity conditions at infinity

$$\sigma_{xy}^\infty = \sigma_{yx}^\infty = S, \quad \{\sigma_{xx}^\infty, \sigma_{yy}^\infty, m_{xz}^\infty, m_{yz}^\infty\} \to 0 \quad \text{as} \quad r = \sqrt{x^2 + y^2} \to \infty, \tag{18}$$

with $\mathcal{L} = \sum_{j=1}^2 \mathcal{L}_j$.

Further, as it is customary in the classical theory of elasticity, we introduce the unknown density $h(x)$ as the slope function

$$h(x) = \frac{\partial u_x(x)}{\partial x}, \tag{19}$$

which in view of (17), is defined as

$$h(x) = \begin{cases} h_j(x) & \text{for } x \in \mathcal{L}_j \ (j = 1, 2), \\ 0 & \text{for } x \notin \mathcal{L}. \end{cases} \tag{20}$$

For the solution of the boundary value problem the Fourier transform is utilized to suppress the x-dependence in the field equations and the boundary conditions. The direct and inverse Fourier transforms are defined as follows:

$$f^*(\xi, y) = \int_{-\infty}^{+\infty} f(x, y) e^{i\xi x} \, dx, \quad f(x, y) = \frac{1}{2\pi} \int_{-\infty}^{+\infty} f^*(\xi, y) e^{-i\xi x} \, d\xi, \tag{21}$$

where ξ is the Fourier variable and i is the imaginary unit. Transforming the governing field equations (9) provides a pair of fourth order ODEs with constant coefficients whose solution is immediate [Zisis et al. 2014]. The constants that emerge may be subsequently evaluated from the transform of (8) in conjunction with the boundary conditions (15) and (16). Finally, utilizing (10) and (19), the transformed stress functions assume the following form:

$$\Phi^*(\xi, y) = -\frac{\mu}{(1 - \nu)} \frac{e^{-|\xi|y} y}{|\xi|} h^*(\xi), \quad \Psi^*(\xi, y) = 4i\mu\ell^2\xi \left(\frac{e^{-|\xi|y}}{|\xi|} - \frac{e^{-\gamma y}}{\gamma} \right) h^*(\xi) \tag{22}$$

with $\gamma \equiv \gamma(\xi) = \sqrt{\ell^{-2} + \xi^2}$. Accordingly, using (2) and (3) the transformed shear stress σ_{yx}^* becomes

$$\sigma_{yx}^*(\xi, y) = \mu g_{yx}^*(\xi, y) h^*(\xi), \tag{23}$$

with

$$g_{yx}^*(\xi, y) = i \left[\frac{(y\xi - \text{sgn}(\xi))}{1 - \nu} e^{-|\xi|y} - 4\ell^2\xi(|\xi|e^{-|\xi|y} - \xi^2\gamma^{-1}e^{-\gamma y}) \right], \tag{24}$$

where sgn() is the signum function.

Moreover, $h^*(\xi)$ is defined according to (20) and (21)$_1$ as

$$h^*(\xi) = \int_{-\infty}^{\infty} h(t) e^{i\xi t} \, dt = \sum_{j=1}^2 \int_{a_j}^{b_j} h_j(t) e^{i\xi t} \, dt. \tag{25}$$

Employing the inverse Fourier transform $(21)_2$ in conjunction with (25) and reversing the order of integration, the shear stress σ_{yx} can be written as

$$\sigma_{yx}(x, y) = \frac{1}{2\pi} \int_{-\infty}^{\infty} \sigma_{yx}^* e^{-i\xi x} \, d\xi = \frac{\mu}{\pi} \sum_{j=1}^{2} \int_{a_j}^{b_j} G_{yx}(x - t, y) h_j(t) \, dt + S, \tag{26}$$

where the kernel $G_{yx}(x - t, y)$ is evaluated analytically as

$$G_{yx}(x, y) = \frac{1}{2} \int_{-\infty}^{\infty} g_{yx}^*(\xi, y) e^{-i\xi x} \, d\xi = \frac{x(y^2 - x^2)}{(1 - \nu)r^4} + \frac{8\ell^2 x (x^2 - 3y^2)}{r^6} + 4\ell^2 \partial_x^3 K_0\left[\frac{r}{\ell}\right], \tag{27}$$

and $K_n[\ ]$ is the modified Bessel function of the second kind and n-th order. Using the same procedure, all the stress and couple-stress components are derived in *closed form* in the Appendix.

4. Singular integral equation approach

The unknown density function will be now determined by employing the method of singular integral equations (SIEs). In classical elasticity, the general procedure of reducing mixed boundary value problems to singular integral equations is given, e.g., by Erdogan [1978]. An application of the technique within the context of couple-stress elasticity for crack problems can be found in [Gourgiotis and Georgiadis 2008; 2007], and for contact problems in [Zisis et al. 2014; 2015; Gourgiotis et al. 2016; Karuriya and Bhandakkar 2017; Song et al. 2017; Wang et al. 2018].

The requirement that the crack-faces are free of shear tractions (see (14)) in the disjoint intervals (a_1, b_1) and (a_2, b_2) leads to the following system of coupled integral equations for the unknown densities $h_j(t)$ ($j = 1, 2$):

$$\int_{a_1}^{b_1} G_{yx}(x - t, 0) h_1(t) \, dt + \int_{a_2}^{b_2} G_{yx}(x - t, 0) h_2(t) \, dt = -\frac{\pi S}{\mu}, \quad x \in \mathcal{L}. \tag{28}$$

Moreover, to ensure uniqueness of the crack problem the following closure conditions must be satisfied:

$$\int_{a_1}^{b_1} h_1(t) \, dt = 0 \quad \text{and} \quad \int_{a_2}^{b_2} h_2(t) \, dt = 0. \tag{29}$$

For the solution of the coupled system of integral equations (28), it is expedient to separate the kernel to its singular and regular parts. To this purpose, we examine the asymptotic behavior of $G_{yx}(x - t, 0)$ as $x \to t$. Using asymptotic analysis, we may readily write

$$G_{yx}(x - t, 0) = -\frac{(3 - 2\nu)}{(1 - \nu)} \frac{1}{x - t} + R(x - t), \tag{30}$$

where the regular square-integrable kernel $R(x - t)$ is given as

$$R(x - t) = \frac{4}{x - t}\left(\frac{1}{2} + \frac{2\ell^2}{(x - t)^2} - K_2\left[\frac{|x - t|}{\ell}\right]\right) - \frac{4\,\mathrm{sgn}(x - t)}{\ell} K_1\left[\frac{|x - t|}{\ell}\right], \tag{31}$$

which is bounded as $x \to t$.

In view of the above, the following system of SIEs is obtained for the interaction problem of two colinear shear cracks in couple-stress elasticity:

$$-\frac{(3-2\nu)}{(1-\nu)}\sum_{j=1}^{2}\int_{a_j}^{b_j}\frac{h_j(t)}{x-t}\,dt+\sum_{j=1}^{2}\int_{a_j}^{b_j}h_j(t)R(x-t)\,dt=-\frac{\pi S}{\mu},\quad x\in\mathcal{L}.\tag{32}$$

It is worth noting that in classical elasticity, the mode II and mode I interaction problems are governed by the same system of SIEs, i.e.,

$$-\frac{1}{(1-\nu)}\sum_{j=1}^{2}\int_{a_j}^{b_j}\frac{h_j(t)}{x-t}\,dt=-\frac{\pi S}{\mu},\quad x\in\mathcal{L}.\tag{33}$$

However, as it was shown in [Gourgiotis and Georgiadis 2008], in couple-stress elasticity the opening modes are more involved than the shear modes since additional densities must be introduced in order to satisfy the boundary conditions at the crack-faces.

To render the system of SIEs amenable to numerical treatment, the following normalizations are adopted [Erdogan and Wu 1993]:

$$\begin{aligned}
x&=\tfrac{1}{2}(b_k-a_k)\hat{x}+\tfrac{1}{2}(b_k+a_k),\quad a_k<x<b_k,\quad -1<\hat{x}<1,\\
t&=\tfrac{1}{2}(b_j-a_j)\hat{t}+\tfrac{1}{2}(b_j+a_j),\quad a_j<t<b_j,\quad -1<\hat{t}<1,\\
R(x-t)&=\mathcal{N}_{kj}(\hat{x},\hat{t}),\quad a_k<x<b_k,\quad a_j<t<b_j,\\
z_{kj}&=(b_j-a_j)^{-1}[(b_k-a_k)\hat{x}+b_k+a_k-b_j-a_j],\quad \mathcal{D}_{kj}(\hat{x},\hat{t})=(z_{kj}-\hat{t})^{-1},
\end{aligned}\tag{34}$$

with $j=(1,2)$ and $k=(1,2)$.

Accordingly, the system in (32) assumes the following form

$$-\frac{(3-2\nu)}{(1-\nu)}\int_{-1}^{1}\frac{h_k(\hat{t})}{\hat{x}-\hat{t}}\,d\hat{t}-\frac{(3-2\nu)}{(1-\nu)}\sum_{j=1}^{2}{}'\int_{-1}^{1}\mathcal{D}_{kj}(\hat{x},\hat{t})h_j(\hat{t})\,d\hat{t}$$

$$+\sum_{j=1}^{2}\tfrac{1}{2}(b_j-a_j)\int_{-1}^{1}\mathcal{N}_{kj}(\hat{x},\hat{t})h_j(\hat{t})\,d\hat{t}=-\frac{\pi S}{\mu},$$

$$k=(1,2),\quad -1<\hat{x}<1,\tag{35}$$

where the prime indicates that the summation does not include the term corresponding to $j=k$.

Following [Gourgiotis and Georgiadis 2007], the unknown densities $h_k(\hat{t})$ can be written as a product of a regular bounded function and a singular function characterizing the asymptotic behavior near the crack-tips. Within the framework of couple-stress elasticity, asymptotic analysis near a mode II crack-tip [Huang et al. 1997; Gourgiotis and Georgiadis 2007; 2011] showed that the crack-face sliding displacement has the same asymptotic behavior as in the classical LEFM. Such a behavior was also corroborated by the uniqueness theorem for crack problems in couple-stress elasticity which imposes the requirement of boundedness for crack-tip displacements [Grentzelou and Georgiadis 2005]. The densities can be

expressed now in the following form:

$$h_k(\hat{t}) = \frac{\chi_k(\hat{t})}{\sqrt{1 - \hat{t}^2}}, \quad -1 < \hat{t} < 1, \quad k = (1, 2), \tag{36}$$

where the $\chi_k(\hat{t})$ are sufficiently smooth functions.

For the solution of the system of SIEs in (35), the standard Gauss–Chebyshev quadrature is employed. For details, the reader is referred to [Erdogan 1978; Gourgiotis and Georgiadis 2007; 2008]. The discretized form of the system of SIEs becomes

$$-\frac{(3-2\nu)}{(1-\nu)} \frac{\pi}{N} \sum_{i=1}^{N} \frac{\chi_k(\hat{t}_i)}{\hat{x}_m - \hat{t}_i} - \frac{(3-2\nu)}{(1-\nu)} \frac{\pi}{N} \sum_{j=1}^{2} {}' \sum_{i=1}^{N} \mathcal{D}_{kj}(\hat{x}_m, \hat{t}_i) \chi_k(\hat{t}_i)$$

$$+ \frac{\pi}{N} \sum_{j=1}^{2} \sum_{i=1}^{N} \tfrac{1}{2}(b_j - a_j) \mathcal{N}_{kj}(\hat{x}_m, \hat{t}_i) \chi_j(\hat{t}_i) = -\frac{\pi S}{\mu}, \quad k = (1, 2), \tag{37}$$

where the integration points $\hat{t}_i$ and collocation points $\hat{x}_m$ are given respectively as

$$\begin{aligned}
\hat{x}_m &= \cos(m\pi/N) & \text{with} \quad m = 1, \dots, N-1, \\
\hat{t}_i &= \cos((2i-1)\pi/(2N)) & \text{with} \quad i = 1, \dots, N.
\end{aligned} \tag{38}$$

Equation (37) together with the auxiliary conditions (29) provide a $2N$ algebraic system of equations with $2N$ unknowns: $\chi_1(\hat{t}_i)$ and $\chi_2(\hat{t}_i)$ $(i = 1, \dots, N)$. From the solution of the system the densities $h_k(t)$ are evaluated and then the stress and couple-stress components can be readily computed using (49)–(52).

5. Results and discussion

In what follows, numerical results are presented regarding the crack-face displacements, the stress intensity factors (SIFs) and the energy release rates (ERRs) of the shear cracks. All the results are presented in terms of the three microstructural ratios: α/ℓ, β/ℓ, and δ/ℓ (or combinations of them), where the geometrical parameters (α, β, δ) are defined in (13). It is assumed that in all cases $\beta > \alpha$, which implies that the right crack is always larger than the left one. Our purpose is to examine the possible deviations from the predictions of classical LEFM when the lengths of the cracks and the separation length between them becomes comparable to the characteristic material length of couple-stress elasticity. Two configurations are examined:

(i) a micro-macrocrack interaction where the ratio β/α is large and α/ℓ is small, and

(ii) a micro-microcrack interaction where the lengths of both cracks are comparable to the characteristic material length ℓ of the couple-stress theory (i.e., both α/ℓ and β/α are small).

5.1. *Crack-face displacements.* The crack-face sliding displacements for the two colinear shear cracks can be readily evaluated by integrating (19) and using (29). Figure 2 shows the influence of the ratio α/ℓ on the normalized sliding crack-face displacements of both cracks. It is remarked that as the crack lengths become comparable to the characteristic length ℓ, the material exhibits a more stiff behavior, i.e.,
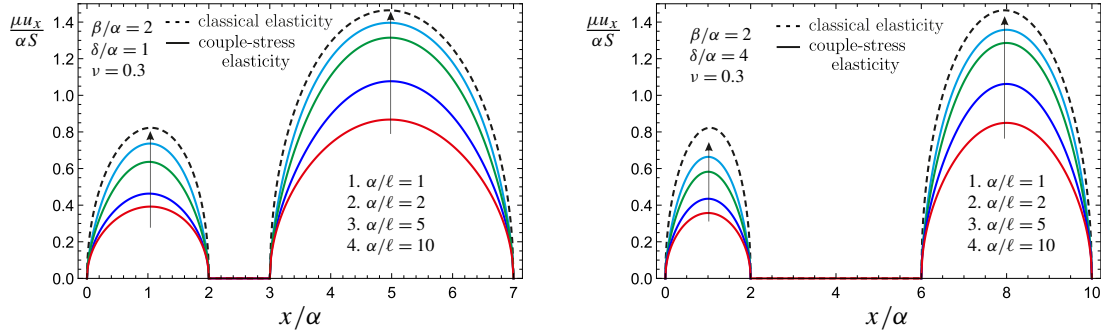
Figure 2. Variation of the normalized upper crack-face sliding displacement versus the normalized distance x/α when (left) the distance between the cracks is $\delta = \alpha$, and (right) the distance between the cracks is $\delta = 4\alpha$. In all cases, $\beta/\alpha = 2$ and $\nu = 0.3$.
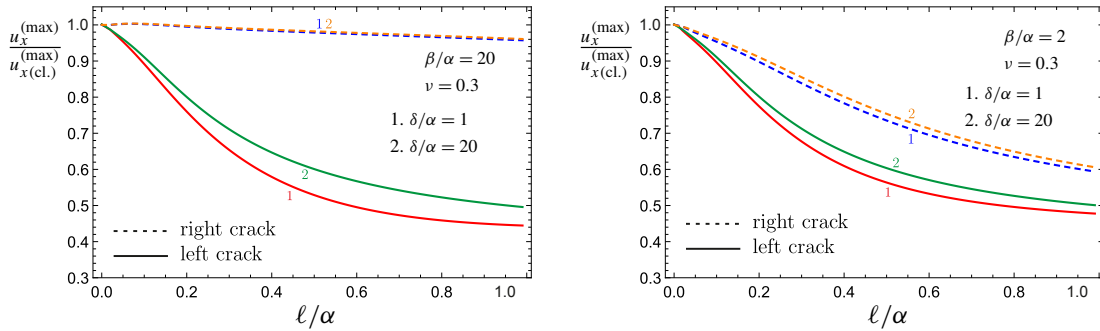
Figure 3. Variation of the ratio of the maximum sliding displacement in couple-stress and classical elasticity versus ℓ/α for (left) $\beta/\alpha = 20$, micro-macrocrack interaction, and (right) $\beta/\alpha = 2$, micro-microcrack interaction.

the crack-face displacements become smaller in magnitude as compared to the classical elasticity result (dashed line).

The stiffening effect is more clearly depicted in Figure 3 where the ratio of the maximum displacement in couple-stress elasticity $u_x^{(\max)}$ to the respective one in classical elasticity $u_{x\,(\text{cl.})}^{(\max)}$ is plotted against ℓ/α for two different values of the geometric ratios δ/α and β/α. It is observed that the decrease in the maximum couple-stress sliding displacement of the smaller (left) crack is more pronounced for higher values of the ratio β/α, i.e., in the case of micro-macrocrack interaction and for smaller ratios δ/α. It is remarked further that for $\ell/\alpha = 1$ the decrease in the maximum sliding displacement for the smaller crack can be up to 50% (Figure 3).

5.2. Stress intensity factors. The stress intensity factors (SIFs) K_{II} at the four crack-tips are defined as

$$K_{II}^{(a_k)} = \lim_{x \to a_k^-} \sqrt{2\pi(a_k - x)}\,\sigma_{yx} \quad \text{and} \quad K_{II}^{(b_k)} = \lim_{x \to b_k^+} \sqrt{2\pi(x - b_k)}\,\sigma_{yx}, \tag{39}$$

with $k = (1, 2)$. The dominant singular behavior of the shear stress in the vicinity of the crack-tips is due to the singular integrals in (26). Using standard asymptotic results regarding Cauchy-type integrals

[Muskhelishvili 1953], the near-tip shear stresses may be written as

$$
\begin{aligned}
\sigma_{yx}(x \to a_k^-, 0) &= -\frac{\mu(3-2\nu)}{\pi(1-\nu)} \lim_{\hat{x} \to -1^-} \int_{-1}^{1} \frac{\chi_k(\hat{t})}{\sqrt{1-\hat{t}^2}(\hat{x}-\hat{t})} \, d\hat{t} \\
&= \frac{\mu(3-2\nu)}{(1-\nu)} \frac{\chi_k(-1)}{\sqrt{2}} (-1-\hat{x})^{-1/2}, \quad \hat{x} < -1,
\end{aligned}
\tag{40}
$$

$$
\begin{aligned}
\sigma_{yx}(x \to b_k^+, 0) &= -\frac{\mu(3-2\nu)}{\pi(1-\nu)} \lim_{\hat{x} \to +1^+} \int_{-1}^{1} \frac{\chi_k(\hat{t})}{\sqrt{1-\hat{t}^2}(\hat{x}-\hat{t})} \, d\hat{t} \\
&= -\frac{\mu(3-2\nu)}{(1-\nu)} \frac{\chi_k(+1)}{\sqrt{2}} (\hat{x}-1)^{-1/2}, \quad \hat{x} > 1,
\end{aligned}
\tag{41}
$$

with $k = (1, 2)$.

Accordingly, the SIFs assume the following form

$$
\begin{aligned}
K_{II}^{(a_k)} &= \frac{\mu(3-2\nu)}{(1-\nu)} \sqrt{\frac{\pi(b_k - a_k)}{2}} \chi_k(-1), \qquad k = (1, 2), \\
K_{II}^{(b_k)} &= -\frac{\mu(3-2\nu)}{(1-\nu)} \sqrt{\frac{\pi(b_k - a_k)}{2}} \chi_k(+1), \quad k = (1, 2).
\end{aligned}
\tag{42}
$$

The values of the unknown densities at the crack-tips $\chi_k(\pm 1)$ can be evaluated using Krenk's interpolation technique [1975]. It is worth noting that in classical elasticity the SIFs are evaluated analytically for the case of two finite length colinear cracks (see, e.g., [Yokobori and Ichikawa 1967]). For the inner crack-tips (b_1, a_2), the classical SIFs assume the following form:

$$
\begin{aligned}
K_{II\,\text{cl.}}^{(b_1)} &= \frac{\sqrt{2\pi}S}{2} \sqrt{\frac{b_2 - b_1}{(a_2 - b_1)(b_1 - a_1)}} \left((b_1 - a_1) - (a_2 - a_1) f(m) \right), \\
K_{II\,\text{cl.}}^{(a_2)} &= \frac{\sqrt{2\pi}S}{2} \sqrt{\frac{a_2 - a_1}{(b_2 - a_2)(a_2 - b_1)}} \left((b_2 - a_2) - (b_2 - b_1) f(m) \right),
\end{aligned}
\tag{43}
$$

with

$$
f(m) = \frac{K[m] - E[m]}{K[m]}, \quad m = \sqrt{\frac{(b_2 - a_2)(b_1 - a_1)}{(b_2 - b_1)(a_2 - a_1)}},
\tag{44}
$$

where $K[m]$ and $E[m]$ are the complete Elliptic integrals of the first and second kind with modulus m.

Figure 4 illustrates the variation of the normalized SIF $K_{II}^{(a_2)}/K_{II}^{(N)}$ of the crack-tip a_2 with respect to the normalized separation distance δ/α in couple-stress and classical elasticity. $K_{II}^{(N)}$ is the nominal macrocrack SIF, i.e., the SIF that would prevail in the absence of the microcrack 2α. In classical elasticity the nominal SIF is $K_{II}^{(N)} = S\sqrt{\pi\beta}$. In the couple-stress case the nominal SIF depends also upon the microstructural ratio α/ℓ and is always higher than the classical one as it was shown in [Gourgiotis and Georgiadis 2007]. It is observed that the normalized SIF is always greater than unity which, in turn, implies that the presence of the microcrack amplifies the shear stresses at the inner tip (a_2) of the macrocrack creating thus a stress aggravation effect. It is worth noting, however, that for smaller α/ℓ ratios, i.e., when the length of the microcrack becomes comparable to the material microstructure, this
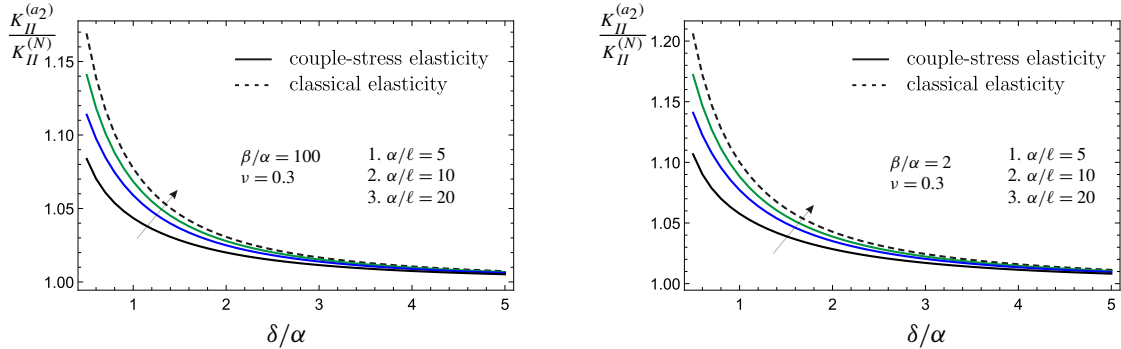
Figure 4. Variation of the normalized SIF $K_{II}^{(a_2)}/K_{II}^{(N)}$ of the inner crack-tip a_2 versus the normalized separation distance δ/α for various values of the microstructural ratio α/ℓ: (left) $\beta/\alpha = 100$, micro-macrocrack interaction, and (right) $\beta/\alpha = 2$, micromicrocrack interaction.
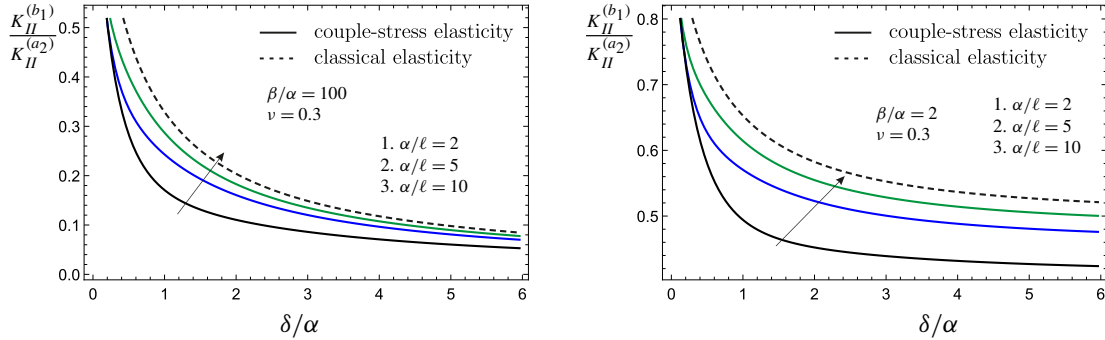
Figure 5. Variation of the ratio of the SIFs $K_{II}^{(b_1)}/K_{II}^{(a_2)}$ of the inner crack-tips in couplestress and in classical elasticity versus the normalized separation distance δ/α for various values of the microstructural ratio α/ℓ: (left) $\beta/\alpha = 100$, micro-macrocrack interaction, and (right) $\beta/\alpha = 2$, micro-microcrack interaction.

stress aggravation becomes less pronounced. Moreover, comparing Figure 4, left, with Figure 4, right, we note that:

(i) the length of the larger crack does not affect significantly the variation of the normalized SIF, and

(ii) that the interaction between the two cracks can be neglected when the separation distance is $\delta > 5\alpha$.

Figure 5 depicts the variation of the ratio of the SIFs $K_{II}^{(b_1)}/K_{II}^{(a_2)}$ of the inner crack-tips: b_1 (left crack) and a_2 (right crack) with respect to the normalized separation distance δ/α for various microstructural ratios α/ℓ. Figure 5, left, shows the case of a micro-macrocrack interaction with $\beta/\alpha = 100$, while Figure 5, right, examines the case of a micro-microcrack interaction with $\beta/\alpha = 2$. The ratio is always below unity which shows that the crack propagation will be initiated from the tip of the largest crack. Moreover, in both cases, a significant decrease in the SIFs ratio is observed as compared to the classical elasticity result (dashed line) for decreasing values of α/ℓ. In light of the above and bearing also in mind that $K_{II}^{(a_2)}$ decreases with increasing ℓ/α (see Figure 4), we may conclude that the effect of the larger

crack to the microcrack is less pronounced when couple-stress effects are taken into account. Finally, we note that as $\ell/\alpha \to 0$ the SIFs ratio in couple-stress theory tends to its classical counterpart.

5.3. *Energy release rates.*

The J-integral was first established in the context of couple-stress elasticity by Atkinson and Leppington [1974; 1977] In the static case, the J-integral is identified as the energy release rate (ERR) and is path-independent [Lubarda and Markenscoff 2000]. For the evaluation of the ERR a rectangular shaped contour is considered centered at the crack-tip, with vanishing "height" along the y-direction and of length 2ε [Freund 1990]. Letting $\varepsilon \to 0$ allows us to use only the asymptotic near-tip fields. For the plane-strain case considered here, the J-integral assumes the following form [Gourgiotis et al. 2012]

$$
J = -2 \lim_{\varepsilon \to +0} \int_{c_t-\varepsilon}^{c_t+\varepsilon} \left\{ \sigma_{yy}(x, +0) \frac{\partial u_y(x, +0)}{\partial x} + \sigma_{yx}(x, +0) \frac{\partial u_x(x, +0)}{\partial x} + m_{yz}(x, +0) \frac{\partial \omega(x, +0)}{\partial x} \right\} dx
$$

$$
= -2 \lim_{\varepsilon \to +0} \int_{c_t-\varepsilon}^{c_t+\varepsilon} \sigma_{yx}(x, +0) \frac{\partial u_x(x, +0)}{\partial x} \, dx, \tag{45}
$$

where c_t denotes the location of the crack-tip, i.e., $c_t = \{a_1, b_1, a_2, b_2\}$. Note that the normal stress $\sigma_{yy}(x, \pm 0)$ and the couple-stress $m_{yz}(x, \pm 0)$ are *zero* along the whole crack line ($y = 0$) for the shear mode case.

Now, by utilizing the asymptotic solutions (40) and (41) in conjunction with (20) and (36) and Fisher's theorem for products of singular distributions (see, e.g., [Georgiadis 2003; Gourgiotis et al. 2012; Gourgiotis and Piccolroaz 2014]), we derive the final expressions for the ERRs in couple-stress elasticity:

$$
\begin{aligned}
J_{II} &= \frac{\mu(3-2\nu)}{2(1-\nu)} \frac{\pi(b_k - a_k)}{2} \chi_k^2(-1) \text{ at crack-tip } a_k, \quad k = (1, 2), \\
J_{II} &= \frac{\mu(3-2\nu)}{2(1-\nu)} \frac{\pi(b_k - a_k)}{2} \chi_k^2(+1) \text{ at crack-tip } b_k, \quad k = (1, 2).
\end{aligned} \tag{46}
$$

Comparing the above results with (42), the following relations can be established connecting the SIFs and the ERRs in couple-stress plane-strain elasticity

$$
J_{II} = \frac{(1-\nu)}{2\mu(3-2\nu)} K_{II}^2, \tag{47}
$$

while the respective relation in classical LEFM is

$$
J_{II}^{(\text{cl.})} = \frac{(1-\nu)}{2\mu} K_{II_{\text{cl.}}}^2. \tag{48}
$$

The variation of the ratio of the ERR in couple-stress theory to the respective one in the classical theory is shown in Figure 6 with respect to the microstructural ratio ℓ/α for a constant separation distance $\delta = 2\alpha$. The inner crack-tips b_1 and a_2 of the two colinear shear cracks are examined. It is observed that in all cases, the ratio $J_{II}/J_{II}^{(\text{cl.})}$ tends to unity when the characteristic material length tends to zero, $\ell \to 0$. This finding shows that the couple-stress solution converges to the classical one when the material microstructure is not considered. On the other hand, when $\ell \neq 0$, the ratio $J_{II}/J_{II}^{(\text{cl.})}$ decreases monotonically with increasing values of ℓ/α which implies that the couple-stress theory predicts a *strengthening effect* since a reduction of the crack driving force takes place as the material microstructure becomes more pronounced.
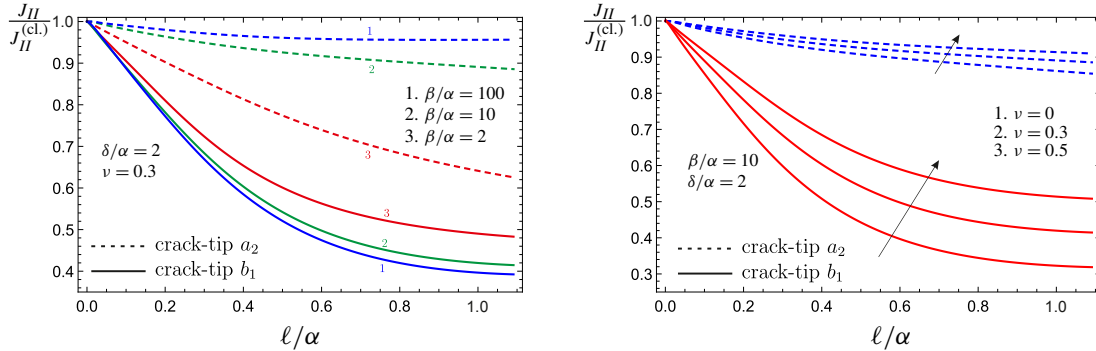
Figure 6. Variation of the ratio of the ERRs in couple-stress and classical elasticity versus the microstructural ratio ℓ/α for various values of (left) β/α, and (right) the Poisson's ratio ν. The inner crack-tips b_1 (solid lines) and a_2 (dashed lines) are examined.

More specifically, it is noted that in the case of the micro-macrocrack interaction, $\beta/\alpha = 100$ (Figure 6, left), the ERR at the tip b_1 of the microcrack (blue solid line) decreases significantly as compared to its classical counterpart for increasing ratios ℓ/α. On the other hand, couple-stresses have little effect on the ERR at the crack-tip a_2 of the macrocrack (blue dashed line) as the ratio $J_{II}/J_{II}^{(cl.)}$ remains close to unity for all values of ℓ/α. These findings show that:

(i) the macrocrack strongly affects the behavior of the microcrack,

(ii) the presence of the microstructure shields the microcrack, and

(iii) the larger the macrocrack, the less significant the couple-stress effects are on its crack driving force.

Finally, regarding the effects of the Poisson's ratio, it is observed from Figure 6, right, that the strengthening effects are more pronounced for smaller values of ν.

The influence of the normalized separation distance δ/α upon $J_{II}/J_{II}^{(cl.)}$ is examined in Figure 7 for a micro-macrocrack configuration (Figure 7, left) and a micro-microcrack configuration (Figure 7, right). The strengthening of the microcrack due to the presence of the microstructure is observed also in this case. When the cracks are of comparable length (Figure 7, right) then there is a limiting separation distance above which the interaction between the microcracks can be neglected. For $\beta = 2\alpha$ the limiting distance is $\delta > 10\alpha$ (Figure 7, right — dashed lines). In this case, the cracks behave as single cracks in an infinite couple-stress material, a problem that has been previously studied by Gourgiotis and Georgiadis [2007].

The variation of the ratio of ERRs $J_{II}/J_{II}^{(cl.)}$ with respect to ℓ/δ is illustrated in Figure 8 for various values of β/α and a fixed ratio $\delta/\alpha = 1$. The inner crack-tips b_1 and a_2 are examined. It is observed that in the case of the micro-macrocrack interaction problem, $\beta/\alpha = 100$ (blue lines), the ERR for the b_1 crack-tip (blue solid line) suffers a significant decrease (compared to the classical value) as the separation distance becomes comparable to the material length ℓ, highlighting again the fact that the macrocrack shields the microcrack further when the material microstructure is more pronounced. On the other hand, the decrease in the ERR is less significant when considering the a_2 crack-tip of the macrocrack (dashed blue line) since the crack length is much larger than the material length scale. Note also that unlike the previous cases, the ratio is not monotonically decreasing for all values of ℓ/δ. Indeed, although the ratio experiences a decrease initially, then for $\ell/\delta > 0.6$ it starts to gradually increase again, remaining however always below unity. A similar behavior is noted for the micro-microcrack interaction case, $\beta/\alpha \leq 2$, with
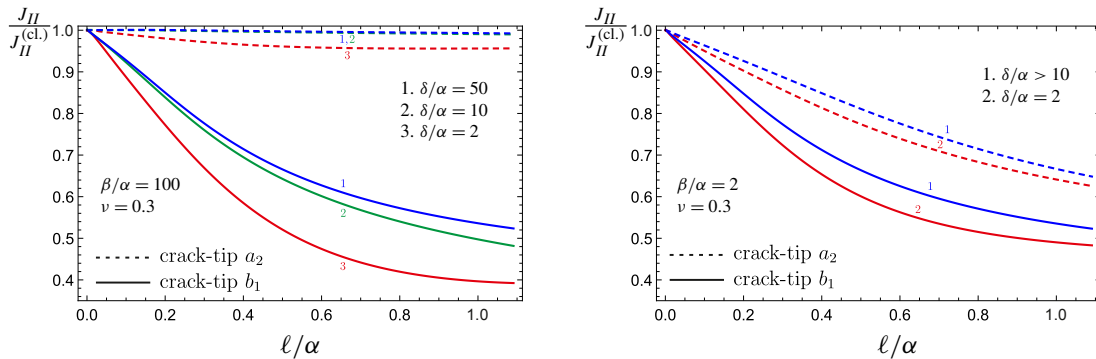
Figure 7. Variation of the ratio of the ERRs in couple-stress and classical elasticity versus the microstructural ratio ℓ/α for various values of the normalized separation distance δ/α: (left) micro-macrocrack interaction, and (right) micro-microcrack interaction. The inner crack-tips b_1 (solid lines) and a_2 (dashed lines) are examined.
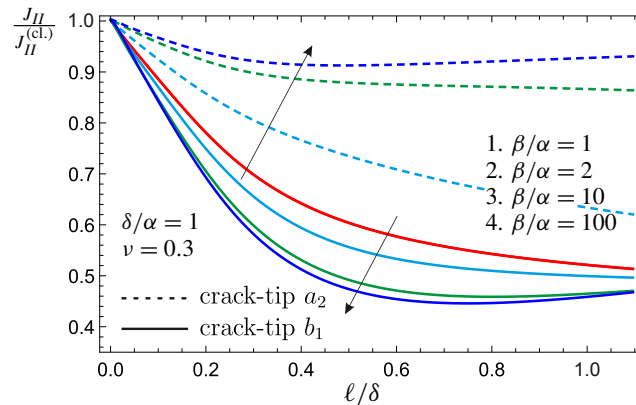

Figure 8. Variation of the ratio of the ERRs in couple-stress and classical elasticity versus ℓ/δ for various values of the geometrical ratio β/α. The inner crack-tips b_1 (solid lines) and a_2 (dashed lines) are examined.

the smallest (left) crack suffering again the greatest decrease. In the case $\beta/\alpha = 1$ both curves (red curve in Figure 8) coincide.

Figure 9 illustrates the variation of the normalized ERR, $J_{II}/J_{II}^{(N)}$, at the crack-tip b_1 of the microcrack, with respect to the microstructural ratio ℓ/α in couple-stress elasticity (solid lines) and classical elasticity (dashed lines). $J_{II}^{(N)}$ is the nominal microcrack ERR, i.e., the ERR that would prevail in the absence of the macrocrack. $J_{II}^{(N)}$ can be obtained from the current solution by letting $\delta/\alpha \to \infty$. Two cases are examined:

 (a) the micro-macrocrack interaction ($\beta/\alpha = 100$), and

 (b) the micro-microcrack interaction ($\beta/\alpha = 2$).

A significant aggravation of the ERR is observed in the micro-macrocrack case (irrespective of the theory employed) as the separation distance δ becomes comparable to the microcrack length 2α (Figure 9, left). In classical elasticity (dashed lines), the ratio $J_{II}/J_{II}^{(N)}$ remains constant since the classical solution does
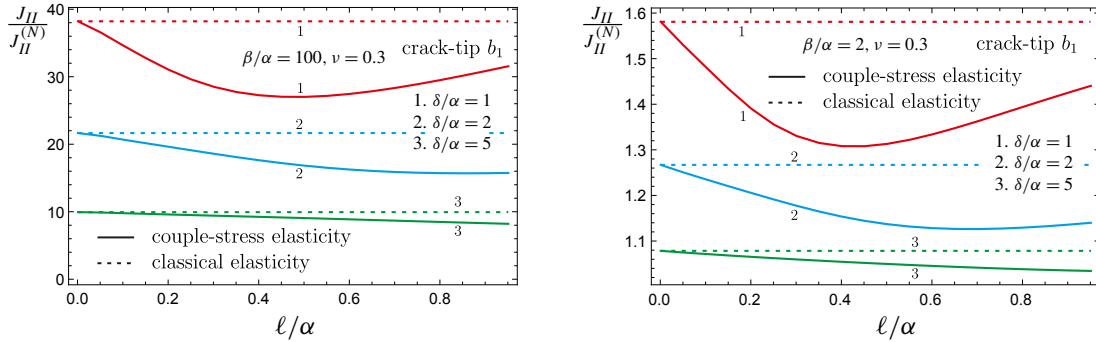
Figure 9. Variation of the normalized ERR at crack-tip b_1 (small crack) versus the microstructural ratio ℓ/α for various values of δ/α: (left) $\beta/\alpha = 100$, and micro-macro crack interaction (right) $\beta/\alpha = 2$, micro-micro crack interaction.

not depend upon ℓ. When couple-stress effects are taken into account, the ratio $J_{II}/J_{II}^{(N)}$ decreases as compared to the classical result, which implies that the material microstructure shields the microcrack. The decrease is more pronounced for smaller separation distances and higher values of ℓ/α. A less pronounced decrease is observed if we examine the corresponding ratio for the α_2 crack tip of the macrocrack. In the micro-microcrack case ($\beta/\alpha = 2$, Figure 9, right), the effect of the larger crack (2β) upon the smaller one (2α) is less significant (as expected) but the couple-stress effects are still dominant especially for small values of the ratio δ/α.

6. Conclusions

The interaction problem of two colinear shear cracks was investigated within the context of couple-stress elasticity. Two configurations which are of special interest were examined in detail: a micro-macrocrack interaction, and a micro-microcrack interaction. It was shown that significant deviations from the predictions of the classical LEFM are found when the geometrical parameters of the problem become comparable to the material length scale of couple-stress theory. Smaller crack-face displacements were observed when the crack-lengths become of the same order as the characteristic material length, corroborating thus the well-known stiffening effect that occurs in all gradient-type theories. As in the classical theory, the presence of the microcrack causes an aggravation of the SIF at the inner tip of the macrocrack. Nonetheless, this aggravation is less pronounced when couple-stress effects are taken into account. The couple-stress theory predicts also strengthening effects since a reduction of the crack driving force in both cracks takes place as the material microstructure becomes more distinct. Finally, it was found that the effect of the macrocrack on the microcrack becomes milder when couple-stresses are considered which verifies that the material microstructure shields the microcrack. The results obtained in the present study will enhance our understanding of the failure mechanisms that govern brittle materials and shed some light on the role of the microstructure in fracture on the microscale.

Appendix: Stress and couple-stress components

The full-field expressions for the stress components $\sigma_{pq}(x, y)$ and the couple-stress components $m_{qz}(x, y)$ are derived by employing the inverse Fourier transform $(21)_2$ in conjunction with the definitions (25).

Reversing the order of integration, we readily obtain

$$\sigma_{pq} = \frac{1}{2\pi}\int_{-\infty}^{\infty}\sigma_{pq}^{*}e^{-i\xi x}\,d\xi = \frac{\mu}{\pi}\sum_{j=1}^{2}\int_{a_j}^{b_j}G_{pq}(x-t,y)h_j(t)\,dt + S(1-\delta_{pq}), \tag{49}$$

$$m_{qz} = \frac{1}{2\pi}\int_{-\infty}^{\infty}m_{pz}^{*}e^{-i\xi x}\,d\xi = \frac{\mu}{\pi}\sum_{j=1}^{2}\int_{a_j}^{b_j}H_{qz}(x-t,y)h_j(t)\,dt, \tag{50}$$

where the indices p and q take the values $\{x,y\}$ and δ_{pq} is the Kronecker delta. The kernel functions G_{pq} and H_{qz} are evaluated in closed form as

$$
\begin{aligned}
G_{xx}(x,y) &= \frac{y(3x^2+y^2)}{(1-\nu)r^4} + \frac{8\ell^2 y(y^2-3x^2)}{r^6} - 4\ell^2\partial_x^2\partial_y K_0\!\left[\frac{r}{\ell}\right], \\[4pt]
G_{yy}(x,y) &= \frac{y(y^2-x^2)}{(1-\nu)r^4} - \frac{8\ell^2 y(y^2-3x^2)}{r^6} + 4\ell^2\partial_x^2\partial_y K_0\!\left[\frac{r}{\ell}\right], \\[4pt]
G_{xy}(x,y) &= \frac{x(y^2-x^2)}{(1-\nu)r^4} + \frac{8\ell^2 x(x^2-3y^2)}{r^6} - 4\ell^2\partial_x\partial_y^2 K_0\!\left[\frac{r}{\ell}\right], \\[4pt]
G_{yx}(x,y) &= \frac{x(y^2-x^2)}{(1-\nu)r^4} + \frac{8\ell^2 x(x^2-3y^2)}{r^6} + 4\ell^2\partial_x^3 K_0\!\left[\frac{r}{\ell}\right],
\end{aligned}
\tag{51}
$$

$$
\begin{aligned}
H_{xz}(x,y) &= \frac{4\ell^2(y^2-x^2)}{r^4} + 4\ell^2\partial_x^2 K_0\!\left[\frac{r}{\ell}\right], \\[4pt]
H_{yz}(x,y) &= -\frac{8\ell^2 xy}{r^4} + 4\ell^2\partial_x\partial_y K_0\!\left[\frac{r}{\ell}\right],
\end{aligned}
\tag{52}
$$

where $r=\sqrt{x^2+y^2}$. Notice that the kernels in (49) and (50) are derived by replacing x with $x-t$ in the above relations. Moreover, we note that the classical elasticity kernels are derived from the above equations by neglecting the terms that involve the characteristic length ℓ.

References

[Anderson and Lakes 1994] W. B. Anderson and R. S. Lakes, "Size effects due to Cosserat elasticity and surface damage in closed-cell polymethacrylimide foam", *J. Mater. Sci.* **29**:24 (1994), 6413–6419.

[Atkinson 1984] B. K. Atkinson, "Subcritical crack growth in geological materials", *J. Geophys. Res.* **89**:B6 (1984), 4077–4114.

[Atkinson and Leppington 1974] C. Atkinson and F. G. Leppington, "Some calculations of the energy-release rate G for cracks in micropolar and couple-stress elastic media", *Int. J. Fract.* **10**:4 (1974), 599–602.

[Atkinson and Leppington 1977] C. Atkinson and F. G. Leppington, "The effect of couple stresses on the tip of a crack", *Int. J. Solids Struct.* **13**:11 (1977), 1103–1122.

[Baxevanakis et al. 2017] K. P. Baxevanakis, P. A. Gourgiotis, and H. G. Georgiadis, "Interaction of cracks with dislocations in couple-stress elasticity, II: Shear modes", *Int. J. Solids Struct.* **118-119** (2017), 192–103.

[Bigoni and Drugan 2007] D. Bigoni and W. J. Drugan, "Analytical derivation of Cosserat moduli via homogenization of heterogeneous elastic materials", *J. Appl. Mech.* (*ASME*) **74**:4 (2007), 741–753.

[Bigoni and Gourgiotis 2016] D. Bigoni and P. A. Gourgiotis, "Folding and faulting of an elastic continuum", *Proc. R. Soc. Lond. A* **472**:2187 (2016), art. id. 20160018.

[Deng and Nemat-Nasser 1994] H. Deng and S. Nemat-Nasser, "Microcrack interaction and shear fault failure", *Int. J. Damage Mech.* **3**:1 (1994), 3–37.

[Dyskin and Pasternak 2015] A. V. Dyskin and E. Pasternak, "Asymptotic analysis of fracture propagation in materials with rotating particles", *Eng. Fract. Mech.* **150** (2015), 1–18.

[Erdogan 1978] F. Erdogan, "Mixed boundary-value problems in mechanics", pp. 1–86 in *Mechanics today, IV*, edited by S. Nemat-Nasser, Pergamon, Oxford, 1978.

[Erdogan and Wu 1993] F. Erdogan and B. Wu, "Interface crack problems in layered orthotropic materials", *J. Mech. Phys. Solids* **41**:5 (1993), 889–917.

[Evans and Faber 1984] A. G. Evans and K. T. Faber, "Crack-growth resistance of microcracking brittle materials", *J. Am. Ceram. Soc.* **67**:4 (1984), 255–260.

[Freund 1990] L. B. Freund, *Dynamic fracture mechanics*, Cambridge Univ. Press, 1990.

[Georgiadis 2003] H. G. Georgiadis, "The mode III crack problem in microstructured solids governed by dipolar gradient elasticity: static and dynamic analysis", *J. Appl. Mech.* (*ASME*) **70**:4 (2003), 517–530.

[Goodarzi et al. 2016] A. Goodarzi, M. Fotouhi, and H. M. Shodja, "Inverse scattering problem of reconstruction of an embedded micro-/nano-size scatterer within couple stress theory with micro inertia", *Mech. Mater.* **103** (2016), 123–134.

[Gourgiotis and Bigoni 2016a] P. A. Gourgiotis and D. Bigoni, "Stress channelling in extreme couple-stress materials, I: Strong ellipticity, wave propagation, ellipticity, and discontinuity relations", *J. Mech. Phys. Solids* **88** (2016), 150–168.

[Gourgiotis and Bigoni 2016b] P. A. Gourgiotis and D. Bigoni, "Stress channelling in extreme couple-stress materials, II: Localized folding vs faulting of a continuum in single and cross geometries", *J. Mech. Phys. Solids* **88** (2016), 169–185.

[Gourgiotis and Bigoni 2017] P. A. Gourgiotis and D. Bigoni, "The dynamics of folding instability in a constrained Cosserat medium", *Phil. Trans. R. Soc. A* **375**:2093 (2017), art. id. 20160159.

[Gourgiotis and Georgiadis 2007] P. A. Gourgiotis and H. G. Georgiadis, "Distributed dislocation approach for cracks in couple-stress elasticity: shear modes", *Int. J. Fract.* **147**:1-4 (2007), 83–102.

[Gourgiotis and Georgiadis 2008] P. A. Gourgiotis and H. G. Georgiadis, "An approach based on distributed dislocations and disclinations for crack problems in couple-stress elasticity", *Int. J. Solids Struct.* **45**:21 (2008), 5521–5539.

[Gourgiotis and Georgiadis 2011] P. A. Gourgiotis and H. G. Georgiadis, "The problem of sharp notch in couple-stress elasticity", *Int. J. Solids Struct.* **48**:19 (2011), 2630–2641.

[Gourgiotis and Piccolroaz 2014] P. A. Gourgiotis and A. Piccolroaz, "Steady-state propagation of a mode II crack in couple stress elasticity", *Int. J. Fract.* **188**:2 (2014), 119–145.

[Gourgiotis et al. 2012] P. A. Gourgiotis, H. G. Georgiadis, and M. D. Sifnaiou, "Couple-stress effects for the problem of a crack under concentrated shear loading", *Math. Mech. Solids* **17**:5 (2012), 433–459.

[Gourgiotis et al. 2016] P. A. Gourgiotis, T. Zisis, and K. Baxevanakis, "Analysis of the tilted flat punch in couple-stress elasticity", *Int. J. Solids Struct.* **85-86** (2016), 34–43.

[Grentzelou and Georgiadis 2005] C. G. Grentzelou and H. G. Georgiadis, "Uniqueness for plane crack problems in dipolar gradient elasticity and in couple-stress elasticity", *Int. J. Solids Struct.* **42**:24-25 (2005), 6626–6244.

[Hoagland et al. 1974] R. G. Hoagland, C. W. Marschall, A. R. Rosenfield, G. Hollenberg, and R. Ruh, "Microstructural factors influencing fracture toughness of hafnium titanate", *Mater. Sci. Eng.* **15**:1 (1974), 51–62.

[Huang et al. 1997] Y. Huang, L. Zhang, T. F. Guo, and K.-C. Hwang, "Mixed mode near-tip fields for cracks in materials with strain-gradient effects", *J. Mech. Phys. Solids* **45**:3 (1997), 439–465.

[Kachanov 1993] M. Kachanov, "Elastic solids with many cracks and related problems", *Adv. Appl. Mech.* **30** (1993), 259–445.

[Karuriya and Bhandakkar 2017] A. N. Karuriya and T. K. Bhandakkar, "Plane strain indentation on finite thickness bonded layer in couple stress elasticity", *Int. J. Solids Struct.* **108** (2017), 275–288.

[Koiter 1964] W. T. Koiter, "Couple-stresses in the theory of elasticity, I, II", *P. K. Ned. Akad. Wetensc. B* **67** (1964), 17–44.

[Kreher and Pompe 1981] W. Kreher and W. Pompe, "Increased fracture toughness of ceramics by energy-dissipative mechanisms", *J. Mater. Sci.* **16**:3 (1981), 694–706.

[Krenk 1975] S. Krenk, "On the use of the interpolation polynomial for solutions of singular integral equations", *Quart. Appl. Math.* **32** (1975), 479–484.

[Lakes 1983] R. Lakes, "Size effects and micromechanics of a porous solid", *J. Mater. Sci.* **18**:9 (1983), 2572–2580.

[Lakes 2016] R. S. Lakes, "Physical meaning of elastic constants in Cosserat, void, and microstretch elasticity", *J. Mech. Mater. Struct.* **11**:3 (2016), 217–229.

[Lakes 2018] R. S. Lakes, "Stability of Cosserat solids: size effects, ellipticity and waves", *J. Mech. Mater. Struct.* **13**:1 (2018), 83–91.

[Lubarda and Markenscoff 2000] V. A. Lubarda and X. Markenscoff, "Conservation integrals in couple stress elasticity", *J. Mech. Phys. Solids* **48**:3 (2000), 553–564.

[Mindlin 1963] R. D. Mindlin, "Influence of couple-stresses on stress concentrations", *Exp. Mech.* **3**:1 (1963), 1–7.

[Mindlin and Tiersten 1962] R. D. Mindlin and H. F. Tiersten, "Effects of couple-stresses in linear elasticity", *Arch. Ration. Mech. Anal.* **11** (1962), 415–448.

[Morini et al. 2014] L. Morini, A. Piccolroaz, and G. Mishuris, "Remarks on the energy release rate for an antiplane moving crack in couple stress elasticity", *Int. J. Solids Struct.* **51**:18 (2014), 3087–3100.

[Muki and Sternberg 1965] R. Muki and E. Sternberg, "The influence of couple-stresses on singular stress concentrations in elastic solids", *Z. Angew. Math. Phys.* **16** (1965), 611–648.

[Muskhelishvili 1953] N. I. Muskhelishvili, *Singular integral equations*, Noordhoff, Groningen, 1953.

[Nara et al. 2011] Y. Nara, P. G. Meredith, T. Yoneda, and K. Kaneko, "Influence of macro-fractures and micro-fractures on permeability and elastic wave velocities in basalt at elevated pressure", *Tectonophys.* **503**:1-2 (2011), 52–59.

[Noselli et al. 2013] G. Noselli, V. S. Deshpande, and N. A. Fleck, "An analysis of competing toughening mechanisms in layered and particulate solids", *Int. J. Fract.* **183**:2 (2013), 241–258.

[Piccolroaz and Movchan 2014] A. Piccolroaz and A. B. Movchan, "Dispersion and localisation in structured Rayleigh beams", *Int. J. Solids Struct.* **51**:25-26 (2014), 4452–4461.

[Piccolroaz et al. 2012] A. Piccolroaz, G. Mishuris, and E. Radi, "Mode III interfacial crack in the presence of couple-stress elastic materials", *Eng. Fract. Mech.* **80** (2012), 60–71.

[Radi 2008] E. Radi, "On the effects of characteristic lengths in bending and torsion on Mode III crack in couple stress elasticity", *Int. J. Solids Struct.* **45**:10 (2008), 3033–3058.

[Rice et al. 1994] R. W. Rice, C. C. Wu, and F. Borchelt, "Hardness–grain-size relations in ceramics", *J. Am. Ceram. Soc.* **77**:10 (1994), 2539–2553.

[Rose 1986] L. R. F. Rose, "Effective fracture toughness of microcracked materials", *J. Am. Ceram. Soc.* **69**:3 (1986), 212–214.

[Rubinstein 1985] A. A. Rubinstein, "Macrocrack interaction with semi-infinite microcrack array", *Int. J. Fract.* **27**:2 (1985), 113–119.

[Shao and Rudnicki 2000] J. F. Shao and J. W. Rudnicki, "A microcrack-based continuous damage model for brittle geomaterials", *Mech. Mater.* **32**:10 (2000), 607–619.

[Song et al. 2017] H.-X. Song, L.-L. Ke, and Y.-S. Wang, "Sliding frictional contact analysis of an elastic solid with couple stresses", *Int. J. Mech. Sci.* **133** (2017), 804–816.

[Sternberg and Muki 1967] E. Sternberg and R. Muki, "The effect of couple-stresses on the stress concentration around a crack", *Int. J. Solids Struct.* **3**:1 (1967), 69–95.

[Toupin 1962] R. A. Toupin, "Elastic materials with couple-stresses", *Arch. Ration. Mech. Anal.* **11** (1962), 385–414.

[Wang et al. 2017] C. D. Wang, P. J. Wei, P. Zhang, and Y. Q. Li, "Influences of a visco-elastically supported boundary on reflected waves in a couple-stress elastic half-space", *Arch. Mech. Stos.* **69**:2 (2017), 131–156.

[Wang et al. 2018] Y. Wang, H. Shen, X. Zhang, B. Zhang, J. Liu, and X. Li, "Semi-analytical study of microscopic two-dimensional partial slip contact problem within the framework of couple stress elasticity: cylindrical indenter", *Int. J. Solids Struct.* **138** (2018), 76–86.

[Yokobori and Ichikawa 1967] T. Yokobori and M. Ichikawa, "The interaction of parallel elastic cracks and parallel slip bands respectively based on the concept of continuous distribution of dislocations, II", *Rep. Res. Inst. Strength Fract. Mater.* **3**:1 (1967), 15–37.

[Zisis 2018] T. Zisis, "Anti-plane loading of microstructured materials in the context of couple stress theory of elasticity: half-planes and layers", *Arch. Appl. Mech.* **88**:1-2 (2018), 97–110.

[Zisis et al. 2014] T. Zisis, P. A. Gourgiotis, K. P. Baxevanakis, and H. Georgiadis, "Some basic contact problems in couple stress elasticity", *Int. J. Solids Struct.* **51**:11-12 (2014), 2084–2095.

[Zisis et al. 2015] T. Zisis, P. A. Gourgiotis, and F. Dal Corso, "A contact problem in couple stress thermoelasticity: the indentation by a hot flat punch", *Int. J. Solids Struct.* **63** (2015), 226–239.

PANOS A. GOURGIOTIS: `panagiotis.gourgiotis@durham.ac.uk`
Department of Engineering, Durham University, Durham, United Kingdom

SUBMISSION GUIDELINES

ORIGINALITY

Authors may submit manuscripts in PDF format online at the Submissions page. Submission of a manuscript acknowledges that the manuscript is original and has neither previously, nor simultaneously, in whole or in part, been submitted elsewhere. Information regarding the preparation of manuscripts is provided below. Correspondence by email is requested for convenience and speed. For further information, write to contact@msp.org.

LANGUAGE

Manuscripts must be in English. A brief abstract of about 150 words or less must be included. The abstract should be self-contained and not make any reference to the bibliography. Also required are keywords and subject classification for the article, and, for each author, postal address, affiliation (if appropriate), and email address if available. A home-page URL is optional.

FORMAT

Authors can use their preferred manuscript-preparation software, including for example Microsoft Word or any variant of TeX. The journal itself is produced in LaTeX, so accepted articles prepared using other software will be converted to LaTeX at production time. Authors wishing to prepare their document in LaTeX can follow the example file at www.jomms.net (but the use of other class files is acceptable). At submission time only a PDF file is required. After acceptance, authors must submit all source material (see especially Figures below).

REFERENCES

Bibliographical references should be complete, including article titles and page ranges. All references in the bibliography should be cited in the text. The use of BibTeX is preferred but not required. Tags will be converted to the house format (see a current issue for examples); however, for submission you may use the format of your choice. Links will be provided to all literature with known web locations; authors can supply their own links in addition to those provided by the editorial process.

FIGURES

Figures must be of publication quality. After acceptance, you will need to submit the original source files in vector format for all diagrams and graphs in your manuscript: vector EPS or vector PDF files are the most useful. (EPS stands for Encapsulated PostScript.)

Most drawing and graphing packages—Mathematica, Adobe Illustrator, Corel Draw, MATLAB, etc.—allow the user to save files in one of these formats. Make sure that what you're saving is vector graphics and not a bitmap. If you need help, please write to graphics@msp.org with as many details as you can about how your graphics were generated.

Please also include the original data for any plots. This is particularly important if you are unable to save Excel-generated plots in vector format. Saving them as bitmaps is not useful; please send the Excel (.xls) spreadsheets instead. Bundle your figure files into a single archive (using zip, tar, rar or other format of your choice) and upload on the link you been given at acceptance time.

Each figure should be captioned and numbered so that it can float. Small figures occupying no more than three lines of vertical space can be kept in the text ("the curve looks like this:"). It is acceptable to submit a manuscript with all figures at the end, if their placement is specified in the text by means of comments such as "Place Figure 1 here". The same considerations apply to tables.

WHITE SPACE

Forced line breaks or page breaks should not be inserted in the document. There is no point in your trying to optimize line and page breaks in the original manuscript. The manuscript will be reformatted to use the journal's preferred fonts and layout.

PROOFS

Page proofs will be made available to authors (or to the designated corresponding author) at a Web site in PDF format. Failure to acknowledge the receipt of proofs or to return corrections within the requested deadline may cause publication to be postponed.